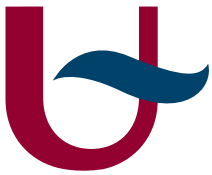

UNIVERSITEIT ANTWERPEN
Faculteit Wetenschappen
Departement Fysica

Magnetic, Calorimetric and Electronic Properties of Vortex States in (3D) Mesoscopic Superconductors

---

Magnetische, calorimetrische en elektronische eigenschappen van vortexmaterie in (3D) mesoscopische supergeleiders

---

（三维）介观超导体中涡旋态的磁学量热学和电子学性质研究

Proefschrift voorgelegd tot het behalen van de graad van
Doctor in de Wetenschappen
aan de Universiteit Antwerpen, te verdedigen door

Ben XU

Promotoren

Prof. Dr. F. M. Peeters

Prof. Dr. M. V. Milošević

Antwerpen

September, 2011

Members of the Jury:

Chairman
Jacques Tempère , Universiteit Antwerpen, Belgium

Promotors
François Peeters , Universiteit Antwerpen, Belgium
Milorad Milošević, Universiteit Antwerpen, Belgium

Members
Feodor Kusmartsev, Loughborough University, United Kingdom
Alejandro Silhanek, Katholieke Universiteit Leuven, Belgium
Sara Bals, Universiteit Antwerpen, Belgium
Wim Vanroose, Universiteit Antwerpen, Belgium

Contact Information

Ben XU
Universiteit Antwerpen
Departement Fysica
Groenenborgerlaan 171
2020 Antwerpen
België
ben.xu@ua.ac.be

Acknowledgements

My PhD work is the biggest challenge that I have taken in my life up to now. At the end of it, it is time to honor all people who significantly influenced my development both, scientific and personal. Before I came Belgium, I am just a 'kid' in Physics study, with a dream of being physicist, but not even finished the course of Quantum Mechanics. So first of all, I would like to thanks my Promotors Prof. Milošević and Prof. Francois, who provided me this valuable chance to realize my dream. Moreover, for your continuous efforts and lots of patience in training me on the way to be a professional physicist. Your constant belief in me and discussions with me put the fundamentals to my further career. And also because of your support, that I was able to travel for conferences and summer schools, and meet many great scientists.

I have privilege to be introduced to the interesting field of modeling of vortex structures by Dr. Vyacheslav Misko. His expertise and unselfish help set me in the right direction. Also I would like to acknowledge all the professors in my study of advanced master in Nano Physics, who laid the foundations for my PhD research.

I am grateful to our collaborators from Mathematical department of University of Antwerp, Wim Vanroose and Nico Schlömer, who help me a lot for the numerical realization, and we had many illuminating discussions. And would like to express my deepest gratitude to Prof. Dr. B. Jankó and Shi-Hsin Lin, from University of Notre Dame, who provide instructive suggestions to my research work.

It is my privilege to work in CMT group. Particular thanks to, Vladan Mlinar and Golibjon Berdiyorov, who guided my through the first several years in my PhD study, step by step. Roeland Geurts and Kwinten Nelissen, who helped me a lot scientifically and personally. My office mate Lucia, William and Hamilton, whom I am enjoy to work with.

同时也非常感谢我在比利时的朋友, 鲍莹师姐, 聂臻唐正夫妇, 李斌晓丹夫妇, 很 开心和你们一起相处的日子。另外, 我们实验室、学校的朋友, 海军, 亚江, 老谭, 石慧凌云夫妇, 林南省, 卢博夫妇, 刘超宇, 田博夫妇, 张凌峰, 很幸运和你们度过 了六年美妙的时光。感谢徐强和小丽姐, 在生活和工作中无微不至的关怀, 情同亲 人。感谢清华大学阮东老师, 是我的良师益友。另外,还有一起来比求学的朋友, 小 麦, 珊珊, 肖, 胡子, 老衣, 大家有缘一起度过了最辛苦的时光。同时对郝运铼同学 表示深深的怀念。最后, 最诚挚的感谢我的夫人, 柯小行(番茄), 她为我的成长付出了非常多, 能 够在这里和她相识相依是我最大的幸福,她是我力量的源泉。还有我的父母,是他们 的言传身教让我走上了正确的道路。

This work was supported by the Flemish Science Foundation (FWO), the Belgian Science Policy (IAP).

Contents

1 Introduction

The year 2008 marked the 100 years centenary of the liquefaction of Helium, and this year is the 100 years centenary of the discovery of superconductivity. After 100 years of development, superconductivity finally becomes implemented: on macroscopic-scale for transportation of electricity in USA and Korea [1] and for powerful magnets in e.g. Large Hadron Collider (LHC) in CERN [2], maglev trains [3] in China and Japan, and nuclear magnetic resonance (NMR) medical magnets all over the world. On the microscopic-scale, it is used as the principle in superconducting quantum interference device (SQUID) and in Josephson junctions, which are basic elements of modern magnetic brain and heart diagnostic tools based on detection of ultra-weak magnetic fields, and also used as futuristic superconducting Qubits, the potential basis of the next generation of computer hardware [4, 5, 6, 7]. In all these applications, the performance is strongly dependent on the behavior of the magnetic flux inside the devices, especially on the mesoscopic scale, where the characteristic features of the superconductors are comparable to the size of the magnetic flux quanta i.e. vortices. In the last decade, most efforts were dedicated to the study of vortices in two-dimensional (2D) mesoscopic superconducting systems. In this thesis, we give a theoretical description of the superconducting states in the three-dimensional (3D) mesoscopic superconductors, with emphasis on novel vortex behavior as a consequence of the confinement in the third dimension, and possible electronic, magnetic and calorimetric evidence of that behavior in experimental measurements.

In the first chapter of this thesis, a brief introduction will be given to several theoretical and experimental aspects of superconductivity. Ginzburg-Landau and Eilenberger equations are first derived, respectively, from phenomenological and microscopic points of view. The critical magnetic fields of a superconductor ($H_{ci,i=1,2,3}$) are thus defined, as well as the coherence length ξ and the magnetic field penetration length λ. Determined by the ratio of λ/ξ, which is known as Ginzburg-Landau parameter κ, superconductors are divided into type-I and type-II. Further it is shown that in bulk type-II materials, the magnetic field penetrates into the superconductor in terms of vortices; ortices inter-

act with each other, with the sample's boundary and with defects inside the sample as well. On top of that, the vortex acts as a quantum well for the quasi-pariticles inside the superconductor, as a result of which the excitation spectrum can be measured by Scanning Tunneling Microscopy (STM). Finally, several other measurement methods are also discussed in the last part of chapter I.

The subsequent three chapters are devoted to discussion of the influence of sample geometry on vortex behavior in 3D superconducting samples. First, in chapter II, the vortex configurations are studied in a mesoscopic superconducting sphere by solving GL equations self-consistently, with full consideration of demagnetization effects. Different superconducting materials are studied, both type-I and type-II ones. Phase diagrams are constructed for different vortex states as a function of the size of the sample. The magnetic field distribution is calculated inside and outside the sample, which provides a guildline to optimize the magnetometry measurements and distinguish different 3D vortex states. In chapter III, in order to study the interaction between vortex states, the sample boundary and a defect with size $\sim \xi$, superconducting samples with a cylindrical hole or a spherical cavity are studied. The interplay of the competing geometries is discussed by changing the size of the perforation, the direction of the applied field and the GL parameter κ. Due to the competing interactions, the asymmetric vortex state is discovered in a perforated superconducting sphere, which has never been found in superconducting disks and cylinders. A further consequence of vortex interaction with the outer surface and inner perforation of the sample, is that flux can penetrate inside the sample in amounts higher than one flux quantum. Again, the vortex phase diagrams are constructed, and the appearance of asymmetric states in the ground state, as well as the multi-vortex states and multi-quanta vortices pinned by the hole are discussed as a function of the hole size and applied field, also in the case of a tilted magnetic field. In chapter IV, the second-order multi-flux quanta vortex entry is discussed for 3D superconductors, enabled by the interplay of the Bean-Livingston and the geometric energy barriers in this case for flux entry. The energy barriers are adjusted by changing the shape and distance between different boundaries, and novel vortex states and novel superconducting states (e.g. the one opposite to surface superconductivity) are found.

The final two chapters of this thesis are focused on thermal and electronic response of the system to the external magnetic field, which can be measured experimentally by calorimetry and transport measurements. In chapter V, the heat capacity dependence on magnetic field is studied for thin (effectively 2D) disks and rings, and a correlation between the features in heat capacity and the vortex entry is shown. In 3D samples, the specific heat or magnetic field curve can indicate when the morphology of the vortices changes deep inside the sample, which is invisible for surface techniques (e.g. STM and MFM/SHPM). As discussed in chapter VI, the heat capacity also exhibits an abrupt change during the giant-to-multi vortex transition, which provides a first clear thermodynamic distinction between these two allotropes of the vortex state for a given vorticity. The microscopic explanation is given by solving the quasi-classical Eilenberger equations, where the local density of states (LDOS) is calculated for a vortex in different materials. The parity phenomena of the low energy excitation in a mesocopic superconducting disk, and the V-shape of the total DOS as function of the energy are shown, which link the measured heat capacity and the DOS distribution. The link between heat capacity and magnetic susceptibility is also discussed, including the related experiments. The thesis is summarized in chapter VII.

1.1 INTRODUCTION TO SUPERCONDUCTIVITY

1.1.1 Historical overview

A milestone was achieved on 10 July 1908 when Heike Kamerlingh Onnes at the Leiden University in Leiden produced, for the first time, liquified helium. On April 8 1911, he reached the temperature of 4.19 K and observed that the resistivity of mercury abruptly disappeared. Later on he reversed the process and found that at 4.2 K the resistance returned to the material [8]. He published several articles about the phenomenon and initially named the phenomenon "supraconductivity" (only later, he adopted the term "superconductivity"). For his liquifaction of Helium, he was awarded the Nobel Prize in Physics in 1913. In the years to follow, superconductivity was found in several other materials. In 1913, Lead was found to superconduct at 7 K, superconductivity in tantalum was announced in 1928 with $T_c = 4.4$K, thorium in 1929 with $T_c = 1.4$K niobium in 1930 with $T_c = 9.2$K, and in 1941 niobium nitride was found to superconduct at 16 K. The transition temperature at which resistance disappeared was named as the critical temperature T_c.

It was generally believed until 1933 that a superconductor was simply an ideal conductor. However the experiments of W. Meissner and R. Ochsenfeld showed that was not entirely true. They discovered that superconductors expelled applied magnetic fields, no matter in which procedure the sample had been cooled through T_c [9]. A superconductor with little or no magnetic field within itself called to be in the Meissner state. Superconductors in the Meissner state show the same behavior as perfect diamagnet, though the origins of these phenomena are fundamentally different. In superconductors the perfect diamagnetism arises from persistent screening currents which flow to oppose the applied field, not solely from the orbital spin spontaneously directing against the applied field as is the case in standard diamagnets. The Meissner state breaks down when the applied magnetic field is too large.

The discovery of the Meissner effect implied that we could treat a transition to the superconducting state as a phase transition and, consequently, apply all the might of the thermodynamic approach to examine the superconducting phase. This led to the phenomenological theory of superconductivity by Fritz and Heinz London in 1935 [10], two decades after the experimental discovery of superconductivity. They postulated two equations, in addition to Maxwell's equations, governing the electromagnetic field in a superconductor. However, they did not identify the microscopic origins of superconductivity. Nevertheless, the two equations provided a correct description of two basic properties of the superconductors: absolute diamagnetism and zero resistance to a dc current. However, in the end of the 1940's, it was clear that at least to one question London theory gave the wrong answer, that the surface energy between adjacent superconducting and normal regions was always negative. This implied that when the superconductor was in an applied magnetic field, it would always maximize the area of the interface ith normal metallic reas large as possible, to decrease the total energy. This was in contradiction to experimental evidence at that time.

The above contradiction was reconciled by the theory proposed by V.L. Ginzburg and L.D. Landau (named Ginzburg-Landau theory) in 1950 which was also phenomenological

but took account of quantum effects [11]. In the beginning the major success of this theory was obtained in handling the so-called intermediate state of superconductors, in which superconducting and normal domains coexist in the presence of magnetic field. There they introduced a pseudo-wave-function ψ as an order-parameter within Landau's general theory of second-order phase transition, which describes the local density of the superconducting electrons. But what are these 'superconducting electrons'? The answer was given in 1957 by J. Bardeen, L. Cooper and J. Schrieffer [12]. In their BCS theory, the interactions between electrons and phonons were taken into account and led to electron-electron attraction, and to the formation of superconducting carriers-the Cooper pairs. The authors were awarded the Nobel prize for this work in 1972. The unification of the microscopic BCS theory and the phenomenological GL theory (close to T_c) was elaborated by L. P. Gor'kov (1958) who developed a method to solve the BCS model problem using Green's functions [13]. By using this method, he found the microscopic interpretations for all phenomenological parameters of the GL theory and defined the theory's range of validity. The works by Gor'kov completed the development of the Ginzburg-Landau-Abrikosov-Gor'kov theory. This theory predicted that superconductors could be divided into two categories now referred to as type-I and type-II, as shown by Abrikosov [14].

In 1962, the first commercial superconducting wire, a niobium-titanium alloy, was developed by researchers at Westinghouse, allowing the construction of the first practical superconducting magnets. In the same year, Josephson made an important theoretical prediction that a supercurrent could flow between two pieces of a superconductor separated by a thin layer of insulator [15]. This phenomenon, now called as the Josephson effect, is often exploited by superconducting devices. It is used in the most accurate available measurements of the magnetic flux quantum $\Phi_0 = \frac{h}{2e}$, and thus (coupled with the quantum Hall resistivity) for the determination of Planck's constant h. Josephson was awarded the Nobel Prize for this work in 1973.

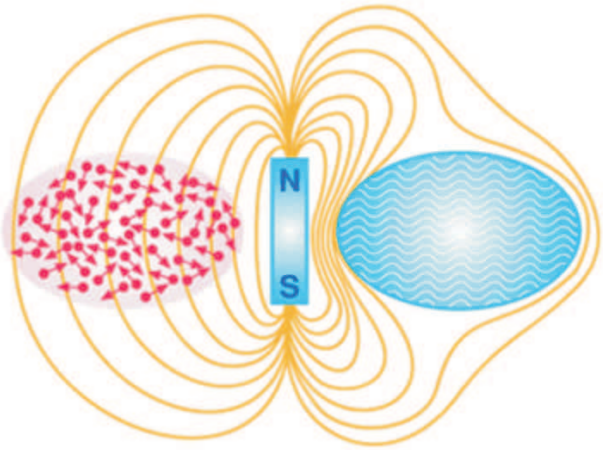

Fig. 1.1 Schematic showing Meissner effect in a superconducting sample (on the right) cooled under the critical temperature in a magnetic field generated by a magnet bar. Below the transition temperature, the magnetic field lines are ejected from the sphere. The electrons correlate in a coherent, collective manner, in contrast to the chaotic or disorderly manner in the left for a normal metal.

Practically everything seemed to be settled until 1986, when Johannes Georg Bednorz and Karl Alexander Müller discovered the LaBaCuO, with a transition temperature of 30K [16], the first compound in the family of *high-temperature superconductors* (HTS). Bednorz and Müller were awarded the Nobel prize in Physics just one year later. Subsequently, materials have been found with higher T_c, such as Yttrium Barium Copper Oxide (YBCO) discovered in 1987 with T_c of 90K [17], Bismuth Strontium Calcium Copper Oxide (BSCCO) discovered with T_c up to 108 K [18], and TBCCO (T=thallium) discovered to have T_c of 127 K [19]. Up to now, the highest T_c under ambient pressure is found in Mercury Barium Calcium Copper Oxide ($HgBa_2Ca_2Cu_3O_x$) at 135 K, under high pressure at 164 K [20]. It is a cuprate-perovskite material [21]. Although three decades of intensive research has been dedicated to explain the superconductivity mechanism, there is not yet a widely accepted theory to provide an answer. Unlike the electron-phonon attraction mechanism, in conventional superconductors in HTS, one is dealing with genuine electronic mechanism, which is beyond the BCS theory. Recent discoveries have increased the highest-observed T_c in a number of materials to unprecedented levels, such as in heavy fermion ($PuCoGa_5$), carbon nanotubes (CNTs), and graphite interrelated compounds (CaC_6) (from Ref. [22]), where exact mechanisms of superconductivity are also not exactly understood.

T_c (K)	Materials	Class
133	$HgBa_2Ca_2Cu_3O_x$	Copper-oxide
110	$Bi_2Sr_2Ca_2Cu_3O_{10}$(BSCCO)	
90	$YBa_2Cu_3O_7$ (YBCO)	superconductors
77 Boiling point of liquid nitrogen		
55	SmFeAs(O,F)	Iron-based
41	CeFeAs(O,F)	
26	LaFeAs(O,F)	superconductors
20 Boiling point of liquid hydrogen		
18	Nb_3Sn	Metallic
10	NbTi	
9.2	Nb	low-temperature
4.2	Hg (mercury)	superconductors

Two recent highlights in this research field were brought by the discovery of superconductivity in magnesium diboride (MgB_2) in 2001 and iron pnictide compounds in 2008 [23, 24, 25]. MgB_2 was first synthesized with confirmed structure in 1953, but its superconducting properties were not discovered until 2001. It can be considered as a HTS, since its T_c is 39K, which is above the limit of BCS T_c. However it is generally believed to be a conventional superconductor, whose electron-electron interaction is phonon-mediated. The understanding of its properties can be achieved with BCS theory including two energy gaps. Its critical temperature is the highest amongst conventional superconductors, and this compound has been proved to be a useful and a low-cost superconducting material.

Before Fe-based superconductors were discovered in 2008, the term "high-temperature superconductor" was used interchangeably with the term "cuprate superconductor". Now the ferropnictides are added to the HTS group. They are currently the family of compounds with second highest T_c. The first discovery of superconductivity in this family

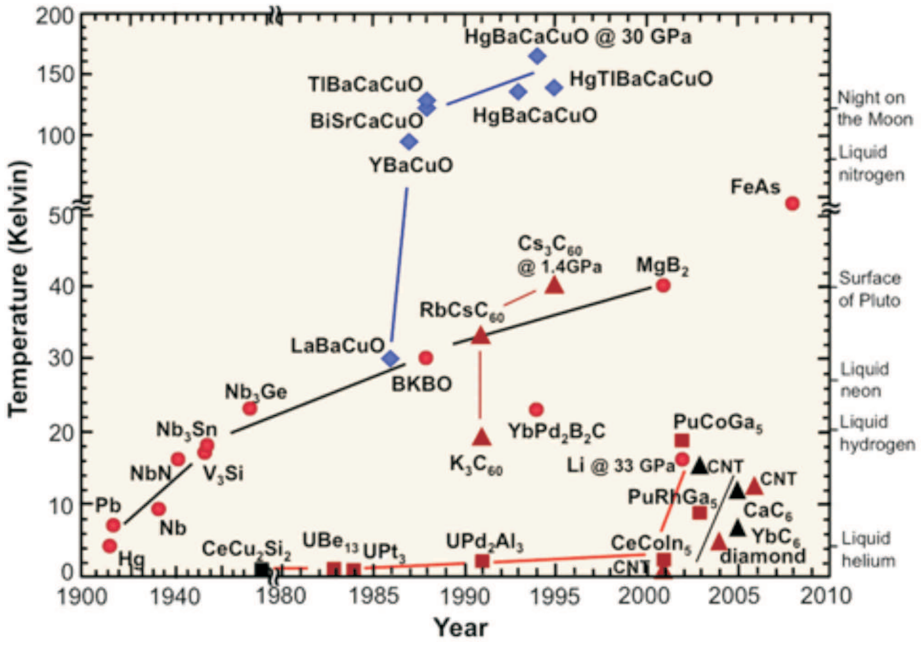

Fig. 1.2 The chronology of discoveries of superconductors, and their critical temperatures. Colors correspond to metallic (red), high-T_c (blue), heavy fermion (purple), and organic superconductors (green).

is in LaFePO at 4K in 2006. Much greater attention was attracted after the analogous material LaFeAs(O,F) was found to superconduct at up to 43K under pressure. Ferropnictides are very different from cuprates, which maybe helpful to from a broad enough material base for a possible new non-BCS-theory of superconductivity.

1.2 THEORIES OF SUPERCONDUCTIVITY

1.2.1 London theory

In this theory several assumptions are made to study superconductivity in the simplest case. First the two-fluid model, where the total electron density is divided into two contributions: one from normal electrons n_n, and the other from superconducting electrons n_s. Second, a homogeneous distribution of superconducting electrons is assumed, i.e. n_s is taken identical everywhere. Finally the influence of the electronic and magnetic fields on n_s is neglected. London equations were deduced to describe the relation between the current, electric field and magnetic field [10]. The first London equation describes the connection between supercurrent density and applied electric field, thus the motion of superconducting electrons

$$\mathbf{E} = \frac{d}{dt}(\Lambda \mathbf{j}_s), \tag{1.1}$$

where

$$\Lambda = m/n_s e^2,$$

simply follows Newton's second law for the superconducting electrons.

The second London equation describes how the applied magnetic field penetrates into the superconductor, and gives the relation between the supercurrent and the magnetic field

$$\mathbf{H} + \lambda^2 \text{curl curl } \mathbf{H} = 0. \tag{1.2}$$

When the London gauge is implemented for the vector potential as

$$\text{div}\mathbf{A} = 0, \tag{1.3}$$

with Maxwell equation curl$\mathbf{H} = 4\pi/c\, \mathbf{j}_s$ and $\mathbf{H} = \text{curl}\mathbf{A}$, one obtains

$$\mathbf{j}_s = -\frac{c}{4\pi\lambda^2}\mathbf{A}. \tag{1.4}$$

Let us consider a semi-infinite superconductor for $x > 0$, where the surface coincides with $x = 0$ plane, under applied magnetic field H_0. We solve the second London equation (1.2) with the boundary conditions $H(0) = H_0$, $H(\infty) = 0$. The solution is

$$H = H_0 e^{-x/\lambda}, \tag{1.5}$$

which means that the magnetic field decreases by increasing the distance from the surface of the superconductor. The characteristic length of decay is λ, called the London magnetic field penetration length:

$$\lambda = \left(\frac{mc^2}{4\pi n_s e^2}\right)^{1/2}. \tag{1.6}$$

It indicates that the screening (Meissner) supercurrent at the surface decreases over the same length. Following the two fluid model, λ is also temperature dependent, as

$$\lambda(T) = \frac{\lambda(0)}{[1 - (T/T_c)^4]^{1/2}}. \tag{1.7}$$

1.2.2 Ginzburg-Landau (GL) theory

In London theory, quantum effects are not considered, contrary to the theory developed by Ginzburg and Landau in 1950 [11]. The essential part of this theory was to introduce a complex-order parameter $\psi(r)$ as pseudowavefunction of the superconducting electrons, where $|\psi(r)|^2$ is to represent the local density of superconducting electrons, $n_s(r)$. The GL theory is based on the theory of second-order phase transitions by Landau, which demonstrates a phenomenon of discontinuously switching symmetry while the gradually changing state of the system crosses the transition temperature. This theory is based on an expansion of the free energy in powers of the order parameter, which is small near the transition temperature. This starting point already limits the validity of the GL theory to the temperature region close to the critical temperature, $T_c - T \ll T_c$. The

variational method is applied to this assumed expansion of the free-energy density in powers of $|\psi|^2$ and $|\nabla\psi|^2$, bringing about two coupled GL equations, for $\psi(r)$ and for the vector potential $A(r)$ respectively, capable of dealing with an inhomogeneous distribution of $\psi(r)$ and a nonlinear response to fields. In the following sections, the main principles of GL theory will be covered.

1.2.2.1 Free-energy density and two GL equations

- Homogeneous distribution of Ψ (without magnetic field)

$$\begin{aligned} |\Psi(r)|^2 &= n_s/2, \\ \mathcal{G}_{0s} &= \mathcal{G}_n + \alpha|\Psi|^2 + \frac{\beta}{2}|\Psi|^4. \end{aligned} \tag{1.8}$$

$|\Psi(r)|^2$ is the density of Cooper pairs, $\mathcal{G}_{0s}$ is the free energy density of the superconductor in the absence of magnetic field. $\mathcal{G}_n$ is the free energy density of the normal state, α and β are phenomenological expansion coefficients depending on the superconducting material. Minimization of the free energy with respect to $|\Psi|^2$, leads to $|\Psi_0|^2 = -\alpha/\beta$. The temperature dependence of α is $\alpha \propto (T - T_c)$, while β is positive and temperature independent.

- With magnetic field

Near T_c, since Ψ is small and varies slowly in space, the Gibbs free energy density can be expressed in power of Ψ as

$$\mathcal{G}_s = \mathcal{G}_n + \alpha|\Psi|^2 + \frac{\beta}{2}|\Psi|^4 + \underbrace{\frac{1}{2m^*}\left|\left(-i\hbar\nabla - \frac{e^*}{c}\mathbf{A}\right)\Psi\right|^2}_{I} - \underbrace{\frac{(\mathbf{H}-\mathbf{H_0})^2}{4\pi}}_{II}. \tag{1.9}$$

Term I in the equation is the kinetic energy of Cooper pairs, where mass m^* of the Cooper pair is two times the mass of an electron m, and likewise, $e^* = 2e$. Term II describes the magnetic energy of the magnetic field generated by supercurrents, which is simply the difference between the applied magnetic field and the local one.

- Two GL equations

The total energy of the superconducting system can be obtained from the volume integration of Eq. (1.9), and the equilibrium state is reached when the variations of this total energy with respect to Ψ^* and $\mathbf{A}$ become zero. The former can be written as

$$\int\left\{a\Psi\delta\Psi^* + \frac{1}{2m^*}\left[(-i\hbar\nabla - \frac{e^*}{c}\mathbf{A})\Psi(i\hbar\nabla - \frac{e^*}{c}\mathbf{A})\delta\Psi^*\right] + \beta|\Psi|^2\Psi\delta\Psi^*\right\}dV_s = 0. \tag{1.10}$$

Let $\varphi = (-i\hbar\nabla - \frac{e^*}{c}\mathbf{A})\Psi$. By using relationship $\nabla\cdot(c\nu) = \nu\cdot\nabla c + c\nabla\cdot\nu$, where c is a scalar, the second term in Eq. (1.10) can be written as

$$\frac{1}{2m^*}\varphi(i\hbar\nabla - \frac{e^*}{c}\mathbf{A})\delta\Psi^* = \frac{1}{2m^*}i\hbar\left[\nabla\cdot(\delta\Psi^*\varphi) - \delta\Psi^*\nabla\cdot\varphi\right] - \frac{1}{2m^*}\varphi\frac{e^*}{c}\mathbf{A}\delta\Psi^*.$$

Following Gauss theorem $\int \nabla \cdot \mathbf{T} dV_s = \oint \mathbf{n} \cdot \mathbf{T} dS_s$,

$$\int dV_s \frac{1}{2m^*} \varphi (i\hbar\nabla - \frac{e^*}{c}\mathbf{A})\delta\Psi^* = \int dV_s \frac{1}{2m^*}(-i\hbar\nabla - \frac{e^*}{c}\mathbf{A})^2 \Psi\delta\Psi^* + \oint_s i\hbar \frac{1}{2m^*}\mathbf{n}\cdot\varphi\delta\Psi^* dS_s.$$

Eq. (1.10) can only be satisfied if

$$a\Psi + \beta|\Psi|^2\Psi + \frac{1}{2m^*}\mathbf{\Pi}^2\Psi = 0, \tag{1.11}$$

$$\oint_s \mathbf{n}\cdot(i\hbar\frac{1}{2m^*}\mathbf{\Pi}\Psi\delta\Psi^*)dS = 0 \Rightarrow \mathbf{n}\cdot\mathbf{\Pi}\Psi|_{boundary} = 0, \tag{1.12}$$

which are the first Ginzburg-Landau equation and the boundary condition, respectively, with $\mathbf{\Pi} = \Big(-i\hbar\nabla - \frac{e^*}{c}\mathbf{A}\Big)$.

The variation of Eq. (1.9) with respect to the vector potential $\mathbf{A}$ is

$$\int \Big\{ \Big(-i\hbar\nabla - \frac{e^*}{c}\mathbf{A}\Big)\Psi\frac{-e^*}{c}\delta\mathbf{A}\Psi^* + \frac{-e^*}{c}\delta\mathbf{A}\Psi\Big(i\hbar\nabla - \frac{e^*}{c}\mathbf{A}\Big)\Psi^*\Big\}dV$$
$$+\frac{1}{4\pi}\int \Big(\mathrm{rot}\mathbf{A} - \mathbf{H}\Big)\cdot\mathrm{rot}\delta\mathbf{A}dV = 0. \tag{1.13}$$

The first integral can be written as

$$\int \Big[\frac{i\hbar e}{m^*c}(\Psi^*\nabla\Psi - \Psi\nabla\Psi^*) + \frac{4e^2}{m^*c^2}|\Psi|^2\mathbf{A}\Big]\cdot\delta\mathbf{A}dV = 0. \tag{1.14}$$

By using the vector identity $\nabla\cdot(\mathbf{a}\times\mathbf{b}) = \mathbf{b}\cdot(\nabla\times\mathbf{a}) - \mathbf{a}\cdot(\nabla\times\mathbf{b})$, the second integral becomes

$$\frac{1}{4\pi}\int\Big\{\delta\mathbf{A}\cdot\mathrm{rotrot}\mathbf{A} + \mathrm{div}[\delta\mathbf{A}\times(\mathrm{rot}\mathbf{A} - \mathbf{H}_0)]\Big\}dV = 0. \tag{1.15}$$

By using Gauss's theorem

$$\int \mathrm{div}[\delta\mathbf{A}\times(\mathrm{rot}\mathbf{A} - \mathbf{H}_0)]dV = \oint_s d\mathbf{S}[\delta\mathbf{A}\times(rot\mathbf{A} - \mathbf{H}_0)], \tag{1.16}$$

which turns out to be zero if one chooses the integral surface to be far from the superconductor, where $\mathbf{A} = \mathbf{A_0}$. Eq. (1.13) finally takes the form

$$\int\Big[\frac{i\hbar e}{m^*c}\Big(\Psi^*\nabla\Psi - \Psi\nabla\Psi^*\Big) + \frac{4e^2}{m^*c^2}|\Psi|^2\mathbf{A} + \frac{1}{4\pi}\mathrm{rotrot}\mathbf{A}\Big]\cdot\delta\mathbf{A}dV = 0, \tag{1.17}$$

which combined with the Maxwell equation

$$\mathbf{j}_s = \frac{c}{4\pi}\mathrm{rotrot}\mathbf{A}, \tag{1.18}$$

gives the second GL equation as

$$\mathbf{j}_s = -\frac{i\hbar e}{m^*}\Big(\Psi^*\nabla\Psi - \Psi\nabla\Psi^*\Big) - \frac{4e^2}{m^*c}|\Psi|^2\mathbf{A}. \tag{1.19}$$

To summarize, the two coupled non-linear GL equations are:

$$\alpha\Psi + \beta|\Psi|^2\Psi + \frac{1}{2m^*}\left(-i\hbar\nabla - \frac{e^*}{c}\mathbf{A}\right)^2\Psi = 0, \tag{1.20}$$

$$\mathbf{j}_s = -\frac{i\hbar e^*}{2m^*}\left(\Psi^*\nabla\Psi - \Psi\nabla\Psi^*\right) - \frac{e^{*2}}{m^*c}|\Psi|^2\mathbf{A}. \tag{1.21}$$

The first equation is similar to Schrödinger's equation for electrons, with the energy eigenvalue α and the nonlinear term acting as a repulsive potential of Ψ on itself. Wave functions $\Psi(r)$ are therefore favored and spread as uniformly as possible in space.

For a superconductor in a dielectric medium, the natural boundary conditions mean that no superconducting current passes through the superconductor-dielectric interface, i.e.

$$\left(-i\hbar\nabla - \frac{e^*}{c}\mathbf{A}\right)\Psi\Big|_n = 0. \tag{1.22}$$

In the case of a superconductor-metal interface, equation (1.22) must be generailized to

$$\left(-i\hbar\nabla - \frac{e^*}{c}\mathbf{A}\right)\Psi\Big|_n = \frac{i\hbar}{b}\Psi, \tag{1.23}$$

where $b > 0$ is a real constant, to account for the leakage of Cooper pairs from the superconductor into the metal. In analogy, $b < 0$ models the interface with a superconductor with higher T_c.

- Gauge invariance of the GL theory

Because of the multiple possibilities for choosing the vector potential $\mathbf{A}$ for a magnetic field, it is very important to check whether the GL equations remain unchanged under different choices of $\mathbf{A}$. The transformation

$$\mathbf{A} = \mathbf{A}' + \nabla\varphi, \tag{1.24}$$

where $\varphi(r)$ is a single-valued scalar function, does not affect the magnetic field:

$$\mathbf{H} = \nabla\times\mathbf{A} = \nabla\times\mathbf{A}', \quad \text{since} \quad \nabla\times\nabla\varphi = 0.$$

If we take the following transformation of the superconducting order parameter:

$$\Psi = \Psi' \exp\left[i\frac{2\pi}{\Phi_0}\varphi(r)\right], \tag{1.25}$$

it can be easily shown that both GL equations remain unchanged. In our calculations in the remainder of this thesis, the London gauge is used, i.e.

$$\mathbf{A}_x = -\frac{1}{2}\mathbf{H}_y x,\ \mathbf{A}_y = \frac{1}{2}\mathbf{H}_x y,\ \mathbf{A}_z = 0;\ \text{in Cartesian coordinates,} \tag{1.26}$$

or

$$\mathbf{A}_r = 0\ \mathbf{A}_\varphi = \frac{1}{2}\mathbf{H}r,\ \mathbf{A}_z = 0;\ \text{in cylindrical coordinates.} \tag{1.27}$$

1.2.2.2 Characteristic lengths

- The coherence length $\xi(T)$

In absence of magnetic field, in one dimensional case the wavefunction Ψ can be normalized to its bulk value Ψ_0, and the first GL equation for $f = \Psi/\Psi_0$ can be written as

$$\frac{\hbar^2}{2m^*|\alpha|}\frac{d^2f}{dx^2} + f - f^3 = 0, \tag{1.28}$$

which introduces the characteristic length $\xi(T)$ for spatial variation of Ψ as

$$\xi(T) = \sqrt{\frac{\hbar^2}{2m^*|\alpha|}} \propto \sqrt{\frac{1}{1-t}}, \tag{1.29}$$

with $t = T/T_c$. The importance of $\xi(T)$ as characteristic length for variation of Ψ can be made even more evident by considering a linearized form of Eq. (1.29), where we set $f(x) = 1 - g(x)$, and $g(x) \ll 1$. Then the equation can be expanded in the first order in g, as

$$\xi^2 g''(x) + (1+g) - (1 + 3g + \cdots) = 0, \tag{1.30}$$

and we get $g(x) \sim e^{-\pm\sqrt{2}x/\xi(T)}$, which shows that the small disturbance of Ψ from Ψ_0 will decay in a characteristic length of order $\xi(T)$. On the other hand, by taking curl of both sides of the second GL equation and Maxwell equation, one can easily get the London equations, and the same definition of the magnetic penetration length λ as in Eq. (1.6). However, in the GL model, $\lambda \sim (1-t)^{-1/2}$ which is different from the two fluid model and Eq. (1.7). The exact temperature dependence of ξ and λ is related to the purity of the superconductor, defined by the electron mean free path l_{el} [26, 27]:

$$\begin{aligned}
\xi(T) &= 0.74\xi_0(1 - T/T_{c0})^{-1/2}, \text{ when } \quad l_{el} \gg \xi_0 \text{ (pure case)}, \\
\text{and } \lambda(T) &= \frac{\lambda_L(0)}{\sqrt{2}}(1 - T/T_{c0})^{-1/2}, \\
\xi(T) &= 0.855\sqrt{\xi_0 l_{el}}(1 - T/T_{c0})^{-1/2}, \text{ when } \quad l_{el} \ll \xi_0 \text{ (dirty case)}, \\
\text{and } \lambda(T) &= \frac{\lambda_L(0)}{\sqrt{2}}\sqrt{\frac{\xi_0}{1.33 l_{el}}}(1 - T/T_{c0})^{-1/2},
\end{aligned} \tag{1.31}$$

where ξ_0 and $\lambda_L(0)$ are the BCS coherence length and the London penetration depth at zero temperature, respectively.

- Validity of GL theory

In principle the validity of the GL theory is limited to the vicinity of the critical temperature T_c. It is also required to contain slow spatial changes of Ψ and $\mathbf{A}$, and the correct series expansion of the Gibbs free energy density $\mathscr{G}$ [28]. In practice, and especially if the Gibbs free energy is expanded to higher order terms of $t = 1 - T/T_c$ [29], the validity of GL formalism can reach further below T_c. In the early theoretical works, De Gennes demonstrated that the GL model was valid for any temperature lower than T_c in strong

magnetic fields [27]. In the studies of mesoscopic superconductors the GL theory has been successfully used deep into the superconducting phase [30, 31, 32].

The condition of slowly varying Ψ imposes that $\xi(T) \gg \xi_0$. This condition changes in case of dirty superconductors ($l_{el} \ll \xi_0$), where the validity range for the GL theory is much broader. In this case, the characteristic scale of inhomogeneity is the mean free path l_{el} and the GL theory can be applied when $\xi(T), \lambda(T) \gg l_{el}$. The comparison of the critical current measurements in 'dirty' thin Al stripes with the theoretical predictions of BCS and GL formalisms has shown that two theories agree with each other down to temperatures below $0.1T_c$ [33].

1.2.2.3 Numerical approach The coupled GL equations are solved self-consistently. In the presence of the applied magnetic field, the orderparameter is obtained through the first equation Eq. (1.20), thus brings forth the corresponding superconducting current from expression Eq. (1.21). The variation of vector potential $\delta\mathbf{A}$ induced by the current is calculated using Fourier transformation, and the new vector potential is brought in turn into the first equation Eq. (1.20) to solve the new orderparameter. The whole process from above runs iteratively till the system reaches equilibrium state. Hereby, we introduce the numerical processes used to solve both GL equations in the following section.

- Solving the first GL equation

For a constant applied magnetic field, we have solved the coupled GL equations self-consistently, in a finite-difference representation of the order parameter and the vector potential on a three-dimensional (3D) Cartesian space grid (x, y, z), with grid spacings smaller than 0.1ξ. For convenience, the dimensionless form of both GL equations are used, where the physical quantities are rescaled as:

$$\begin{aligned} X &= x \cdot \xi(0)(= \hbar/\sqrt{-2m^*\alpha(0)}) \\ \Psi &= \psi \cdot \psi_0(= \sqrt{-\alpha(0)/\beta}) \\ \mathbf{A} &= A \cdot A_0(= c\hbar/2e\xi(0)) \\ \mathbf{H} &= H \cdot H_{c2}(= c\hbar/2e\xi(0)^2 = \sqrt{2}\lambda H_c/\xi(0)) \end{aligned}$$

and the two dimensionless GL equations become

$$(-i\nabla - \mathbf{A})^2\Psi = \Psi[(1-t) - |\Psi|^2], \tag{1.32}$$

$$-\kappa^2\Delta\mathbf{A} = \frac{1}{2i}(\Psi^*\nabla\Psi - \Psi\nabla\Psi^*) - |\Psi|^2\mathbf{A}. \tag{1.33}$$

The first equation is best to besolved by iteration methods. According to Kato *et al.* [34], the first GL equation can be written in a time-dependent form as

$$\frac{\partial\Psi}{\partial t} = -\frac{1}{12}\left[\left(\frac{\nabla}{i} - \mathbf{A}\right)^2\Psi - (1 - \frac{T}{T_c})\Psi + |\Psi|^2\Psi\right] + f(r,t). \tag{1.34}$$

Next the complex link variable $U_\mu^{r1,r2} = \exp(\int_{r1}^{r2}\mathbf{A}_\mu(r)d\mu)$, $\mu = x, y, z$, is introduced [34], preserving the gauge-invariant properties of the GL equations. In that case, the

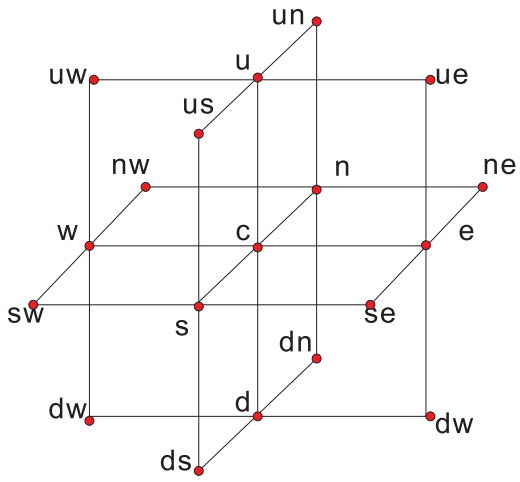

Fig. 1.3 The 3D Cartesian grid-point lattice used in the simulations, u and d represent the points before and after the center point in z direction, w and e in x direction, and s and n in y direction.

first and second derivatives of Eq. (1.34) can be written as

$$\left(\frac{\partial}{i\partial\mu} - \mathbf{A}_\mu\right)^2 \Psi \quad \rightarrow \quad -\frac{U_\mu^{\mu+1,\mu}\Psi_{\mu+1} - 2\Psi_\mu + U_\mu^{\mu-1,\mu}\Psi_{\mu-1}}{a_\mu^2}$$
$$\stackrel{if\ \mu=z}{=} \quad -\frac{U_z^{u,c}\Psi_u - 2\Psi_c + \Psi_z^{d,c}}{a_z^2}. \tag{1.35}$$

$$\left(\frac{\partial}{i\partial\mu} - \mathbf{A}_\mu\right)\Psi \quad \rightarrow \quad i\frac{U_\mu^{\mu+1,\mu}\Psi_{\mu+1} - \Psi_\mu}{a_\mu}$$
$$\stackrel{if\ \mu=z}{=} \quad i\frac{U_z^{u,c}\Psi_u - \Psi_c}{a_z}. \tag{1.36}$$

Finally, the discretized time dependent GL equation becomes

$$\frac{\partial\Psi}{\partial t} = -\frac{1}{12}\Bigg[-\frac{U_x^{e,c}\Psi_e}{a_x^2} - \frac{U_x^{w,c}\Psi_w}{a_x^2} - \frac{U_y^{s,c}\Psi_s}{a_y^2} - \frac{U_y^{n,c}\Psi_n}{a_y^2} - \frac{U_z^{u,c}\Psi_u}{a_z^2}$$
$$- \frac{U_z^{d,c}\Psi_d}{a_z^2} + 2\frac{\Psi_c}{a_x^2} + 2\frac{\Psi_c}{a_y^2} + 2\frac{\Psi_c}{a_z^2} - (1 - \frac{T}{T_c})\Psi_c + |\Psi_c|^2\Psi_c\Bigg]. \tag{1.37}$$

Here the nonlinear term is a potential source of numerical difficulties. In order to overcome this, the nonlinear term is calculated from the initial value of Ψ in the first step, and used as a constant contribution to the system through the procedure of seeking the equilibrium value of Ψ in the next step. In this way, the problem becomes effectively linearized. After obtaining the equilibrium value of Ψ under the condition of the old nonlinear contribution, the nonlinear term is updated from the newly calculated Ψ, and substituted back in the equation for the next run. In this recurrent procedure based on a Gauss-Seidel technique, convergence is finally reached and the first GL equation is solved [35]. The boundary condition for the order parameter in a superconductor in contact

with an insulator or with vacuum, is given by

$$\mathbf{n}\cdot(-i\nabla-\mathbf{A})\Psi\Big|_{boundary}=0, \tag{1.38}$$

where $\mathbf{n}$ is the unit vector normal to the surface of the superconductor. It is also discretized, by using Eq. (1.36), as

$$\frac{1}{i}\frac{U_{\mu}^{\mu+1,\mu}\Psi_{\mu+1}-\Psi_{\mu}}{a_{\mu}}\Big|_{boundary}=0, \tag{1.39}$$

where μ is the axis perpendicular to the boundary at the given point. The value of Ψ obtained from the first GL equation, is further used in the second GL equation Eq. (1.38) to obtain the supercurrent density. Here the link variable approach is applied again, and the expression of the supercurrent can be transformed into:

$$\mathbf{j}_{\mu}=\frac{1}{2}\Big[\sum_{\mu}\Psi^{*}\frac{1}{i}\frac{U_{\mu}^{\mu+1,\mu}\Psi_{\mu+1}-\Psi_{\mu}}{a_{\mu}}\Psi+c.c.\Big],\ \mu=x,y,z. \tag{1.40}$$

From the supercurrents a new value for the vector potential can be calculated using the second GL equation. The newly obtained vector potential is substituted back in the first GL equation and the whole procedure described above is repeated until a convergent solution of both GL equations is obtained. In this way, we solve two coupled GL equations self-consistently for given magnetic field. Once a solution is obtained, the free energy density of the superconducting system can be obtained from:

$$\mathcal{F}=\frac{1}{V}\int\Big[2(\mathbf{A}-\mathbf{A_0})\cdot\mathbf{j}-|\Psi|^{4}\Big]dV, \tag{1.41}$$

where $\mathbf{A_0}$ denotes the vector potential of the initially applied magnetic field, in the absence of a superconductor. Eq. (1.41) is derived from the full expression for Gibbs free energy:

$$\begin{aligned}\mathcal{F}&=\frac{\mathcal{G}_{sH}-\mathcal{G}_{nH}}{H_c^2V/8\pi}\\ &=\int\Big\{-2|\Psi|^2+|\Psi|^4+2|(-i\nabla-\mathbf{A})\Psi|^2+2\kappa^2(\mathbf{H}-\mathbf{H}_0)^2\Big\}dV.\end{aligned} \tag{1.42}$$

By applying Gauss theorem $\int\nabla\cdot\mathbf{D}dV=\oint\mathbf{n}\cdot\mathbf{D}dS$, the third term of the integrand in Eq. (1.42) can be written as

$$\begin{aligned}\int\Big|\Big(-i\nabla-\mathbf{A}\Big)\Psi\Big|^2dV=\oint\mathbf{n}\cdot\Big[\Psi^{*}\Big(-i\nabla-\mathbf{A}\Big)\Psi\Big]dS\\ +\int\Psi^{*}\Big(-i\nabla-\mathbf{A}\Big)^2\Psi dV.\end{aligned} \tag{1.43}$$

The first term on the right side equals zero due to the boundary conditions for the SC-vacuum boundary. The second term we can rewrite with the help of the first GL equation and obtain

$$\int\Big|\Big(-i\nabla-\mathbf{A}\Big)\Psi\Big|^2dV=\int\Big(|\Psi|^2-|\Psi|^4\Big)dV. \tag{1.44}$$

Finally, Eq. (1.42) takes the from

$$\mathcal{F} = \int \left[\left(\mathbf{H} - \mathbf{H_0} \right)^2 \kappa^2 - \frac{1}{2} |\Psi|^4 \right] dV. \tag{1.45}$$

Using the vector relations $\nabla \cdot (\mathbf{a} \times \mathbf{b}) = \mathbf{b} \cdot (\nabla \times \mathbf{a}) - \mathbf{a} \cdot (\nabla \times \mathbf{b})$, $\mathbf{a} \times (\nabla \times \mathbf{a}) = 0$, the London gauge $\nabla \cdot \mathbf{A} = 0$, and the relation $\mathbf{j} = -\kappa^2 \nabla^2 \mathbf{A}$, one obtains Eq. (1.41) for energy in units of $H_c^2 V / 8\pi$.

- Solving the second GL equation

For low-κ superconducting materials, i.e. weak type-II or type-I ones ($\kappa \lesssim 1$), or the thickness of the sample is larger and comparable to the penetration depth λ, the demagnetization effect must be considered in the simulation of the equilibrium superconducting state in an applied magnetic field. In other words, the contribution of the superconducting current to the total magnetic vector potential should be taken into account, where the self-consistent calculation should be carried out by including the second GL equation. We show two optional ways to solve this equation numerically, i.e. the Fast Fourier transform (FFT) and the multi-grid method.

In the London gauge, when $\nabla \cdot \mathbf{A} = 0$, the second GL equation is reduced to 3 ordinary partial differential equations of the Poisson type, as

$$-\kappa^2 \Delta \mathbf{A} = \mathbf{j}. \tag{1.46}$$

In the self-consistent calculation, the variation $\delta \mathbf{A}$ of vector potential is calculated each time. $\delta \mathbf{A} = 0$ is the boundary condition we take, since the influence of the superconducting current is negligible as it is far away from the sample. Thus, we can carry out the discrete Fourier transformation of the Dirichlet boundary condition, as

$$\mathbf{A}(x, y, z) = \sum_{i=0}^{N_x} \sum_{j=0}^{N_y} \sum_{k=0}^{N_z} \mathbf{A_k} \sin\left(\frac{l\pi x}{L_x} \right) \sin\left(\frac{m\pi y}{L_y} \right) \sin\left(\frac{n\pi z}{L_z} \right), \tag{1.47}$$

so that

$$\Delta \mathbf{A} = \left[-\left(\frac{l\pi}{L_x} \right)^2 - \left(\frac{m\pi}{L_y} \right)^2 - \left(\frac{n\pi}{L_z} \right)^2 \right] \sum_{i=0}^{N_x} \sum_{j=0}^{N_y} \sum_{k=0}^{N_z} A_k \sin\left(\frac{l\pi x}{L_x} \right) \sin\left(\frac{m\pi y}{L_y} \right) \sin\left(\frac{n\pi z}{L_z} \right). \tag{1.48}$$

We introduce the term $Q = \left[-\left(\frac{l\pi}{L_x} \right)^2 - \left(\frac{m\pi}{L_y} \right)^2 - \left(\frac{n\pi}{L_z} \right)^2 \right]$, and the corresponding $V j_k$ can be obtained by reverse Fourier transformation, as

$$\mathbf{j_k}(x, y, z) = \frac{2}{N_x} \frac{2}{N_y} \frac{2}{N_z} \sum_{l=0}^{N_x} \sum_{m=0}^{N_y} \sum_{n=0}^{N_z} \mathbf{j} \sin\left(\frac{l\pi x}{L_x} \right) \sin\left(\frac{m\pi y}{L_y} \right) \sin\left(\frac{n\pi z}{L_z} \right). \tag{1.49}$$

As a consequence, we can write down the following equation

$$\mathbf{j}'_\mathbf{k} = \frac{-\kappa^2}{Q} \mathbf{A_k}, \tag{1.50}$$

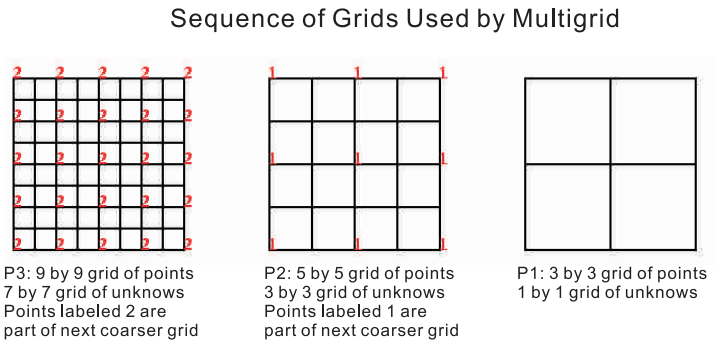

Fig. 1.4 Sequence of grids used by multigrid, P(i) denote the problem of solving a discrete Poisson equation on a$(2^i+1)$by(2^i+1) grid, with $(2^i\text{-}1)^2$ unknowns [36].

where $j'_k = \frac{N_x}{2}\frac{N_y}{2}\frac{N_z}{2}j_k$. Finally, the variation of vector potential $\delta\mathbf{A}$ can be obtained by the Fourier transformation. However, in 2D cases, the vector potential is expanded in a continuous way with free boundary condition in z direction, as

$$a_{lm}(z) = \int_{-\infty}^{\infty} dk a_{lm}(k)\exp(2\pi i z k), \tag{1.51}$$

and the current inside the sample, which is assumed homogeneously distributed in z direction, can be approximated by a step function, with the Fourier transformation:

$$\mathbf{j}(x,y,z) = \mathbf{j}(x,y)d\frac{\sin(\pi k d)}{\pi k d}. \tag{1.52}$$

Following the similar FFT transformation procedure, the coefficient $a_{lm}(k)$ can be expressed as:

$$a_{lm}(k) = \frac{d}{\kappa^2}\frac{\mathbf{j}_{lm}}{(2\pi k)^2 + lm^2}\frac{sin(\pi k d)}{\pi k d}, \tag{1.53}$$

and finally it reads:

$$a_{lm}(z) = \begin{cases} \frac{b_{lm}}{\kappa^2 lm^2}(1-\cosh(lmz)\exp(-d\,lm/2)) & \text{if } z \le d/2 \\ \frac{b_{lm}}{\kappa^2 lm^2}(\sinh(d\,lm)\exp(lmz/2)) & \text{if } z \ge d/2 \end{cases}. \tag{1.54}$$

The Fourier coefficients take the form

$$a_{lm} = \frac{\mathbf{j}_{lm}}{\kappa^2 lm^2}\frac{1-\exp(-d|lm|/2)}{lm^2}, \tag{1.55}$$

which reduces to

$$\begin{array}{ll} a_{lm} = \frac{1}{\kappa^2}\frac{\mathbf{j}_{lm}}{lm^2}, & d \to \infty, \text{ (for bulk samples)} \\ a_{lm} = \frac{d}{\kappa^2}\frac{\mathbf{j}_{lm}}{2|lm|}, & d \ll 1, \text{ (for thin samples).} \end{array} \tag{1.56}$$

For thin samples, this leads to the definition of an effective κ, dependent on the sample's thickness, as $\kappa^2_{eff} = \kappa^2/d$.

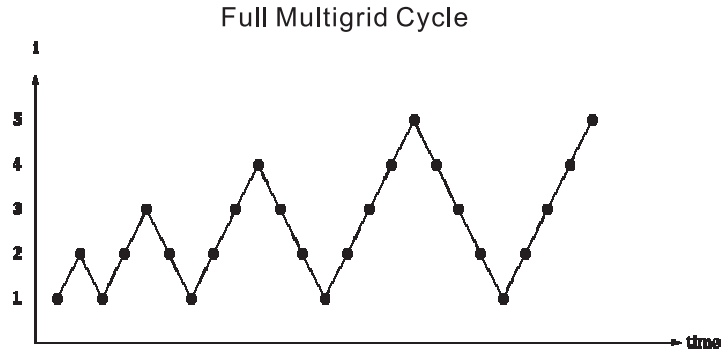

Fig. 1.5 Full multigrid cycle [36].

Another useful option for solving the Poisson equation numerically is the multi-grid method. To explain how the algorithm works, we need some operators which take a problem on each grid. Each of them either improves it or transforms it to a related problem on a different grid.

The restriction operator R(i) takes a pair (b(i),x(i)), consisting of a problem P(i) (P(i)x(i)=b(i), where b(i) is the right-hand-side of the equation and x(i) is the approximate solution), and maps it to (b(i-1),x(i-1)), which is a simpler problem on the next coarser grid, with starting guess x(i-1) (the sequence from left to right in Fig. 1.4):

$$(b(i-1), x(i-1)) = \mathrm{R}(i)(b(i), x(i)). \tag{1.57}$$

The restriction is implemented simply by computing a weighted average of each grid point value with its nearest neighbors.

The interpolation operator In(i-1) takes an approximate solution x(i-1) for P(i-1) and converts it to an approximation x(i) for the problem P(i) on the next finer grid (the sequence from right to left in Fig. 1.4):

$$(b(i), x(i)) = \mathrm{In}(i-1)(b(i-1), x(i-1)). \tag{1.58}$$

Its implementation also requires just a weighted average with nearest neighbors. The solution operator S(i) takes a problem P(i) and approximate solution x(i), and computes an improved x(i):

$$x_{\mathrm{improved}}(i) = \mathrm{S}(i)(b(i), x(i)). \tag{1.59}$$

The improvement is obtained by damping the "high frequency components" of the error. This is also implemented by averaging with nearest neighbors, and is a variation of the Jacobi's method. This completes the V-cycle of the multigrid methods.

In summary, for each multigrid V-cycle (MGV), the algorithm

- Starts with a problem on a fine grid (b(i), x(i)).
- Improves it by damping the high frequency error $x(i) = \mathrm{S}(i)(b(i), x(i))$.

- Approximates the error in the fine grid problem $(b(i), x(i))$ with a problem on the next coarser grid $\mathrm{R}(i)(b(i), x(i))$.
- Solves the coarser problem recursively.
- Maps the coarse solution back to the fine grid $\mathrm{In}(i-1)(\mathrm{MGV}(\mathrm{R}(i)(b(i), x(i))))$.
- Subtracts the correction computed on the coarse grid from the fine grid solution $x(i) = x(i) - d(i)$.
- Improves the solution some more $x(i) = \mathrm{S}(i)(b(i), x(i))$.

1.2.3 BCS theory

1.2.3.1 Basics of BCS theory The wave function of a Cooper pair is given by

$$\psi(\mathbf{r}_1 - \mathbf{r}_2) = \sum_k g(k) e^{ik(\mathbf{r}_1 - \mathbf{r}_2)}, \tag{1.60}$$

where $g(k)$ is the probability of one electron occupying the state of $\hbar k$ and the other occupying the state of $-\hbar k$. Because of the Pauli-principle, $g(k)$ equals to 1 when $k < k_F$, since the state is fully occupied when $k < k_F$. The wave function of all the electrons in the superconductor can also be expressed in a similar way, without considering the odd and even numbers of the electrons,

$$\phi_N(\mathbf{r}1, \mathbf{r}2 \ldots \mathbf{r}_N) = \phi(\mathbf{r}_1 - \mathbf{r}_2)\phi(\mathbf{r}_3 - \mathbf{r}_4) \ldots \phi(\mathbf{r}_{N-1} - \mathbf{r}_N). \tag{1.61}$$

By taking Fourier transformation from k to N, with N representing the number of the electrons in a particular state, one has

$$\phi_N = \sum_{k_1} \sum_{k_2} \cdots \sum_{k_{N/2}} g_{k_1} g_{k_2} \cdots g k_{N/2} \cdots a^\dagger_{k_1\downarrow} a^\dagger_{-k_1\uparrow} \cdots a^\dagger_{k_{N/2}\downarrow} a^\dagger_{-k_{N/2}\uparrow} \phi_0, \tag{1.62}$$

where the operator $a^\dagger_{k_\alpha\downarrow}$ is a Wigner-Jordan creation operator, and generates an electron in state (k_α) by acting on the vacuum state ϕ_0. The annihilation operator is denoted as $a_{k_\alpha\downarrow}$. Operators $a^\dagger_{k_\alpha\downarrow}$ and $a_{k_\alpha\downarrow}$ obey the anti-commutation relations of Fermion operators. The BCS ground states can then be expressed by

$$\Psi_G = \prod_k (1 + g_k a^\dagger_{k\downarrow} a^\dagger_{-k\uparrow})\phi_0. \tag{1.63}$$

By introducing u_k and v_k, $g_k = v_k/u_k$, we have

$$\Psi_G = \prod_k (u_k + v_k a^\dagger_{k\downarrow} a^\dagger_{-k\uparrow})\phi_0, \tag{1.64}$$

with $u_k^2 + v_k^2 = 1$. This implies that the probability of the pair $(k\uparrow, -k\downarrow)$ being occupied is $|v_k|^2$, and the probability that it is not occupied is $|u_k|^2 = 1 - |v_k|^2$.

The reduced Hamiltonian or pairing Hamiltonian can be written as

$$\mathscr{H} = \sum_{k\sigma} \epsilon_k n_{k\sigma} + \sum_{kk'} V_{kk'} a^*_{k\uparrow} a^*_{-k\downarrow} a_{-k'\downarrow} a_{k'\uparrow}. \tag{1.65}$$

The ground state of the system can be obtained by minimizing the expectation value of the sum by setting

$$\delta\Big\langle \psi_G \Big| \sum_{k\sigma} \xi_k n_{k\sigma} + \sum_{kk'} V_{kk'} a^*_{k\uparrow} a^*_{-k\downarrow} a_{-k'\downarrow} a_{k'\uparrow} \Big| \psi_G \Big\rangle = 0, \tag{1.66}$$

where $\xi_k = \epsilon_k - \mu$ is the single-particle kinetic energy relative to the Fermi energy, and $V_{kk'}$ are the interaction terms, which scatter from a state with $(k\uparrow, -k\downarrow)$ to one with $(k'\downarrow, -k'\uparrow)$. Thus the minimization equation can be expressed as

$$\partial E_s / \partial v_k^2 = 0, \tag{1.67}$$

where the energy is

$$E_s = \sum_k 2\xi_k v_k^2 + \sum_{kk'} V_{kk'} v_{k'} u_k v_k u_{k'}.$$

It follows that

$$\frac{v_k u_k}{1 - 2v_k^2} = \frac{\Delta_0}{2\xi_k}, \tag{1.68}$$

where

$$\Delta_0 = V \sum_k{}' v_k u_k \tag{1.69}$$

and $\sum_k{}'$ is the sum over k restricted to layer $\hbar\omega_D$ around Fermi surface. Δ_0 can be obtained in the form

$$\Delta_0 \approx 2\hbar\omega_D \exp\Big(-\frac{1}{N(0)V} \Big), \tag{1.70}$$

where $N(0)$ is the DOS at the Fermi level. As an example, for Debye temperature $\hbar\omega_D \sim 100$K and $N(0)V \sim 0.3$, we obtain $\Delta_0 \sim 4$K.

The ground state energy of the superconductor is measured as the difference from the ground-state energy of the normal metal, i.e., we seek the quantity

$$\begin{aligned} E &= E_s - E_n \\ &= \sum_{k<k_F} 2\xi_k (v_k^2 - 1) + \sum_{k>k_F} 2\xi_k v_k^2 - V \sum_{kk'}{}' v_k u_k v_{k'} u_{k'} \\ &= \sum_{k>k_F} 2\xi_k \Big(1 - \frac{\xi_k}{E_k} \Big) - \frac{\Delta_0^2}{V} \\ &= -\frac{1}{2} N(0) \Delta^2(0) \quad \text{(by integrating } \xi \text{ from 0 to } \hbar\omega_c). \end{aligned} \tag{1.71}$$

Expression (1.70) for the gap function shows that Δ is proportional to the Debye energy window $\hbar\omega_D$. Debye frequency ω_D is different for isotopes of the same element, and is dependent on mass M. This implies that the thermodynamic critical field H_c and T_c should show the same dependence on M. The dependence of H_c (or T_c) on the isotopic mass is called the *isotope effect*. This relationship indicates the importance of the attractive electron-phonon interaction.

1.2.3.2 Elementary excitations and the density of states The wave function of this many particles system can be expressed as

$$\widetilde{\Psi} = \gamma^{\dagger}_{k,\sigma}\Psi_G. \tag{1.72}$$

$\gamma^{\dagger}_{k,\sigma}$ is the create operator for the elemental excitation, satisfying the Fermionic anti-commutation relationship, proposed by Bogoliubov [37] and Valatin [38] as

$$\begin{aligned} \gamma^{\dagger}_{k,\sigma} &= u_k a^{*}_{k,\sigma} - \sigma v_k a_{-k,-\sigma}, \\ a_{k,\sigma} &= u^{*}_k \gamma_{k,\sigma} - \sigma v_k \gamma^{\dagger}_{-k,-\sigma}. \end{aligned} \tag{1.73}$$

which is also known as Canonical transformation, with normalization condition

$$u^{*}_k u_k + v^{*}_k v_k = 1. \tag{1.74}$$

The Bogoliubov quasiparticle operators incorporate two features. The formula for $\gamma^{*}_{k,\sigma}$ implies that there are two ways to create an electron excitation with $(k,\uparrow)$: to add an electron with $(k,\uparrow)$ or to destroy the existing electron state with $(-k,\downarrow)$ to create a hole state with $(k,\uparrow)$. After bringing the Canonical transformation into the the field operators

$$\begin{aligned} \Psi(\mathbf{r},\sigma) &= \sum_k e^{ik\mathbf{r}} a_{k,\sigma}, \\ \Psi^{\dagger}(\mathbf{r},\sigma) &= \sum_k e^{-ik\mathbf{r}} a^{\dagger}_{k,\sigma}, \end{aligned}$$

which satisfies the Fermionic anticommutation relation, one can get

$$\begin{aligned} \Psi(\mathbf{r},\sigma) &= \sum_n [u^{*}_n(\mathbf{r})\gamma_{n,\sigma} - v_n(\mathbf{r})\gamma^{\dagger}_{n,-\sigma}], \\ \Psi(\mathbf{r},-\sigma) &= \sum_n [u^{*}_n(\mathbf{r})\gamma_{n,-\sigma} + v_n(\mathbf{r})\gamma^{\dagger}_{n,\sigma}], \end{aligned} \tag{1.75}$$

The effective Hamiltonian can be expressed as

$$\begin{aligned} H_e &= \int d^3\mathbf{r}\Big[\sum_{\sigma} \Psi^{\dagger}(\mathbf{r},\sigma)H_0(\mathbf{r})\Psi(\mathbf{r},\sigma) + U(\mathbf{r})\Psi^{\dagger}(\mathbf{r},\sigma)\Psi(\mathbf{r},\sigma) + \\ &+ \Delta(\mathbf{r})\Psi^{\dagger}(\mathbf{r},\uparrow)\Psi^{\dagger}(\mathbf{r},\downarrow) + \Delta^{*}(\mathbf{r})\Psi(\mathbf{r},\downarrow)\Psi(\mathbf{r},\uparrow)\Big], \end{aligned} \tag{1.76}$$

with

$$H_0 = -\frac{\hbar^2}{2m}\left(\nabla - \frac{ie}{\hbar c}\mathbf{A}\right)^2 - \mu \tag{1.77}$$

and U($\mathbf{r}$) is the mean (one-electron) potential, and $\Delta(\mathbf{r})$ is often referred to as the pairing potential.

Substituting Eq. (1.75) into Eq. (1.76), and using the anticommutation relationship of the field operators, one obtains

$$\begin{aligned} [H_e, \Psi_{\uparrow}(\mathbf{r})] &= -[H_0 + U(\mathbf{r})]\Psi_{\uparrow}(\mathbf{r}) - \Delta(\mathbf{r})\Psi^{\dagger}_{\downarrow}(\mathbf{r}), \\ [H_e, \Psi_{\downarrow}(\mathbf{r})] &= -[H_0 + U(\mathbf{r})]\Psi_{\downarrow}(\mathbf{r}) + \Delta(\mathbf{r})\Psi^{\dagger}_{\uparrow}(\mathbf{r}). \end{aligned} \tag{1.78}$$

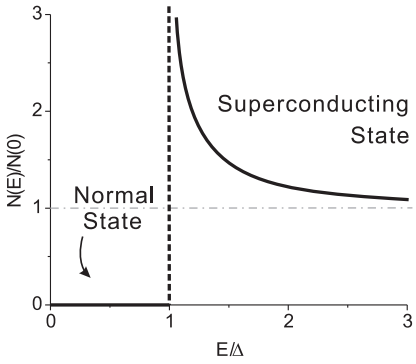

Fig. 1.6 Density of states in the superconducting compared to the normal state. All **k** states whose energies fall in the gap in the normal metal are raised in energy above the gap in the superconducting state.

Using Eq. (1.75), we find Bogoliubov's equations

$$\begin{aligned} \epsilon_n u_n(\mathbf{r}) &= [H_0 + U(\mathbf{r})]u_n(\mathbf{r}) + \Delta(\mathbf{r})v_n(\mathbf{r}), \\ \epsilon_n v_n(\mathbf{r}) &= -[H_0^* + U(\mathbf{r})]v_n(\mathbf{r}) + \Delta^*(\mathbf{r})u_n(\mathbf{r}). \end{aligned} \tag{1.79}$$

Since $E_k = \sqrt{\epsilon_k^2 + \Delta_0^2}$, the density of states can be expressed as

$$\frac{N_s(E)}{N(0)} = \frac{d\epsilon}{dE} = \frac{E}{(E^2 - \Delta^2)^{1/2}}, \text{ when } E > \Delta. \tag{1.80}$$

Therefore, a divergent behavior of the density of the state is expected when $E = \Delta$, which is shown in Fig. 1.6.

1.2.3.3 Gor'kov equations We start from the *grand canonical Hamiltonian* for an electron in magnetic field

$$\begin{aligned} H &= H_0 + V = \int d^3\mathbf{r}\Psi_\sigma^\dagger(\mathbf{r})\left\{\frac{1}{2m}\left(-i\hbar\nabla + \frac{eA(r)}{c}\right)^2 - \mu\right\}\Psi_\sigma(\mathbf{r}) \\ &- \frac{1}{2}g\int d^3r\Psi_\sigma^\dagger(\mathbf{r})\Psi_{-\sigma}^\dagger(\mathbf{r})\Psi_{-\sigma}(\mathbf{r})\Psi_\sigma(\mathbf{r}), \end{aligned} \tag{1.81}$$

where the inter-particle interaction is included by an attractive delta-function with magnitude $g > 0$. The Hartree-Fock contribution V_{HF} is usually omitted in the calculations, since V_{HF} is assumed to be the same in both normal and superconducting phases, and does not affect the comparison between the two states. Therefore the total effective Hamiltonian becomes

$$\begin{aligned} H &= H_0 - g\int d^3\mathbf{r}[\langle\Psi_\sigma^\dagger(\mathbf{r})\Psi_{-\sigma}^\dagger(\mathbf{r})\rangle\Psi_{-\sigma}(\mathbf{r})\Psi_\sigma(\mathbf{r}) \\ &+ \Psi_\sigma^\dagger(\mathbf{r})\Psi_{-\sigma}^\dagger(\mathbf{r})\langle\Psi_{-\sigma}(\mathbf{r})\Psi_\sigma(\mathbf{r})\rangle]. \end{aligned} \tag{1.82}$$

Heisenberg operators are introduced as follows

$$\begin{aligned} \Psi_{K\uparrow}(\mathbf{r}t) &= e^{H_{\text{eff}}t/\hbar}\Psi_\uparrow(\mathbf{r})e^{-H_{\text{eff}}t/\hbar}, \\ \Psi_{K\downarrow}^\dagger(\mathbf{r}t) &= e^{H_{\text{eff}}t/\hbar}\Psi_\downarrow^\dagger(\mathbf{r})e^{-H_{\text{eff}}t/\hbar}, \end{aligned} \tag{1.83}$$

which satisfy the linear equations of motion

$$\begin{aligned}\hbar\frac{\partial\Psi_{K\uparrow}(\mathbf{r}t)}{\partial t} &= -(\Pi-\mu)\Psi_{K\uparrow}(\mathbf{r}t) - g\langle\Psi_\uparrow(\mathbf{r}t)\Psi_\downarrow(\mathbf{r}t)\rangle\Psi^\dagger_{K\downarrow}(\mathbf{r}t),\\ \hbar\frac{\partial\Psi^\dagger_{K\downarrow}(\mathbf{r}t)}{\partial t} &= (\Pi-\mu)\Psi^\dagger_{K\downarrow}(\mathbf{r}t) - g\langle\Psi^\dagger_\uparrow(\mathbf{r}t)\Psi^\dagger_\downarrow(\mathbf{r}t)\rangle\Psi_{K\uparrow}(\mathbf{r}t),\end{aligned} \tag{1.84}$$

where $\Pi = \frac{1}{2m}\Big(-i\hbar\nabla + \frac{eA(r)}{c}\Big)^2$. The single particle Green's function can be defined as

$$\mathscr{G}(\mathbf{r}t,\mathbf{r}'t') = -\langle T_t[\Psi_{K\uparrow}(\mathbf{r}t)\Psi^\dagger_{K\uparrow}(\mathbf{r}'t')]\rangle. \tag{1.85}$$

T represents the product operator which orders the field operators with the latest time on the left and includes an additional factor of -1 for each interchange of fermion operators. The equation of motion is rewritten for this single particle Green's function as

$$\begin{aligned}&\hbar\frac{\partial}{\partial t}\mathscr{G}(\mathbf{r}t,\mathbf{r}'t') = -\hbar\delta(t-t')\langle\Psi_{K\uparrow}(\mathbf{r}t),\Psi^\dagger_{K\uparrow}(\mathbf{r}'t')\rangle - \left\langle T_t\left[\hbar\frac{\partial\Psi_{K\uparrow}(\mathbf{r}t)}{\partial t}\Psi^\dagger_{K\uparrow}(\mathbf{r}'t')\right]\right\rangle\\ &= -\hbar\delta(\mathbf{r}-\mathbf{r}')\delta(t-t') - \left[\frac{1}{2m}\Big(-i\hbar\nabla + \frac{eA(r)}{c}\Big)^2 - \mu\right]\times\mathscr{G}(\mathbf{r}t,\mathbf{r}'t')\\ &+g\langle\Psi_\uparrow(\mathbf{r})\Psi_\downarrow(\mathbf{r})\rangle\langle T_t[\Psi_{K\uparrow}(\mathbf{r}t)\Psi^\dagger_{K\uparrow}(\mathbf{r}'t')]\rangle.\end{aligned} \tag{1.86}$$

By introducing two new functions

$$\begin{aligned}\mathscr{F}(\mathbf{r}t,\mathbf{r}'t') &= -\langle T_t[\Psi_{K\uparrow}(\mathbf{r}t)\Psi_{K\downarrow}(\mathbf{r}'t')]\rangle,\\ \mathscr{F}^\dagger(\mathbf{r}t,\mathbf{r}'t') &= -\langle T_t[\Psi^\dagger_{K\downarrow}(\mathbf{r}t)\Psi^\dagger_{K\uparrow}(\mathbf{r}'t')]\rangle,\end{aligned} \tag{1.87}$$

and also

$$\Delta(\mathbf{r}) = g\mathscr{F}(\mathbf{r}t^+,\mathbf{r}t) = -g\langle\Psi_\uparrow(\mathbf{r})\Psi_\downarrow(\mathbf{r})\rangle = g\langle\Psi_\downarrow(\mathbf{r})\Psi_\uparrow(\mathbf{r})\rangle, \tag{1.88}$$

where $t^+ = t+0$, one obtains Gor'kov equations as follows

$$\begin{aligned}\left[-\hbar\frac{\partial}{\partial t} - \frac{1}{2m}\Big(-i\hbar\nabla + \frac{eA(r)}{c}\Big)^2 - \mu\right]\mathscr{G}(\mathbf{r}t,\mathbf{r}'t') &+ \Delta(\mathbf{r})\mathscr{F}^\dagger(\mathbf{r}t,\mathbf{r}'t')\\ &= \hbar\delta(\mathbf{r}-\mathbf{r}')\delta(t-t'),\\ \left[-\hbar\frac{\partial}{\partial t} - \frac{1}{2m}\Big(-i\hbar\nabla + \frac{eA(r)}{c}\Big)^2 - \mu\right]\mathscr{F}(\mathbf{r}t,\mathbf{r}'t') &= \Delta(\mathbf{r})\mathscr{G}(\mathbf{r}'t',\mathbf{r}t),\\ \left[\hbar\frac{\partial}{\partial t} - \frac{1}{2m}\Big(i\hbar\nabla + \frac{eA(r)}{c}\Big)^2 - \mu\right]\mathscr{F}^\dagger(\mathbf{r}t,\mathbf{r}'t') &= \Delta^*(\mathbf{r})\mathscr{G}(\mathbf{r}t,\mathbf{r}'t').\end{aligned} \tag{1.89}$$

1.2.3.4 Derivation of Eilenberger equations In the case of singlet paring, one can introduce the following term

$$\check{G}(\mathbf{r}t,\mathbf{r}'t') = \begin{pmatrix}\mathscr{G}(\mathbf{r}t,\mathbf{r}'t') & \mathscr{F}(\mathbf{r}t,\mathbf{r}'t')\\ -\mathscr{F}^\dagger(\mathbf{r}t,\mathbf{r}'t') & \mathscr{G}(\mathbf{r}'t',\mathbf{r}t),\end{pmatrix}, \tag{1.90}$$

and

$$\check{G}^{-1}(\mathbf{r}) = \begin{pmatrix} -\hbar\frac{\partial}{\partial t} - \frac{1}{2m}\left(-i\hbar\nabla + \frac{eA(r)}{c}\right)^2 - \mu & -\Delta(\mathbf{r}) \\ \Delta^*(\mathbf{r}) & \hbar\frac{\partial}{\partial t} - \frac{1}{2m}\left(i\hbar\nabla + \frac{eA(r)}{c}\right)^2 - \mu \end{pmatrix}, \quad (1.91)$$

so that the Gor'kov equations can be written as

$$\check{G}^{-1}(\mathbf{r})\check{G}(\mathbf{r}t, \mathbf{r}'t') = \check{1}\delta(\mathbf{r} - \mathbf{r}'). \quad (1.92)$$

Taking the Fourier transformation as

$$\begin{aligned} \check{G}(\mathbf{r}t, \mathbf{r}'t') &= \frac{1}{\beta}\sum_n e^{-i\omega_n(t-t')}\check{G}(\mathbf{r}, \mathbf{r}'; i\omega_n), \\ \check{G}(\mathbf{r}, \mathbf{r}'; i\omega_n) &= \int_0^\infty e^{i\omega_n(t-t')}\check{G}(\mathbf{r}t, \mathbf{r}'t')dt, \end{aligned} \quad (1.93)$$

the term $\check{G}(\mathbf{r}t, \mathbf{r}'t')$ can be written as

$$\check{G}(\mathbf{r}, \mathbf{r}'; i\omega) = \begin{pmatrix} G(\mathbf{r}, \mathbf{r}'; i\omega_n) & F(\mathbf{r}, \mathbf{r}'; i\omega_n) \\ -F^\dagger(\mathbf{r}, \mathbf{r}'; i\omega_n) & G(\mathbf{r}', \mathbf{r}; i\omega_n), \end{pmatrix} \quad (1.94)$$

and

$$\check{G}^{-1}(\mathbf{r}) = \begin{pmatrix} -i\omega_n - \frac{1}{2m}\left(-i\hbar\nabla + \frac{eA(r)}{c}\right)^2 - \mu & -\Delta(\mathbf{r}) \\ \Delta^*(\mathbf{r}) & i\omega_n - \frac{1}{2m}\left(i\hbar\nabla + \frac{eA(r)}{c}\right)^2 - \mu \end{pmatrix}. \quad (1.95)$$

Since we want to consider small vibrations of the relative coordinate, it is convenient to take the difference between Gor'kov equations for two different locations $\mathbf{r}$ and $\mathbf{r}'$, as

$$\check{G}^{-1}(\mathbf{r}, i\omega_n)\check{G}(\mathbf{r}, \mathbf{r}'; i\omega_n) - \check{G}(\mathbf{r}, \mathbf{r}'; i\omega_n)\check{G}^{-1}(\mathbf{r}', i\omega_n) = \check{0}, \quad (1.96)$$

i.e.

$$\begin{aligned} \frac{\nabla^2 - \nabla'^2}{2m}\check{1}\check{G} + i\omega_n[\sigma^z, \check{G}] &- \check{\Delta}(k, \mathbf{r})\check{G} - \check{G}\check{\Delta}(k', \mathbf{r}') \\ &- \frac{ie}{mc}\{A(\mathbf{r})\cdot\nabla\sigma^z\check{G} + A(\mathbf{r}')\cdot\nabla'\check{G}\sigma^z\} = 0, \end{aligned}$$

where

$$\check{\Delta}(k, \mathbf{r}) = \begin{pmatrix} 0 & \Delta(k, \mathbf{r}) \\ -\Delta^*(k, \mathbf{r}) & 0 \end{pmatrix}. \quad (1.97)$$

Further we have

$$\begin{aligned} \frac{\nabla^2 - \nabla'^2}{2m}\check{G} + i\omega_n[\sigma^z, \check{G}] &- \left[\frac{\check{\Delta}(k, \mathbf{r}) + \check{\Delta}(k', \mathbf{r}')}{2}, \check{G}\right] - \left[\frac{\check{\Delta}(k, \mathbf{r}) - \check{\Delta}(k', \mathbf{r}')}{2}, \check{G}\right]_+ \\ &- \frac{ie}{mc}\{A(\mathbf{r})\cdot\nabla\sigma^z\check{G} + A(\mathbf{r}')\cdot\nabla'\check{G}\sigma^z\} = 0, \end{aligned}$$

where [] is the commutator, and $[]_+$ is the anticommutator. Here we introduce the quasi-classical approximation, where the characteristic length of the oscillation of the physical properties in the relative coordinate is smaller than the wave length of the electron k_F^{-1}, the coherence length ξ and the magnetic field penetration length λ. In this case we can take the average of the magnitude of the oscillation in the center of mass. We introduce the coordinate of the center of mass R and relative coordinate R' as $\nabla = \nabla_{R'} + \frac{1}{2}\nabla_R$ and $\nabla' = -\nabla_{R'} + \frac{1}{2}\nabla_R$. Therefore

$$\left[\frac{\check{\Delta}(k,\mathbf{r}) + \check{\Delta}(k',\mathbf{r}')}{2}, \check{G}\right] \sim [\check{\Delta}(k,R), \check{G}],$$
$$\left[\frac{\check{\Delta}(k,\mathbf{r}) - \check{\Delta}(k',\mathbf{r}')}{2}, \check{G}\right]_+ \sim 0,$$

and

$$\{A(\mathbf{r})\cdot\nabla\sigma^z\check{G} + A(\mathbf{r}')\cdot\nabla'\check{G}\sigma^z\} \sim A(R)\cdot\{\nabla\sigma^z\check{G} + \nabla'\check{G}\sigma^z\}.$$

Eq. (1.96) becomes

$$\frac{\nabla_R\nabla_{R'}}{m}\check{G} - [i\omega_n\sigma^z + \check{\Delta}(k,R), \check{G}] - \frac{ie}{mc}A(R)\cdot\left\{[\sigma^z, \Delta_{R'}\check{G}] + \frac{1}{2}[\sigma^z, \Delta_R\check{G}]_+\right\} = 0,$$

where the Fourier transformation with respect to the relative coordinate is taken as

$$\check{G}(\mathbf{r},\mathbf{r}';i\omega_n) = \int\frac{dk}{(2\pi)^3}\check{G}(k,R;i\omega_n)e^{ikR'}.$$

Considering that

$$\frac{\nabla_R\nabla_{R'}}{m}\check{G} \approx v_F\nabla_R\check{G},$$

which is far greater than the last term $\frac{e}{2mc}A\nabla_R\check{G}$, we have

$$-iv_F\cdot\nabla_R\check{G}(k,R;i\omega_n) = \left[i\omega_n\sigma^z - \check{\Delta}(k,R) + \frac{e}{c}v_F\cdot A(R)\sigma^z, \check{G}(k,R;i\omega_n)\right]. \quad (1.98)$$

Another approximation can be made as

$$\frac{d^3k}{(2\pi)^3} = 2\pi N(0)d^2k_F\rho(k_F)\frac{dE(k)}{2\pi},$$

where

$$N(0) = \int_{S_F}\frac{d^2k_F}{(2\pi)^3}\frac{1}{|v(k_F)|}$$

is the total normal density of states for one spin at the Fermi surface S_F and

$$\rho(k_F) = \left((2\pi)^3N(0)|v(k_F)|\right)^{-1}$$

is the normal density of states for one spin at k_F, normalized to

$$\int_{S_F}d^2k_F\rho(k_F) = 1.$$

This approximation, which is essential for the derivation to follow, is usually excellent. It might fail, however, if the Fermi surface is dominated by very fine structures, e.g., if $E(k)$ varies considerably over energy intervals ω_0 or momentum intervals $1/\xi$ or $1/\lambda$.

Next we construct the so-called 'energy integrated' Green's function $g(k, \mathbf{R}; i\omega_n)$, where variable ω remains the same but the magnitude of k (actually E_k) is integrated over. The unit vector $\hat{k}$ remains since, for a nonuniform system, E_k depends on the direction in k space. The definition of the energy integrated Green's function is

$$g(\hat{k}, \mathbf{R}; i\omega_n) = \frac{i}{\pi} \int dE_k G(k, \mathbf{R}; i\omega_n), \tag{1.99}$$

which is analogous to the 'ω-integrated' distribution functions but without a convergence factor $e^{-i\omega_n t}$. The 'normalization' is included in the following way for homogenous superconducting sample:

$$\begin{aligned} g(\hat{k}, \mathbf{R}; i\omega_n) &= \frac{i}{\pi} \int \frac{(\hbar\omega_n + E_k) dE_k}{(\hbar\omega_n - E_k + i0)(\hbar\omega_n + E_k - i0)} \\ &= \frac{i}{\pi} \int \frac{\hbar\omega_n dE_k}{(\hbar\omega_n - E_k + i0)(\hbar\omega_n + E_k - i0)}. \end{aligned} \tag{1.100}$$

The second equality sign is satisfied when E_k is odd, and thus the poles of Eq. (1.100) are located at $E_k = \hbar\omega_n \pm i0$. The corresponding residues for these two poles are $\pm\pi i\hbar\omega$, and $g(\hat{k}, \mathbf{R}; i\omega_n) = \pi i\hbar\omega / E_{k0}$. In a similar way, $f^*(\hat{k}, \mathbf{R}; i\omega_n)$ can be evaluated as $-\Delta^*/E_{k0}$. By substituting values of g and f into the expression for $\check{g}$, one gets the normalization condition

$$\check{g}\check{g} = \check{1} \tag{1.101}$$

and the Eilenberger equation as

$$-iv_F \cdot \nabla_{\mathbf{R}} \check{g}(k, \mathbf{R}; i\omega_n) = \left[i\omega_n \sigma^z - \check{\Delta}(k, \mathbf{R}) + \frac{e}{c} v_F \cdot A(\mathbf{R}) \sigma^z, \check{g}(k, \mathbf{R}; i\omega_n) \right], \tag{1.102}$$

or written separately

$$\begin{aligned} -iv_F \cdot \nabla g + \Delta^*(\hat{k}, \mathbf{R}) f - \Delta(\hat{k}, \mathbf{R}) f^\dagger &= 0, \\ -iv_F \cdot \nabla \tilde{g} - \Delta^*(\hat{k}, \mathbf{R}) f + \Delta(\hat{k}, \mathbf{R}) f^\dagger &= 0, \\ -iv_F \cdot \left(\nabla - \frac{2ie}{c} A \right) f - 2i\omega_n f - \Delta(\hat{k}, \mathbf{R})(g - \tilde{g}) &= 0, \\ iv_F \cdot \left(\nabla + \frac{2ie}{c} A \right) f^\dagger - 2i\omega_n f^\dagger - \Delta(\hat{k}, \mathbf{R})(g - \tilde{g}) &= 0, \end{aligned} \tag{1.103}$$

where

$$g = g(\hat{k}, \mathbf{R}; i\omega_n), \tilde{g} = g(-\hat{k}, \mathbf{R}; -i\omega_n), f = f(\hat{k}, \mathbf{R}; i\omega_n), \text{and } f^\dagger = f^\dagger(\hat{k}, \mathbf{R}; i\omega_n).$$

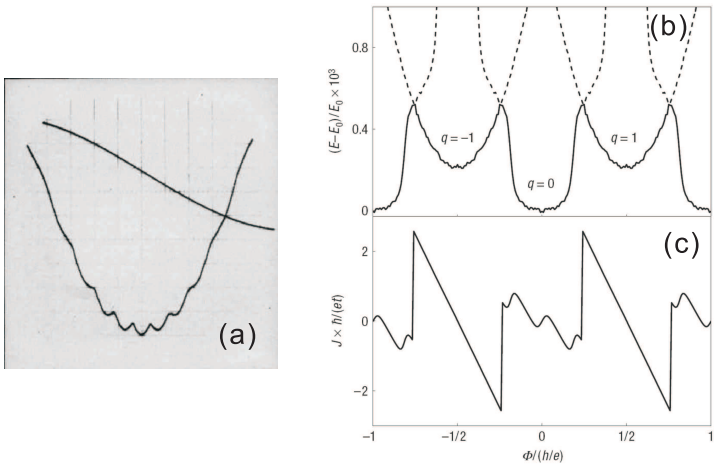

Fig. 1.7 (a) Parks' experiment: the resistance of tin cylinder at its superconducting transition temperature as a function of magnetic field. Upper trace: magnetic field sweep. After substrating the parabolic background, the variation of the resistance showed the periodicity of single flux quantum 2h/e [39]. (b) Flux dependence of total energy $(E(\Phi) - E(0))/E(0)$ and (c) total circulating current J(b) as a function of flux Φ in units of h/e [40].

1.3 VORTICES IN SUPERCONDUCTORS

1.3.1 Fluxoid quantization

Consider a bulk superconductor with the cavity piercing through. When the external field H_0 is applied parallel to the cavity, and temperature is decreased down to below T_c where specimen reaches superconducting state, the field is expelled from the interior of the superconductor, while inside the cavity some "frozen" magnetic flux remains. In the following, we discuss some fundamental properties of the trapped magnetic flux in superconductors.

Consider a contour C enclosing the cavity inside the superconductor, where the supercurrent $\mathbf{j}_s = 0$. According to the expression for the supercurrent in Eq. (1.36), we have

$$\mathbf{j}_s = \frac{2e\hbar}{m}|\psi|^2\nabla\phi - \frac{4e^2}{mc}|\psi|^2\mathbf{A},$$

where $|\psi|$ and ϕ are the magnitude and phase of the order parameter respectively. The contour integral of vector potential along the path C can be calculated as

$$\oint_c \mathbf{A}\cdot d\mathbf{l} = \frac{c\hbar}{2e}\oint_c \nabla\phi\cdot d\mathbf{l}. \tag{1.104}$$

From Eq. (1.104), one can see that ϕ is a multiple-valued function. It changes by a certain value after every full turn around the hole. However the wavefunction Ψ must be single-valued. Therefore, we have to stipulate that the change in ϕ after each turn around the hole containing the magnetic flux must be an integral multiple of 2π. Indeed, the

addition of $2\pi n$ where $n = 0, 1, 2 \ldots$ to ϕ does not change the function $\Psi(r) = \psi(r)e^{i\phi}$ since $e^{i2\pi n} = 1$. Therefore $\oint_C \nabla\phi \cdot d\mathbf{l} = 2\pi n$ and Eq. (1.104) can finally be written as

$$\Phi = n\Phi_0, \quad \text{where} \quad \Phi_0 = \frac{\hbar c}{2e}. \tag{1.105}$$

This shows that the magnetic flux enclosed in the hole can only assume values which are integer multiples of the minimal possible magnetic flux, the magnetic flux quantum Φ_0. The value of Φ_0 is defined above and equals to 2.07×10^{-7}G cm^2. The generalized expression of Eq. (1.105) to the case of any contour (even with non-zero current) is

$$\Phi = n\Phi_0 - \frac{mc}{4e^2} \oint_C \frac{\mathbf{j}_s}{|\psi|^2} \cdot d\mathbf{l}. \tag{1.106}$$

However, the validity of the $\hbar c/2e$ periodicity of the flux quantization is not always true. It only applies in superconducting s-wave rings or hollow cylinders with inner diameter d, with $d \gg \xi$, where ξ is the coherence length [41, 42, 43]. In the opposite regime, when $d \lesssim \xi$, the discrete quantum nature of the electronic states in the ring plays an important role and the energies at half-integer and integer flux quanta are generally different; correspondingly, the superconducting behavior as a function of field has the periodity of only $\hbar c/e$ [40].

1.3.2 Vortex

In type-II superconductors, the interface energy between a superconducting and a normal region is negative, implying that the separated domains of normal and superconducting states are energetically favorable for the system in an external applied magnetic field. In type-I bulk superconductor, the system exhibits the Meissner-Ochsenfeld effect until superconductivity is destroyed by the applied magnetic field. In a type-II superconductor, magnetic field penetrates in a very special way: as quantized vortex filaments. Every filament (or vortex) has a normal core which can be approximated by a long thin cylinder with its axis parallel to the external magnetic field. In the center of the core, the order parameter ψ is zero and the size of the core is of order of the coherence length ξ. The vortex current decreases away from the core with characteristic length $\sim \lambda$, the penetration length. The direction of the vortex current and spatial profiles of ψ and the magnetic field and current are shown in Fig. 1.8.

Each vortex carries one magnetic fluxon, as discussed in Sec. 1.3.1. In a large film of a type-II superconductor, vortices try to arrange themselves at distances $\sim \lambda$ from each other and form a regular triangular lattice, which was first predicted by Abrikosov when he discovered a two-dimensional periodic solution of the GL equations [44]. This state of a superconductor is referred to as the *mixed state* because it is characterized by a partial penetration of the magnetic field in the interior of the specimen so that the sample contains interrelated superconductivity and normal regions. The existence of the mixed state in type-II superconductors has been verified by experiments, where the first direct experimental demonstration was done via Bitter decoration by Essmann and Träuble in 1967 [45].

- The field of an isolated vortex

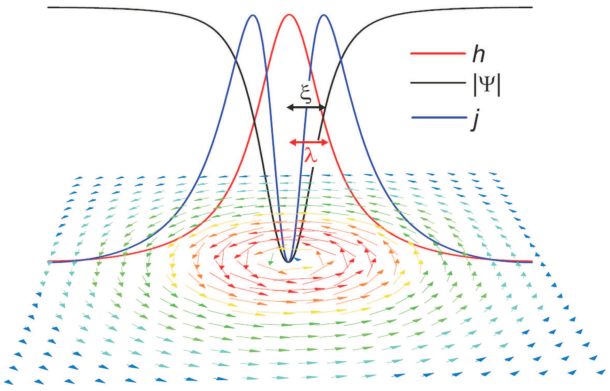

Fig. 1.8 Cross section and vector plot of the super-currents of an isolated vortex in a type-II superconductor. The modulus of the order parameter $|\Psi|$, the local magnetic field $\mathbf{h}$ and the the circulating screening currents $\mathbf{j}$ are shown as a function of the radial distance from the center of the vortex.

We consider the case of a typical type-II superconductor, where $\kappa \gg 1$ (i.e. $\lambda \gg \xi$), and $|\Psi|^2 = 1$ at a distance of $r \gg \xi$. From the second GL equation (Eq. (1.21)), where we took the curl of both sides, we obtain

$$\mathbf{H} + \lambda^2 \text{curl curl}\mathbf{H} = \frac{\Phi_0}{2\pi}\text{curl}\nabla\theta. \tag{1.107}$$

Around the vortex core, we have the following relationship

$$\int \text{curl}\nabla\theta \cdot dS = \oint \nabla\theta \cdot d\mathbf{l} = 2\pi, \tag{1.108}$$

so that

$$\text{curl}\nabla\theta = 2\pi\delta(r)\mathbf{e}_v, \tag{1.109}$$

where $\mathbf{e}_v$ is the unit vector along the vortex. As a result, the solution of Eq. (1.107) subjected to the boundary condition $H(\infty) = 0$ is

$$H = \frac{\Phi_0}{2\pi\lambda^2}K_0(r/\lambda), \tag{1.110}$$

where K_0 is the Bessel function with imaginary argument. By setting a cut-off at $r = \xi \ll \lambda$, one obtains an approximate field in the center of a vortex as

$$H(0) \approx \frac{\Phi_0}{2\pi\lambda^2}\ln\kappa. \tag{1.111}$$

A more accurate value of $H(0)$ can be obtained by considering if the variation of $\Psi(r)$ inside the vortex core [46] as: $H_0 = \Phi_0/2\pi\lambda^2(\ln\kappa - 0.18)$.

1.3.3 Critical magnetic fields

- The lower critical field H_{c1}

The lower critical field H_{c1} is the lowest field at which the formation of vortices in a type-II superconductor becomes thermodynamically favorable. In the case that a typical London superconductor is considered and also the variation of Ψ is neglected, the London expression for the free energy can be written as

$$\epsilon = \frac{1}{8\pi}\int(\mathbf{H}^2 + \lambda^2(\text{curl}\mathbf{H})^2)dV. \tag{1.112}$$

The first term is the magnetic energy density, and the second term is the kinetic energy density of the supercurrent, which comes from

$$W_{kin} = \frac{n_s m v_s^2}{2},$$
$$\text{curl}\mathbf{H} = \frac{4\pi}{c}\mathbf{j}_s.$$

By using the formula

$$(\text{curl}\mathbf{H})^2 = \mathbf{H}\cdot\text{curl curl}\mathbf{H} - \text{div}[(\text{curl}\mathbf{H})\times\mathbf{H}], \tag{1.113}$$

and

$$\int \text{div(curl)}\mathbf{H}\times\mathbf{H}]dV = \oint[(\text{curl}\mathbf{H})\times\mathbf{H}]\cdot dS, \tag{1.114}$$

we get

$$\epsilon = \frac{1}{8\pi}\int \mathbf{H}\cdot(\mathbf{H} + \lambda^2\text{curl curl}\mathbf{H})dV. \tag{1.115}$$

Since we have the relation of Eq. (1.107), the equation above can be written as

$$\epsilon = \frac{\Phi_0}{8\pi}H(0) = \left(\frac{\Phi_0}{4\pi\lambda}\right)^2 \ln\kappa. \tag{1.116}$$

The Gibbs free energy density is $G = F - \mathbf{B}\cdot\mathbf{H}_0/4\pi$, thus in the case of a vortex which carries one magnetic flux quantum Φ_0, we have

$$\mathcal{G} = \epsilon - \frac{\Phi_0 H_0}{4\pi}. \tag{1.117}$$

$\mathcal{G} = 0$ determines the field where the formation of vortex starts to be favored, i.e.,

$$H_{c1} = \frac{4\pi\epsilon}{\Phi_0} = \frac{\Phi_0}{4\pi\lambda^2}ln\kappa. \tag{1.118}$$

- The upper critical field H_{c2}

For bulk materials, when the magnetic field is increased above H_{c1}, the density of flux lines increases as well, and the system is expected to transit into the normal state when the distance between flux lines becomes comparable to the vortex core diameter. The applied magnetic field at this point is denoted as the upper critical field H_{c2}. For fields close to H_{c2} the superconducting order parameter is small, thus we can use linearized GL approach to describe the system. Then Eq. (1.20) becomes

$$\alpha\Psi + \frac{1}{2m^*}\left(-i\hbar\nabla - \frac{e^*}{c}\mathbf{A}\right)^2\Psi = 0. \tag{1.119}$$

This is the same equation as the Schrödinger equation for particles in a constant magnetic field, giving Landau levels as solutions. We take the Landau gauge $\mathbf{A} = H_0 x \mathbf{e}_y$ and separate the variables by writing $\Psi_{n,k_z,k_y}(x,y,z) = e^{ik_z z + ik_y y} u_n(x)$. Then equation Eq. (1.119) can be written as

$$\left[-\frac{\hbar^2}{2m^*}\frac{d^2}{dx^2} + \frac{1}{2}m^*\omega_c^2(x-x_0)^2 \right] u_n(x) = \epsilon_n u_n(x), \tag{1.120}$$

where $x_0 = (\phi_0/2\pi H_0)k_y$ and $\epsilon_n = -\alpha - (\hbar^2 k_z^2/2m^*)$. Equation (1.120) above is the Schrödinger equation of a harmonic oscillator with frequency $\omega_c = |e^*|H_0/m^*c$ with energies

$$\epsilon_n = (n + \frac{1}{2})\hbar\omega_c. \tag{1.121}$$

Here only the smallest eigenvalue, $n = 0,\ k_z = 0$ solution is meaningful as a description of the onset of superconductivity. Hence

$$H_{c2} = -\frac{2m^*ca}{\hbar e^*} = \frac{\phi_0}{2\pi\xi^2}. \tag{1.122}$$

- Surface superconductivity and the third critical field H_{c3}

For the realistic superconducting samples with finite size, the influence of surfaces on the nucleation of superconductivity must be considered. Saint-James and de Gennes [47] showed that superconductivity can nucleate at a metal-insulator interface for the value of a parallel field H_{c3} higher by a factor of 1.695 than H_{c2}. At H_{c3} the superconducting sheath of thickness $\sim \xi(T)$ is formed at the surface, with $\psi \to 0$ in the interior of the sample, and this state is referred to as *surface superconductivity*. The exact result can be obtained in a simple variational approach suggested by Kittel. In his approach, the trial function was taken to be

$$\Psi = f(x)e^{ik_y y} = e^{-ax^2}e^{ik_y y}, \tag{1.123}$$

with x measured from the sample surface. This choice automatically satisfies the boundary condition of $\partial\psi/\partial x|_{surface} = 0$, when the gauge choice $\mathbf{A}$ is along $\mathbf{e}_y$. Substituting expression of Eq. (1.123) in the expression of Gibbs free energy density of Eq. (1.8) and then differentiating under the integral yields

$$H_{c3} \approx \left(\frac{\pi}{\pi - 2}\right)^{1/2} \frac{\Phi_0}{2\pi\xi^2} = 1.66 H_{c2}. \tag{1.124}$$

Therefore, in a magnetic field parallel to the surface, superconductivity nucleates in a surface layer of thickness $\sim \xi$ at a field almost 70 percent higher than the nucleation field of superconductivity in the bulk volume of the material.

- Surface energy and two types of superconductors

Here we consider a semi-infinite superconductor with a surface adjoining a normal metal, in the presence of the applied magnetic field equal to the thermodynamic critical field H_c, at which superconductivity and normal state have the same energy. At the boundary,

both the magnetic field and the superconducting condensate experience smooth changes, over length scales of penetration depth λ and coherence length ξ, respectively. The energy difference between the normal metal and the superconducting region stems from (i) the presence of the ordered superelectrons which lower the energy density by $g_n - g_s$, and (ii) the positive "magnetic" contribution $\frac{1}{2}\mu_0 H_c^2$ acquired by canceling the flux inside the superconductor. If the boundary is stable, the equilibrium between these energies must be reached, i.e., $\frac{1}{2}\mu_0 H_c^2 = g_n - g_s$. However, these two contributions vary with different length scales (λ and ξ), which means they will not cancel each other near the surface, unless $\lambda = \xi$. The difference between the two contributions is called the *surface energy* (σ_{ns}), which is approximately $\frac{1}{2}\mu_0 H_c^2(\xi - \lambda)$ per unit area of the boundary. Therefore it is natural to classify superconductors according to the value of the ratio $\kappa = \lambda/\xi$. As first shown by Gor'kov [13], the precise boundary between type I positive and type II negative surface energy superconductors is determined by $\kappa = \frac{1}{\sqrt{2}}$.

Parameter κ was first introduced in the Ginzburg-Landau theory and is now known as the Ginzburg-Laudau parameter. The ratio of two characteristic lengths can be expressed as

$$\kappa = \frac{\lambda(T)}{\xi(T)} = \frac{2\sqrt{2}\pi H_c(T)\lambda^2(T)}{\Phi_0}. \tag{1.125}$$

Special consideration is required to show that the exact crossover from positive to negative surface energy occurs for $\kappa = 1/\sqrt{2}$. This was also found by numerical integration by Ginzburg and Landau in their original paper. Thus, in the vicinity of T_c we have

$$\kappa < \frac{1}{\sqrt{2}},\ \sigma_{ns} > 0,\ \text{type I superconductivity},$$
$$\kappa > \frac{1}{\sqrt{2}},\ \sigma_{ns} < 0,\ \text{type II superconductivity}.$$

The validity of this condition may also be extended to temperatures far from T_c, by considering the appropriate temperature dependence of κ, for example, in dirty superconductors. A number of works have been devoted to find the exact temperature dependence of the coherence length and the penetration depth. For example, in recent experiments on Pb nanowires Stenuit *et al.* [48] found that the following temperature dependence of the coherence length and the penetration depth

$$\begin{aligned} \xi(T) &= \xi(0)\sqrt{|1-t^4|}/(1-t^2), \\ \lambda(T) &= \lambda(0)/\sqrt{|1-t^4|}, \end{aligned}$$

with conclusion that a temperature dependence of the GL parameter $\kappa = \kappa(0)/(1+t^2)$, where $t = T/T_{c0}$, gives the best fit of experimental data.

Fig. 1.9 summarizes the magnetic properties of type-I and type-II superconductors. It is important to notice that the rigid distinction in Fig. 1.9 only holds for bulk superconductors. In mesoscopic samples with size comparable to ξ and λ, the behavior of the superconductor depends not only on κ but also on the geometric parameters. As shown in Fig. 1.9, bulk samples are pure type-I superconductors when $\kappa < 0.42$, and the system changes from Meissner state to normal state at H_c. In the region of $0.42 < \kappa < 0.71$ the sample remains type-I but has a surface superconductivity for fields between H_c and H_{c3}. When $\kappa > 0.71$, sample turns into a type-II superconductor, with three critical

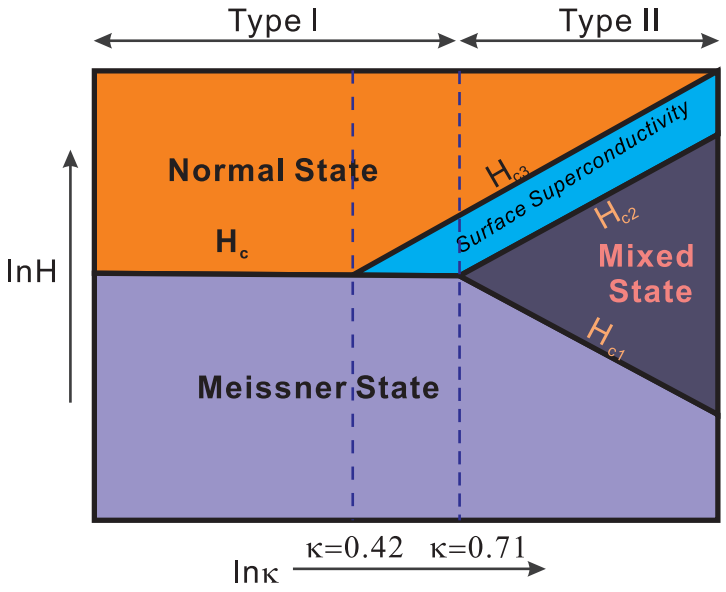

Fig. 1.9 The dependence of the magnetic behavior of bulk superconductors on the value of the Ginzburg-Landau parameter κ. H_c and $H_{ci}|_{i=1,2,3}$ are explained in the text and denote the critical fields determining regions with different behavior. (after Ref. [49]).

fields $H_{ci}|_{i=1,2,3}$, which divides the superconductors into Meissner state, mixed state and surface superconductivity.

These phases (Meissner, mixed and normal) can also be identified by the equilibrium magnetization

$$\mathbf{M} = \frac{\mathbf{B} - \mathbf{H}}{4\pi}, \tag{1.126}$$

where $\mathbf{B}$ is the magnetic induction and can be obtained by averaging the local magnetic field over the sample volume. In the Meissner state all magnetic flux is expelled ($\mathbf{B} = 0$) from the interior of the sample and therefore $\mathbf{M} = -\mathbf{H}/4\pi$. For absolute values of the field $H > H_{c1}$, type-II superconductors are in the mixed state. The incoming magnetic flux causes a smooth decrease of the magnetization $|\mathbf{M}|$ down to zero at the second critical field H_{c2}, where superconductivity is suppressed. The different behavior of type-I and type-II superconductors can be seen in Fig. 1.10, shows for the ideal case. In reality, the intermediate state in a type-I superconductor is expected to exist in the range of applied magnetic field of

$$1 - \eta < \frac{H}{H_c} < 1, \tag{1.127}$$

with η the demagnetization factor, ranging from zero in the limit of a long, thin cylinder or thin plate in a parallel field to $\frac{1}{3}$ for a sphere, $\frac{1}{2}$ for a cylinder in a transverse field, or to unity for an infinite flat slab in a perpendicular field [26].

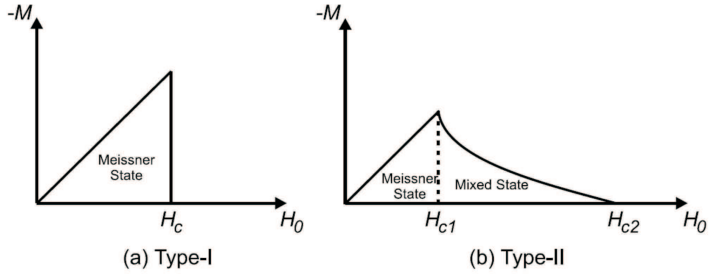

Fig. 1.10 The magnetization as a function of the applied magnetic field for type-I and type-II superconductors [50].

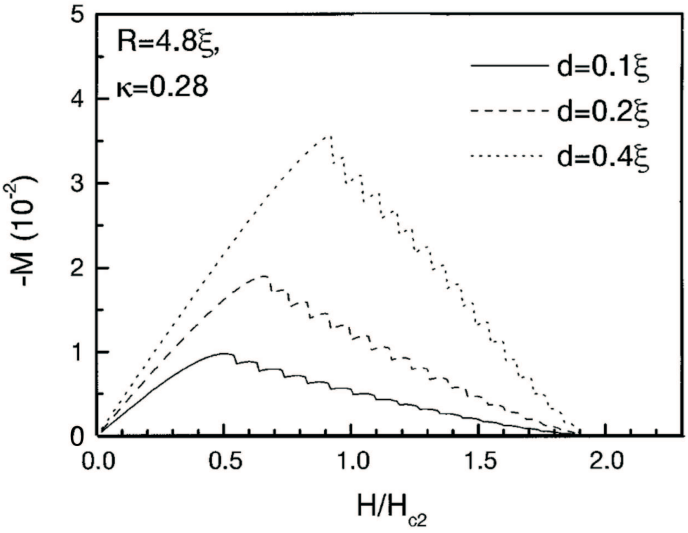

Fig. 1.11 The magnetization of a disk in increasing magnetic field for $R = 4.8\xi$, $\kappa = 0.28$ and different disk thickness [51].

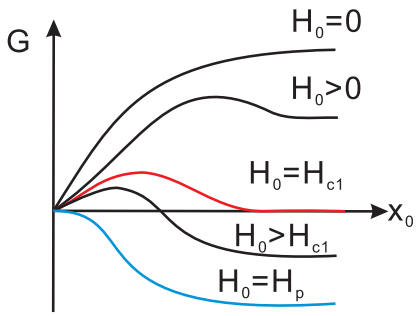

Fig. 1.12 Gibbs free energy of an isolated vortex as a function of its distance from the surface for different values of applied field H_0.

1.3.4 Vortex interactions

1.3.4.1 Interaction between vortices In bulk type-II superconductors, a number of vortices exist in the sample and they interact strongly with each other. The interaction distance of two parallel vortices is of the order of the penetration length λ. When two parallel vortices of the same orientation move into a distance smaller than λ, they start to repel each other. Suppose these two vortices are located at positions r_1 and r_2. The force between these two vortices is

$$\mathbf{f} = \mathbf{j}_{12} \times \Phi_0 \tag{1.128}$$

where $\mathbf{j}_{12}$ is the current density induced by the first vortex at the center of the second vortex (or vice versa). This formula is also valid in a more general case: the Lorentz force acting on the vortex core (per unit length) has the same expression, when there is an externally applied current $\mathbf{j}$.

1.3.4.2 Interaction of a vortex with the surface of a superconductor Up to now, we considered only the thermodynamic equilibrium for the entry of vortices into superconductors. For example, we assumed that the vortex will penetrate into the sample once this is energetically favorable, at the lower critical magnetic field H_{c1}. This is however not true in the presence of a surface. In order to enter the sample, the vortex must first overcome an energy barrier at the surface, which is named Bean-Livingston barrier [52].

This barrier can be described by assuming an antivortex is present outside the superconductor at the image position with respect to the vortex. The vortex and such an imaged antivortex attract each other while the mirror surface currents arising from the applied field repel the vortex. The net effect of this potential barrier is shown in Fig. 1.12 as a function of applied field, and leads to initial flux entry at field H_p which is larger than H_{c1}. In Fig. 1.12 one can see that the field $H_0 = H_{c1}$ is the lowest field at which the vortex entry is thermodynamically favorable. However, the vortex penetration is prevented by the Bean-Livingston barrier. As we continue to increase the field H_0, the barrier shrinks but does not disappear and the vortex is still unable to penetrate the superconductor. In other words the superconductor remains in the Meissner state which is now metastable. The barrier finally vanishes at field $H_0 = H_p$, which is often referred to as the superheating field for the Meissner state, or the flux penetration field.

The direct consequence of the Bean-Livingston barrier is the well established hysteresis in the magnetization curve of a homogeneous type-II superconductor near H_{c1}, for magnetic field (or energy) swept up and down [52].

1.3.4.3 Interaction of a vortex with defects in a superconductor In this section, the interaction between a single vortex and a defect is considered. The size of the defect discussed here satisfies the inequality $d > \xi(T)$, so that microscopic mechanism of pinning is not important. The energy of an isolated vortex is positive, due to the normal core of diameter $\sim 2\xi$, and raises the energy of the superconducting state by $H_c^2/8\pi$ per unit volume, where H_c is the thermodynamic critical field. If the vortex is trapped inside a cavity, within the sample, its normal core is outside the superconducting material, which reduces the system energy by $H_c^2/8\pi$ per unit volume. This lowered energy essentially means that the vortex is attracted by the cavity. The force can be calculated as a derivative of the energy with respect to the position. For the vortex changing its position by $\sim \xi$ near the edge of the cavity, force can be obtained as [53]

$$\mathbf{f}_p \approx H_c^2 \xi / 8. \tag{1.129}$$

If the defect is a spherical cavity, then the pinning force varies with the diameter d of the cavity, as $\mathbf{f}_p \approx H_c^2 \xi d/8$ [53].

The dielectric or normal inclusions with the size of the order of ξ can also act as effective pinning centers in a superconductor. By introducing such inclusions, the critical current of the superconductor for a given magnetic field can increase by several orders of magnitude. Crystalline imperfections can also act as pinning centers, such as dislocations, dislocation walls, grain boundaries, twin boundaries and interfaces between superconductors with different parameters. In high-T_c superconductors, the coherence length ξ is so small, that the optimal vortex pinning centers can be only introduced by heavy particles irradiation. The ion-beam irradiation typically forms cylindrical amorphous normal regions in the superconducting material which are referred to as columnar defects [54].

1.3.5 Mesoscopic superconductors

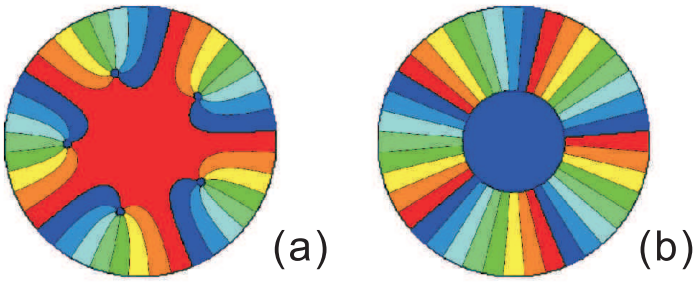

Fig. 1.13 The phase plot for the multivortex (a) and the giantvortex (b) state in a superconducting disk.

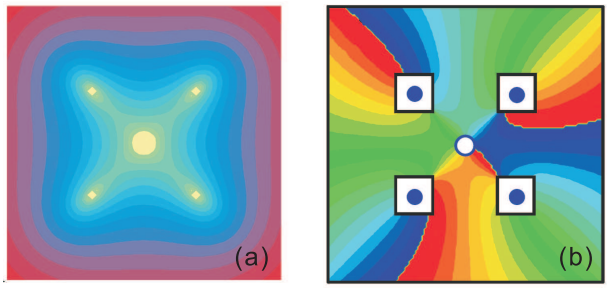

Fig. 1.14 (a) The Cooper pairs density plot for the vortex-antivortex (VAV) state with four vortices in the corners and one antivortex in the center (with a 16× zoom) [55]. (b) The phase plot for the VAV state in (a), but with four artificial pinning sites [56]. The phase change around the antivortex in the clockwise direction is -2π, which is contrary to the vortex case of 2π phase circulation.

1.3.5.1 Vortex configuration In mesoscopic regime, the size of the superconductor is comparable to characteristic lengths ξ and λ. Therefore, the vortex configuration is not only determined by on the interaction between vortices, but also by the geometrical confinement imposed by the sample geometry. This makes the behavior of the mesoscopic samples significantly different from the bulk materials. Due to the competition of vortex interactions and the confinement, the vortices try to form bulk-like triangular Abrikosov lattice in the sample far away from the boundaries, and at the same time obey sample shape when close to the boundaries. These competing interactions lead to the shell vortex structures in disks [50, 57, 58] and the square and triangular vortex distributions in square and triangular samples [59, 60, 61]. The smaller the size of the superconductors, the stronger the confinement acting on vortices. As a consequence, vortices in mesoscopic samples can form a novel state with a single normal core containing several flux quanta, so called *giant vortex* (GV) state [50]. The corresponding state with same vorticity, but with separated single-flux-quantum vortices, is designated as *multi-vortex* (MV) state. In two-dimensional superconductors, the transition between MV and GV state can be realized by decreasing the size of the sample, or increasing the thickness of the sample which increases the demagnetization ability of the sample, i.e. the screening currents, and increases confinement. A similar phenomenon takes place also by increasing applied field or temperature.

Not only the geometry of the vortex configuration is influenced by the shape of the superconductor, but also the stability range of different vortex states. For the squares and triangles, the vortex states with matching symmetry to the sample shape are more stable than other states. Note also that close to the superconducting/normal transition, the surface superconductivity can no longer be distinguished in the mesoscopic superconductors, as it bears resemblance to the giant-vortex state.

The cases when the vorticity is not consistent with the symmetry of the sample are also often interesting. For example, it is possible that additional vortex-antivortex (VAV) pairs nucleate, in order for the vortex configuration to match the symmetry of the sample shape without changing total vorticity [55, 62, 61]. For example, in the superconducting square the triangular configuration of vortices change to four vortices located in the four corners, with the antivortex in the center. The stability region of such a VAV molecule

can be enhanced by introducing the artificial pinning of matching symmetry. However, these states remain unobserved experimentally to date [56].

1.3.5.2 Vortex interactions The magnetic field of the first vortex entry H_p in a finite sample is higher than the low critical field of H_{c1}, due to the Bean-Livingston (BL) energy barrier. In London theory, this barrier is demonstrated as the competition of the vortex attraction to the sample surface and its repulsion by screening currents, see Sec. 1.3.4.2. This model was further developed for cylindrical samples [63, 64, 65], thin disks [66, 67, 68] and rings [69, 70, 71]. In mesoscopic samples, however, the sample size is comparable to the characteristic length of decay of the superconducting current away from the boundary. For that reason, a discrepancy arises between the Ginzburg-Landau approach and the London theory, which decreases by increasing sample size [72]. The energy barrier also strongly depends on the GL parameter κ: smaller κ enhances the barrier. For polygonal superconductors, the profile of the barrier changes along the sample edges: the lowest barrier is found at the middle of the sides and highest at the corners of the sample. In superconducting disks, the barrier is azimuthally uniform, but the radial position of the barrier can be changed by the applied magnetic field. The barrier gradually shifts from the inner boundary to the outer one with increasing field.

Finally, note that even in the absence of a vortex inside the sample (when sample is smaller $\lesssim 2\xi$), hysteresis in the magnetization can still be found at the transition between the superconducting and the normal state. This hysteresis is due to metastability created by a *volume barrier* [73] instead of the BL surface barrier. There exist two local minima in the free energy, corresponding to two different values of the order parameter, of the superconducting and normal states respectively, between which a maximum of energy acts as a barrier to inhibit the system switching from one state to the other.

1.3.6 Experimental characterization of vortex states

The penetration depth and coherence length are key length scales in a superconductor. In terms of vortices, ξ is the size of the vortex core and λ describes the extent of the vortex magnetic field inside the superconductor. Scanning Tunneling Microscopy (STM) and Spectroscopy (STS) are the experimental techniques to observe directly the electronic density of the states in the vortex structure, thus also ξ. The penetration depth affects the field profile of the vortex which can be imaged by e.g. the magnetic force microscopy (MFM), superconducting quantum interference device (SQUID) magnetometry and susceptometry, and scanning Hall probe microscopy (SHPM). For imaging the vortex matter in general, there are numerous issues to consider when selecting the measurement technique, such as spatial resolution, ease of interpretation, extent of sample preparation, temperature and field range, dynamic speed, magnetic field sensitivity, etc.

1.3.6.1 Scanning Tunneling Microscopy (STM) and Spectroscopy (STS) The fundamental principle of the scanning tunneling microscopy (STM) is the quantum tunneling, which takes place through a thin potential barrier between two electrodes. The setup consists of a very sharp tip controlled by piezoelectric devices (converting voltage into mechanical deformation). By applying a voltage (V_t) between the tip and the sample,

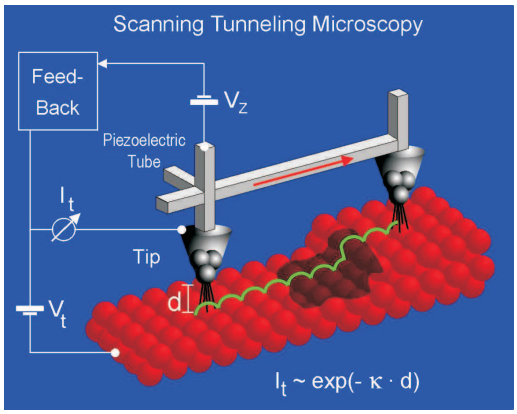

Fig. 1.15 Experimental realization of scanning tunneling microscopy.

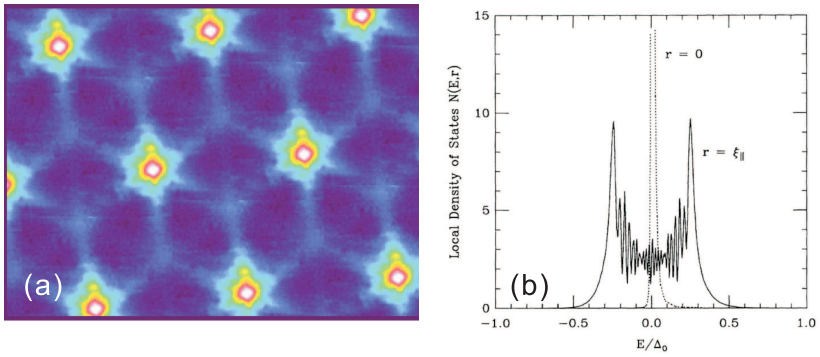

Fig. 1.16 (a) The STM image from Ref. [74], a six fold "star"-shaped LDOS around the vortex. (b) The zero-bias peak at the vortex center and the splitting of it when measured at $\xi_{\|}$ away from the vortex center[75].

a current can flow (I_t) between these electrodes when their distance is reduced to a few atomic diameters. The amplitude of the current strongly depends on the distance between the tip and the sample, and of course also on the potential difference V_t. The origin of the contrast in the STM image of superconductors is the variation of the quasiparticle density of states (DOS) for different positions of the tip during scanning the surface. In conventional low temperature superconductors, this is easily understood using the simple BCS model

$$N_s(E) = N_n(E_F)\frac{|E|}{\sqrt{E^2-\Delta(T)^2}}, \quad |E| > \Delta(T) \tag{1.130}$$

$$N_s(E) = 0, \quad |E| < \Delta(T) \tag{1.131}$$

The effect of the temperature is included via,

$$\frac{dI}{dV} = e\beta \int_{-\infty}^{\infty} N_s(r,E)g(E-eV_t)dE,$$

where $g(E) = -\partial f(E)/\partial E$, the $N_s(r, E)$ is the superconducting DOS at the location of the tip **r**, f(E) is the Fermi-Dirac distribution function and g(E) is the thermal broadening function.

Inside the vortices, it is the spatial variation of the gap $\Delta(r)$, in particular its vanishing in the vortex core (acting as a quantum well), that gives rise to the vortex bound states, predicted by Caroli, Matricon and de Gennes (CMdG) [76]. This normal-core picture of the vortex is, however, correct only for "dirty" superconductors, which heavily contain impurities or defects.

There are several different ways to visualize vortices by STM:

- Topographic mode. By fixing the bias voltage (V_t) just at the maximum gap value, i.e. $eV_t = \Delta$, vortices can be visualized by the Z(x,y) deflection of the tip in the standard STM topographic mode (i.e. feedback on). The problem is that this voltage is small and consequently the current is usually small. As a consequence, the tip must be very close to the surface.

- Current mode. Essentially the same as the topographic mode but the current I_t(x,y) is recorded and the feedback condition is relaxed.

- Conductance mapping. During the scanning, the conductance dI/dV(x,y) is recorded using standard lock-in techniques. The modulated bias is set at the superconducting gap edge, at zero bias, or another constant value of the voltage.

- Full conductance mapping. During the scanning, a complete I(V) spectrum is acquired at each pixel (x,y) of the image. Thus, the conductance map dI/dV(x,y) is known for each bias within the voltage sweep.

  Note the possible misinterpretations of the vortex images: the vortices appear as bright spots (higher values) in the current or topographic modes but can be bright or dark spots in the STS modes depending on the selected bias.

In 1989, Hess *et al*, first succeeded in observing the bound states, namely, the local density of states (LDOS) in and around a vortex, with Scanning Tunneling Microscope (STM) [74]. They revealed the true electronic structure of the vortex in a clean type-II superconductor, 2H-$NbSe_2$, and the existence of a striking zero-bias peak at the vortex center. Hess *et al* further found out that the LDOS around the vortex was shaped like a "star" at a fixed energy with orientation dependent on the energy, that is, the sixfold star shape rotates as the bias voltage varies [77]. Soon after this observation, Gygi and Schlueter proposed an explanation for this rotation of the star-shaped LDOS [78]. On the basis of a sixfold perturbation, they interpreted the lower and higher energy stars as bonding or antibonding states respectively. However, some features of the star-shaped LDOS observed in later STM experiments could not be sufficiently understood by this perturbation scheme.

Motivated by experiments, several theoretical works were carried out. Shore,*et al* predicted that the zero-bias peak should split into two, if STM spectra were taken at some distance from the vortex center along a radial line [75]. The splitting indicates that the bound quasiparticle around a vortex has a dispersion relation between its angular momentum and energy. This theoretical prediction was actually confirmed by later

experiments of Hess. The zero-bias peak and its splitting along a radial line showed that the vortex had rich internal electronic structure. The simple normal-core picture of vortices did break down in clean type-II superconductors.

Over the past years, STM investigations of high temperature superconductors have revealed unusual characteristics of the superconducting gap. The superconducting gap in HTSs is much larger than expected from the BCS mean field value. In addition, the temperature dependence of the tunneling conductance spectra in YBCO and BSCCO single crystals are different from BCS predictions. In particular BSCCO(2212) single crystals show a gap above the critical temperature (called *pseudogap*), in both underdoped and overdoped samples and the CMdG states are apparently absent. This *pseudogap* was firstly shown by Renner *et al* [79]. Strikingly, in BSCCO(2201) overdoped single crystals, the pseudogap is observed up to very high temperatures of about 70K (while T_c is only of the order of 10K). In optimally doped YBCO, no indication of a pseudogap above T_c is observed. This is consistent with other striking differences between the two systems and supports the interpretation of the pseudogap in terms of strong superconducting fluctuations.

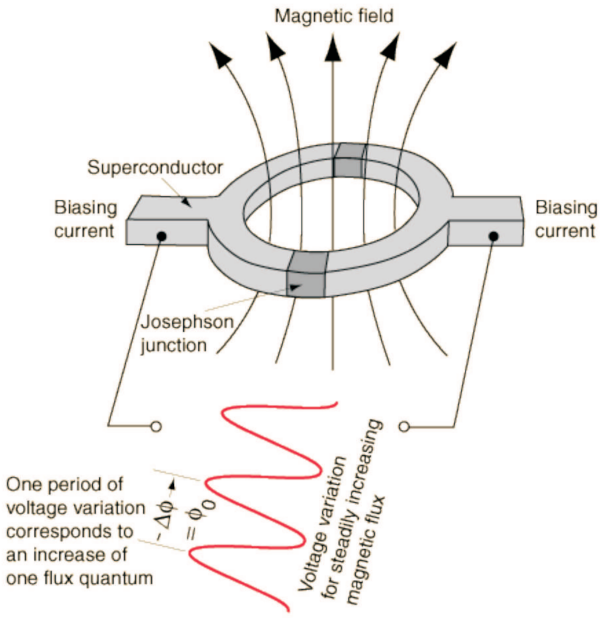

Fig. 1.17 The schematic depiction of a SQUID

1.3.6.2 SQUID magnetometry The superconducting quantum interference devices (SQUIDs) are currently the most sensitive magnetic flux detectors. The scanning SQUID microscope has several advantages over other vortex imaging techniques, such as high field local sensitivity, accurate determination of local field strength (compared to MFM and Bitter decoration) and no limitation on the sample thickness (in contrast to the Lorentz microscope). In spite of the limited spatial resolution of $1 \sim 10\mu m$, SQUID microscopy is a powerful tool for nondestructive vortex observation in superconducting thin films

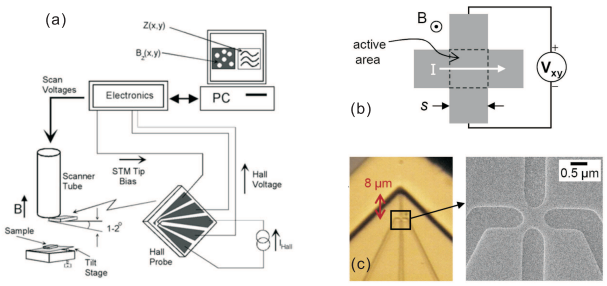

Fig. 1.18 (a) Schematic diagram of the scanning Hall probe microscope. (b) The Hall cross, the Hall voltage V_{xy} is proportional to the current I in the x direction and the z component of the magnetic field B within the active area. (c) Second generation Hall probes, with 0.25 μm^2 cross-section (can be made down to 0.01 μm^2 in size) [80].

and devices in a weak field (smaller than the Earth field), which is especially important for electronic device applications.

A SQUID consists of two superconductors separated by thin insulating layers to form two parallel Josephson junctions, see Fig. 1.17. Scanning SQUIDs measure the magnetic flux through a small pick-up loop, $\Phi = \int_{loop} \mathbf{B} \cdot d\mathbf{S}$. The width of the superconducting wires is the limiting factor for the SQUID pick-up loop size, since the wire width cannot be smaller than the penetration depth of the superconducting material. The high sensitivity of the SQUID devices is associated with measuring changes in magnetic field related to one flux quantum. One of the discoveries that had to do with Josephson junctions was that the flux in superconductors is quantized in units of

$$\Phi_0 = \frac{2\pi\hbar}{2e} \approx 2.067 \times 10^{-15} \mathrm{T} \cdot m^2. \tag{1.132}$$

If a constant biasing current is maintained in the SQUID device, the measured voltage oscillates with the changes in phase at two junctions, which depends on the change in the magnetic flux. Counting the oscillations allows one to evaluate the flux change which has occurred.

Scanning SQUID microscopy (SSM) has been developed and implemented by a number of groups to study the vortex behavior in superconducting materials. A landmark application of SSM was the observation of half flux quanta trapped or generated at the tri-crystal point in high-Tc cuprate thin films, which confirmed the d-wave symmetry of the order parameter in these "unusual" superconductors [17,18]. SSM succeeded in observation of Josephson vortices in the CuO_2 planes in cuprate superconductors[19].

1.3.6.3 Scanning Hall probe microscopy (SHPM) Hall probes are based on the principle of the Hall effect, discovered by Hall in 1879. If a current carrying conductor is placed in a perpendicular magnetic field, transverse voltage (the Hall voltage V_{xy}) appears due to the Lorentz force on the charge carriers. This voltage is proportional to the current and field, and inversely proportional to the carrier density n of the conductor. The Hall effect is often used to determine n and the sign of the charge carries in a material. However, it can also be used to measure a magnetic field if n is known. The basic geometry of a

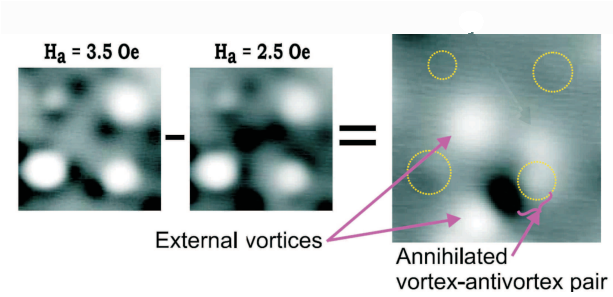

Fig. 1.19 SHPM images of vortex-antivortex states in a Pb film with magnetic dots on top, obtained at two different effective applied fields at $T = 5K$, and their difference image showing the annihilation of a vortex-antivortex pair, and an addition of two vortices in increasing magnetic field [81].

Hall probe, a Hall cross, and the setup of the whole instrument are shown in Fig. 1.18. The equation for the Hall effect in three dimensions is given by

$$V_{xy} = -\frac{I_x B_z}{n_{3D} q t}, \tag{1.133}$$

where q is the charge of the current carriers and t is the conductor thickness in the z direction. Decreasing n_{3D} increases the response of the Hall voltage to changes in magnetic field. In the two-dimensional case, conductor has very low carrier density, and the Hall effect equation can be written as

$$V_{xy} = -\frac{I_x B_z}{n_{2D} e} = -R_H I_x B_z, \tag{1.134}$$

with the charge carriers taken to be electrons ($q = -e$) and the Hall coefficient defined as $R_H = (n_{2D} e)^{-1}$. The Hall cross is made of a two-dimensional electron gas device, which scans above the surface of the magnetic material. The profile of the strength of the Hall potential directly demonstrates the distribution of the magnetic field.

The advantage of SHPM, compared to the other techniques, are the direct magnetic field measuring, the non-invasive, quick data acquisition (about 1 image/second) and quick delivery of absolute values of the magnetic field. Nowadays the main challenge is to develop the instrument with spatial resolution well below $0.1\mu m$, but SHPM is still very suitable for imaging of vortices in both bulk and mesoscopic samples. For example, the real-time ($\sim$ 1 frame/s) flux profiles [80, 82] were studied in bulk samples and also in superconductor/ferromagnet heterostructures. Recently, SHPM was for the first time used to image the vortex-antivortex molecules in superconducting Pb films with magnetic dots on top [81] and inplane [83].

1.3.6.4 Calorimetry Heat capacity can also play a significant role in determining the parameters of the superconductor and the description of the transition between different vortex states.

One of the reasons to use calorimetry in superconductivity is the expected discontinuity of the specific heat of the superconductor at the critical temperature. This can be

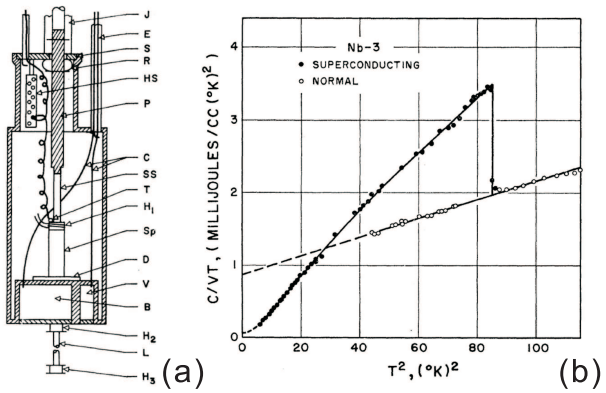

Fig. 1.20 (a) Calorimeter used to measure determine specific heat, in Ref. [84] (b) measured specific heat of niobium in the superconducting and normal state.

easily obtained from the BCS theory, as

$$\begin{aligned}\Delta C &= (C_s - C_n)\Big|_{T_c} = N(0)k_B\beta^2\left(\frac{d\Delta^2}{d\beta}\right)\int_{-\infty}^{\infty}\left(\frac{-\partial f}{\partial|\xi|}\right)d\xi \\ &= N(0)\left(\frac{-d\Delta^2}{dT}\right)\Big|_{T_c}, \end{aligned} \tag{1.135}$$

where f is the quasi-particle occupation number. Using the approximated value of $\Delta(0) = 1.76k_BT_c$, obtains $\Delta C \approx 9.4N(0)k_B^2T_c$.

The heat capacity measurement for the vortex states in the mesoscopic superconductors is a recent achievement, triggered by the very recent progress in attoJoule nanocalorimetry [85, 86]. The specific heat of the mesoscopic sample is difficult to measure individually. Instead, one measures an array of samples (the number of order of 10^5) with same geometric parameters. These samples are separated far away enough from each other to avoid the interaction between them and thus the additive thermal signals. Such arrays of mesoscopic samples are typically patterned by electron beam lithography on a specific heat sensor, and superconductor is deposited by thermal evaporation.

As will be elaborated on in Chapter V, the measured heat capacity as a function of magnetic field shows direct connection to the vortex states of the mesoscopic superconductors, as demonstrated in superconducting disks [87] and rings [88]. The heat capacity monotonically increases with the applied magnetic field, while at the same time it exhibits cascades at each vortex entry, see Fig. 1.21(a). By investigating the behavior of the heat capacity jumps at the superconducting-to-normal state, Fig. 1.21(b) one clearly observes the evidence of the Little-Park oscillations.

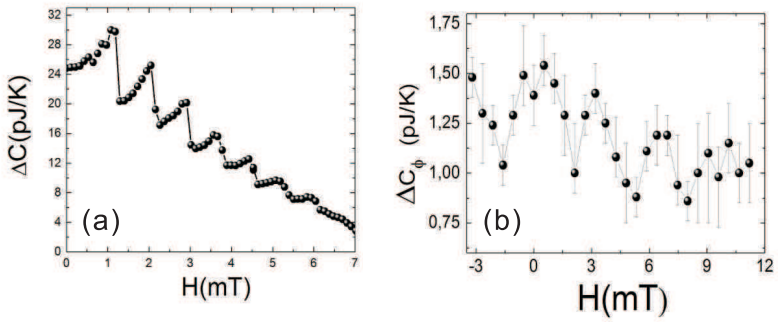

Fig. 1.21 (a) Height $\Delta C(H)$ of the heat capacity discontinuity at the S/N transition for superconducting disk with radius $R = 1.05\mu$m and of thickness $e = 160$nm [87]. (b)Heat capacity jump at the S/N transition $\Delta C(\Phi)$ versus the magnetic flux Φ through a single ring [88].

2

Magnetic properties of vortex states in spherical superconductors

2.1 INTRODUCTION

Recent advances in nano-fabrication techniques will soon enable fast preparation and experimental studies of truly *three-dimensional* (3D) mesoscopic superconductors [89, 90, 91]. It is already known that quantum confinement in thin mesoscopic superconductors, imposed by the sample geometry, has important consequences on both vortex matter and critical properties of the sample. In such essentially two-dimensional (2D) superconductors with sizes comparable to the penetration depth λ and coherence length ξ, numerous works have been done over the past decades, theoretically by Schweigert and Peeters [92, 35], Palacios [93, 94] solving non-linear Ginzburg-Landau equations, Misko [60, 61], Buzdin and Brison [68] using the image method within the London approximation and also experimentally by Moshchalkov [95, 96], Geim [51, 97], and Kanda [98, 99]. The effect of the geometry of the sample on superconductivity has been also thoroughly investigated [100, 59, 101, 61, 102, 103, 104]. However, the sample was always effectively two-dimensional in the latter studies, as the superconducting order parameter was always uniform along the z-axis. This is obviously not the case in three-dimensional samples (e.g. sphere), where the slanted angle of the sample sides with respect to the applied magnetic field plays a significant role. Therefore, the earlier theories based on the 2D London approximation become insufficient, and the 3D Ginzburg-Landau study of the interplay of the applied magnetic field and 3D distribution of the Cooper-pair density becomes essential. This is the first important objective of this chapter.

In previously studied thin mesoscopic samples [35] two fundamental kinds of vortex states were predicted theoretically: (i) the multi-vortex state with a spatial arrangement of single vortices (each carrying one flux quantum) and (ii) the giant vortex state, where several vortices coalesce into a single core, containing multiple flux quanta. The existence of those vortex states in superconducting disks was verified recently in an experiment

using the multiple-small-tunnel-junction method [98]. However, the definition of giant- and multi-vortex states becomes more complicated if the problem is extended to the third dimension, especially in more complicated sample geometries, where vortices are exposed to a 3D interaction with the sample boundary. For example, in [105] a break-up of the vortex structure in a 3D mesoscopic wire with a constriction was predicted. A giant vortex nucleated in the widest part of the wire splitted into a smaller and/or individual vortices near the constriction. Here we study the vortex states in spherical mesoscopic samples (with different radii), and also for different material properties (i.e. Ginzburg-Landau parameter κ) which fine-tune the vortex-vortex interaction [106].

The understanding of the effects of the true three-dimensionality of the studied system is not only important for theoretical purposes but for experiment as well. In transport measurements it now becomes crucial where to attach current/voltage leads to the sample. Similarly, in magnetometry, the exact position of the placed Hall probe above the sample is much more important than for thin 2D samples. In this chapter, we partly address the latter issue, and calculate the stray field around the sample (thus in 3D), the magnetic moment of the sample as a whole, as well as the response of the Hall bar as a function of its position and size.

Our study work is a continuation, but also a considerable extension of the existing studies of spherical superconductors. In Ref. [107], vortex matter in a superconducting sphere was studied using an approach based on the linear Ginzburg-Landau (GL) theory. In Ref. [108], vortex patterns in superconducting shells, with demagnetization effect and nonlinear Ginzburg-Landau are fully considered, also in Ref. [109]. Vortex patterns in superconducting shells were studied in Ref. [110], where no demagnetization effects were taken into account. Ref. [111] dealt with effects of the chosen boundary condition on the vortex patterns in mesoscopic thick disks and spheres, but still remaining in the $\kappa \to \infty$ limit. Within the same limit finite size mesoscopic cylinders and asymmetric spheres were studied in a tilted magnetic field [112]. In the present work, we study superconducting spheres with magnetic screening fully accounted for (for different κ), within the Ginzburg-Landau formalism solved on a 3D grid. Therefore, both the superconducting order parameter and the local magnetic field are calculated self-consistently in 3D space.

The chapter is organized as follows. In Sec. 2.2 we introduce the theoretical model. In Sec. 2.3 we present the phase diagram for all vortex states, as a function of the sample size and applied magnetic field. The importance of the chosen superconducting material (with different Ginzburg-Landau parameter κ) for the vortex behavior is studied in Sec. 2.4. The simulations of the magnetic response of the sample are shown in Sec. 2.5, where the assumed finite size of the Hall bar in magnetometry measurements is taken into account. In Sec. 2.6 we summarize our findings.

2.2 THEORETICAL FORMALISM

In what follows, we consider superconducting spheres characterized by their radius R, and Ginzburg-Landau (GL) parameter $\kappa = \lambda/\xi$, where ξ, λ are coherence length and penetration depth, respectively. We assume all considered samples to be immersed in an insulating medium, and exposed to a uniform magnetic field $\mathbf{H} = (0, 0, H)$. To

numerically treat this system, we follow the numerical approach of Schweigert and Peeters [92]. First, using dimensionless variables and the London gauge div$\mathbf{A} = 0$ for the vector potential $\mathbf{A}$, we rewrite the system of two coupled GL equations in the following form

$$(-i\bigtriangledown_{3D} - \mathbf{A})^2\Psi = \Psi(1 - |\Psi|^2), \tag{2.1}$$

where

$$-\kappa^2\Delta_{3D}\mathbf{A} = \mathbf{j}_{3D}, \tag{2.2}$$

$$\mathbf{j}_{3D} = \frac{1}{2i}(\Psi^*\bigtriangledown_{3D}\Psi - \Psi\bigtriangledown^*_{3D}\Psi) - |\Psi|^2\mathbf{A}, \tag{2.3}$$

is the density of the superconducting current induced by the sample in response to the applied field. Here the distance is measured in units of the coherence length ξ, the vector potential in $c\hbar/2e\xi^2{=}\kappa\sqrt{2}H_c$, and order parameter is scaled to its value in the absence of the magnetic field. Eqs. (2.1-2.2) are then discretized on a uniform cubic grid using the link variable approach [34], in Cartesian coordinates with typically 5 grid points per ξ, and solved in a finite-difference scheme. Eq. (2.2) is solved using three dimensional Fast Fourier transform, in a method similar to known procedures for solving Poisson equation (see e.g. Ref. [113]).

In our calculations, the superconducting order parameter satisfies the Neumann boundary condition

$$(-i\bigtriangledown_{3D} - \mathbf{A})\Psi|_{\rho=\mathbf{R}} = 0, \tag{2.4}$$

while the external applied vector potential has the symmetric form

$$\mathbf{A_x} = -\frac{1}{2}Hy\mathbf{e}_x, \quad \mathbf{A_y} = \frac{1}{2}Hx\mathbf{e}_y, \quad \mathbf{A_z} = 0. \tag{2.5}$$

In additional constriction is that the resulting (total) vector potential must decay to zero ($\mathbf{A} = 0$) far away from the superconductor.

To find the different vortex configurations, which include all stable states (thus the lowest energy *ground* state, and the higher energy *metastable* states), we search for the self-consistent solutions of Eqs. (2.1) and (2.2). If we simulate a field-cooled experimental situation, we initiate the calculation from randomly generated initial conditions (for a zero-field-cooled situation, we start from $\Psi \approx 1$ in the whole sample). Then we slowly change the applied magnetic field and recalculate each time the superconducting state. In such a way, we are able to trace back and forth all found vortex states in the whole region of their stability. For each vortex configuration, found at different applied fields, we calculate the Gibbs free energy (in units of $F_0 = H_c^2/4\pi$) as

$$F = V^{-1}\int_V [2(\mathbf{A} - \mathbf{A}_0)\cdot\mathbf{j}_{3D} - |\Psi|^4]d\mathbf{r}, \tag{2.6}$$

where integration is performed over the sample volume V, and $\mathbf{A}_0$ is the vector potential of the initially applied magnetic field.

To characterize the diamagnetic property of our superconducting sample, we calculate its magnetization in an applied field. Differently from the thermodynamic expression $M = \partial F/\partial H$, we define sample magnetization as the expelled magnetic field from the sample, i.e. as

$$\mathbf{M} = \frac{\langle\mathbf{h}\rangle - \mathbf{H}}{4\pi}, \tag{2.7}$$

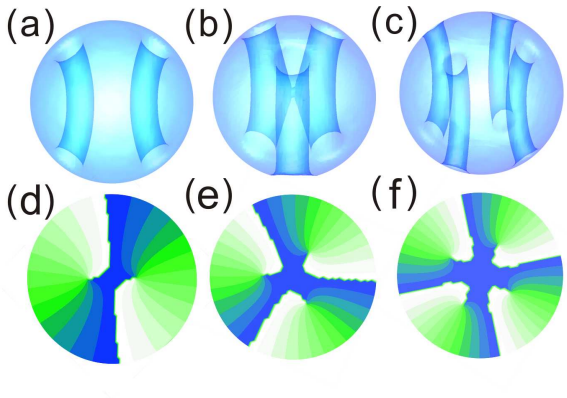

Fig. 2.1 Three-dimensional 10% isoplots of the Cooper-pair density in the sphere with radius $R = 4\xi$, for vorticity $L = 2$, at applied magnetic field $H = 0.61H_{c2}$ (a), $L = 3$ at $H = 0.79H_{c2}$ (b) and $L = 4$ at $H = 1.14H_{c2}$ (c). (d-f) show the corresponding phase contourplots in the equatorial plane of the sample [red color - 0, blue color - 2π].

where $\mathbf{H}$ is the applied magnetic field, and $\mathbf{h} = \mathrm{rot}\mathbf{A}$ is the resulting (total) magnetic field. $<>$ denotes averaging over the particular area (which could be the sample as a whole, or just a surface area of a magnetic detector, e.g. Hall probe, at a particular location above the sample).

2.3 VORTEX STATES IN A MESOSCOPIC SUPERCONDUCTING SPHERE

In this section, we discuss fundamental properties of the vortex configurations in spherical superconductors. Knowing that the density of the superconducting Cooper-pair drops to zero inside the vortex core, we show the 3D isoplots of the low Cooper-pair density inside the sample to best illustrate the vortex configuration. Such plots are shown in Fig. 2.1, each with a corresponding plot of the phase of the order parameter (in the equatorial plane), for states with vorticity $L = 2$ (a,d), $L = 3$ (b,e), and $L = 4$ (c,f). According to the defination of vorticity in Ref. [92], the total number of vortex lines trapped in the sample, that can be deduced from the number of $0 \to 2\pi$ phase changes along the sample rim in Figs. 2.1(d-f). Contrary to the straight vortex lines in the case of superconducting cylinder/disk, in our sample vortices are compressed together in the equatorial plane of the sample, due to the strong screening (Meissner) currents running along the perimeter. At the same time, vortices remain perpendicular to the surface of the sample edge at the point of entry/exit, which results in their strong bowing along the sample (see Fig. 2.1).

Even though compressed in the center of the sample, individual vortices are still clearly separated in both $|\Psi|^2$-isoplots and phase contourplots in Fig. 2.1. We refer to such vortex state as a multi-vortex (MV) state in the remainder of the chapter. However, this nomination may become ambiguous for overlapping vortex lines, which can be expected at higher fields, and a clear numerical threshold must be established to differentiate the MV state from a giant-vortex (GV) state. In Fig. 2.2, we illustrate the used criterion in our calculation, where the Cooper-pair density is plotted across the center of the

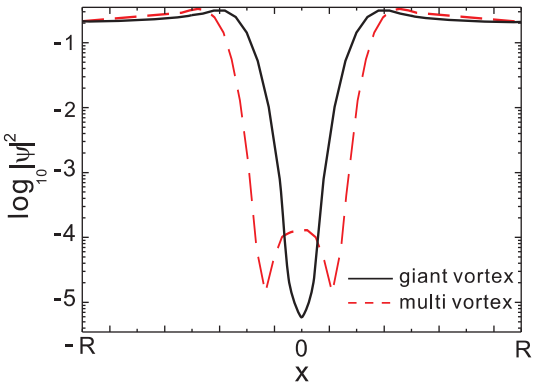

Fig. 2.2 Illustration of the giant-vortex and the multi-vortex state for $L = 2$, at applied magnetic field H = 0.81 H_{c2} and 0.76 H_{c2} respectively, close to the numerical ambiguity. The Cooper-pair density is plotted along the sample diameter, where found minima are taken as singularities of the order parameter.

sample. When a maximal value between found minima of the Cooper-pair density exceeds 10^{-5}, we regard the found state as a collection of singularities, i.e. a multi-vortex state. Otherwise, the numerical precision may be questioned, and we assume a single singularity, characteristic of a giant-vortex.

The main principle of quantum confinement of vortices in mesoscopic superconductors follows from the sample size being comparable to the size of the vortex core. Therefore, we briefly address the influence of our sphere's size on the vortex configurations. In Fig. 2.3, the free energy curves are given as a function of the applied magnetic field, for a superconducting sphere with radius $R = 3\xi$ (a) and $R = 4\xi$ (b). Different energy curves with increasing field correspond to states with gradually incremented vorticity, starting from the vortex-free, Meissner phase ($L = 0$). As can be seen in Fig. 2.3, more vortices can be captured in the larger sample before superconductivity is destroyed. Maximal vorticity is $L_{max} = 9$ for $R = 4\xi$, compared to $L_{max} = 4$ for $R = 3\xi$. The screening of the magnetic field is much more effective in the smaller samples, where the penetration field for vortices is significantly larger [in Fig. 2.3(a) $H_p = 0.902H_{c2}$, compared to $H_p = 0.45H_{c2}$ in (b)]. Namely, a larger superconducting sphere expels proportionally more magnetic flux in the Meissner phase, which results in a *higher* field at the equatorial boundary of the sample for a larger sample than for the smaller ones at the same applied field. Such high magnetic field around larger samples suppresses superconductivity at the sample edge, and creates weak points that facilitate the entry of vortices.

Another influence of the confinement can be observed for larger vorticity. In Fig. 2.3(a), penetrating flux lines are strongly influenced by the proximity of the boundary, and are forced to coalesce into a giant-vortex for all vorticities. For larger samples [e.g. the one in Fig. 2.3(b)], the latter condition is relaxed, and singly-quantized vortices may remain stable in the sample. The solid lines in Fig. 2.3(b) represent the giant-vortex state while the dashed lines show the multi-vortex state. In general, one notes that multi-vortex

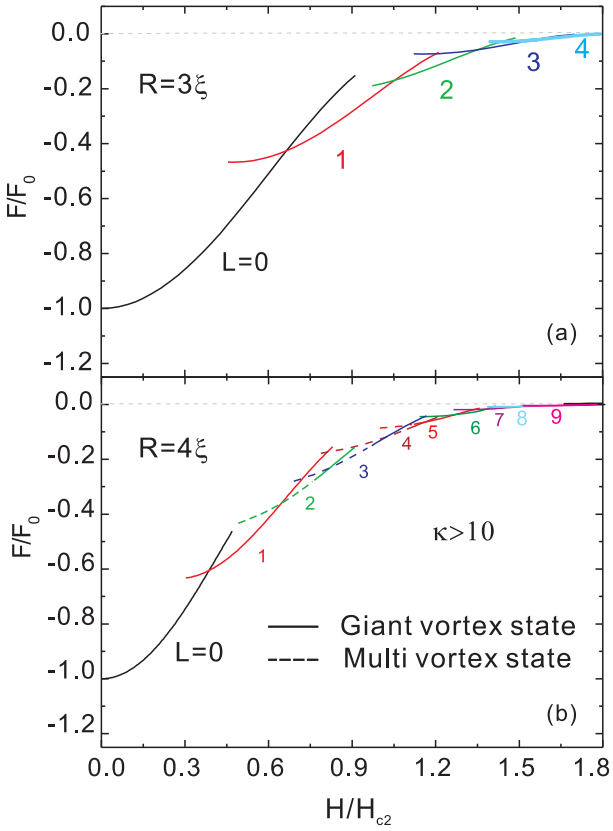

Fig. 2.3 The free energy curves as a function of the applied magnetic field, for spheres with radius $R = 3\xi$ (a) and $R = 4\xi$ (b). Giant-vortex states are indicated by solid curves, while multi-vortex states are denoted by dashed curves.

states are initially formed, as vortices individually enter from the sample boundary. With increasing field, the screening currents strengthen at the equator, compressing the vortices together, which eventually results in the formation of a giant-vortex. In short, MV/GV state transition is a product of the competing interactions in the system, as individual vortices interact repulsively with currents at sample edges (inward force), as well as with each other (outward force). As a comparison, the free energy curves for different vortex states are plotted for a cylinder in Fig. 2.4, with the same radius of 4ξ, and height of 5.5ξ (giving the same volume as the considered sphere). The confinement from the curved boundary of the sphere is replaced by the relatively "looser" and homogenous ones from the cylinder. Thus, more vortices can be formed inside the sample, and multi-vortex states are preferred to the giant-vortex states for the same vorticity.

To systematically study the behavior of vortices for different sizes of the superconducting sphere, we varied the radius of the sample from 1.0ξ to 4.6ξ and recorded the ranges of applied magnetic field in which each of the vortex states represented the ground state of the system. The results are summarized in the phase diagram of Fig. 2.5, for

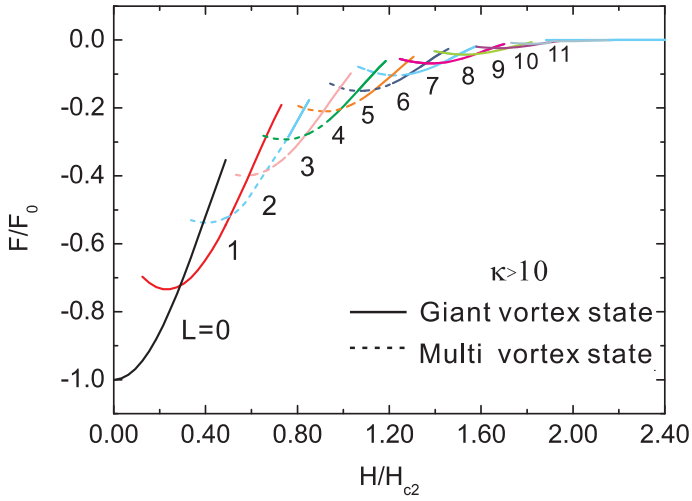

Fig. 2.4 The free energy curves as a function of the applied magnetic field, for a cylinder with radius R = 4ξ and height d= 5.5ξ. Giant-vortex states are indicated by solid curves, while multi-vortex states are denoted by dashed curves.

the Ginzburg-Landau parameter $\kappa = 10$. Three main parts can be identified in the figure - the Meissner phase (left-bottom), normal state (i.e. destroyed superconductivity, top-right), and the mixed (vortex) state (between the other two). The upper critical field of the sample is found to be $1.78H_{c2}$ for $R = 4.5\xi$, which is $\sim 80\%$ larger than the critical field of bulk samples, and increases further as the sphere is made smaller (dramatic increase is found for $R < 2\xi$, see Fig. 2.5).

The vortex state region in the equilibrium vortex phase diagram is very rich, as the maximal vorticity in the sample rises to $L_{max} = 13$ for $R = 4.6\xi$. As explained earlier, larger samples favor the formation of multi-vortex states, as is indeed shown by the shaded area in Fig. 2.5. Moreover, one should note that for fixed vorticity and increasing size of the sample, we find a lower nucleation field for the MV state, but a higher transition field to a GV state (dashed lines). The found transition lines between different L-states seem to be mostly equidistant in the phase diagram, as they should be due to the flux quantization effects. In addition, the aforementioned curves have a parabolic-like behavior, suggesting their R^2 dependence remnant of the flux quantization through the equatorial plane of the sample. However, it is apparent that the $L = 1$ state shows a pronounced stability in comparison with other states. To illustrate this better, we constructed Fig. 2.6, in which the ground-state field-stability region ΔH is given for each state as a function of the sphere radius.

The found non-monotonic behavior of ΔH follows from an initial hampering of the stability region by the destruction of superconductivity. Only after the vortex state is succeeded by one of a higher vorticity can ΔH reach its full extent, which results in the corresponding maximum in all curves shown in Fig. 2.6. However, it is most interesting to observe the location of these maxima with respect to the dashed line in Fig. 2.6, which gives ΔH and R needed for the addition of exactly one flux quantum to the system.

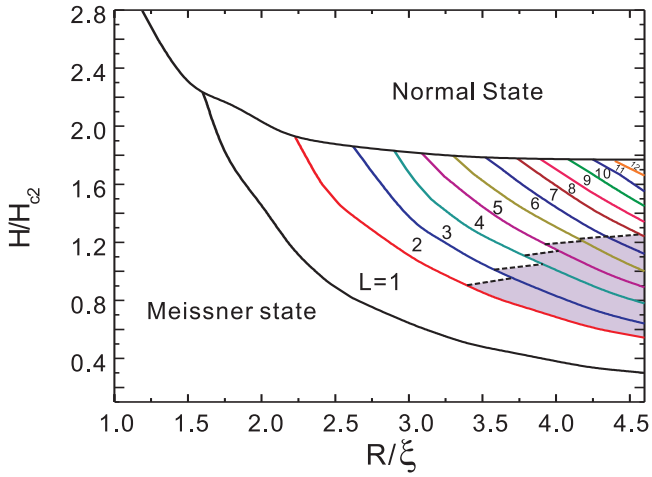

Fig. 2.5 The phase diagram for the ground-state vortex configurations as a function of the applied magnetic field H and the radius of the superconducting sphere (for $\kappa = 10$). Different vortex states are separated by solid curves, while the giant- to multi-vortex transitions are denoted by dashed curves. Shaded areas correspond to the multi-vortex regions.

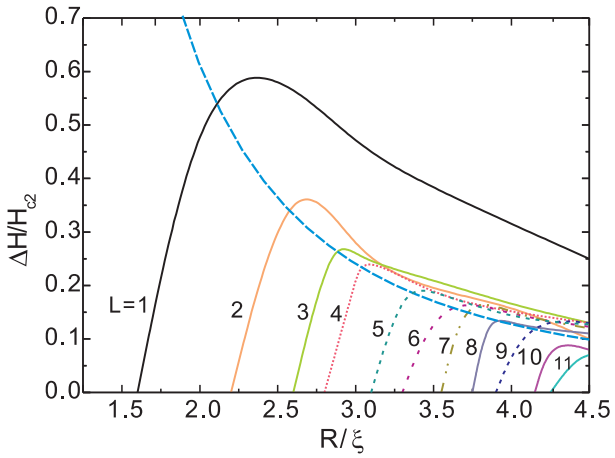

Fig. 2.6 The ground state magnetic field range ΔH for different vortex states, as a function of the sample size. Hyperbolic dashed curve gives the parameters for which exactly $\Delta\Phi = \Phi_0$ is applied through the equatorial plane of the sample.

While the maxima (and the follow-up points) of higher vorticity curves nicely sit on or just above the curve $\Phi_0 = \pi c\hbar/2e$, the curve for the $L = 1$ state significantly deviates from the expected values. The fact that larger flux is needed for the penetration of the first vortex in the mesoscopic sample is already a known fact [114] (in here considered samples $\Phi_{0\to1} = 2.5 \div 3.0\Phi_0$), but the pronounced stability of the $L = 1$ state with respect to applied flux ($\Delta\Phi = 2.36\Phi_0$) is a unique property of spherical superconductors,

caused by both symmetry and the three-dimensionality of the sample. In the single-vortex state, the vortex line connects the poles of the sphere, ideally placed in the center of the sample. In such a symmetric configuration, vortex currents ideally compensate the increasing screening currents, which prolongs further flux entry. In addition, the new vortex line breaks the existing radial symmetry, and also causes either shortening or bowing of the first vortex, due to its new off-center position. All of these processes cost energy, and increase the energy barrier for flux penetration. For similar reasons, further flux entry (e.g. $L = 2$ to $L = 3$ transition) is more energetically favorable, as (i) distinct weak points are created for vortex entry (e.g. n weak points between $L = n$ existing vortices on a ring), and (ii) existing vortices rearrange in a new configuration while keeping similar self-geometry.

2.4 VORTEX BEHAVIOR IN SPHERES OF DIFFERENT MATERIALS

In the previous section we considered a rather extreme type-II superconducting sphere, with GL parameter $\kappa > 10$ (for more info, see also Refs. [107] and [111]). However, very few low-T_c superconducting materials (Mo_3Ge and borocarbides for example) are known to be of such type, except e.g. $NbSe_2$ which is also anisotropic (in high-T_c materials κ is also large, but coupling between layered structure of the cuprate planes must be taken into account [115]). From a theoretical point of view, the issue of lower κ is rather important, as it means that screening currents can no longer be marginalized in the data analysis, and calculation also becomes much more numerically demanding (i.e. the influence of Eq. (2.2) in our formalism rises). When considering vortex matter, κ is one of the crucial sample properties as it governs the behavior of the vortex-vortex interaction. Therefore, contrary to thin samples which in most cases exhibit extreme type-II behavior (where effective GL parameter is defined as $\kappa^* = \kappa^2/d$, d being the thickness), properties of 3D superconducting samples directly depend on the characteristic lengths of the constituent material. For comparison, in this section we consider samples with $\kappa < 10$, with some emphasis on the $\kappa \approx 1$ case, thus e.g. niobium spheres.

To begin with, we compare two samples with radius $R = 3\xi$, and κ equal 10 and 1 respectively. In Fig. 2.7, the free energy curves for those samples are plotted versus the applied magnetic field. One can see that transitions between successive vortex states move to higher fields when κ is decreased, and the superconducting/normal state transition occurs at somewhat higher applied field. We studied these features carefully, by taking finer steps when changing κ between values of 0.71 and 10. Results are summarized in Fig. 2.8, where we show the field-ranges of different vortex states as the ground state of the system. The $L \to L + 1$ transition fields obviously increase as κ is made smaller, particularly for $\kappa < 1$.

In experimental conditions, the applied magnetic field is usually gradually ramped up during the measurement (the so-called sweep-up of the magnetic field). Therefore, the fields at which each vortex penetrates the sample in the experiments are different from the ones shown in Fig. 2.8. Instead, they correspond to the very last points of the stability of each vortex state in the free energy diagram (due to the slow field variation and the finite Bean-Livingston barrier, the transition to the state with lower energy is only possible when the vortex state is no longer stable). The penetration field H_p

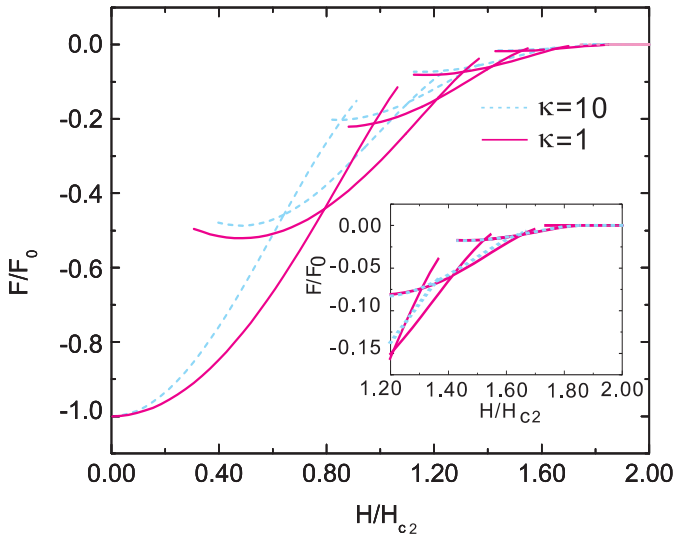

Fig. 2.7 The free energy as a function of the applied magnetic field, for samples with $R = 3\xi$ and $\kappa = 10.0$ (dashed lines) and 1.0 (solid lines). Inset zooms in the high-field region of the diagram.

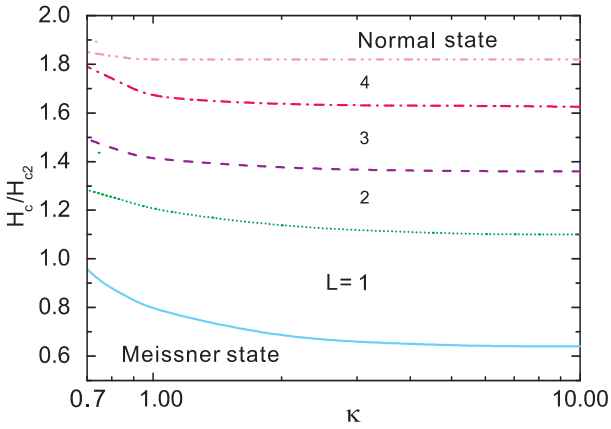

Fig. 2.8 The ground states with different vorticity, in the $H - \kappa$ parameter space, for a sphere with radius $R = 3.0\xi$.

obtained in such a way is plotted as a function of κ in Fig. 2.9. We find similar behavior as in Fig. 2.8, as H_p increases with decreasing κ. As a main difference, we observed that a fourth vortex cannot penetrate the sample for $\kappa < 0.83$ when field is swept up, even when the $L = 4$ state has lower energy than the state with lower vorticity; instead, we find the transition of $L = 3$ directly to the normal state. Still, the $L = 4$ state can be recovered in the reversed regime, when magnetic field is swept down, when the maximal number of flux quanta is trapped in the sample after superconductivity nucleates at the equatorial surface of the sample (i.e. the analogue of surface superconductivity).

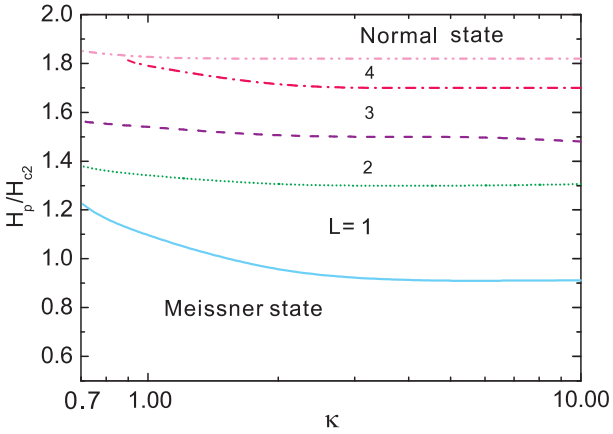

Fig. 2.9 The magnetic fields of successive vortex penetration in the sample of radius $R = 3.0\xi$, as a function of κ (for applied magnetic field gradually swept-up).

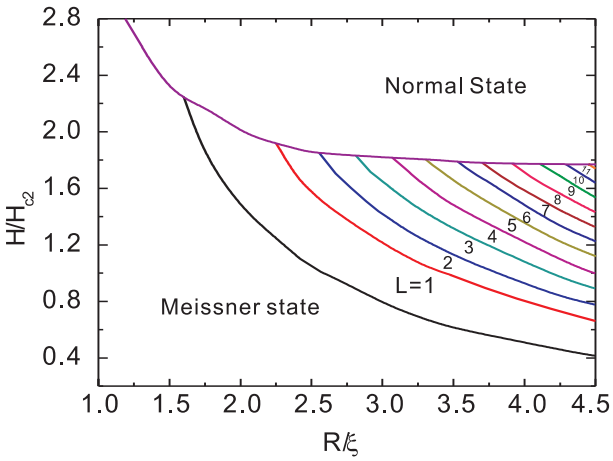

Fig. 2.10 The phase diagram for ground-state vortex configurations as a function of the applied magnetic field H and the radius of the superconducting sphere (for $\kappa = 1.0$). Areas of stability of different vortex states in the ground state are separated by solid curves.

Increased H_p for all vortex states for lower κ follows from the characteristic lengths in the sample. By decreasing κ, we actually decrease the magnetic penetration length λ as the coherence length ξ is kept constant in the simulation. Lower λ not only decreases the field penetration in the surface area, but also increases the surface energy of the normal domains in the superconductor, i.e. vortices, making their nucleation less energetically favorable.

In order to compare the effect of κ on the equilibrium phase diagram, we constructed the $H - R$ phase diagram for $\kappa = 1$, as shown in Fig. 2.10. The first difference to note is

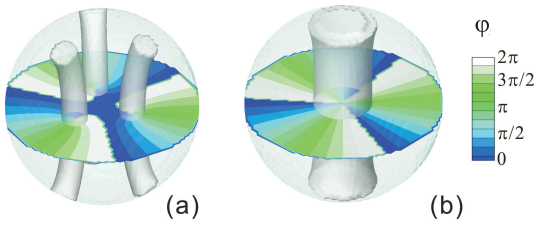

Fig. 2.11 The phase of the order parameter in the equatorial plane (dark/white color - $0/2\pi$ phase) superimposed on the 10% 3D iso-plot of the order parameter in the sample, for a sphere with radius $R = 4\xi$ at applied field $H = 0.90H_{c2}$, for (a) $\kappa = 10$, and (b) $\kappa = 1$.

that the maximal number of vortices that can be accommodated by the sample of radius R increases with increasing κ. For example, in a sphere of radius $R = 4.5\xi$, $L_{max} = 11$ for $\kappa = 1$ while $L_{max} = 12$ for $\kappa = 10$. The second important conclusion is that lower κ values *disfavor multi-vortex states*. In the whole investigated $H - R$ region for $\kappa = 1$ only giant-vortex states were found, compared to the rather large multivortex area present in Fig. 2.5. For clarity, in Fig. 2.11 we show a direct comparison between two $L = 3$ states found in the sphere with $R = 4.0\xi$, but with κ equal 10.0 and 1.0, respectively, both for applied field $H = 0.90H_{c2}$. In Fig. 2.11(a) the phase of the superconducting order parameter changes from 0 to 2π in clockwise direction around each of the three identifiable vortex singularities (multi-vortex), whereas in Fig. 2.11(b), a triple $0 \rightarrow 2\pi$ phase change is found around a single singularity (representing a giant vortex).

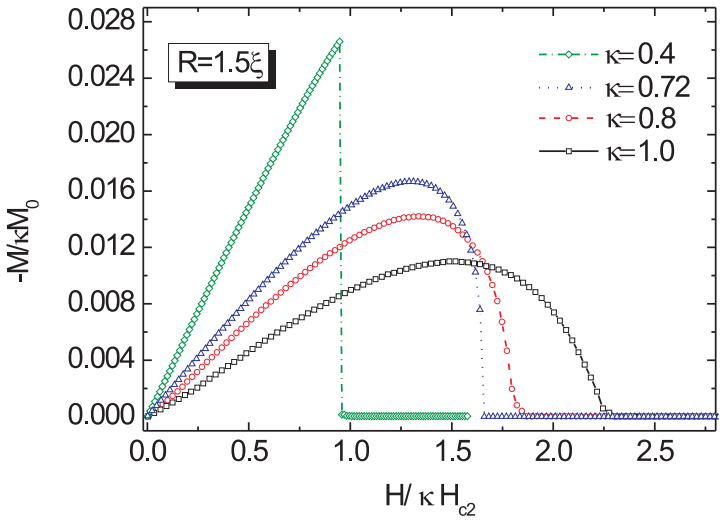

Fig. 2.12 The magnetization curves are plotted as functions of the applied magnetic field, for samples of four different materials, i.e. $\kappa = 1.0$ (open square), $\kappa = 0.8$ (open dot), $\kappa = 0.72$ (open triangle), $\kappa = 0.40$ (open diamond). The size of the sample is $R = 1.5\xi$.

2.4.1 Flux entry in mesoscopic type-I superconducting spheres

In a small superconductor ($R \sim \xi$), superconductivity only exists in the form of a Meissner state. At low fields, the applied magnetic field **H** is entirely expelled, and the magnetization is linear at smaller H. When H increases, the magnetization behaves differently for samples with different GL parameters κ, as shown in Fig. 2.12.

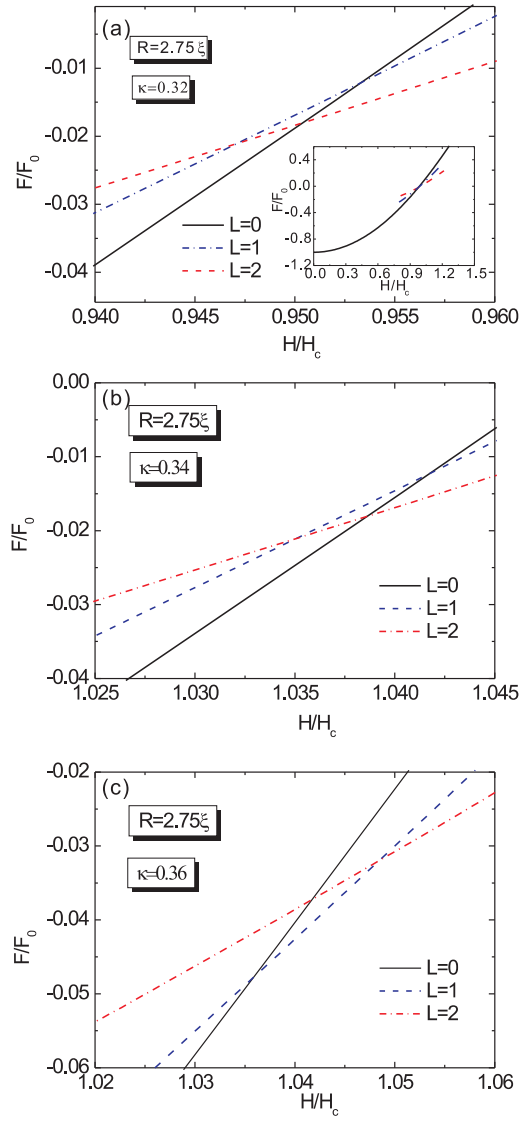

Fig. 2.13 The free energy curves as a function of the applied magnetic field, for sample with radius $R = 2.75\xi$ and $\kappa = 0.32$ (a) (inset shows the position of the cross points in the whole free energy curve), $\kappa = 0.34$ (b) and $\kappa = 0.36$ (c).

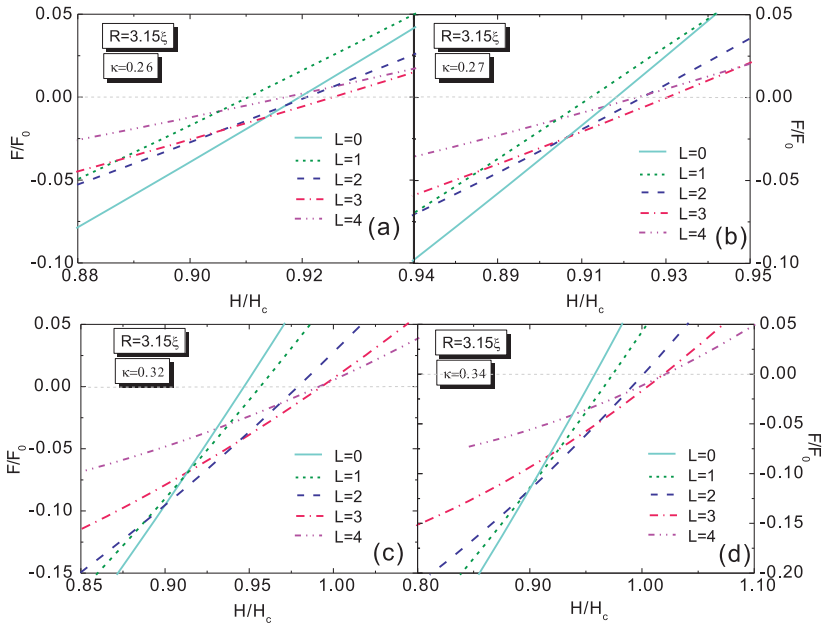

Fig. 2.14 The free energy curves as a function of the applied magnetic field, for sample with radius $R = 3.15\xi$ and κ=0.26 (a), 0.27 (b), 0.32 (c) and 0.34 (d).

For a sample with small κ, such as κ=0.4 and 0.72, the Meissner state ends with an abrupt drop of the magnetization to zero, i.e. the superconductivity to normal state transition is of first order, characteristic for type-I superconductors. For superconductors with higher κ, the magnetization jumps are replaced by smooth dependencies, see e.g. curves for $\kappa = 0.8, 1.0$ in Fig.2.12. The magnetic field gradually penetrates inside the sample, since the screening currents become unable to expel all the flux, while at the same time the size of the sample is not large enough to host a vortex. This gradual penetration of the field makes the S/N transition become a second-order one.

For a sample of larger size, the sample can accomondate vortices, for example, we plot the free energy curves for possible vortex states in a sphere with radius $R = 2.75\xi$ and $\kappa = 0.32$, 0.34 and 0.36 in Fig. 2.13. For $\kappa = 0.32$ (Fig. 2.13(a)), the Meissner state is stable up to very high field, and for increasing field transits to a normal state without nucleation of any vortex states. On the contrary, for $\kappa = 0.36$ (Fig. 2.13(c)) the Meissner state transits to the vortex states in a sequence of increasing vorticity of $L = 1$ to 2. The behavior of the system with $\kappa = 0.34$ is different: the Meissner state transits to vortex states at higher magnetic field, but directly to the state with higher vorticity ($L = 2$) skipping over the state with lower vorticity ($L = 1$). Similar behavior is found in larger samples with lower κ, for example the one with radius $R = 3.15\xi$ and κ between 0.25 and 0.34. Since the maximal vorticity of the sample increases to 3, the transition between different vortex states becomes more complicated. While increasing κ from 0.27 to 0.32, the system exhibits transitions from the Meissner state either to the

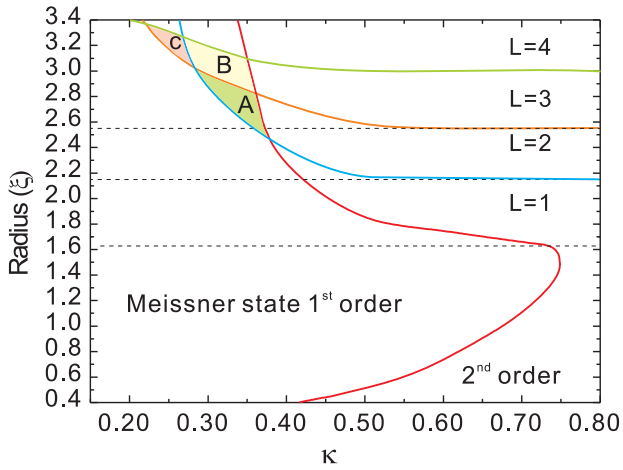

Fig. 2.15 The different vortex states are plotted out for samples with different sizes (in unit of ξ) and also for different Ginzburg-Landau parameter κ.

normal state or directly to $L = 3$, or to a sequence of $L = 2$ and 3, or a gradual, type-II like $L = 1$ to 2 to 3, see Fig. 2.14.

Fig. 2.15 shows the complete $R - \kappa$ phase diagram describing the different transition behaviors discussed above, for a small superconducting sphere, with radius between 0.4ξ and 3.5ξ, and GL parameter κ in the range $0.1 - 0.8$. In the region labelled as "Meissner state 1^{st} order", the sphere shows the typical property of a type-I superconductor, a first order transition from Meissner state to normal state, and no vortex can exist inside the sample till the superconductivity is destroyed. For larger κ and samples with radius smaller than 1.6ξ, a second order transition from the Meissner state to the normal state takes place (for example, the sample of size $R = 1.5\xi$ with $\kappa = 1.0$ in Fig . 2.12).

For samples with radius larger than 1.6ξ, as the external magnetic field is applied, vortices can exist in the samples with κ higher than certain threshold value. The maximum number of vortices in the sample is strongly dependent on the size of the sample. For $\kappa > 0.8$, only 1 vortex can be held in sample of size between 1.6ξ and 2.15ξ, 2 vortices between 2.15ξ and 2.43ξ, 3 vortices between 2.43ξ to 3.0ξ, and so on (see Fig. 2.15). The saturation vorticity of the sample decreases as soon as κ becomes small enough, for example when $\kappa < 0.53$ in samples between 2.15ξ and 2.43ξ, and $\kappa < 0.52$ in sample between 2.43ξ and 3.0ξ. At the same time, lower vorticity states are skipped over during the transition from Meissner state to normal state, such as the missing $L = 1$ state in area B where the system changes directly from $L = 0$ to $L = 2$ followed by $L = 3$ state. When κ becomes even smaller, the states with all vorticity below saturation number n_s are skipped, such as $L = 1$ state in area A where the system changes from $L = 0$ to $L = 2$, and $L = 1$ and 2 states in area C where the system changes from $L = 0$ to $L = 3$.

The different behavior of the energy curves of the vortex states and the Meissner states can explain this unusual sequence of vortex entry. By comparing the energy curves in Fig. 2.13 and Fig. 2.14, one can find that the energy curves of all the states increase as κ decreases. However, the $L = 0$ energy does not increase as fast as the energy of other vortex states, see Fig. 2.16. Since the free energy increases more for higher vorticity, the

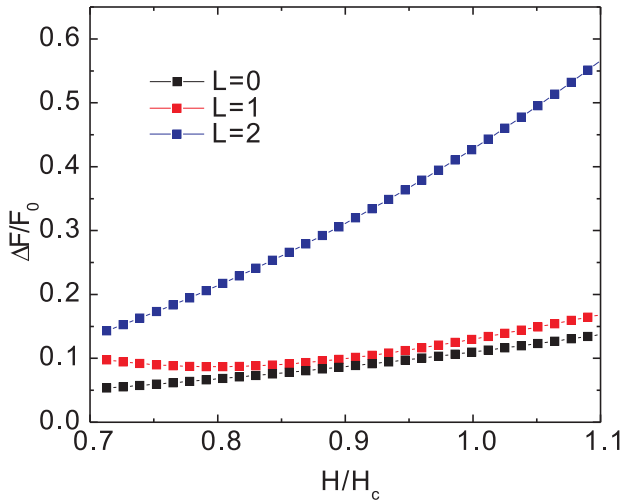

Fig. 2.16 The increments of the free energy for different vortex states from $\kappa = 0.34$ to $\kappa = 0.26$, for samples with the same parameters as Fig. 2.15.

crossing point of the Meissner states and the vortex states moves to the higher magnetic field (i.e., the higher vorticity), as κ becomes smaller, thus leads to the skipping sequence of the vorticity from $L = 1$ to $L = n_s - 1$.

2.5 MAGNETOMETRY RELATED FEATURES

One of the main properties of the superconductor is its diamagnetism, i.e. the ability to expel magnetic field when cooled below the critical temperature. The degree of field expulsion depends on the sample properties, as well as on the actual superconducting state of the sample.

As a measure of the sample's diamagnetism, one can define the resulting magnetic moment or magnetization of the sample. In thermodynamics, the magnetization of a sample in magnetic field is defined as the derivative of the Gibbs free energy over the applied field [27]. In experiments on the other hand, the magnetization of the sample is

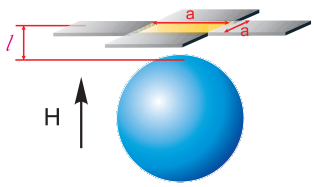

Fig. 2.17 Schematic view of a Hall cross (size of active area $a \times a$) at distance l above a mesoscopic superconducting sphere with radius R.

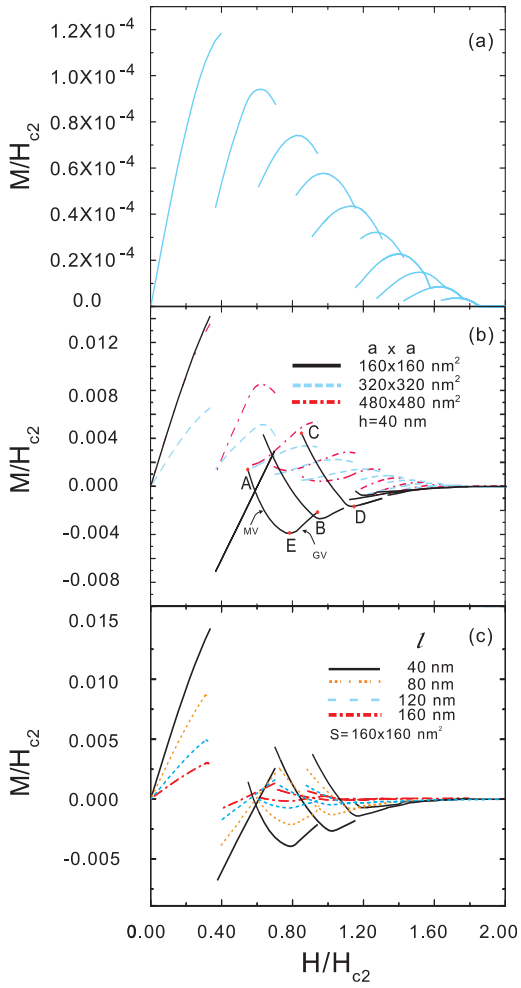

Fig. 2.18 The magnetization curves as a function of the applied magnetic field H. (a) The magnetization of the sample as a whole, corresponding the theoretical definition from thermodynamics; (b) Response of the Hall sensors of different size, placed at 40 nm above the sample; (c) The response of a 160×160 nm^2 probe, when placed at 40, 80, 120 and 160 nm above the sample.

measured by magnetometery, and is taken proportional to the measured voltage on a Hall sensor of particular size. In other words, the measured magnetization equals the amount of flux expelled from the superconductor through a Hall sensor placed at a particular height above the sample. For that reason, in this section we study the response of such a sensor depending on its size and position, in an applied magnetic field H, using Eq. (2.7). For continuity with previous sections, we consider a superconducting sphere with radius $R = 4\xi$, but take for coherence length $\xi = 100$ nm, and $\kappa = 1$ (close to the parameters of Nb sample, at $T = 0.8T_c$). We assume a square active area of the Hall cross (see Fig. 2.17), and consider three different sizes of 160×160 nm^2, 320×320 nm^2 and 480×480 nm^2, and the measurement heights of 40, 80, 120 and 160 nm above

the sample. In what follows, we simulate the magnetometry experiments during the sweep up/down of the applied magnetic field. The magnetization curve following from the thermodynamic definition is plotted in Fig. 2.18(a), in comparison with the one obtained using Eq. (2.7). Strong hysteretic behavior is observed, due to finite energy barriers for flux entry/exit. One can find the magnetization in Fig. 2.18(a) is much smaller than that in Figs. 2.18(b) and (c). This is because of the averaging effects of positive and negative *local* magnetization inside the whole 3D sample.

In Fig. 2.18(b), we compare the measured signals of the Hall sensors of different sizes. The curves obtained for larger sensors, i.e. 320×320 nm^2 and 480×480 nm^2 [dashed and dash-dotted line in Fig. 2.18(b)] behave the same as the magnetization calculated for the sample as a whole in Fig. 2.18(a) (since the active area of the sensor is almost as large as the cross-section of the sample). However, the magnetization curves qualitatively change for the Hall sensor of size 160×160 nm^2 [solid line in Fig. 2.18(b)].

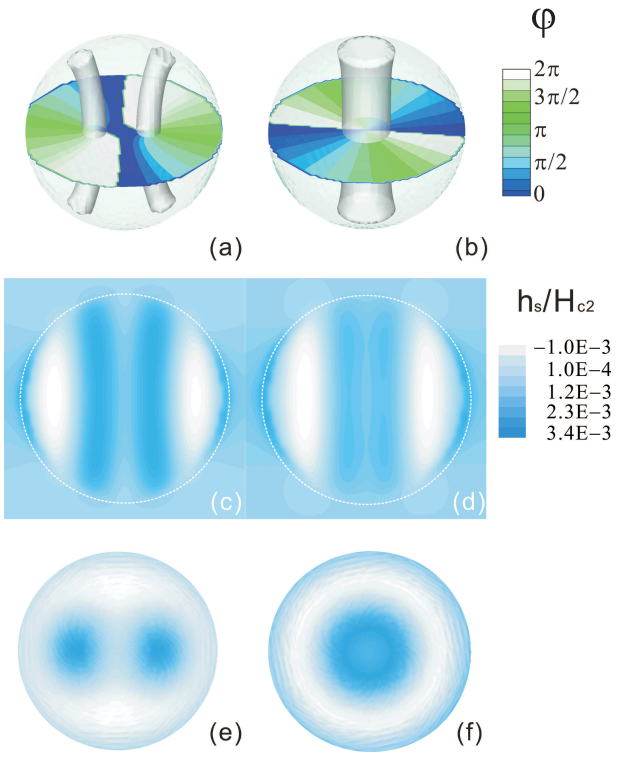

Fig. 2.19 (a,b) The phase in the equatorial plane and 3D iso-plot of the order parameter in the sample for the points A (a) and B (b) in Fig. 2.18(b) (showing the MV and GV state for $L = 2$). (c-e) Corresponding field distribution around the superconducting sphere, for points A (c,e) and B (d,f). Side view of the sample is shown in (c,d), and top view in (e,f). In all graphs, only the response field of the superconductor is plotted ($\mathbf{h}_s = \mathbf{h} - \mathbf{H}$), changing from negative (light color) to a positive extreme (dark color). Sample edge is indicated by the white dashed line.

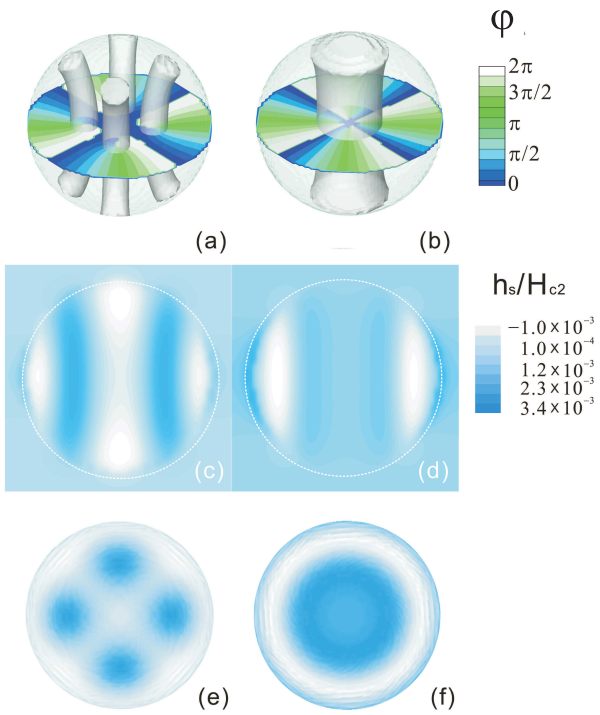

Fig. 2.20 Same as Fig. 2.19, but corresponding to the points C (a) and D (b) in Fig. 2.18(b).

Namely, on the paths AE and CD the magnetization *decreases* as the applied magnetic field is increased, *contrary* to the corresponding parts of the other curves in Fig. 2.18(b). To clearly understand this feature, we investigate the distribution of the superconducting condensate and the magnetic field for particular applied fields, i.e. points A, B, C, D, E in Fig. 2.18(b). Fig. 2.19 shows the magnetic field distribution around the sample [side view (c,d) and top view (e,f)] for points A and B, which reside on the $L = 2$ curve [see the phase contourplots in Fig. 2.19(a,b)]. The magnetization curve CD corresponds to the $L = 4$ vortex state, with properties shown in Fig. 2.20.

From the phase plots it is already clear that points B and D in Fig. 2.18(b) correspond to the response from the giant-vortex states, whereas A and C denote the multi-vortex states. The distribution of the stray magnetic field that the sample generates in response to the applied field at points A and B are plotted in Fig. 2.19(c-f). Here, dark (light) color indicates positive (negative) peak of the magnetic field.

In the case of the giant-vortex [see Figs. 2.19(d,f) and Figs. 2.20(d,f)], the magnetic field is strongest in the vortex core. With increasing field, the screening currents flowing along the sample edges increase, and compress the vortex in the center. Therefore, with increasing field the Hall sensor sitting right above the vortex detects more of the screening field of the Meissner currents, and the measured magnetization *increases*. On the other hand, in the case of the multi-vortex [see Figs. 2.19(c,e) and Figs. 2.20(c,e)], the stray

magnetic field has a local minimum in the center of the sample, between the vortices. In a ring distribution of the vortices (each with a vortex current circulating around it), the current in the central region has effectively the anti-vortex direction, thus the same as the screening current at the edge. With increasing applied magnetic field, vortices are compressed closer together, which now *decreases* the magnetization signal coming from the central antivortex-like currents. Therefore, if we look back at the AB curve in Fig. 2.18(b), we can conclude that along the AE path we have a multivortex state, whereas along the EB path a giant-vortex state is formed. For the same reason, the curve found for $L = 4$ state demonstrates a multi-vortex state on the shown CD path. To conclude, the concave shape of the magnetization curves measured by a comparatively small Hall sensor indicates the multi- to giant-vortex transition at the inflexion point of the curve.

That the shown distinction between the giant- and multi-vortex states in the magnetization curves is not an accidental property we illustrate further in Fig. 2.18(c). There we show the magnetization curves measured by the 160×160 nm Hall sensor placed at *different heights* above the sample. Of course, closer proximity of the sensor to the sample is always desired, as the signal is more pronounced. However, Fig. 2.18(c) clearly shows that the features of the magnetization curves are maintained even for larger separation between the Hall bar and the superconducting sample. At higher measurement heights, GV-MV distinction is still feasible as long as the signal does not succumb below the noise level.

2.6 CONCLUSIONS

In this chapter, superconducting and magnetic properties of mesoscopic superconducting spheres are studied. The full three-dimensionality of the problem is taken into account, and the two coupled non-linear Ginzburg-Landau equations are solved self-consistently on a 3D grid, with demagnetization effects being fully considered. Found vortex states illuminate the 3D aspect of the study; although they form structures essentially similar to the ones found earlier in superconducting disks, vortices tend to bend in the equatorial plane of the sphere while remaining perpendicular to the spherical surface of the sample at the points of entry and exit. Vortex configurations are studied in detail for different radii of the sample and the equilibrium vortex phase diagram is shown for a type-II sample. Both giant- and multi-vortex states are found. However, multi-vortex states are found unstable with respect to lower values of the Ginzburg-Landau parameter κ. In other words, the appearance of multi-vortex states is not determined only by the sample size (i.e. confinement), but also by the choice of the superconducting material. The latter also influences the magnetic response of the sample, which we studied considering known experimental techniques. In a hypothetic experiment, we calculated the response of a Hall bar with square active area, as a function of its size and the measurement height above the sample. We found distinct features of the magnetization curves measured by comparatively small Hall probes, which can be used to experimentally distinguish the giant-vortex from the multi-vortex states.

Publications. The results presented in this chapter were published as:

- Ben Xu, M. V. Milošević, F. M. Peeters, *Magnetic properties of vortex states in spherical superconductors*, Phys. Rev. B. **77**, 144509 (2008)

3

Vortex matter in spherical mesoscopic superconductors with a hole

3.1 INTRODUCTION

During the past decade, the properties of mesoscopic superconductors became one of the major directions in the research in superconductivity. In thin, practically two-dimensional (2D) samples, the superconducting state is strongly influenced by the sample geometry in the plane. So-called vortex matter deals with flux patterns in superconductors in an applied magnetic field, and becomes particularly rich in truly three-dimensional (3D) samples, as both geometry and the orientation of the magnetic field must be taken into account. Applications of superconductors in electronic circuits and ultra-high field magnets require knowledge and control of the behavior of critical parameters of the sample, i.e. critical temperature T_c, critical current J_c and critical magnetic field H_c [26]. The latter is of particular interest in mesoscopic superconductors, which easily exhibit an increase of the critical field beyond H_{c2}, the characteristic magnetic field value for type-II superconductors. Further enhancement of H_c is feasible by introducing perforations in the sample, which trap the applied field and reduce the effective field in the superconducting material. Such a study was done by Baelus and co-workers [116] for a thin superconducting disk with a hole. The hole provides a trap for the magnetic flux, and helps to establish the paramagnetic response of the sample. The number of trapped magnetic flux quanta depends on the size of the hole, which determines the final arrangement of vortices into a giant- or multi-vortex state (a multi-quanta vortex versus a collection of individual vortices on a shell) in the superconductor. Same work reports also on the symmetry-breaking of the vortex state by shifting the hole away from sample's center leading to one dimensional-like vortices [117], which were recently observed [118].

Furthermore, the introduction of holes in superconducting samples leads to an increase of J_c as well, since perforations limit the mobility of the flux lines (and are therefore

called vortex pinning centers) which in turn prevents dissipation [119]. In this respect, most theoretical and experimental works up to now were restricted to 2D samples, i.e. patterned films and thin polygons [120, 121, 122]. Tunable pinning can be achieved by changing the 3D geometry of the pinning centers, such as in the case of blind holes where thickness of the bottom layer determines the pinning strength [123]. Recently, advances in sample fabrication, nano-lithography and electrochemistry, made possible experiments on 3D samples of controlled geometry [91]. Therefore, it is timely to bring forward the corresponding theoretical analysis, and several very recent works have set grounds for understanding of vortex matter in 3D. For example, spherical superconducting shells with the restriction of extremely small thickness were studied by Du [124] and recently revisited by Gladilin *et al.* [108]. Nucleation of superconductivity in type-II spherical superconductors was calculated in Ref. [107] and the extension to different boundary conditions in Ref. [111]. Extreme type-II superconducting cylinders were studied in a tilted magnetic field in Ref. [125]. In the previous chapter and Ref. [126], we showed a study of vortex matter with full consideration of demagnetization effects, for the case of mesoscopic spheres.

The role of pinning centers in 3D was only studied for the case of bulk samples. Doria and Zebende [127] investigated superconductors with a cubic array of pinning centers with a size comparable to the coherence length. They established the conditions for entrance of vortices into the pinning center, and studied the maximal possible number of vortices that fit inside. Pinned vortex lines exhibited a clear 3D nature, often interacting towards a triangular vortex lattice away from the pinning centers, while curving towards a square arrangement in the vicinity of the pinning sites.

In this chapter, we analyze the influence of confinement on flux trapping by a hole or cavity, due to the presence of the sample boundary (unlike the bulk case). For comparison with earlier works, we preserve the spherical shape of the sample, and study the influence of complete or partial perforation on vortex matter, and that for the case of radially symmetric and non-symmetric samples. In addition, we investigate vortex structure transitions in a tilted magnetic field.

This chapter is organized as follows. The studied samples and theoretical formulation of the problem are presented in Sec. 3.2. The vortex states in spherical samples with a centered cylindrical perforation in axial magnetic field are discussed in Sec. 3.3. We introduce 3D asymmetry to the system, by tilting the magnetic field acting on the samples in Sec. 3.4. The conclusions are presented in Sec. 3.5.

3.2 THEORETICAL APPROACH

We consider type II superconducting samples (i.e. for characteristic lengths $\lambda > \xi$), of spherical shape with radius R with a piercing hole of radius R_h respectively (see Fig. 1). These samples are immersed in an insulating medium (e.g. air or vacuum), and exposed to a uniform magnetic field H, applied under a tilt angle θ with respect to the z-axis. Using dimensionless variables and the London gauge $\mathrm{div}\vec{A} = 0$ for the vector potential $\vec{A}$, we write the system of two coupled Ginzburg-Landau (GL) equations in the following

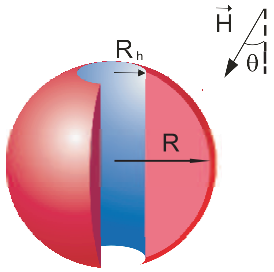

Fig. 3.1 The oblique view of the spherical sample (radius R) with a cylindrical perforation of radius R_h in applied magnetic field H under a tilt angle θ.

form

$$(-i\vec{\nabla} - \vec{A})^2\Psi = \Psi(1 - |\Psi|^2), \tag{3.1}$$

$$-\kappa^2\Delta\vec{A} = \frac{1}{2i}(\Psi^*\vec{\nabla}\Psi - \Psi\vec{\nabla}\Psi^*) - |\Psi|^2\vec{A}, \tag{3.2}$$

where the right side of Eq. (3.2) is the density of the superconducting current $\vec{j}$ induced by the sample in response to the applied field. Here the distance is measured in units of the coherence length ξ, the vector potential A in $c\hbar/2e\xi^2{=}\kappa\sqrt{2}H_c$, and the order parameter Ψ is scaled to its value in the absence of the magnetic field. The GL parameter equals $\kappa = \lambda/\xi$, where ξ, λ are coherence length and penetration depth, respectively. To numerically treat this system, we discretize Eqs. (3.1-3.2) on a uniform cubic grid using the link variable approach [34, 92], with typically 5 grid points per ξ, and solve the equations self-consistently in a finite-difference scheme, where Eq. (3.2) is solved using three dimensional Fast Fourier transform.

In our calculations, the superconducting order parameter satisfies the Neumann boundary condition on the sample surface, as well as on the boundaries of the hole

$$(-i\vec{\nabla} - \vec{A})\Psi|_{\rho=R \text{ and } r=R_h} = 0, \tag{3.3}$$

while the initially applied vector potential A_0 takes the form $A_{0x} = -\frac{1}{2}H(y\cos\theta - z\sin\theta)$, $A_{0y} = \frac{1}{2}Hx\cos\theta$, $A_{0z} = -\frac{1}{2}Hx\sin\theta$.

The convergent solution of Eqs. (3.1-3.2) gives a superconducting state as a local energy minimum. In search for all stable states for given conditions (thus the lowest energy *ground* state, and the higher energy *metastable* states), we repeat the calculation using different initial conditions. For a realistic comparison with a field-cooled experiment, we initiate the calculation from randomly generated and very weak superconducting order parameter, while in a zero-field-cooled situation, we start from $\Psi \approx 1$ in the whole sample. Once a solution is found, we are able to trace that state back and forth in its whole field stability range, by gradually sweeping up/down the applied magnetic field and recalculate each time the superconducting state starting from the previously found one. For all found vortex configurations we calculate the Gibbs free energy (in units of

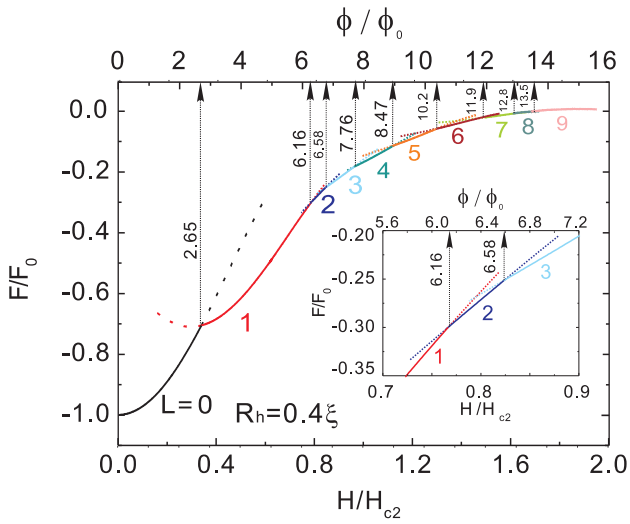

Fig. 3.2 The free energy curves as a function of the applied magnetic field ($\theta = 0°$), in units of $F_0 = H_{c2}^2/4\pi$, for a superconducting sphere with radius R= 4ξ, with a centered cylindrical hole of radius $R_h = 0.4\xi$. The upper x-axis gives the applied flux through the equator of the sphere. Metastable states are shown by dotted curves. The inset shows a zoom of the energy levels for states with vorticity $L = 1, 2$, and 3.

$F_0 = H_{c2}^2/8\pi$, where $H_{c2} = c\hbar/2e\xi^2 = \sqrt{2}\kappa H_{c1} = \Phi_0/2\pi\xi^2$,) as

$$F = \frac{1}{V}\int_V [2(\vec{A} - \vec{A}_0)\cdot\vec{j} - |\Psi|^4]d^3r, \tag{3.4}$$

where integration is performed over the sample volume V. Comparison of obtained energy levels of different vortex states enables us to discuss their (meta-)stability as a function of relevant parameters. The demagnetization of the sample is considered in the same way as in the Chapter I.

3.3 SPHERICAL SAMPLES WITH A PERFORATION, IN AXIAL MAGNETIC FIELD

In what follows, we consider the superconducting sphere with a cylindrical perforation, in an applied field parallel to the perforation ($\theta = 0°$). Fig. 3.2 shows the free energy of the found vortex states as function of the magnetic field, for a sample of radius $R = 4\xi$, made of strong type-II material (we took $\kappa > 10$ everywhere in the chapter, except as otherwise indicated) with a cylindrical hole of radius $R_h = 0.4\xi$. The first vortex enters in the ground state for field $H = 0.34H_{c2}$, corresponding to an applied flux through the equatorial plane of $\Phi \approx 2.65\Phi_0$. This field is lower, comparing to a sample with the same parameters but withoug hole. Such very effective screening of flux is characteristic of mesoscopic superconductors, and has already been observed in superconducting disks

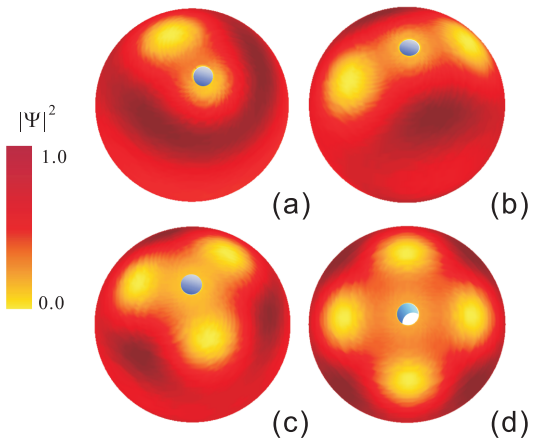

Fig. 3.3 The surface plots of the Cooper-pair density for a $R = 4\xi$ superconducting sphere with a cylindrical hole of radius $R_h = 0.4\xi$. The figures show the (n_o, L)=(1,2) (a), (1,3) (b), (1,4) (c) and (1,5) (d) multi-vortex states (n_o is the hole occupation number, L the vorticity).

[116]. However, in our case the Meissner state is followed by a pronounced stable $L = 1$ state (L being the vorticity), which remains in the ground state over a field range of $\Delta H = 0.42H_{c2}$ - corresponding to the additional flux of over $3.47\Phi_0$! Surprisingly, the subsequent vortex states show rather conventional stability ranges corresponding roughly to the addition of a single flux quantum, except the $L = 2$ state which is found in the ground state only for $0.77 < H/H_{c2} < 0.82$, i.e. for $\Delta\Phi \approx 0.42\Phi_0$ (see inset of Fig. 3.2). Thus the $L = 1$ state exhibits pronounced stability at the expense of the $L = 2$ state.

To understand this, we examined closely the vortex configurations themselves, some of which are shown in Fig. 3.3 as the Cooper-pair density plots on the surface of the sample. Contrary to the known vortex states found in mesoscopic spheres [126], in the present case there is always a vortex located in the center of the sample, pinned by the hole. It is already well established that maximal number of vortices that can be pinned by a cylindrical hole depends on the hole radius and is usually called the saturation number n_s [54, 128, 129, 130]. For $R_h = 0.4\xi$ we found that n_s equals one, the following, second vortex in the sample cannot reside in the hole, and the Bean-Livingston barrier for its entry is enforced by the repulsion from the already pinned first vortex. Eventually, at significantly higher field, vortex enters the sample but *remains located at the periphery*, resulting in a cylindrically asymmetric degenerate state shown in Fig. 3.3(a). This unique state was never predicted before for radially symmetric samples in a homogeneous field, but somewhat similar symmetry breaking (in appearance, not origin) was found in disks with magnetic coating [131].

For clarity, we adopt here the notation (n_o, L) for the vortex state, where n_o gives the actual number of vortices in the hole i.e. the hole occupation number. Figs. 3.3(b-d) show the states $(n_o, L) = (1, 3-5)$ respectively, and illustrate the ordering of additional vortices on a ring around the central hole (and the pinned vortex).

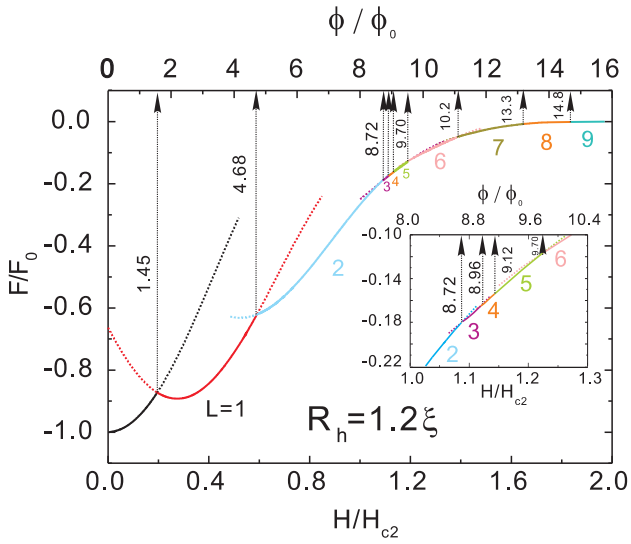

Fig. 3.4 The free energy curves as a function of the applied magnetic field, for $R = 4\xi$ and $R_h = 1.2\xi$. Same notation as in Fig. 3.2 is used. The inset shows a zoom of the energy levels for states with vorticity $L = 2, 3, 4, 5$ and 6.

Obviously, the vortex structure in the considered samples is strongly affected by the size of the hole. Fig. 3.4 shows the free energy plot for a sample with a larger hole of radius $R_h = 1.2\xi$. Compared with Fig. 3.2, the critical magnetic field for superconducting-to-normal state transition becomes higher, as larger hole facilitates in general the expulsion of the magnetic field from the superconducting material. Nevertheless, the first vortex penetration field is *twice* lower for the sample with $R_h = 1.2\xi$, as larger hole also attracts more magnetic flux inside the hole. $L = 1$ vortex state is thus found very stable for both samples, but the $L = 2$ state exhibits very different behavior, becoming far more stable for a larger hole radius. The explanation lies in the hole occupation number n_o, which becomes larger with hole radius, and equals 2 for $R_h = 1.2\xi$. In other words, the $L = 2$ state becomes a giant-vortex of vorticity 2 trapped in the hole, which preserves the radial symmetry and has enhanced stability compared to the broken symmetry $L = 2$ state found for $R_h = 0.4\xi$.

Having obtained the complete energy spectra for different vortex configurations for samples with $R = 4\xi$ and the hole radius R_h varying from 0 to 2.2ξ, we were able to construct an equilibrium vortex phase diagram that is shown in Fig. 3.5 as a function of the magnetic field H. The Meissner state is found less stable with increasing hole radius because the bigger sized hole is easier to accommodate a vortex. And the flux trapped inside the hole can be calculated as: $\Phi = BS = n\Phi_0$ and because $S = \pi R_h^2$, therefore we have $B \sim n/R_h^2$. But this is only true if the hole is big enough to accommodate a vortex, i.e. $R_h > \xi$, otherwise only one vortex can be accommodated. The critical field of the sample increases with hole size, especially for samples with $R_h > 1.4\xi$, where the surface superconductivity is greatly enhanced. The maximal vorticity remains the same (i.e. $L_{max} = 9$), when $R_h < 2.2\xi$. For each vortex state with $n_o < L \leq L_{max}$, n_o

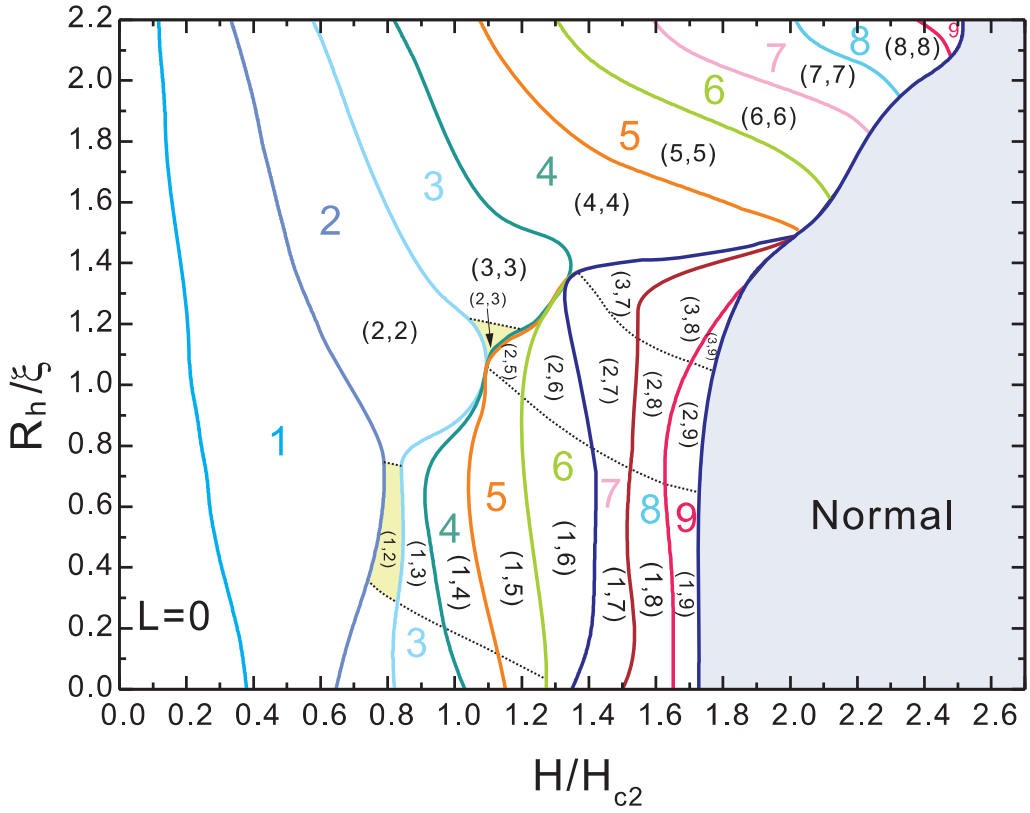

Fig. 3.5 The ground-state vortex phase diagram. Solid lines show the relation between the hole radius R_h and the applied magnetic field H at which the $L \to L+1$ transitions take place for a superconducting sphere of radius $R = 4.0\xi$. Shaded regions denote the parameter values at which broken-symmetry vortex states are stabilized. The regions with different hole-occupation n_o are separated by dashed lines, notation (n_o,L) indicates n_o number of vortices are trapped in the hole, and L is the total vorticity inside the sample.

vortices can be trapped in the hole, all the other $L - n_o$ vortices have to nucleate in the superconducting area to form a shell. And to first order the magnetic field for nucleation of the next vortex will be almost independent of the hole radius when R_h is smaller or of the order of ξ. Different vortex states exist for a certain vorticity in the same sized SC sample, between which first-order transitions are found when magnetic field changes, like (2,7) and (3,7) for $L = 7$ vortex state. Shaded areas indicate the stability regions of the broken-symmetry states, and are always followed by 'necking' of the transition lines towards adjacent vortex states. In other words, each asymmetric state has a narrower stability region than a corresponding symmetric state. Besides the already discussed $L = 2$ state for smaller hole, an asymmetric vortex state was also found for $L = 3$ states as well, obviously for the hole size allowing for a larger occupation number (in this case $n_o = 2$). Similarly to the $R_h = 0.5\xi$ case, we found very narrow regions of stability for the radially asymmetric vortex states in Fig. 3.5 - e.g. for $0.95\xi < R_h < 1.2\xi$, note the suppressed $L = 2 \to 3 \to 4 \to 5$ transition with increasing field (see also Fig. 3.4).

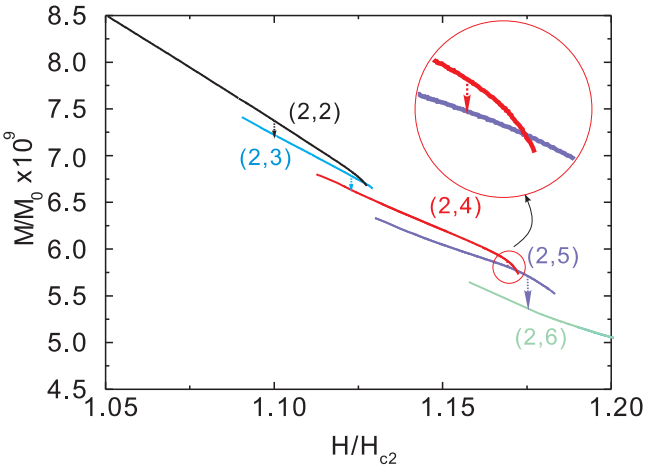

Fig. 3.6 The magnetization curves for vortex states (2,2), (2,3), (2,4) and (2,5), corresponding to the states shown in the inset of Fig. 3.4. Solid lines index the stable states for field sweep up/down, while the vertical dotted lines show the equilibrium transition points. Insert magnifies the area where equilibrium transition happens for vortex state changing from (2,4) to (2,5).

In addition to the disfavored symmetry of the states (asymmetric (2,3), and linear (2,4) state), the competition between the flux expulsion, additional vortices being repelled by the ones already in the hole, and the magnetic pressure inwards, also contributes to this 'necking' effect. As a result of these competing interactions, the transitions between the aforementioned states are weakly first order. This is clear from the magnetization curves for the $R_h = 1.2\xi$ case shown in Fig. 3.6. The magnetization of the sample is weakly discontinuous for the thermodynamic transition from the vortex states (2,2) to (2,3), as well as for the transition between states (2,4) and (2,5). This explains the weak first-order manifestation of those phase transitions but the vortex entry in superconductors is of course always of first-order.

Note however that all these competing interactions are fine-tuned by the size of the hole. As the size of the hole is increased, its influence on the vortex states grows. As a first result, we observed the 'necking' and even disappearance of some *symmetric* vortex states for larger holes in Fig. 3.5.

The proximity of the already trapped flux inside the hole to the equator of the sample hampers the entry of additional vortices. Instead, we found the surprising result that the suppression of superconductivity on the equatorial waist becomes energetically more favorable than the entrance of a single vortex. With increasing field however, the magnetic pressure for flux entry grows, and eventually overwhelms the repulsion by the trapped vortices. At that (large) field, a multi-vortex entry becomes possible, and we observe the simultaneous entry of several flux quanta, which will be discussed in detail in the next chapter. In the present case, we identified $R_h = 1.25\xi$ as a characteristic phase transition point, above which multi-quanta vortex entry is feasible. Note e.g. the transition $L = 3 \to 7$ for $R_h = 1.40\xi$ (see Fig. 3.7), where the vortex states in between are *completely missing*, and even do not exist as metastable states. The entrance of these 4

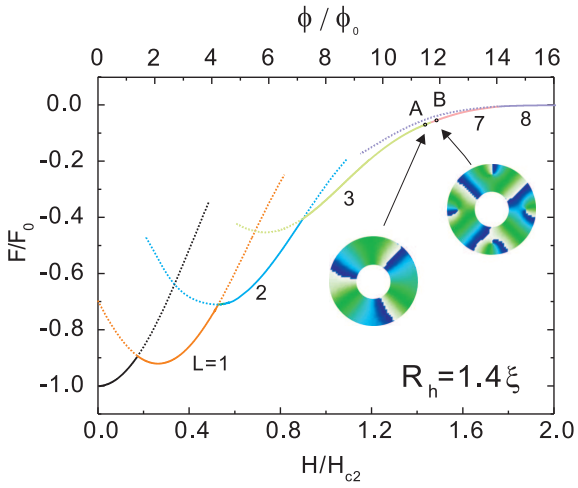

Fig. 3.7 The free energy curves are plotted versus the applied magnetic field, for $R = 4\xi$ and $R_h = 1.4\xi$. Same notation as used in Fig. 3.2. The insets are phase plots in the equatorial plane illuminating the vortex states adjoining the change from $L = 3$ to $L = 7$, which correspond to points A and B in the energy curves.

vortices is a *continuous* process where near point A in Fig. 3.7, the four vortices nucleate at the equator of the sphere and move towards the central hole with increasing magnetic field. For $R_h = 1.50\xi$, the forces get in perfect balance, and *no vortex entry is possible beyond* $L = 4$, i.e. $n_0 = L$, (instead, superconductivity is gradually destroyed from the waist inside). As n_o increases non-linearly with further increase of R_h beyond 1.5ξ, our sample becomes effectively a narrow superconducting ring [116], and only trapped, giant-vortex states are found. This is illustrated in Fig. 3.8 for a sample with $R_h = 3.2\xi$, where free energy curves demonstrate approximately quantized stability of each vortex state.

To reinforce our message regarding the influence of hole-size on the flux patterns, we plot the Cooper pair density of three vortex states in Fig. 3.9, all found for $L = 3$ but for different hole radii. For small R_h, one vortex is pinned and two remain on opposite sides of the hole; for larger R_h the hole attracts one more vortex, and a single remaining vortex resides on the sample periphery (broken-symmetry state); finally, for an even larger hole, all three vortices are trapped in the hole. Once more, we emphasize here that the broken symmetry states were found for vorticity up to $L = 3$, for hole radii for which $L - n_o = 1$, i.e. all vortices but one resided in the hole.

Due to its influence on the magnetic screening and intervortex interaction, the Ginzburg-Landau coefficient κ is clearly very important for the vortex states of broken symmetry. In Fig. 3.10, we show the calculated stability region of the asymmetric vortex configuration $(1, 2)$ for values of the Ginzburg-Landau parameter κ between 0.8 and 2. We found that both lower and upper critical magnetic field for the stability of this state *decrease* with increasing κ, but their difference *increases*. This increasing of the field stability

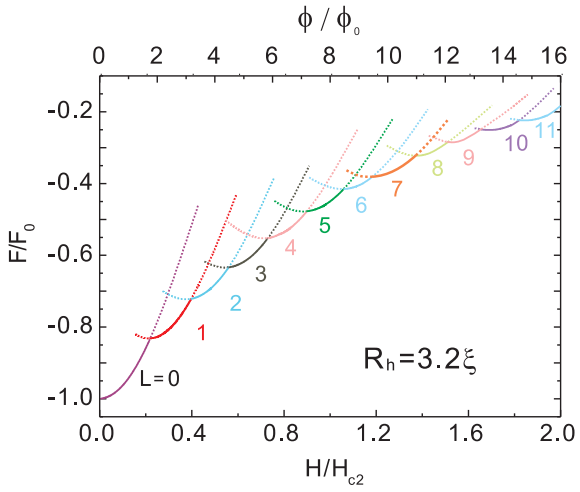

Fig. 3.8 The free energy as a function of the applied magnetic field for a sphere of radius $R = 4\xi$, with a perforation of radius $R_h = 3.2\xi$.

range becomes slower for samples with bigger κ especially when $\kappa > 2$. The two insets show the phase plots in the equatorial plane of the sample for two values of κ, 0.9 and 1.6. Those illustrate that the single vortex gradually approaches the hole and the pinned vortex with decreasing κ. This is caused by the strengthened screening of the applied field towards the hole, and weakened inter-vortex repulsion, which both favor the formation of the giant vortex in the hole and leads to the narrowing of the stability range of the asymmetric vortex state.

The appearance of the broken symmetry states is a characteristic feature for our spherical samples, which is absent in a superconducting cylinder. We briefly address here the properties of a cylinder with radius $R = 4\xi$ and thickness $d = 5.3\xi$, having the same volume as the sphere with radius $R = 4\xi$. After introducing the hole of radius $R_h = 0.4\xi$ in the cylinder, we repeated our study of the ground vortex states, and determined that states of broken symmetry are *not realizable* in this geometry (energy diagram and found states are shown in Fig. 3.11). Namely, the Bean-Livingston (BL) barrier in cylinders is much higher than in spheres, and vortices will enter the sample at higher fields, already strong enough to confine all vortices in the hole. Note also that all vortices entering the cylinder are straight, columnar objects, and BL barrier per length of the vortex is far higher than when the vortex enters in a single weak point on the equator of a sphere. In other words, the curvature of the sample surface appears to be essential for the stabilization of the broken symmetry state, almost as if the single vortex on the sample perimeter finds comfort in its 3D curving. As one reason, the self-energy of the vortex becomes significantly affected by its curved elongation and the consequent interaction between its top and bottom parts.

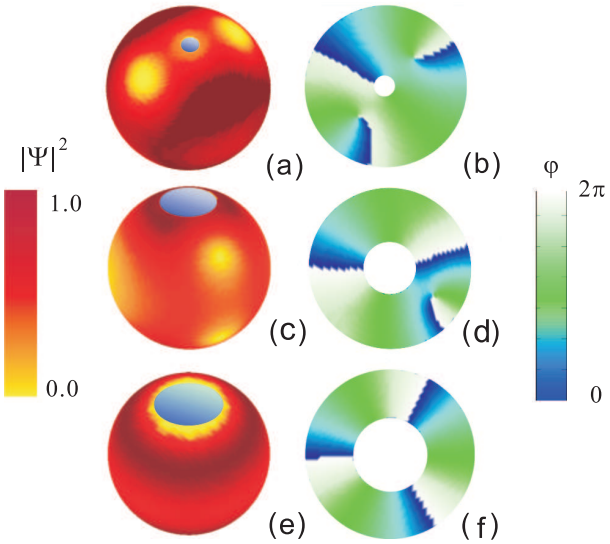

Fig. 3.9 The surface plots of Cooper-pair density and the equatorial phase plots of $L = 3$ states in a $R = 4\xi$ sphere with a hole, i.e. $(n_o, L) = (1, 3)$ state for $R_h = 0.4\xi$ and $H = 0.9H_{c2}$ (a,b); $(2, 3)$ state for $R_h = 1.2\xi$ and $H = 1.1H_{c2}$ (c,d), and $(3, 3)$ state for $R_h = 1.6\xi$ and $H = 1.3H_{c2}$ (e,f).

3.4 SPHERE WITH CENTRAL PERFORATION IN A TILTED MAGNETIC FIELD

It is already known that thin, effectively two-dimensional, superconductors bear weak sensitivity to an in-plane magnetic field, having the critical field in that direction scaling inversely to the sample thickness. In other words, the physics of vortex matter in such samples remains virtually unaffected by the tilted magnetic field, except for high-T_c superconductors where different spatial components of the field may lead to the appearance of crossing pancake and Josephson vortex lattices (see e.g. Ref. [132]).

The tilt of the magnetic field with respect to peculiarities of the sample boundaries is obviously important for the vortex matter in three-dimensional superconducting elements. There, 3D quantum confinement reflects through the interactions between the screening currents and the trapped flux lines, and consequently vortex phenomenology becomes far richer than in 2D cases. The behavior of mesoscopic cylinders and asymmetric spheres was recently studied in Ref. [125] and Ref. [112] respectively, and unique giant-to-multi vortex splitting at the sample edge was found, and the influence of asymmetry-induced torque was discussed. In the present case, we analyze the influence of a cylindrical perforation on the superconducting properties of a mesoscopic sphere, with emphasis on the deterministic influence of the defect's geometry on the vortex states, and the interplay of competing symmetries, i.e the one of the sample, the one of the

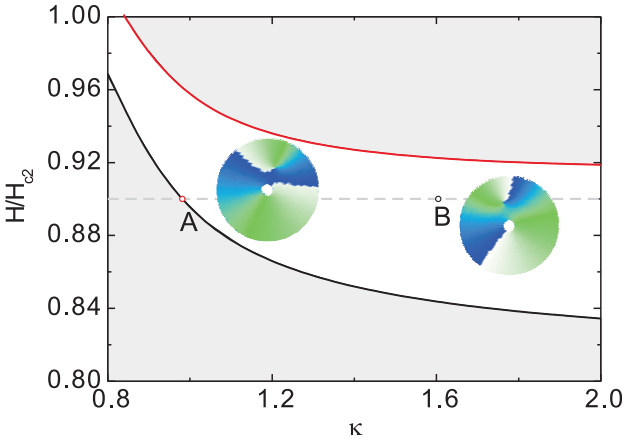

Fig. 3.10 The field stability region (white area) of the asymmetric $(1, 2)$ vortex state as function of the GL parameter κ. The phase plots in the equatorial plane are shown for applied magnetic field $H = 0.9H_{c2}$, and $\kappa = 0.9$ (point A) and $\kappa = 1.6$ (point B), to illustrate the varying distance between the hole and the strayed vortex.

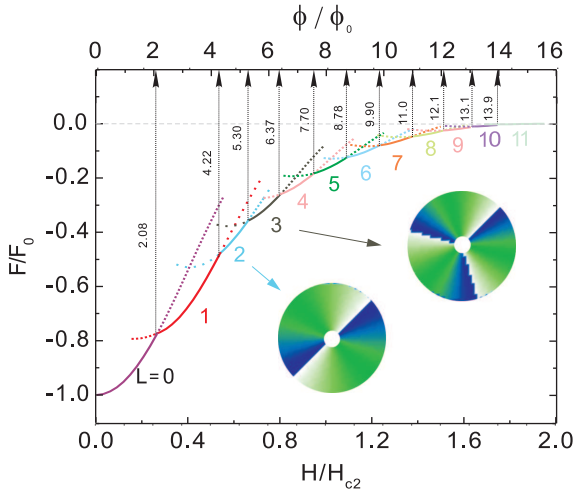

Fig. 3.11 The free energy curves for a cylindrical superconductor with radius $R = 4\xi$, thickness $d = 5.3\xi$ and the radius of the central hole $R_h = 0.4\xi$. Insets show the contourplots of the superconducting phase for the vortex states $L = 2$ and $L = 3$.

introduced perforation, and the one stemming from the imposed direction of the applied field.

We continue the study using the same sample as in the preceding sections, i.e. a sphere with radius $R = 4.0\xi$, with a cylindrical perforation of radius $R_h = 1.2\xi$. The free energy curves and surface plots of the Cooper-pair density of vortex states in axially

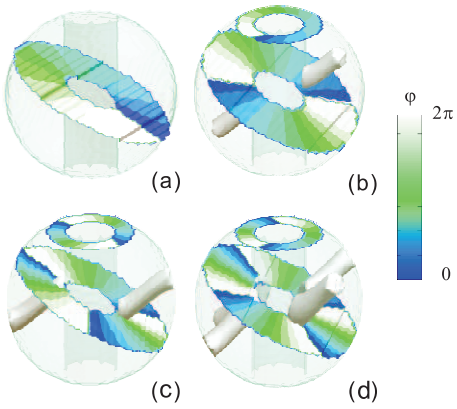

Fig. 3.12 The phase of the order parameter in the plane perpendicular to the direction of the applied magnetic field (dark/white color - $0/2\pi$ phase) superimposed on the 10% 3D isoplot of the Cooper-pair density (smoothed) in the spherical sample with radius $R = 4\xi$ and circular perforation of radius $R_h = 1.2\xi$, in a magnetic field $H = 0.38H_{c2}$ (a), $H = 0.66H_{c2}$ (b), $H = 0.78H_{c2}$ (c), and $H = 1.06H_{c2}$ (d), tilted under angle $\theta = 30^\circ$ with respect to the perforation.

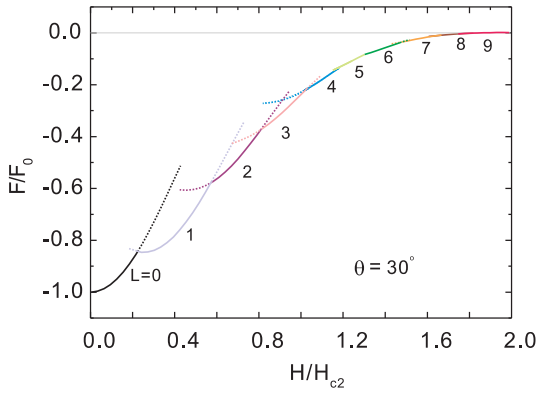

Fig. 3.13 The free energy curves as a function of the applied magnetic field, for a superconducting sample with radius $R = 4.0\xi$ and $R_h = 1.2\xi$, the magnetic field is applied in a tilt angle $\theta = 30^\circ$.

applied magnetic field ($\theta = 0^\circ$) were already shown in Fig. 3.4. In what follows, we gradually rotate the applied magnetic field from longitudinal ($\theta = 0^\circ$) to transverse direction ($\theta = 90^\circ$), with particular attention to $\theta = 30^\circ$, 45°, 60° and 90° cases.

Fig. 3.12 shows the iso-surfaces of Cooper-pair density and the corresponding phase plots for vortex states with vorticity $L = 1 - 4$ [(a-d), respectively], found for $\theta = 30^\circ$. The contourplots of the superconducting phase are given: (i) in the plane perpendicular to the applied magnetic field, indicating the total vorticity in the sample, and (ii) in the higher latitude plane, perpendicular to the perforation, showing the number of vortices trapped inside the hole. This emphasizes the point raised in Ref. [126], that the definition

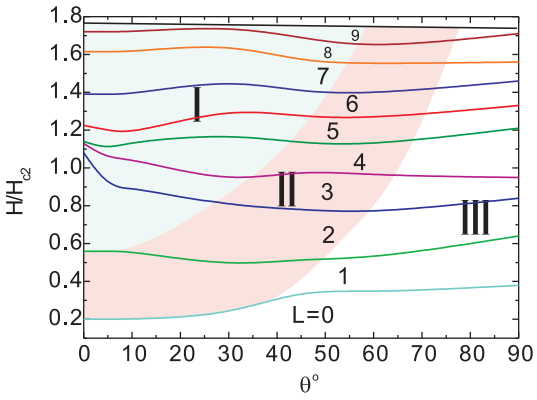

Fig. 3.14 The same samples as Fig. 3.13, the stability regions for different vortex states are plotted as function of the angle θ of tilting magnetic field. Areas I, II and III index vortex configurations with different number of vortices inside the hole, which equals 2, 1 and 0 respectively(shown in different colors).

of vorticity in 3D is more complicated than in 2D, as the plane needed for a contourplot of the phase is not uniquely defined.

As shown in Fig. 3.12(a), the single vortex case does not differ greatly from the $\theta = 0°$ case, with a vortex being located inside the hole regardless of the tilt angle. We found such behavior of the $L = 1$ state up to a tilt angle of $\theta = 50°$. The following flux line entering the sample in a $L = 2$ state finds its equilibrium position inside the superconductor, roughly aligning with the direction of the applied field [Fig. 3.12(b)]. Note however that this vortex tube is interrupted by the hole, and remains perpendicular to the inner and outer surface of the sample in its both ends. Such discontinuity of the vortex line is particularly visible in Fig. 3.12(c), where a third added vortex enters the hole due to competing interactions; due to strong interaction with the doubly quantized vortex in the hole and its associated screening currents, one remaining flux line in the sample is clearly disconnected in two equivalent parts, both equally shifted vertically from the symmetry axis with respect to the direction of the applied field. Note that very similar behavior of a single vortex can be obtained in two completely separated semi-spheres. However, further increase of vorticity restores the full influence of the sample geometry. For $L = 4$, two flux lines in the superconducting part of the sample in Fig. 3.12(d) show similar behavior to the one of Fig. 3.12(c), but also minimize their energy by arranging along the parallels of latitude of the sample.

In Fig. 3.13, free energy curves are plotted as a function of the magnitude of the applied magnetic field for the above discussed sample. Compared to the free energy curves in the $\theta = 0°$ case (see Fig. 3.4), all the less energetically favorable vortex states (e.g. $L = 4$ and $L = 5$), become more stable for $\theta = 30°$. Namely, their unique properties discussed in Sec. 3.3 were a direct consequence of the interaction with the perforation, whose influence ceases with increase of the tilt angle θ. For example, the stability range of the $L = 1$ and $L = 2$ state gradually decreases when the tilt angle θ is increased to 60°, while at the same time those ranges for $L = 3$, 4, and 5 increase(see Fig. 3.14). Namely,

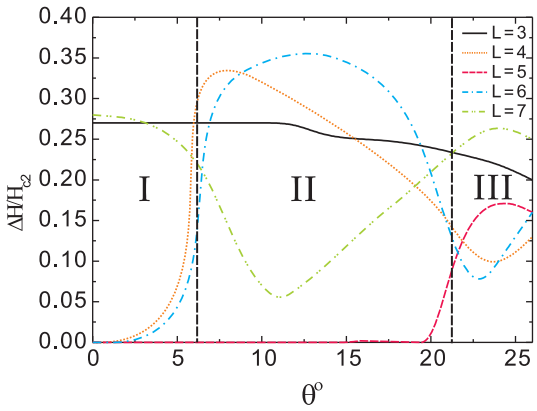

Fig. 3.15 The stability regions ΔH for vortex states 3, 4, 5, 6 and 7, versus the tilting angle θ of the applied magnetic field, for sample with radius $R = 4\xi$ and circular perforation of radius $R_h = 1.4\xi$. The region I, II and III index the area where $n_c = 0$, 1 and 2, respectively.

the increased deviation of the angle from the direction of the perforation *decreases* the stray flux through the hole and enhances the screening effects. As a consequence, the stability range of the Meissner state broadens in the ground-state, at the expense of the $L = 1$ state.

The number of vortices trapped inside the hole increases with the tilting of the magnetic field, which plays an important role in the behavior of the vortex entrance. To get a complete understanding of this phenomenon, we carried out the calculation by scanning the field up/down for a series of fields for different tilt angle θ. Here, one more parameter n_c is introduced to indicate the number of vortices that cross the hole with both ends along the field direction. Indeed, we found that in the case of $n_s = 3$, n_c increased from 0 to 1 (with total vorticity equals 4, when θ increased from 0° to 6°), and then to 2, where total vorticity equals 5 ($\theta = 22°$). And its influence on the entrance behavior can be concluded from Fig. 3.15, where the stability region ΔH for the different vortices are plotted as function of the tilting angle of the field, for the sample with radius $R = 4\xi$ and circular perforation of radius $R_h = 1.4\xi$. The aforementioned $3 \to 7$ transition is shown in region I, for $\theta = 0° \to 6°$. When $\theta > 6°$, the $L > 4$ and the multivortex entrance is now $L = 4 \to 6$ (see Fig. 3.15). Whereas the $L = 7$ vortex state is compressed by the waist inwards due to the penetration of the magnetic field, especially for the cases with larger stability of $L = 4$ and 6. The compression becomes weaker when the field is tilted markedly, where the $L = 4$ and 6 is not as dominant as in the smaller angle cases. This interaction of the stability between broarder vortex states continuous till $\theta = 22°$, where the $L = 5$ with $n_c = 2$ is possible to be the ground state, and at the same time the continuous penetration as single vortex becomes possible resulting in the transitions like $3 \to 4 \to 5 \to 6 \to 7$ as found earlier for a full sphere [126].

With the increase of the tilt angle (Fig. 3.14), the magnetic field becomes more dominant in directing the nucleating vortices, i.e. vortex lines lie preferentially in the direction of the field. This is illustrated in Fig. 3.16, where the iso-surfaces of Cooper-pair density and the phase plots are shown for the $\theta = 60°$ case. The first obvious

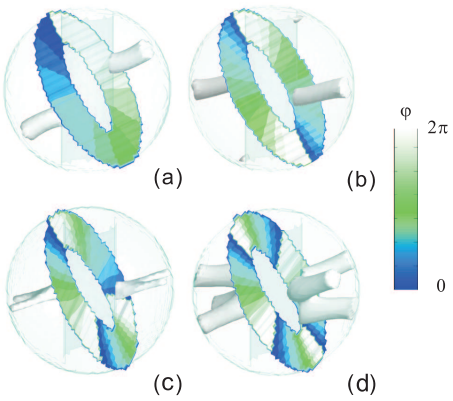

Fig. 3.16 Same as Fig. 3.12, but now for a tilt angle $\theta = 60°$ and magnitude of the field $H = 0.44H_{c2}$ (a), $H = 0.66H_{c2}$ (b), $H = 0.97H_{c2}$ (c) and $H = 1.01H_{c2}$ (d).

difference in comparison with Fig. 3.12 is that the hole becomes less able to trap vortices for larger tilt angles. As a consequence, the $L = 3$ state in Fig. 3.16(c) now resembles the $L = 4$ state in Fig. 3.12(d), while present $L = 4$ configuration shows three entwining vortex lines outside the hole. It is easy to conclude that final vortex arrangement strongly depends on the number of flux quanta inside the hole, as this influences both the vortex-vortex interaction in the system as well as the intensity of the screening currents around the hole and along the perimeter (in 3D). In Fig. 3.14, the number of vortices inside the perforation is shown for different total vorticity inside the sample. For the chosen geometric parameters of the sample, maximum two vortices may be confined inside the hole for $L > 2$ and $\theta = 30°$ and for $L > 4$ and $\theta = 45°$. This shows that the hole occupation number depends on the overall interactions in the system, i.e. not only on the size of the hole and tilt angle of the field, but also on the number of flux lines present which tend to reduce their density and minimize their mutual repulsion by pushing some of the vortices inside the hole. Still, no more than one vortex was found residing in the hole, regardless of total vorticity, for $\theta > 57°$, and no vortices at all were found in the hole for angles $\theta > 83°$.

The fact that some of the vortex lines for a given tilted applied field get strayed into the hole is not only important for the final vortex configuration, but it also has certain experimental consequences. Namely, one of the regularly used experimental methods for studies of flux behavior in superconductors is Hall magnetometry, where a Hall probe placed above (or below) the sample, in the direction of applied field, is used to detect the magnetic response of the sample [133](see inset of Fig. 3.17(a)). The typical magnetic signal of a mesoscopic superconductor would comprise quantized jumps in the magnetization in increased magnetic field, each associated with a vortex entry (carrying roughly a flux quantum) [51]. Using Eq. (2.7), we calculated the magnetization of our spherical samples in the direction of the applied field, through an imaginary Hall probe much larger than the sample itself, placed at distance ξ above the sample. Results are shown in Fig. 3.17(a), for tilt angle of the field $\theta = 60°$. It is immediately apparent that not all jumps found in magnetization curves in a sweep-up regime are of equal size, as some of them

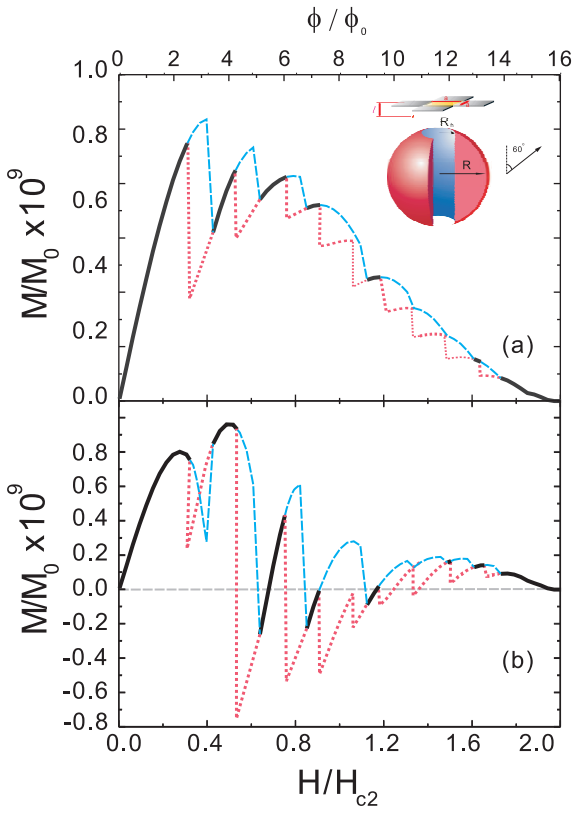

Fig. 3.17 Magnetization as function of the applied magnetic field H, as obtained from a Hall magnetometer (with size $a > 2R$) placed in the direction of applied field (a), or above the perforation (b), in the case where magnetic field is directed $\theta = 60^\circ$ from the cylindrical hole. The dashed lines indicate the process of magnetic field sweeping up, dotted lines for sweeping down and solid lines for regions which exist in both processes.

appear to be carrying fractional flux [97]. However, the situation becomes inverted in Fig. 3.17(b), where the Hall probe was placed above the hole, not in the direction of the field. Therefore, the three-dimensionality of the structure plays a trick on the magnetic measurement, as vortices guided away from the probe by the perforation in Fig. 3.17(a), manifest on the magnetization curve as an effectively fractional jump, with relative size of $2.8\Phi_0$ for $\theta = 60^\circ$ compared to the full Φ_0 jumps. Note also that channeled flux decays with increasing field for vortices present in the sample.

In the above discussion, we have deliberately neglected the $\theta = 90^\circ$ case; this case is naturally similar to the above ones as it follows the others by gradual increase of the tilt angle of the applied field. However, with field being completely perpendicular to the perforation (the applied field practically does not "see" the perforation), and with no vortices being trapped by the hole (see Fig. 3.14), this case requires special attention. The isoplots of obtained vortex configurations are shown in Fig. 3.18. In our study of

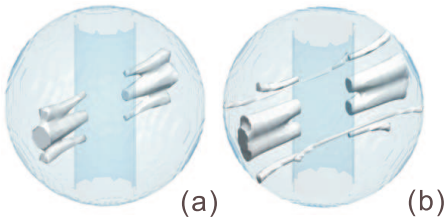

Fig. 3.18 The 10% 3D isoplots of the Cooper-pair density in the sample in transversely applied magnetic field ($\theta = 90°$, for (a) fields $H = 0.97H_{c2}$ and (b) $H = 1.31H_{c2}$.

the different tilt angles for the applied field, vortices were always attracted by the hole, being ultimately completely trapped inside of it, or just piercing through the cylindrical perforation. Note however that in the latter case vortex lines always formed polygonal structures on the sample surface, due to their mutual repulsion. In the present case, the pinning of vortices by the perforation results in one-dimensional vortex matter, as flux lines arrange along the hole in a linear fashion. The maximal number of vortices along a single line is $L = 5$, and subsequent vortices at higher fields pierce the sample aside of the hole, preserving the mirror symmetry of the vortex state (see Fig. 3.18(b)). This vortex ordering is obviously influenced by the size of the sample and the radius of the perforation, as flux lines see the perforation as a strip of width $2R_h$. Therefore, rich structural transitions between linear and zig-zag pinned vortex patterns can be expected in this system [134], bearing in mind the interaction of those same vortices on the curved surface of the sample.

Vortex chains observed in the $\theta = 90°$ case, and vortex states consisting of pinned (trapped in the hole) and tilted flux lines in other cases are characteristic vortex configurations for the unique sample geometry in this study. However, besides the sample geometry and tilt angle of the applied field, the actual value of the applied magnetic field is a very important factor for the vortex matter in this system. For one thing, it determines the number of vortices in the sample whose inter-vortex repulsion is one of the key elements in the formation of the vortex state. However, the exact value of the applied field also induces the corresponding screening response of the sample, i.e. for a fixed vorticity, slow changes of the applied field result in varying intensity of the Meissner currents across the sample. This again affects the vortex lines, increasing/decreasing the magnetic pressure exerted on them towards particular parts of the sample. Typical vortex re-configurations due to this effect are shown in Figs. 3.19 and 3.20.

We have identified earlier the number of vortices trapped inside the hole as one of the prominent features of vortex matter in perforated spheres. Fig. 3.20 shows the fine influence of gradually changing applied magnetic field on the latter key property. Namely, we have shown that in the $\theta = 0°$ case vortices become more compressed towards the hole when magnetic field is increased. However, in the $\theta > 0°$ case this is quite opposite as the trapped flux line as well as the magnetic flux inside the hole may gradually emerge from it when the magnitude of the applied field is raised. Fig. 3.20 shows a sequence of images of this unique vortex deconfinement transition, obtained for the $L = 2$ state in the $\theta = 60°$ case.

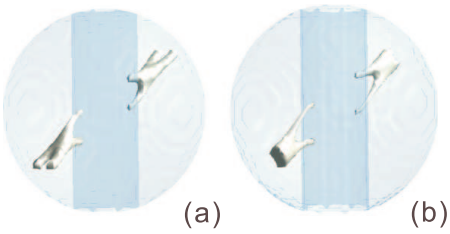

Fig. 3.19 The 30% 3D isoplots of the Cooper-pair density, illustrating the unique structural vortex transition in a sphere with radius $R = 4\xi$ and perforation of $R_h = 1.2\xi$, at magnetic field $H = 0.85H_{c2}$ (a) and $H = 1.06H_{c2}$ (b) applied under angle $\theta = 45°$.

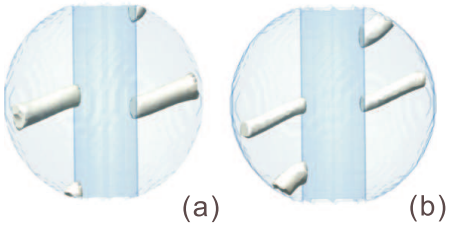

Fig. 3.20 Same as in Fig. 3.19, but for a tilt angle $\theta = 60°$, with (a) $H = 0.55H_{c2}$ and (b) $H = 0.72H_{c2}$.

Differently from the vortex state shown in Fig. 3.16(c) where two individual vortices on the surface coalesced into a perforation, Fig. 3.19(a) shows the state with two anti-crossing vortices. In desire to remain orthogonal to the inner surface of the sample (i.e. cylindrical hole), two vortices are arranged one above the other, while remaining next to each other on the outer surface of the sample. However, with increasing magnetic field, the balance of all forces in the system causes rearrangement of the flux lines, removes the energy costly crossing and reduces the length of each vortex line. As a result, vortices are finally parallel to each other, in the plane defined by the meridian of the sample and the sample axis [Fig. 3.19(b)].

It is interesting to study how the multi-vortex entry phenomenon found in previous section is influenced by tilting the magnetic field. There, we found the remarkable *continuous* transition $L = 3 \to 7$ when the field increases, as a process of the nucleation of four vortices at the equator of the sphere. When the applied magnetic field is tilted slightly away from the z-axis from 1° to 5°, we observed the *reduced* stability region of this continuous process of vorticity change, from $\triangle H = 0.061H_{c2}$ for angle $\theta = 1°$ to $\triangle H = 0.03H_{c2}$ for $\theta = 5°$. The vortex state (3,7) is always found to be the ground state in these cases, while at the same time, the metastable state (4,4) is found. The two vortex states are shown in Figs. 3.21 (a) and (b), respectively. The energy difference between these two states decreases with tilting of the field. For example, one of the four hole-bound vortices for the (4,4) state extends outside of the hole (see Fig. 3.21(d)), following the field direction, which lowers the energy of the whole system. Even for the

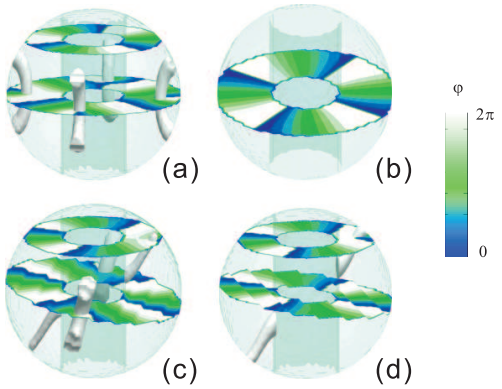

Fig. 3.21 The phase of the order parameter in the plane perpendicular to the direction of the applied magnetic field (dark/white color - $0/2\pi$ phase) superimposed on the 10% 3D isoplot of the Cooper-pair density in the spherical sample with radius $R = 4\xi$ and circular perforation of radius $R_h = 1.4\xi$, in a magnetic field $H = 1.43H_{c2}$ (a), $H = 1.45H_{c2}$ (b), $H = 1.39H_{c2}$ (c), and $H = 1.36H_{c2}$ (d), the tilting angle is $\theta = 1^\circ$ for upper layer, and $\theta = 10^\circ$ for lower layer, with $n_c = 1$.

(3,7) state, two vortices on the side of the hole can also penetrate deeper inside the sample because of the weaker repulsion from the central current around the hole. As a result of this, the other two vortices, generally pushed away from the hole. These two vortex states of (3,7) and (4,4) become energetically comparable when the tilting angle becomes larger than 6°, where the (4,4) is stable, and the (4,6) can be found for higher magnetic field.

3.5 CONCLUSIONS

In this chapter, the superconducting properties and vortex behavior are thoroughly studied in a mesoscopic superconducting sphere with a cylindrical perforation. The full three dimensionality of demagnetization effects is taken into account, in a self-consistent numerical solution of the Ginzburg-Landau equations. We reported different vortex configurations, defined by the interplay of competing symmetries in the system, by changing the size of the perforation, direction of the applied field, and Ginzburg-Landau parameter κ. For applied field parallel to the hole, we discovered unique asymmetric vortex ordering, never found in the case of superconducting cylinders, stemming from the competition of the symmetry of the perforation and the sample outline.

We constructed a $R_h - H$ vortex phase diagram, where the appearance of asymmetric states in the ground state, as well as of multi-vortex states and multi-quanta vortices pinned by the hole are discussed as a function of the hole size (R_h) and applied field (H). We also found a series of non-uniform transitions in vorticity vs. applied field for intermediate sizes of the hole, in a specific regime in which our sample has little resemblance in behavior to either full sphere, or thin ring limit.

In the case when applied field was tilted with respect to the sample axis, we analyzed the competing interactions in the system that guide the flux lines in the sample either along the direction of the field, or completely inside the perforation. For different tilt angles θ, we studied the vortex configurations, the transitions between them, and the number of flux quanta trapped in the hole. Analyzed transitions include ones for fixed vorticity, where we found novel vortex reordering and vortex deconfinement from the hole as a function of slowly varying field. We also studied the magnetic response of vortex states when a Hall probe placed in the direction of applied field, or above the perforation; due to the three-dimensionality of the vortex structure, we identified features on the $M(H)$ curves that correspond to vortex entry, but appear to carry fractional flux when measured by Hall magnetometry. Moreover, the magnetic signal contains features related to each vortex entry, effectively seeing the perforation as a pinning channel while simultaneously arranging on the curved outer surface of the sample. By tilting the applied magnetic field, we shed light on the complicated 3D interactions between vortices and the samples' boundary.

Publications. The results presented in this chapter were published as:

- Ben Xu, M. V. Milošević and F. M. Peeters, *Vortex matter in oblate mesoscopic superconductors with a hole: broken symmetry vortex states and multi-vortex entry*, New Jounal of Physics **11**, 013020 (2009)

4

Second-order transition with multi-vortex entry in 3D samples

4.1 INTRODUCTION

Vortex entry in superconductors is generally a first-order phase transition. In increasing magnetic field, strong Meissner currents develop in the sample to screen out the applied field. They are largest at the sample edges, where consequently the superconducting order parameter is weakest. After the critical velocity of the superconducting condensate is reached [26], the Cooper-pairs break, and weak points for vortex entry are created at the sample edges. The energy associated with vortex crossing the screening currents in the sample, together with the repulsion experienced from the pre-existing vortices (if any), form together a Bean-Livingston barrier, i.e. the energy barrier for vortex nucleation in the sample [52]. Its presence ensures the existence of hysteresis of flux entry and exit in mesoscopic superconductors as a function of the applied magnetic field.

Typically the vortex enters the sample through a weak point, i.e. the surface area that can be as small as a single point in which the critical conditions are met. This is where the three-dimensionality of the vortex line becomes important, since it has to overcome the entire edge of the sample parallel to the magnetic field. As a consequence, the vortex enters the sample gradually, as a function of critical conditions changing in the neighborhood with e.g. further increasing field, and depending on its own elasticity. Finally, the entire vortex enters the sample, but it exceeds its minimal needed length (the sample thickness), and this is energetically costly. This additional contribution to the energy barrier is named *the geometric barrier*, as it stems from the sample shape.

Such a geometrical barrier can be successfully suppressed in samples with curved edges, i.e. with spherical or toroidal shape. Nevertheless, vortex entry remains a first-order transition, unless the action of the Meissner currents driving the entering vortex towards the center of the sample is fully counteracted by another opposing force, so

that the Bean-Livingston barrier vanishes. In what follows, we will show that this is possible in a spherical superconductor with a central perforation. The force opposing the vortex entry will be the repulsion by the previously trapped vortices in the hole. The balance of the competing forces will therefore depend on the applied magnetic field, the size of the sample, the size of the hole, and the vorticity, but also the number of newly entering vortices. As a consequence, some unconventional vortex transitions for mesoscopic superconductors can be expected, some of which are mentioned in the previous chapter.

Our sample is a sphere of radius R, with axial and cylindrical perforation with radius R_h. In the past, a number of works dealt with the properties of a superconducting disk with a hole and rings in general [116, 135], as well as hollow cylinders [136]. The common conclusion was that vortices favorably reside inside the hole, and that such vortex trapping leads to an increased upper critical field of the sample. However, the number of vortices that fit inside a hole depends on the hole itself (its shape and size) [54], but also on the sample geometry, i.e. the proximity of another hole [123], or the proximity of the sample edges. In Fig. 4.1, we show the obtained maximal number of vortices in a hole (saturation vorticity n_s) as a function of the hole radius and the sample radius, and that for a cylinder and a sphere of equal volume. The difference between results for two geometries is astounding, and this is the core objective of this study.

4.2 THEORETICAL FORMALISM

The results are obtained and checked using two variants of the Ginzburg-Landau (GL) formalism, for an extreme type-II superconductor. In one approach, we solve numerically the non-linear GL equation for the order parameter ψ:

$$(-i\overrightarrow{\nabla} - \overrightarrow{\mathbf{A}})^2\psi = (1 - |\psi|^2)\psi, \tag{4.1}$$

in applied vector potential $\overrightarrow{\mathbf{A}} = (Hy/2, -Hx/2, 0)$ from a magnetic field H applied axially to the sample, and with Neumann boundary conditions applied at the sample surfaces. Solution of Eq. (4.1) minimizes the free energy of a sample with volume V: $\mathcal{F}/\mathcal{F}_0 = \frac{1}{V}\int |\psi|^4 dV$, where $\mathcal{F}_0$ is the condensation energy $H_c^2/4\pi$. In above equations, all distances are expressed in units of the coherence length $\xi(T)$, the vector potential in $\phi_0/2\pi\xi_0$, and the order parameter in $\sqrt{-\alpha/\beta}$ with α, β being the GL coefficients. For details of the approach, we refer to Ref. [97].

The second approach is based on the expansion of the order parameter [137], $\Psi = \sum_{k=1}^{N} C_k\psi_k$ in the orthonormal eigenfunctions of the 3D kinetic energy operator

$$\left(i\hbar\overrightarrow{\nabla_{3D}} - e^*\overrightarrow{\mathbf{A}}/c\right)^2 \psi_k/2m^* = \epsilon_k\psi_k.$$

In cylindrically symmetric structures, these eigenfunctions have the form $\psi_{k=(L,n)} = \exp(iL\phi)f_n(r,\theta)$, where L is the angular momentum, ϕ is the azimuthal angle around the sample axis, and the index n counts different states with the same L starting from the lowest-energy one. The eigenfunctions f_n are real and their corresponding eigenvalues are obtained numerically for each L, with Neumann boundary condition applied. The

typical number of considered eigenfunctions is N=10-50, with $L \in (0, 10)$ and $n \in (1, 2)$. And the free energy can be written in terms of complex variables as

$$G - G_n = (\alpha + \epsilon_i)c_i c_i^* + \frac{\beta}{2} A_{kl}^{ij} c_i^* c_j^* c_k c_l \tag{4.2}$$

where the matrix elements $A_{kl}^{ij} = \int d\mathbf{r} \psi_i^* \psi_j^* \psi_k \psi_l$ are calculated numerically. The extremum of the free energy, as the saddle point, is obtained by the eigenvector method as in Ref. [138, 139] A set of coefficients c needs to be taken in to account, therefore, the free energy variation $\delta G = G(c^n) - G(c)$ can be expressed in the proximity of the extremum by the quadratic form of small deviations $\delta = c^n - c$, as follows

$$\delta G = F_m \delta_m^* + B_{mn} \delta_n \delta_m^* + D_{mn} \delta_n^* \delta_m^* + c.c., \tag{4.3}$$

and the $F_m = (\alpha + \epsilon_i)c_m + \beta A_{kl}^{mj} c_j c_k^* c_l$, $B_{mn} = (\alpha + \epsilon_m)I_{mn} + 2\beta A_{kl}^{mn} c_k c_l^*$, $D_{mn} = \beta A_{kl}^{mn} c_k c_l$, and I_{mn} is the unit matrix. The quadratic form of Eq. (4.3), which is Hermitian, can be rewritten in normal coordinates $\delta_m = x_k Q_m^k$ as $\delta_G = 2(\gamma_k x_k + \eta_k x_k^2)$, where $\eta_k = Q_m^k F_m$, the eigenvalues η_k and eigenvectors Q^k are found by solving numerically the following equation:

$$\begin{vmatrix} B + Re(D) & Im(D) \\ Im(D) & B - Re(D) \end{vmatrix} \cdot \begin{vmatrix} Re(Q^k) \\ Im(Q^k) \end{vmatrix} = \eta_k \begin{vmatrix} Re(Q^k) \\ Im(Q^k) \end{vmatrix} \tag{4.4}$$

Moving in the direction with negative free energy gradient $-\eta_k$ we will approach a minimum of the free energy corresponding to the ground or a metastable state. In order to find a saddle point we move to a minimum of the free energy in all directions $x_{k \neq l} = -\gamma_k/(\epsilon + \eta_k)$ except one, which has the lowest eigenvalue, and for which we go to a maximum $x_l = -\gamma_l/(\epsilon + \eta_l)$ and find $c_m^n = c_m + x_k Q_m^k$ for all k. The iteration parameter $\epsilon > 0$ controls the convergence, which is always reached for any initial state close enough to a saddle point. Finally, the energy minimization with respect to the complex variables c_k leads to the order-parameter profile of the stable vortex states.

4.3 NOVEL VORTEX TRANSITIONS

Returning to the results, the data shown in Fig. 4.1(a) demonstrates classic mesoscopic vortex behavior. In a cylinder with small radius, the vortices are compressed laterally into a giant-vortex [98, 140, 141], and the maximal vorticity increases one by one as the sample is made larger. A small perforation placed in the center of the cylinder has very little effect, as confinement dominates and a giant-vortex is formed in the center of the sample regardless of the size of the hole. However, starting from the hole size of c.a. $R_h = 1\xi$, the perforation is able to trap vortices, with the maximal occupation number (saturation number) of the hole proportional to the hole size. The hole also starts to affect the upper critical field of the sample, which leads to an increase of the maximal vorticity of the sample, as shown in Fig. 4.1(a). There the vortex saturation number of the hole n_s cannot be distinguished from the maximal vorticity, since the vortex state at high applied field is always a giant vortex, with the vortex core always located in the center of the sample, i.e. inside the hole.

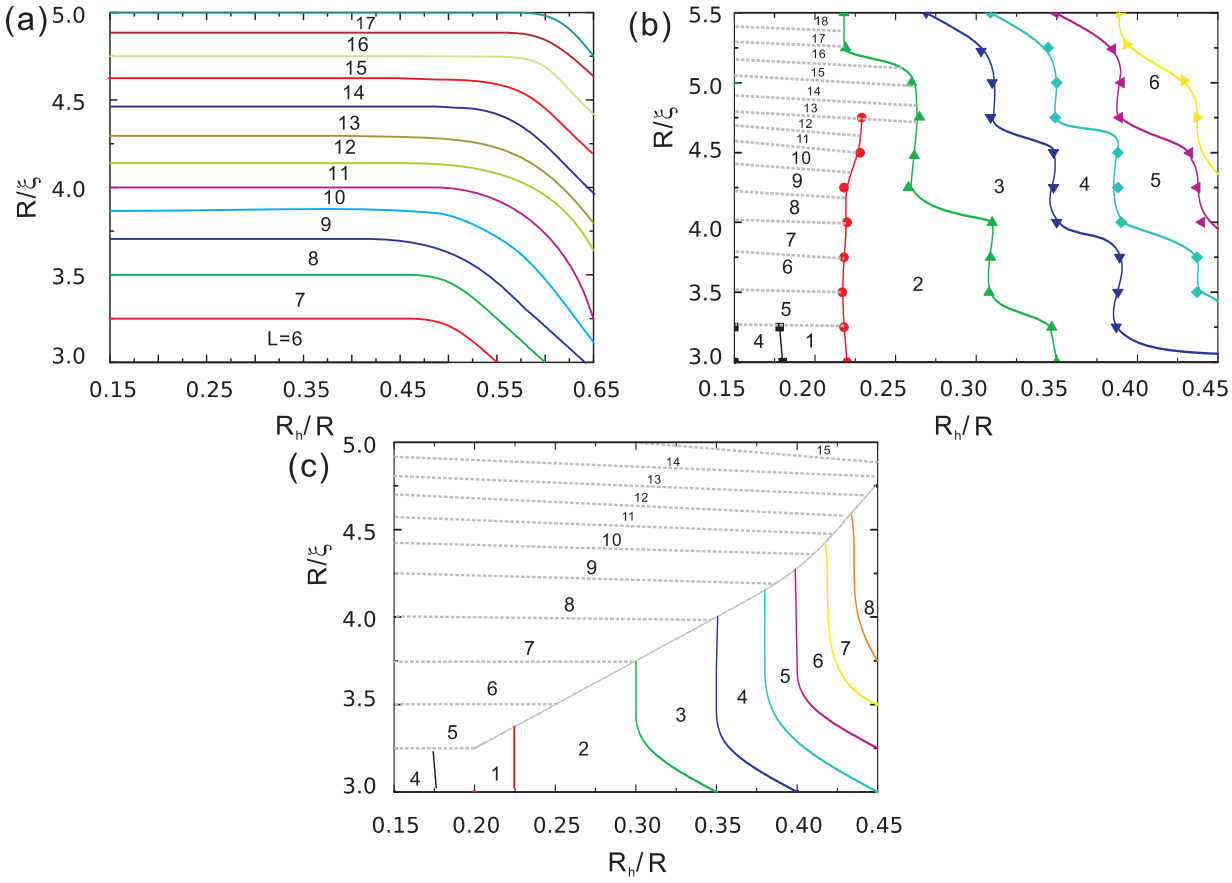

Fig. 4.1 The saturation vorticity of the hole with radius R_h, in a cylinder (a) and a sphere (b) of radius R (and of same volume as the cylinder). (c) The maximal possible vorticity of the sample in (b).

Similar behavior can be found in perforated spheres, however only when the perforation is very small. Beyond $R_h = 0.175R$, the saturation vortex number of the hole becomes independent of the maximal possible vorticity in the sample. It still increases as the hole is made larger, but also has a very strong effect on the final vortex state at the upper critical field. This is illustrated in Fig. 4.1(c), where we show that for geometrical parameters of the cylinder that could host up to 11 vortices ($R = 4.1\xi$, $R_h = 1\xi$), the corresponding sphere has a maximal possible vorticity of just 8 and that is reached at an intermediate magnetic field. Close to the critical field, the vorticity actually drops to just 2, with both vortices trapped inside the hole!

To understand the above astonishing differences in flux entry in samples of different 3D geometry, we show in Fig. 4.2 the calculated free energy landscape for a perforated cylinder (a) and sphere (b), as a function of the applied magnetic field. Both samples are of equal radius $R = 4.0\xi$ and with the same radius of the hole $R_h = 1.4\xi$. As expected,

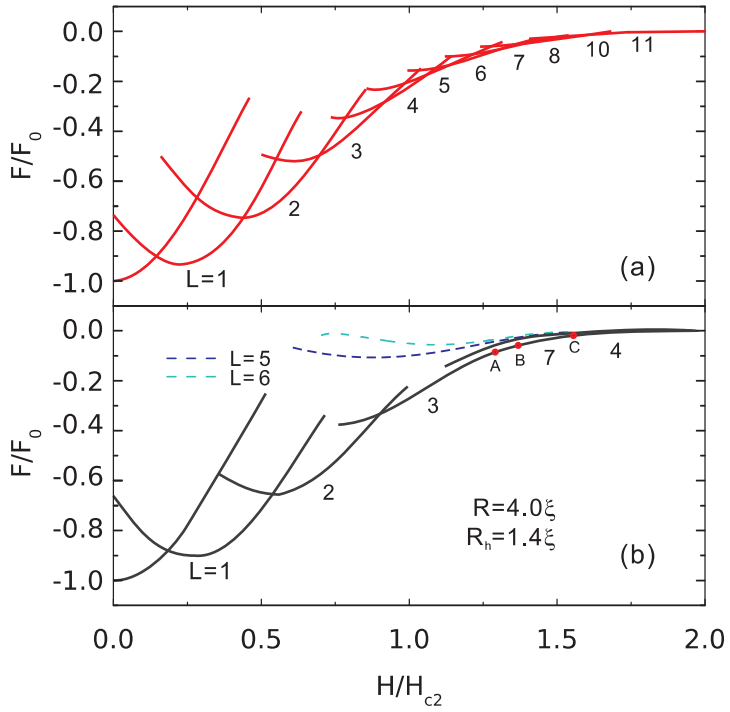

Fig. 4.2 The free energy landscape and stable vortex states as a function of the axially applied magnetic field, in a perforated cylinder (a), compared to a superconducting sphere with a hole (b). In (b), the dashed curves show the higher energy of $L = 5$ and $L = 6$ states, which were not found stable but were artificially constructed by the expansion method.

vortices penetrate sequentially in the cylindrical sample in increasing magnetic field, and the maximal vorticity is 12. On the other hand, the vorticity L of the spherical sample increases gradually up to $L = 3$ in an applied field of $H = 0.75H_{c2}$. Surprisingly, no new energy levels are found in a large range of magnetic field, and the $L = 3$ energy curve stretches up to a high magnetic field of $H = 1.95H_{c2}$. However, the superconducting state does change along this energy line - the vorticity actually changes through a second-order transition from $L = 3$ to $L = 7$, before the final first-order transition to the $L = 4$ state as the field is increased! Thus, in the ground state 3 fluxes are expelled with increasing magnetic field. Characteristic states, labeled A, B, C in Fig. 4.2, are shown in Fig. 4.3(a) as the Cooper-pair density contourplots and the contourplots of the phase of the order parameter in the equatorial plane of the sample. States A and B show the gradual and simultaneous entry of four vortices in the sample in the $L = 3$ state, forming the $L = 7$ state, and state C is the last surviving superconducting state in increased magnetic field for this geometry. There we note the particularly weak order parameter at the sample edges in the central plane. In Fig. 4.3(b), the radial Cooper-pair density profile prior to the destruction of superconductivity is plotted for two spheres with the same radius $R = 4.0\xi$, but with different radius of the hole, $R_h = 0.2R$ and $R_h = 0.35R$. The former corresponds to the giant-vortex formation in the sample, with

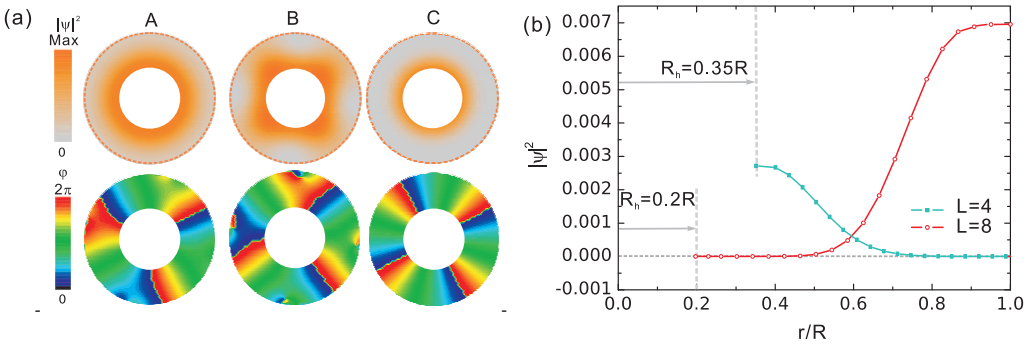

Fig. 4.3 (a) The Cooper-pair density and phase contourplots of the $L = 3$, $L = 7$, and $L = 4$ state, labeled as A, B and C respectively in Fig. 4.2. (b) The radial Cooper-pair density profile prior to destruction of superconductivity in two spheres with radius 4.0ξ but with different radii of the holes (c.f. Fig. 4.1).

maximal vorticity equal 8. On the other hand, the latter is the case of Fig. 4.2, where four vortices are trapped by the hole and no other vortex exists in the sample. Instead, superconductivity is utterly destroyed on the equatorial belt, where the stray magnetic field is largest. The existence of this equatorial normal-state belt is phenomenologically exactly opposite to the case of surface superconductivity, and yet unreported in the field of mesoscopic superconductivity. Beside this, the found second-order, multi-quanta $L = 3 \to 7$ transition is also surprising and unique. In what follows, we analyze these phenomena in greater detail.

The key in the analysis of the above phenomena is the geometry of the sample. Namely, in a spherical sample the geometric barrier is virtually absent, and vortices can nucleate as points on the equator, and grow in length as they approach the center of the sample in increasing magnetic field. However, further vortex entry becomes non-trivial, since the preexisting vortices repel the new ones. This is still not sufficient for the found surprising phenomena, since vortices can still rearrange to an energetic consensus [126, 109]. In the present case however, the central perforation *pins* the first entering vortices, and their rearrangement upon further flux entry is not possible. This enlarges the Bean-Livingston (BL) barrier for the entry of new vortices. This barrier is very firm, since the geometric barrier for pinned vortices to leave the hole is very large. For this reason, vortices are unable to enter the sample beyond the $L = 3$ state in Fig. 4.2, up to the applied field sufficiently large to overcome the BL barrier, at which point new vortices enter the sample through a second-order transition, since the BL barrier is exactly matched by the magnetic 'pressure' from outside the sample. In this particular case, this threshold applied field is also sufficient for four additional flux quanta to enter the sample, and we find the transition to the $L = 7$ state. Further increase of the applied field compresses vortices towards the sample interior, and results finally in the entry of one more vortex into the hole, which is a first-order process. To counteract the repulsion of four vortices trapped in the hole and add more vortices to the system, the field should be increased further, however such a large field induces large equatorial screening currents in the sample and the superfluid velocity exceeds the depairing one. As a result, the normal-

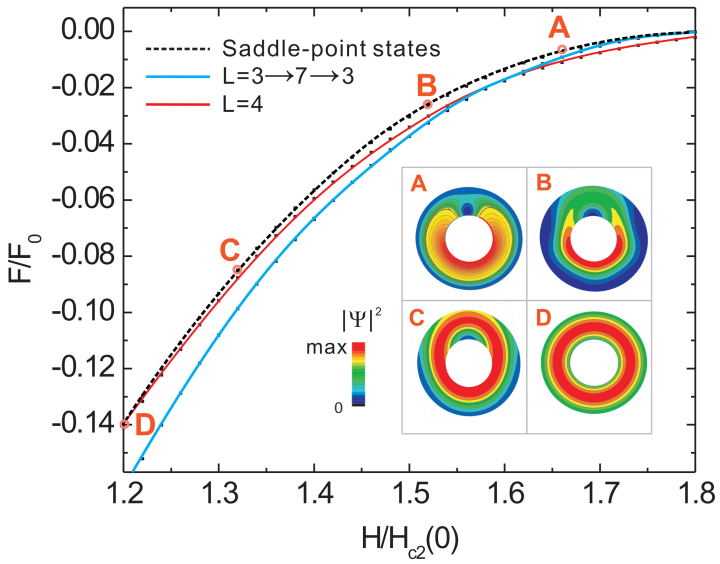

Fig. 4.4 The free energy of the $L = 3$ and $L = 4$ states and the saddle state between them (c.f. Fig. 4.2). In inset, the sequence of saddle points is shown through the Cooper-pair density plots at the equatorial belt of the sample, at different magnetic fields. This sequence shows the penetration of one vortex into the superconductor from outer boundary, finally residing inside the perforation.

state belt is formed, being more energetically favorable than the appearance of new localized vortices in the sample.

4.4 ENERGY BARRIERS AND THERMAL EXCITATIONS

To understand the relation between the state with a zero-order-parameter (normal) equatorial belt and the usual giant vortex state, we examine the saddle point between them, using the expansion method from Ref. [137], as already outlined in the theoretical formalism. In the Fig. 4.4, we show the calculated free energy, and the saddle state as transition from the normal-belt with $L = 3$ state to the $L = 4$ state. As shown in inset of Fig. 4.4, one vortex forms at the normal-belt (inset A), gradually moves inwards (interacting with the currents surrounding the perforation, see insets B and C), and finally merges with the three vortices trapped inside the hole to form the giant vortex state of $L = 4$. The very existence of the saddle state directly proves the first order transition between $L = 3$ and $L = 4$ states at high field, while at the same time no saddle points can be found for the second order transition between $L = 3$ and $L = 7$ states at lower fields, where $L = 3$ state with the normal-belt is formed from $L = 7$ state by increasing magnetic field.

Using the same approach, we can now calculate the energy barrier ΔF between different vortex states and saddle points between them. This is essentially done by subtracting

the energy of the metastable (higher energy) states from that of the saddle points. This is very important in the context of thermal fluctuations, which may drive the system from one equilibrium to another close to T_c, exactly where the GL theory is valid. To give a correct feel of the importance of the thermal fluctuations in the present study, we take the temperature in the calculation of $T = 0.9T_c$, for $T_c = 9$K. In that case, we can rescale the results of Fig. 4.2 to a sample at $T = 0.9T_c$ with size $R = 12.6\xi(0)$ and $R_h = 4.42\xi(0)$. We take $\xi(0) = 10$ nm and for $\kappa = 20$. The shape of the energy barriers between $L = 1$, 2 and 3 states, shown in Fig. 4.5(a), is generally the same as the ones described earlier in Ref. [137], being the highest at the magnetic field where two states interchange as the ground state of the system. However, the most interesting physics in the present system lies beyond the $L = 3$ state, where with increasing magnetic field first the $L = 7$ state is formed, and is then reduced back to the $L = 3$ state with the normal-belt at the equator of the sample. In this case, as shown in Fig. 4.5(b), the energy barrier changes with magnetic field in a somewhat different fashion, with a clear change of $\Delta F(H)$ slope at the $L = 3$-to-7 transition. Upon transition to the $L = 4$ state in the ground-state of the system, the energy barrier decreases very similarly to the states shown in 4.5(a). More importantly, in all curves in Fig. 4.5 the energy barrier is found to be much larger than the thermal energy k_BT. Note however that the barriers become comparable to the thermal energy at high magnetic fields (c.f. Fig. 4.5(b)), so that thermal fluctuations cannot be entirely neglected. It is exactly those magnetic fields where the multi-flux quanta entry in the system can be triggered, and thus thermal fluctuations may hide this phenomenon in experiment. Nevertheless, the latter will take place only in sufficiently large samples where the energy barriers are very low, and not in the truly mesoscopic samples where influence of the sample boundaries is extremely prominent and barriers are high. Note however that in high-T_c samples thermal-driven transitions may take place, since there κ is large which lowers the energy barriers, while T_c is large and increases the thermal energy.

4.5 THE SUPERCURRENTS AT SAMPLE BOUNDARIES

Arguably, the strength of the barriers in a 3D superconducting geometry can be analyzed through the strength of the supercurrents, typically maximal at the outer boundaries. We therefore calculated the current in the sample using

$$\overrightarrow{j_{3D}} = \frac{1}{2i}\left(\Psi^*\overrightarrow{\nabla}_{3D}\Psi - \Psi\overrightarrow{\nabla}_{3D}\Psi^*\right) - |\Psi|^2\overrightarrow{A}, \tag{4.5}$$

and we paid special attention to the current amplitude as a function of applied field at both inner and outer edges of the samples. In Fig. 4.6, we show the results for a perforated cylinder (same as in Fig. 4.2(a)), where the current at the boundary (conventionally) oscillates with each vortex entry. On the other hand, upon vorticity 4, the pinned giant-vortex outgrows the hole, and the inner-edge current (and barrier) vanishes. For comparison, in Fig. 4.7 we show the corresponding plots for a sphere with a hole. In accordance with our findings earlier in this manuscript, the behavior of the currents/barriers is seemingly similar, but actually *opposite*. Namely, beyond $L = 3$ the current and barrier at the equatorial plane diminish, while remaining non-zero at the inner boundary of the sample.

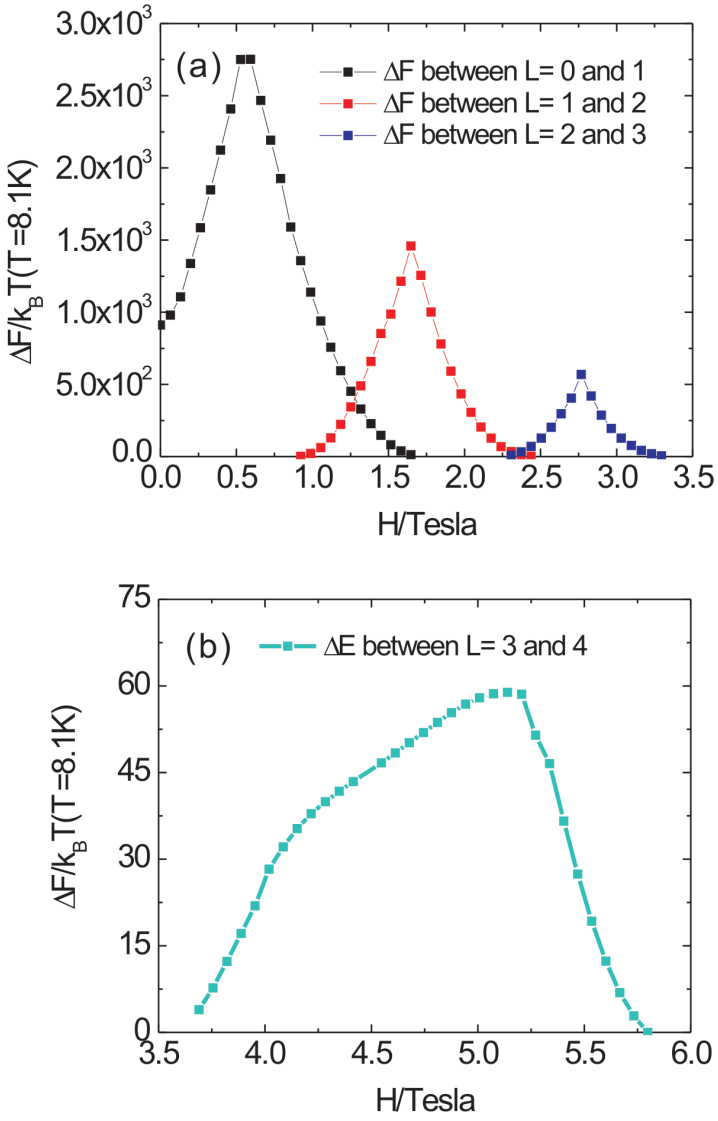

Fig. 4.5 (a) The energy barriers between different vortex states from Fig. 4.2 (with vorticity $L \leq 3$), corresponding to a Nb sample with $R = 126$nm, $R_h = 44.2$nm at $T = 8.1$K, scaled to thermal energy $k_B T$. (b) The energy barrier at high fields, between the vortex state with $L = 4$ and the one with $L = 3$ and a normal equatorial belt.

4.6 TUNING THE GEOMETRY AND THE INTERACTIONS

The interaction between the inner geometric barrier of the hole and the outer Bean-Livingston (BL) boundary formed by trapped vortices in the hole quite obviously depends on the distance between the inner and outer surface of the sample, in other words on

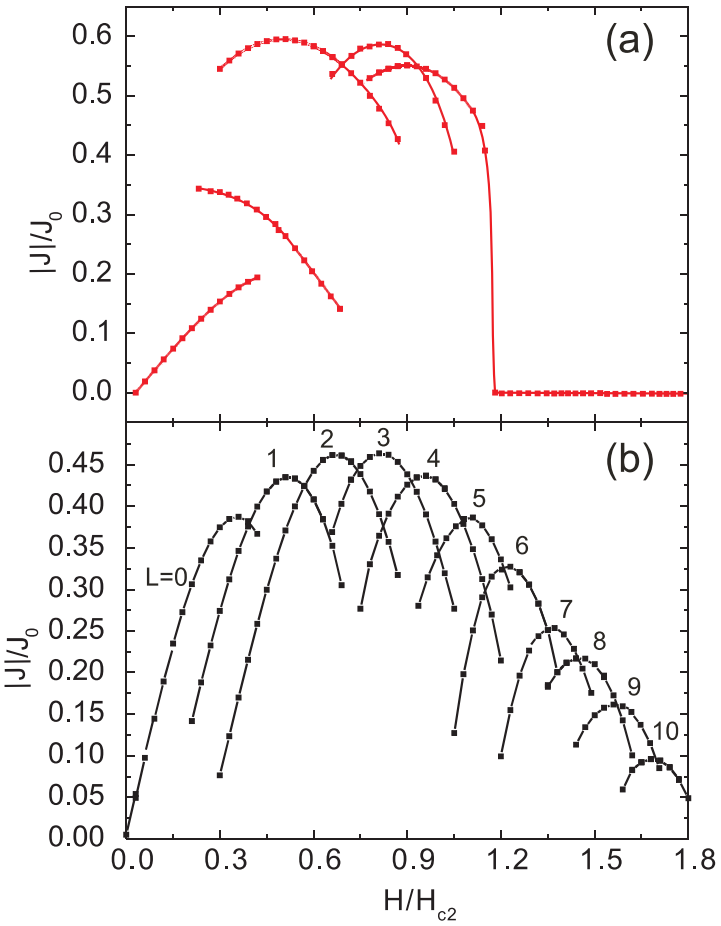

Fig. 4.6 The calculated modulas current density at the inner (a) and outer (b) boundaries of a perforated cylinder, plotted as a function of the applied magnetic field (corresponding to Fig. 4.2).

the R_h/R ratio. We demonstrate this in Fig. 4.8, where we fixed the radius of the hole at $R_h = 1.0\xi$ and varied the radius of the sample from $R = 3.6\xi$ to $R = 3.9\xi$. As can be seen in Fig. 4.1(b), the saturation vorticity n_s of the hole equals two for all the cases considered, and the maximal vorticity is always five. Nevertheless, the sequence of vortex phases and transitions between them in increased applied field is strongly affected by changing the R_h/R ratio. The equatorial contourplots of the phase of the order parameter in three samples are shown as columns in Fig. 4.8, with images arranged top to bottom in correspondence with increasing applied magnetic field. Both first- and second-order transitions between successive vortex states are found, indicated in Fig. 4.8 by open and colored arrows respectively. In the sample with $R = 3.6\xi$, the interaction of the two vortices trapped in the hole and the outer magnetic field is strong, and we find a second-order transition and multi-fluxon entry of 3 vortices simultaneously, which qualitatively corresponds to the $L = 3$ to $L = 7$ transition in Fig. 4.2. However, even in a slightly larger sample, e.g. $R = 3.8\xi$, the BL barrier is lowered at the sample edge and

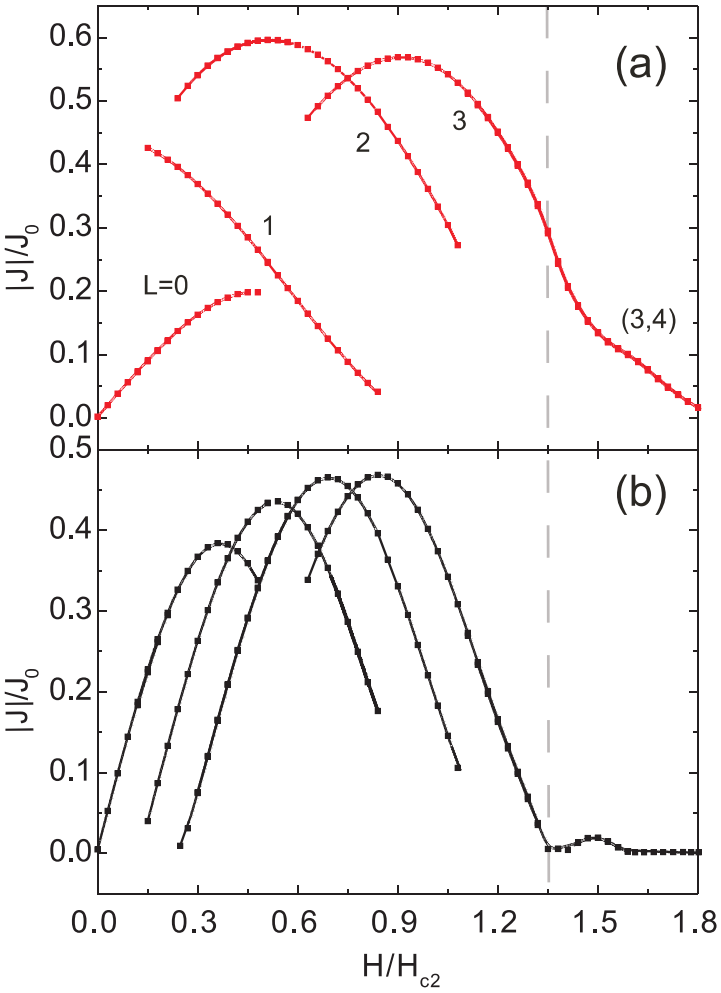

Fig. 4.7 Same as Fig. 4.6, but for a perforated sphere. Dashed line denotes the field where the second-order transition between $L = 3$ and $L = 7$ sets in.

is no longer balanced by the repulsion from the pinned vortices. As a result, one vortex can enter the sample, which appears as a first-order transition as soon as the vortex crosses the Meissner currents at the sample edge. However, by allowing this flux entry, the system restores the balance of forces, and further flux entry from $L = 3$ to $L = 5$ is again of second order! Making the sample just a fraction larger, to a size of $R = 3.9\xi$, leads to first-order $L = 2$ to $L = 3$ and further to $L = 4$ transitions, and the second-order transition is shifted to the last stage - the single vortex entry towards the $L = 5$ state. In summary, by changing the size of the hole and the sample, one manipulates the interaction between inner and outer boundaries and energy barriers, and one can change any of the phase transitions between successive vortex states from first- to second-order, and from individual to multi-flux-quanta events.

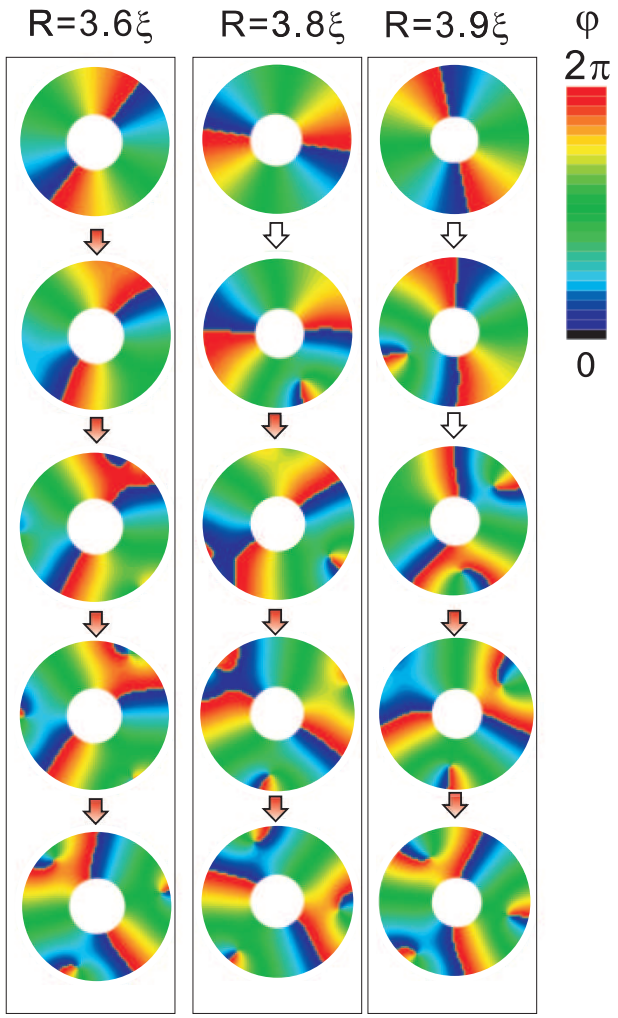

Fig. 4.8 A sequence of vortex-state transitions in the ground state, with indication of the order of the phase transitions (open/colored arrows - first/second order), for different radii of the sample and fixed size of the central hole $R_h = 1.0\xi$. The images are arranged top-to-bottom in increasing applied magnetic field.

4.6.1 The effect on critical magnetic field

The free energy curves in Fig. 4.2 clearly show the strengthening effect that the pinned vortices have on the Bean-Livingston barrier, as the vortex entry between $L = 0-3$ states is shifted to higher fields in samples with a weak geometric barrier. Here we discuss one more effect that the competition of the barriers has on threshold magnetic fields, in this case the upper critical field H_{cr} (at which the superconductivity is destroyed). Our results are summoned in Fig. 4.9, for spherical samples with radii $R = 3.25\xi$, $R = 3.75\xi$ and 4.25ξ, as a function of the size of the hole. Each curve exhibits a rather flat stage

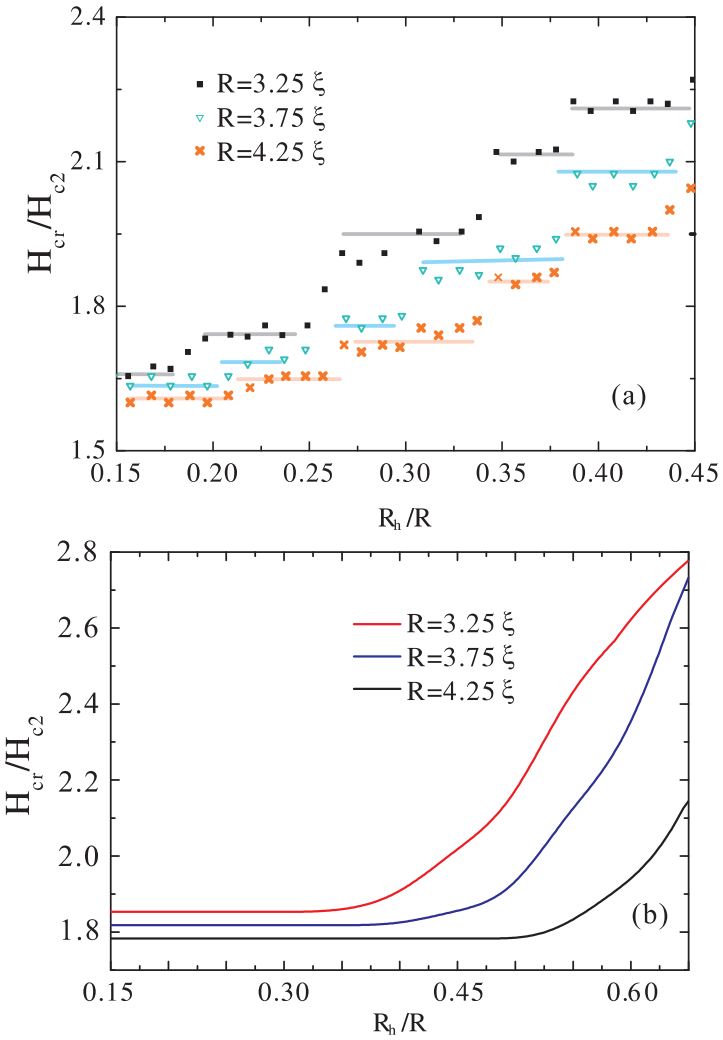

Fig. 4.9 (a) The evolution of the upper critical field H_{cr} of a spherical sample of radius R as a function of the size of the central hole R_h, for samples of three different outer radii. (b) *Idem.* for a cylindrical sample of the same volume.

when the perforation is small, which corresponds to the states of weak inner geometric barrier, and the formation of giant-vortex states in the sample, up to high vorticity (such as the $L = 8$ state shown in Fig. 4.3(b)). This main contribution to demagnetization comes from the screening current near the outer edges, which is practically unaffected by the hole. However, a sufficiently large hole can trap a number of vortices, and in doing so effectively preserve the superconducting condensate near the inner surface of the sample, while rejecting the penetration of new vortices from the outer boundary. As discussed above, this eventually leads to a gradual suppression of superconductivity from equator inwards and enhances the critical field H_{cr} in a step-like manner as a function

of the size of the hole. A step increase in H_{cr} is found for every R_h/R ratio for which the interplay of barriers allows one more vortex to enter the hole, and this increases the barrier for further flux entry, and therefore increases the upper critical field. These steps are clearly visible in Fig. 4.9(a), and are commonly found for all considered samples for $R_h = 0.28R$, $0.35R$ and $0.40R$. Furthermore, in the same range of R_h/R ratios, the upper critical field of the sample is enhanced beyond that of a corresponding cylinder with a hole, as shown in Fig. 4.9(b).

4.7 CONCLUSIONS

In summary, we discussed the effect of the interplay of the geometric barrier and the Bean-Livingston barrier on vortex states and transitions between them in extreme type-II superconductors. The subtle interplay of the energy barriers can be achieved by adjusting the shape and distances between different boundaries in the system, as we demonstrate on an example of a spherical sample with a central cylindrical hole. In this case, the curvature of the outer boundary minimizes the strength of the geometric barrier for vortex entry, while the cylindrical shape of the hole strongly pins the existing vortices of the sample in an axially applied magnetic field. These pinned vortices affect in turn the Bean-Livingston barrier at the outer surface of the sample, and postpone further flux entry in the sample. As a consequence, a series of sequential first- and second-order vortex phase transitions is realized, some of which can comprise several flux quanta entering the sample simultaneously, which is all very different from conventional behavior of mesoscopic superconductors, e.g. cylinders (as shown for comparison). Finally, the lack of the outer geometrical barrier in these samples can lead to the formation of a unique state at high magnetic fields, where nucleation of vortices is no longer favorable and superconductivity is gradually suppressed from the equatorial belt of the sample inwards, i.e. the exact opposite scenario to surface superconductivity.

Publications. The results presented in this chapter were published as:

- Ben Xu, M. V. Milošević and F. M. Peeters, *Second-order multiple-quanta flux entry into a perforated spherical mesoscopic superconductor*, Phys. Rev. B **82**, 214501 (2010)

5

Calorimetric properties of mesoscopic superconductors

5.1 INTRODUCTION

Submicron superconducting devices are envisaged as a base for futuristic electronics, due to their low resistance and enhanced critical parameters compared to bulk materials [95, 97]. Mesoscopic superconducting devices already found a number of exotic applications, such as in astronomy - as the microbolometer of time-resolved terahertz spectroscopy [142], as dark matter detectors [143], or as single photon detectors [144]. In latter systems, the intrinsic thermodynamic properties are of crucial importance, related to the energy needed for the heating of the system or to the heat released when the system changes its state. Yet, the theoretical understanding of such calorimetric properties of mesoscopic superconducting samples is in its infancy as compared to the extensively studied electromagnetic and transport properties of such samples.

In bulk superconducting materials, the specific heat shows sizeable jumps at the critical field for the superconducting/normal (S/N) state transition, which was one of the most important proofs for the existence of superconducting condensation [26]. In type-II superconducting materials, the experimental and analytical analysis of the specific heat was done in Refs. [145, 146] as a function of applied magnetic field H. They found that the amplitude of the jump in the heat capacity at the S/N transition decreases as the applied magnetic field is increased (simultaneously, the critical temperature decreases). Another important aspect of this work is that, when the specimens are heated in a constant magnetic field, the heat capacity exhibits a very large peak at low temperature followed by a discontinuous drop in heat capacity at a higher temperature. The latter is connected with the second-order S/N transition at $H = H_{c2}$. Similar phenomenon was also found in disordered superfluid ^{3}He [147], as the specific heat of superfluid ^{3}He, disordered by a silica aerogel, is found to have a sharp discontinuity marking the thermodynamic transition to superfluidity (with lower amplitude and at a reduced temperature

from that of bulk ^{3}He). The formerly described peak however is associated with the entrance of the magnetic flux into the specimen [145, 84].

Calorimetric investigation of mesoscopic systems brings an innovative and complementary point of view to condensed matter studies [88, 85, 148]. Recently, it has become possible to study the heat capacity of submicron-sized superconducting samples due to the large progress in attoJoule calorimetry [85, 149]. The first heat capacity measurements of the phase transitions between vortex states in mesoscopic singly connected superconductors were recently performed by Bourgeois *et al.* [85], and Ong *et al.* [87]. The experiments were carried out on large arrays of mesoscopic two dimensional disks and rings, to maximize the output signal. Heat capacity curves versus temperature or field were found to clearly indicate the number of vortices threading the sample, where each entrance or exit of a vortex caused a jump from one heat capacity level to another. As for superconducting rings, oscillations in the size of the discontinuity of the heat capacity at the S/N transition were found and the measured oscillations of ΔC_p with field showed a more pronounced amplitude than anticipated. The corresponding theoretical calculation and understanding is still lacking, and this is the primary objective of this work.

A general theoretical description of the specific heat behavior of the mixed state in superconductors was first discussed by de Gennes [27] and Fetter [150]. At low and intermediate fields, the difference of the specific heat between vortex states and the fully superconducting state is proportional to $-BT(\partial^2 H_{c1}\,/\partial T^2)/4\pi$, and also to a free energy functional $\mathcal{F}[H]$, which is complicated and must be calculated numerically (especially for a mesoscopic sample containing a dense distribution of vortices). In his analysis, de Gennes also described the specific heat change between two different vortex states, which is proportional to the obtained difference in $(\partial B_i/\partial H)$ [27], leading to the prediction of specific heat jumps at magnetic fields for which a vortex enters or leaves the sample. Other attempts to describe calorimetric properties of superconductors have used the BCS theory or the Eilenberg equations [151]. However, the applicability of the latter approaches is limited to infinite periodic samples, due to the computational difficulties related to the mesoscopic boundary and the current-field coupling effects. Therefore, it is more convenient to study the thermal properties of these systems in the framework of a mean-field Ginzburg-Landau theory. For example, Bray [152] simulated the behavior of the specific heat in bulk and thin film superconducting samples in a uniform magnetic field, by the use of the "free fluctuation theory" and screening theory. Fink [153] and Tinkham [26] described the heat capacity behavior in the case of a hollow superconducting cylinder and its relation to fluxoid quantization. Zhang [154] extended these approaches to mesoscopic superconducting rings for susceptibility calculations and Deo *et al.* [148] considered the heat capacity of superconducting disks, but restricted their analysis to the linearized Ginzburg-Landau theory.

There is therefore still a need for an approach that includes the influence of the quantized fluxoid states on the specific heat of mesoscopic samples, including the demagnetization effects, for mesoscopic samples of arbitrary geometry and size, plus for an arbitrary direction of applied magnetic field. This is an exact purpose of this chapter; we present our state-of-the-art theoretical calculation, based on the full, non-linear Ginzburg-Landau (GL) theory. This theory has been extensively used in the past to describe the electromagnetic properties of two dimensional superconductors [50], where

now we carefully incorporate and study the thermal relationships of different factors, the kinetic energy of the condensate and the magnetic response of the sample. The present numerical approach allows to describe not only 2D mesoscopic superconducting systems, but also mesoscopic 3D samples, where the configuration of vortices is even more intricate due to the complex influence of the shape of the boundary and also the direction of the applied magnetic field. As we will show, in such cases, the heat capacity can be a useful tool to discriminate the delicate changes in vortex configurations.

We start from the specific heat calculations for two-dimensional mesoscopic superconducting disks and rings, where the relevant parameters are mostly taken from the experiments of Bourgeois and co-workers [87, 88]. The studied samples and theoretical formulation of the problem are presented in Sec. 5.2. The calorimetric calculations for the disk geometry are presented in Sec. 5.3. The corresponding thermal signatures of superconducting rings are shown in Sec. 5.4. Section 5.5 is devoted to 3D calorimetric response of superconducting cylinders, and our results are summarized in Sec. 5.6.

5.2 THEORETICAL APPROACH

We consider mesoscopic superconducting disks and rings made of type-I material (Al), which are immersed in an insulating media and exposed to a perpendicular uniform magnetic field H. To be able to calculate the specific heat, we explicitly include the temperature dependence in the Ginzburg-Landau (GL) formalism for the description of the superconducting system. The superconducting-normal state Gibbs free energy difference in the GL approach can be expressed as

$$\begin{aligned} \mathcal{G} &= \mathcal{G}_{SH} - \mathcal{G}_{NH} = \int \left\{ \alpha |\Psi|^2 + \beta \frac{|\Psi|^4}{2} + \right. \\ &+ \left. \frac{1}{2m^*} \left| \left(\frac{\hbar \nabla}{i} - \frac{e^* \vec{A}}{c} \right) \Psi \right|^2 + \kappa^2 \frac{(\vec{h} - \vec{H})^2}{8\pi} \right\} dV, \end{aligned} \tag{5.1}$$

where the $\mathcal{G}_{SH}$ and $\mathcal{G}_{NH}$ correspond to the free energy of the sample in the superconducting and the normal state, respectively, at applied magnetic field $\vec{H}$ ($\vec{h}$ denotes the resulting, total local field in and around the superconductor) [26]. The GL parameter κ equals λ/ξ, where λ is the penetration depth. Minimization of Eq. (5.1) leads to two coupled GL equations, the first being

$$(\frac{\nabla}{i} - \vec{A})^2 \Psi + |\Psi|^2 \Psi - (1 - T)\Psi = 0. \tag{5.2}$$

The derivation of the GL equations assumes the London gauge $\mathrm{div}\vec{A} = 0$ for the vector potential $\vec{A}$. All variables in Eq. (5.2) are dimensionless: the distance is measured in units of the coherence length $\xi(T = 0)$, the vector potential $\vec{A}$ in $c\hbar/2e\xi(0)$ (magnetic field in $H_{c2}(0) = c\hbar/2e\xi(0)^2 = \kappa\sqrt{2}H_c(0)$), and the order parameter Ψ is scaled to its value in the absence of the magnetic field.

However, the first GL equation is only sufficient for the description of extreme type-II samples or for an extremely thin superconducting film where screening effects can be

neglected. Otherwise the demagnetization effects must be taken into account, and the second GL equation is needed:

$$-\kappa^2 \Delta \vec{A} = \frac{1}{2i}(\Psi^* \vec{\nabla} \Psi - \Psi \vec{\nabla} \Psi^*) - |\Psi|^2 \vec{A}. \tag{5.3}$$

The right side of Eq. (5.3) is the density of the superconducting current $\vec{j}$ induced by the sample in response to the applied field. Note that for the quasi-2D system, i.e. small but non-negligible thickness d of the sample, the variations of the magnetic field and order parameter in the z-direction can be neglected, and Eq. (5.3) may be averaged over the sample thickness d. In that case, κ^2 in Eq. (5.3) becomes the effective GL parameter $\kappa_e = \kappa^2 \xi / d$.

Here we solve the GL equations self-consistently in a finite-difference scheme [34, 92]. We use the Neumann boundary conditions $(-i\vec{\nabla} - \vec{A})\Psi|_{boundary} = 0$ for the order parameter on all sample surfaces, including the inner boundaries (if any). The convergent solution of Eqs. (5.2) and (5.3) determines the superconducting state corresponding to the local energy minimum. In search for all stable states for given conditions (thus the lowest energy *ground* state, and the higher energy *metastable* states), we repeat the calculation using different initial conditions. For a realistic comparison with a field-cooled experiment, we initiate the calculation from a randomly generated and very weak superconducting order parameter, while in a zero-field-cooled situation, we start from $|\Psi| \approx 1$ in the whole sample. Once a solution is found, we are able to calculate the specific heat of the superconducting state based on the relation:

$$C_p(H,T) = C(H,T) - C_N(H,T) = -T \frac{\partial^2 \mathcal{G}}{\partial T^2}, \tag{5.4}$$

where C denotes the total heat capacity of the sample, and C_N is the heat capacity of the sample in the normal state (all in units of $C_0 = H_c^2(0)V/(8\pi T_c)$). In the calculations, we start from the equilibrium states and oscillate the temperature of the system with amplitude $10^{-4} T_{c0}$ (T_c at $H = 0$), and then perform the second derivation numerically to obtain the specific heat for given parameters.

It should be mentioned here that solving Eq. (5.3) directly results in a finite magnetization of the sample. Instead of the thermodynamic expression for magnetization $M = \partial \mathcal{G} / \partial H$, we define in accordance with experimental reality, i.e. as the quantity of expelled magnetic field from the sample in applied field H:

$$\vec{M} = \frac{\langle \vec{h} \rangle - \vec{H}}{4\pi}, \tag{5.5}$$

where $\vec{h} = \mathrm{rot}\vec{A}$ is the local magnetic field in the sample, and $<>$ denotes averaging over the area of interest (e.g. a surface area of a magnetic detector at a given location with respect to the sample).

5.3 HEAT CAPACITY OF MESOSCOPIC SUPERCONDUCTING DISKS

In what follows, the sample is an aluminium disk of radius $R = 6\xi(0)$ and thickness $d = \xi(0)$ (see inset of Fig. 5.1). This corresponds to the experimental sample of Ong

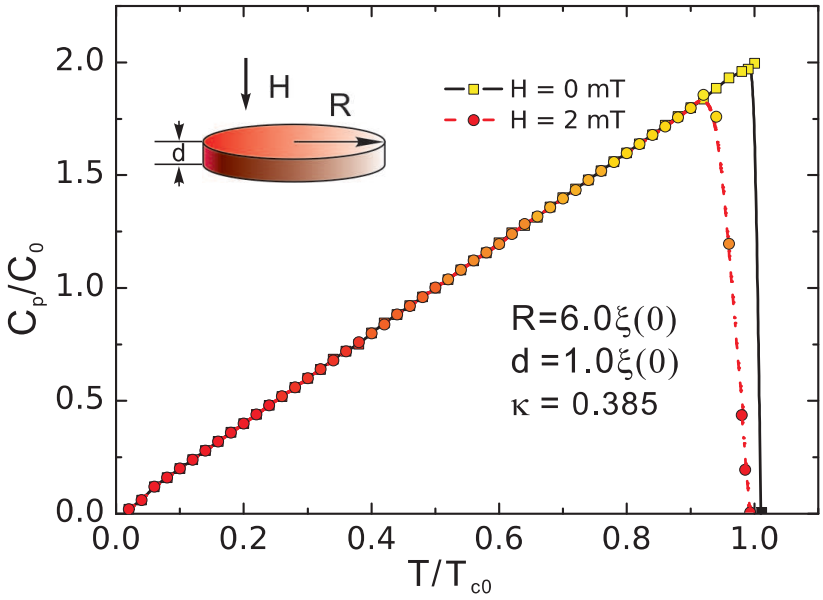

Fig. 5.1 Heat capacity of a superconducting aluminium disk as a function of temperature in the absence and in presence of the magnetic field H. The calculation is done in the zero-field-cooled regime. Inset depicts the sample.

et al. [87], where $\xi(0)$ was roughly estimated to 182 nm and $\lambda(0)$ to 70 nm. This results in the GL parameter $\kappa \approx 0.385$, which is firmly in the type-I regime. Often in experiments Al samples are thinner than $\lambda(0)$ [155, 156], which makes them effectively type-II ($\kappa_e > 1/\sqrt{2}$), and conventional mesoscopic behavior of the superconducting state and vortex matter is found. In earlier works [50, 116, 51], the vortex entry and distinction between giant and multi-vortex states was thoroughly discussed. Surprisingly, Ong *et al.* [87] also discuss their findings from the standpoint of a type-II sample. While modeling the latter experiment, we correct this somewhat, as explained further.

Conventionally, the behavior of the superconducting state in mesoscopic type-II superconductors as a function of applied magnetic field is discussed with respect to the upper critical field H_{c2}. In the present case, we scale the field to the thermodynamic critical field H_c, which in our sample equals $H_c(0) = \Phi_0/2\sqrt{2}\pi\xi(0)\lambda(0) \approx 18.34$ mT, with $H_c(T) = H_c(0)(1-T/T_c)$. Since penetration depth $\lambda(0)$ is comparable to the thickness d and increases with temperature, a homogenous distribution of magnetic field across the sample thickness can be assumed. Nevertheless, we use the three-dimensional treatment of the two coupled Ginzburg-Landau equations, taking thus fully into account the 3D demagnetization effects. We are interested in two calorimetric sets of data - one for the heat capacity versus magnetic field under fixed temperature, and the other for the case of fixed magnetic field, and the variation of the heat capacity versus temperature.

In Fig. 5.1 the $C_p[= C_{total} - C_N]$ curve for the forementioned superconducting disk is presented as a function of temperature (scaled to T_{c0}). When present, the field was always applied after the sample had been cooled down to zero temperature, i.e. we work

in the zero-field-cooled regime. We subsequently increase the temperature gradually. We monitor the heat capacity of the Meissner state, although at higher temperatures vortices may enter the system in the ground-state. However, due to the finite Bean-Livingston barrier and the absence of fluctuations [52], fluxoids are generally unable to enter the sample during the temperature sweep. In absence of applied field, the $L = 0$ state shows a discontinuity at T_c, analogously to the behavior of bulk superconductors (see Fig. 5.1). The critical temperature is often determined by the temperature at half-height of the C_p jump, and the size $\Delta C(H)$ of the heat capacity discontinuity can be extracted at the S/N transition.

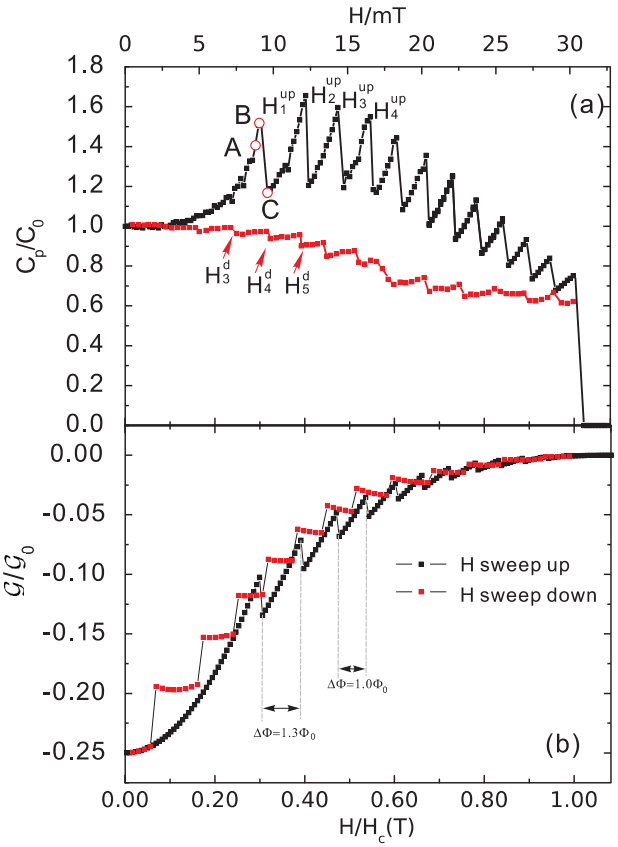

Fig. 5.2 (a) Heat capacity $C_p(H,T)$ is plotted as a function of the applied magnetic field at temperature $T = 0.5T_{c0}$, for increasing and decreasing magnetic field. The data shows pronounced hysteretic behavior. H_L^{up} shows the penetration field of the $L-th$ vortex in the system and H_L^d is the vortex expulsion field (the transition to a $L-1$ state). (b) The free energy curves versus the magnetic field for the magnetic field swept-up and down. The unit of the free energy $\mathcal{G}_0$ is $H_c^2(0)/8\pi$.

In their attoJoule measurements, Ong *et al.* [87] showed the possibility of modulating the heat capacity of mesoscopic disks by a magnetic field and investigated the response of the different vortex states. Namely, the heat capacity is directly linked to the flux

distribution inside the sample and the resulting vorticity. Since the corresponding theoretical calculations are missing up to date, we perform here the numerical "experiment": we fix the temperature in the absence of applied field (to $0.5T/T_{c0}$), and then sweep-up the magnetic field continuously towards the destruction of superconductivity, while recording all found vortex states along the way. Subsequently, we decrease the magnetic field down to zero, again in search for stable vortex states. For each recorded equilibrium state, we then vary the temperature with $\Delta T = 10^{-4}T_{c0}$ from the original one, in order to calculate the variation of the free energy and the heat capacity according to Eq. (5.4). The temperature step is kept small to ensure the precision of the calculation, but also to avoid any change in the original vortex state.

At this point, we should clarify that vortex states found in the experiment are not the signature of type-II superconductivity. To show this in comparison with experimental data, we scale the applied magnetic field value to $H_c(T)$ and specific heat to C_0; C_0 equals $H_c^2(0)V/(8\pi T_{c0})$ (V is the sample volume), which amounts to 4.5×10^{-5} pJ/K for a single disk, but equals 18.9 pJ/K for large arrays of the samples (number of disks $N = 4.2 \times 10^5$) as was the case in the experiment.

The obtained heat capacity $C_p(H,T)$ versus magnetic field for fixed temperature is shown in Fig. 5.2(a). Starting from zero field, the disks remain in the Meissner state ($L = 0$) up to $H \approx 0.30H_c(T)$ where C_p abruptly jumps to a lower value. This is the calorimetric signature of the first-order phase transition $L = 0 \to L = 1$, where one vortex penetrates the disk. As the field is increased further, we observe a cascade of successive phase transitions $L \to L + 1$, until the superconducting/normal second-order transition is reached. Although this scenario perfectly resembles the type-II samples, the found vortex states actually represent the *intermediate state of a type-I superconductor*. The ratio between the thickness and the diameter of the sample is 1/12, and using the calculation of the demagnetizing field of a largest inscribed ellipsoid from Ref. [157], we found that at applied field of $H \approx 0.30H_c(T)$ the field at the sample edges equals $H_c(T)$ and flux penetrates our type-I sample (see also Fig. 7 in Ref. [157]). Also in accordance with the conventional theory of type-I superconductivity, the superconducting state is finally destroyed at $H \approx H_c$.

Note that due to the mesoscopic size of our type-I sample, all found flux states are giant-vortex states. After the first penetration field, the stability field region for the following vortex state is approximately $0.09H_c(T)$. The latter value provides for added flux of $\Delta\Phi \approx 1.3\Phi_0$ through the system, and corresponds well to the experimental data (Fig. 4 in Ref. [87]). As indicated in Fig. 5.2, the added flux decreases with further increasing vorticity to $1.0\Phi_0$, showing that the flux quantization applies to the entire sample at high fields (at lower fields the flux is quantized inside the zero-current path, located between the giant vortex and the encircling Meissner currents). The total flux at the penetration field for the $L = 1$ vortex state is much higher than for the successive vortex states, because of the superheating of the Meissner phase, and is readily observed even in type-II samples [50]. Note the different definition of the heat capacity in our calculation as compared to the experiment; in experiment, the superconducting part of the specific heat is shown after subtraction of the whole background from the measured signal, while in our calculation $C_{total}(T,H) - C_N(T,H)$ is used. As a result, we have a different starting value of the heat capacity of the Meissner phase in the absence of magnetic field, and a different background curvature while changing the magnetic field.

The behavior of the heat capacity of the superconducting disk in increasing magnetic field can be explained by considering the temperature dependence of the different terms in the free energy in the Ginzburg-Landau theory. For $H < H_L^{up}$ (the penetration field of the $L-th$ vortex in the system, where the $L-1 \rightarrow L$ transition takes place), we observe an increase of the specific heat with increasing H. In the microscopic scheme of the BCS theory, the increase of temperature excites more quasi-particles in the system, and the well-known temperature dependence of the energy gap Δ can be derived $\frac{\Delta(T)}{\Delta(0)} \approx 1.74(1-\frac{T}{T_c})^{1/2}$, for temperatures close to T_c. In the Ginzburg-Landau theory, the temperature dependence of the order parameter resembles the one of the energy gap Δ, i.e. the density of Cooper-pairs decreases with temperature and decreases the heat capacity of the superconducting sample. This contribution enters the free energy through the term containing $|\psi|^4$. However, in mesoscopic samples, we find that the temperature dependence of the field-dependent term in the Ginzburg-Landau free energy is of crucial importance (in reduced form of the free energy, this term can be written as $(\vec{A}-\vec{A}_0)\cdot\vec{j}$, where $\vec{A}_0$ is the vector potential of the applied field, and $\vec{j}$ is the supercurrent, see Ref. [50]).

Let us now consider the above two different contributions of the free energy to the total heat capacity, specifically the $|\psi|^4$ term (C_Ψ, related to the depletion of the condensate) and the other from the superconducting current contribution (C_J, related to the kinetic energy of the condensate), which we show in Fig. 5.3. The total heat capacity shows a cascade of discontinuities for different vortices, but the major contribution of these jumps is different for low and high vorticity. For example, C_Ψ contributes mostly to the plateau of the vortex states of $L=1$ and $L=2$, but the steep background of C_p is due to C_J. Looking at C_J, the difference between the vortex states at their critical fields are present even for higher vorticity states, but those jumps are small compared to the oscillations of C_Ψ. In these calculations, while keeping $\xi(0) = 182$nm, we took the Ginzburg-Landau parameter $\kappa = 1.18$, thus clearly type-II.

The two contributions C_J and C_p to the specific heat can be investigated for different materials, i.e. with different Ginzburg-Landau parameter κ.[1] To compare with Fig. 5.3, we now show the total heat capacity and its two components C_J and C_p for different vortex states when $\kappa = 0.64$ (Fig. 5.4), thus just under the type-I/II transition. In both figures, one can find that the difference of C_Ψ between adjacent vortex states is small for lower vorticity, while the amplitude of the oscillation is much higher for higher vorticity, especially those close to the S/N transition point. It is these high vorticity oscillations that contribute most to the behavior of the total heat capacity at high magnetic field. C_J shows a larger oscillation amplitude for smaller κ, i.e. more than a factor of two larger for $\kappa = 0.64$ as compared to $\kappa = 1.18$ because of the strong Meissner currents in the type-I sample. Also interesting are the vortex states (and values of the magnetic field) where the contribution C_J drops from positive to negative. In Fig. 5.3, such switching happens several times, along the curves of the vortex states $L = 1-3$, while in the case of $\kappa = 0.64$, it happens only for vorticity $L = 1$, and remains negative afterwards. Therefore, type-I samples are more susceptible to heating at high fields than the type-II ones.

[1] To change κ in our simulations, we fix the coherence length and vary the penetration depth.

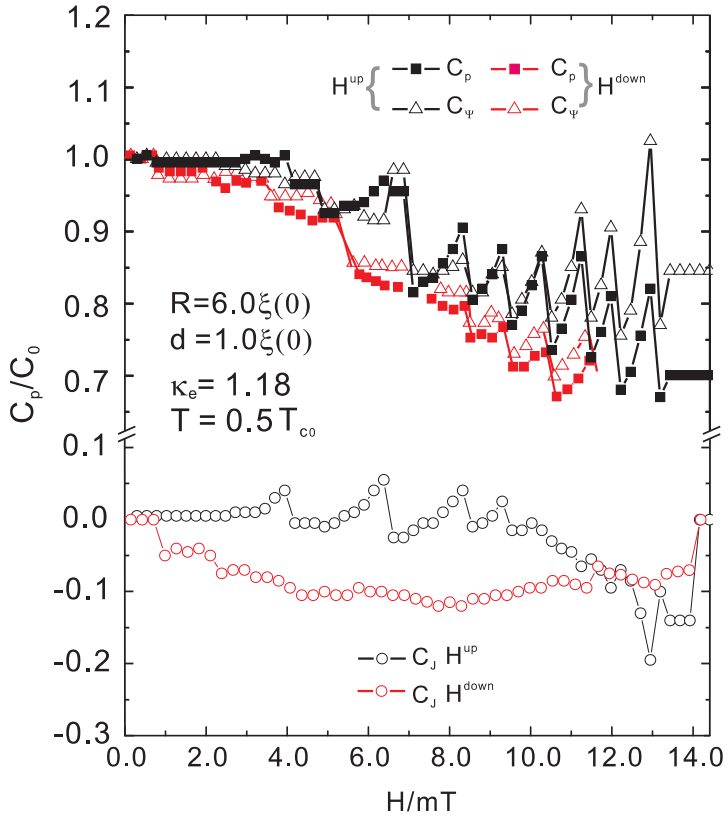

Fig. 5.3 The heat capacity (filled squares) is plotted for a disk sample with Ginzburg-Landau parameter $\kappa = 1.18$. The two components of the heat capacity C_Ψ (open triangles) and C_J (open dots) are shown. The calculations are done for sweeping-up and down the magnetic field.

In general, we can conclude that the major contribution to the lower vorticity oscillations is due to the superconducting current, and at high vorticity due to the depletion of the condensate. The heat capacity decreases with increasing applied magnetic field, and the size of the decline is controlled by the Ginzburg-Landau parameter κ.

To obtain a more detailed understanding of C_J for lower vorticity states, we plot the calculated distribution of the supercurrent in Fig. 5.5. As shown in the insets, the current has only an azimuthal component, and is cylindrically symmetric for the shown states. Three characteristic magnetic fields are chosen: (i) the field for which the system is in the Meissner state, where the superconducting current preserves a high density of superconducting order parameter; (ii) the field prior to the $L = 0 \to 1$ transition, and (iii) at the $L = 0 \to 1$ transition. When the magnetic field is increased for the system in the $L = 0$ state, the density of the superconducting current increases in order to expel the applied magnetic field. The maximum of the current density is reached prior to the penetration field, upon which the current becomes bipolar - anticlockwise inside the vortex core, and clockwise otherwise (see insets of Fig. 5.5(a)). Fig. 5.5(b) shows the variation of the superconducting current with temperature, calculated for a temperature

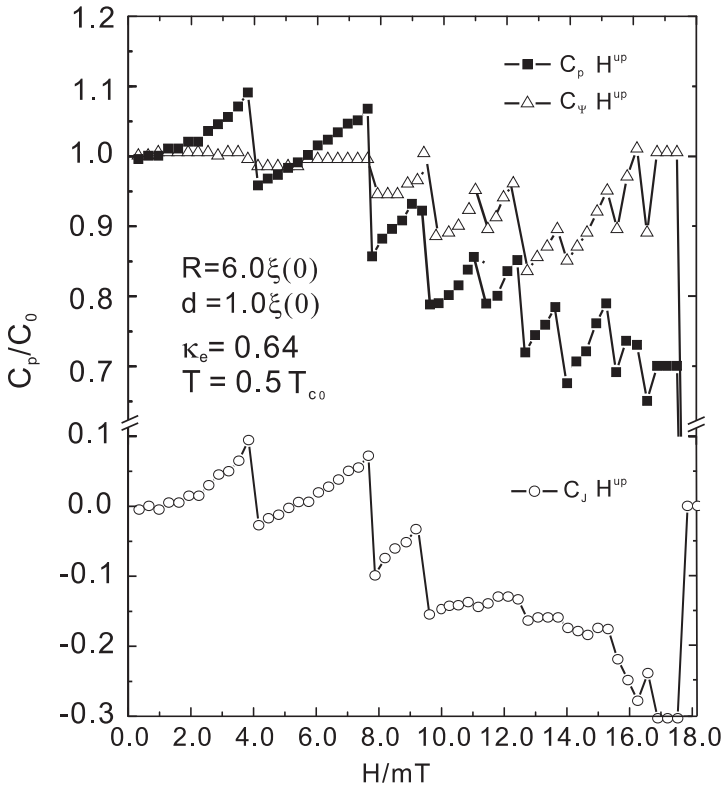

Fig. 5.4 The same as Fig. 5.3 but now for $\kappa = 0.64$.

increase by $\Delta T = 0.005 T_{c0}$. The variation of the current achieved for $L = 1$ is much larger than that of the $L = 0$ state, which reflects the observed difference in the heat capacity. Namely, latter feature shows that the contribution of temperature to the kinetic energy of the Cooper-pairs is larger for the $L = 1$ state, therefore less energy is needed to heat up the system. Notice from Fig. 5.2 that $C_p(H = 0.28H_c(T)) < C_p(H = 0.27H_c(T))$ since $\Delta J(H = 0.30H_c(T)) > \Delta J(H = 0.27H_c(T))$.

The jumps in the heat capacity between the different vortex states can be expressed more precisely using thermodynamic arguments. The theory of the specific heat in the mixed state is already well established, for the case of extreme type-II superconductors where screening is negligible (see Ref. [27]). The discontinuity in the specific heat at the given phase transition can then be calculated as

$$C_i - C_j = \frac{-T}{4\pi}\left(\frac{dH^*}{dT}\right)^2 \left[\left(\frac{\partial B_i}{\partial H}\right)_T - \left(\frac{\partial B_j}{\partial H}\right)_T\right], \tag{5.6}$$

where B stands for magnetic induction. Here we apply the above expression to the transition between the different vortex states, where i represents the vortex state of vorticity L just below the field H_{L+1}^{up}, and j represents the $L+1$ vortex state at the field just above H_{L+1}^{up}. Clearly, $(\partial B_i/\partial H)_T = 1 + 4\pi(\partial M_i/\partial H)_T$. Therefore, we conclude

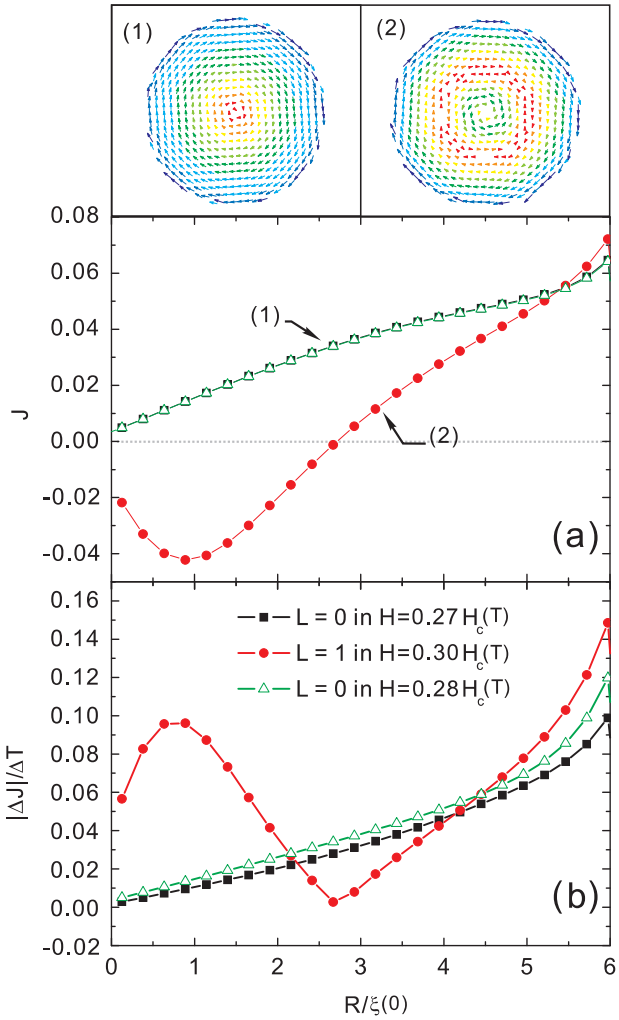

Fig. 5.5 (a) The distribution of the azimuthal superconducting current in the radial direction inside the superconducting disk, for the same parameter as used in Fig. 5.2, for H=0.27, 0.28 and $0.30H_c(T)$. Insets (1-2) show the vector plots of the current for vorticity 0 and 1, with magnitude indicated by color coding changing from red (minimum) to blue (maximum). (b) The variation of current shown in (a) with temperature ($\partial j/\partial T$), for applied field $H = 0.27H_c(T)$ (system in the Meissner state, point A in Fig. 5.2), field $H = 0.28H_c(T)$ (close to H_1^{up}, point B in Fig. 5.2), and field $H = 0.30H_c(T)$ (point C in Fig. 5.2, $L = 1$ state).

that we will be able to predict the size of the jump of the specific heat taken that we know $H^*(T) = H_{L+1}^{up}$ and the magnetization of each vortex state, and vice versa. From the calorimetry calculation of the specific heat we can derive the magnetic susceptibility

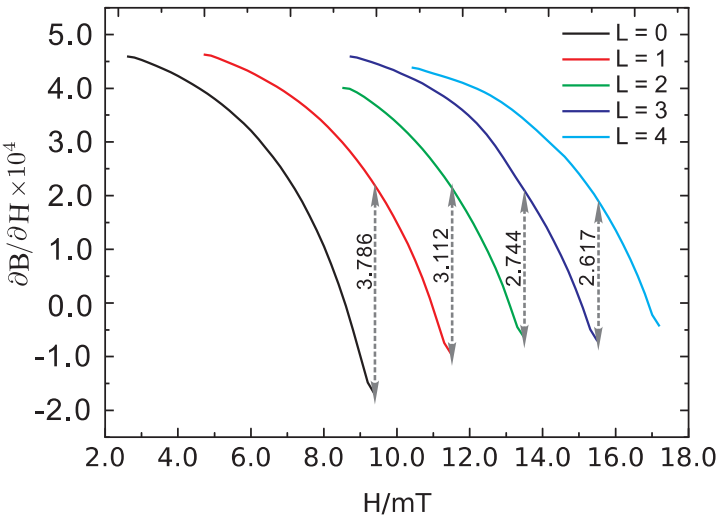

Fig. 5.6 The magnetic susceptibility $(\partial B_i/\partial H)_T$ as a function of the applied magnetic field at temperature $T = 0.5T_c$, for different vortex states. The $L \to L+1$ transitions are shown in the figure, and the corresponding values of the jump of the magnetic susceptibility between two subsequent phases are given.

$(\partial B_i/\partial H)_T$ [2]. In Fig. 5.6 we show the magnetic susceptibility for each vortex state as a function of the applied magnetic field, corresponding to the diagrams of Fig. 5.2. We calculated $(\partial B_i/\partial H)_T$ using Eq. (5.5) and compared the jump in susceptibility with the result from Eq. (6.12). We found a discrepancy of just 10%, although the sample is mesoscopic and type-I, none of which is included in the original theory from Ref. [27].

In the second part of our calculation, we focus on the influence of a constant perpendicular magnetic field on the heat capacity at the superconducting/normal transition (critical temperature, height, width of the transition, etc.). We fix the applied magnetic field and then calculate the specific heat while scanning temperature. For a better comparison with existing experimental data, we apply two strategies. In one, we sweep down the temperature starting from the normal state under given magnetic field which corresponds to the experimental field-cooled (FC) regime. In another, we start from zero temperature and sweep it up under fixed magnetic field (zero-field-cooled (ZFC) procedure). The two cases are physically very different, as shown in Fig. 5.7(a). In the FC regime, when the system is cooled down from the normal state, it remains in the first nucleated L state as T is swept down (in the present case, $L = 0$). Therefore, we observed no features in the heat capacity, except at the S/N phase transition. In the ZFC regime, when increasing temperature, the vorticity of the system may change. Namely, in the shown case, we found the $L = 1$ state at low temperatures, which becomes unstable at temperature $T = 0.68T_{c0}$ and a transition to $L = 0$ is observed through the jump in $C_p(T)$.

[2]Note however that $(\partial B_i/\partial H)_T$ diverges at the phase transition point.

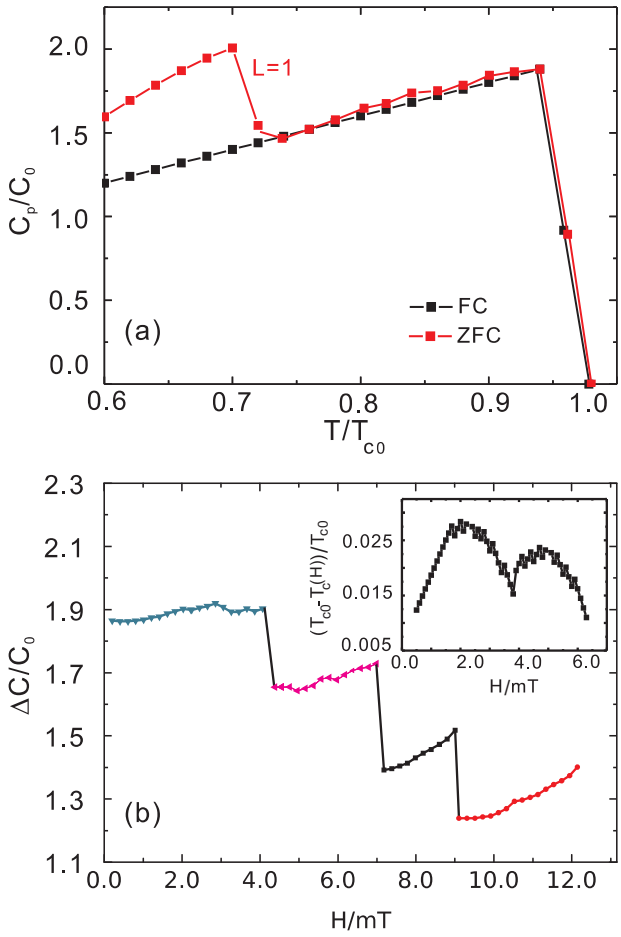

Fig. 5.7 (a) $C_p(T)$ plots under fixed field $H = 0.014H_c(0)$ in field-cooled and zero-field-cooled regimes, for the sample with the same parameters as in Fig. 5.1(b) $\Delta C(H)$ at the S/N phase transition as a function of the applied magnetic field (different vortex states are shown in different colors). Inset shows the oscillation of the critical temperature as a function of applied magnetic field, derived from the observed discontinuity of $C_p(T)$.

We also considered the dependence of the jump in $C_p(T)$ (ΔC) at the S/N transition on the applied magnetic field. In bulk samples, ΔC shows a monotonous decrease with H [26], while in mesoscopic superconducting systems this is not the case. We calculated $C_p(T)$ for a series of magnetic fields H, ranging from 0 to 0.40 H_{c2}, in increasing temperature, and recorded the value of ΔC at each $T = T_c(H)$. As shown in Fig. 5.7(b), the found discontinuity is largest for the Meissner state, and decreases in a step-like manner for the states with higher vorticity. Simultaneously, we record the critical temperature vs. applied field (shown in the inset of Fig. 5.7(b)). This temperature is defined

as the temperature at which the discontinuity of the heat capacity takes place .[3] The critical temperature $T_c(H)$ exhibits a cusp-like, but decreasing, behavior (usually called Little-Parks oscillations, although those were found in transport measurements [158]), the $\Delta C(H)$ exhibits a discontinuity at each cusp of $T_c(H)$ i.e. for each new vortex state. The stability region for each L-state is approximately 0.1 H_{c2}, which is in good agreement with the experimental results of Ref. [87], adding the magnetic flux through the disk of about Φ_0. Note that corresponding theoretical work was done in Ref. [148], where the modulated $\Delta C(H)$ was calculated for disks but no discontinuities were found. This difference most likely can be attributed to the different temperature dependence taken in the Gibbs free energy, but may also result from a full consideration of the nonlinear terms and the inclusion of the 3D demagnetization in our approach, instead of the 2D linearized simulation without screening effects taken in Ref. [148]. We find that before each discontinuity in increasing field, the value of ΔC_p *increases*. This can be understood from the fact that the difference of magnetic susceptibility between the normal state and the different vortex states drops with increase of the vorticity, while for fixed vortex state this difference increases with applied magnetic field.

5.4 HEAT CAPACITY OF MESOSCOPIC SUPERCONDUCTING RINGS

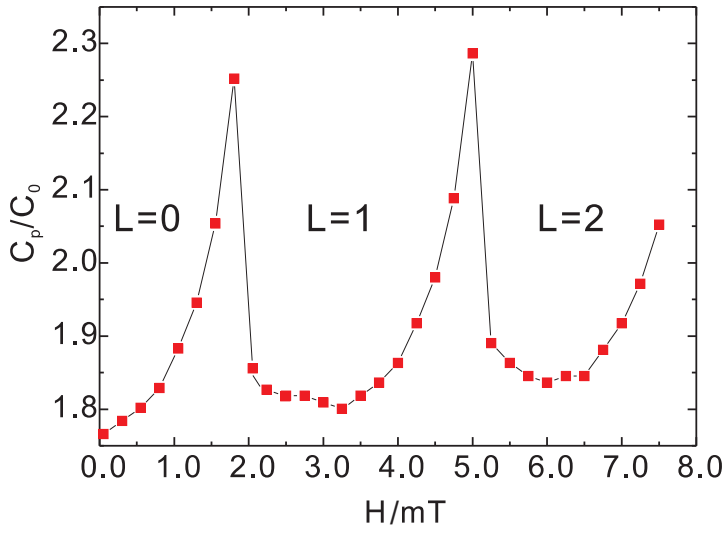

Fig. 5.8 The superconducting part of the heat capacity $C_p(H)$ of the sample at temperature $T = 0.80T_{c0}$ as a function of the magnetic field H perpendicular to the plane of the rings. For the magnetic field in the range 0 to 6 mT, we plot the heat capacity for the $L = 0,\ 1,\ 2$ states.

[3]The bulk-like linear dependence of the transition temperature on the critical field H_{c2} ,$T_{c,b} \approx [1 - H_{c2}(T)/H_{c2}(0)]T_{c0}$ is subtracted from the actual result, in order to highlight the modulation of the critical temperature by the applied magnetic field.

In this section, we apply our numerical approach to study the behavior of the heat capacity of superconducting rings, both in the regimes of constant temperature and of constant magnetic field. The geometric parameters of the studied rings are: the outer and inner diameters are $D = 1100$ nm and $D_0 = 748$ nm, respectively (thus of width $w = 176$ nm), and thickness $d = 30$ nm. For the coherence length $\xi(0)$ and penetration depth $\lambda(0)$, we take 182 nm and 70 nm respectively [88]. Being thin, these superconducting rings can be considered as a two-dimensional system, as all relevant quantities are distributed homogeneously across the sample in the z-direction. To accommodate this in the theoretical formalism, we use the effective Ginzburg-Landau parameter $\kappa = \kappa^2\xi/d$ in Eq. (5.3). The unit of the heat capacity in the calculations remains C_0, and in the present case equals 1.92 pJ/K (for an array of $N = 2.47 \times 10^6$ rings, see Ref. [88]).

First, we perform calculations for the heat capacity when varying the magnetic field, in the range from 0 mT to 6 mT, at fixed temperature $T = 0.8T_{c0}$. The energy of the vortex state in a ring decreases and then increases with magnetic field due to the switching of the current from Meissner to vortex like at the energy minimum. Here, the heat capacity $C_p(H)$ shows corresponding oscillatory behavior, as shown in Fig. 5.8. In the considered field range, the system was stabilized in states $L = 0$, $L = 1$ and $L = 2$, in increasing magnetic field. The found period of oscillations is c.a. 3 mT, which is in conformity with the oscillation period of $\Delta H = 3.17$ mT measured in the experiment of Bourgeois *et al.* [88] In our theoretical simulations, the observed period of H corresponds to a flux of one flux quantum Φ_0 through the circular area of diameter $D_{eff} = 937$ nm [116, 159], thus larger than the inner diameter of the rings. Note that in Fig. 5.8 the superconducting heat capacity is *minimal* in the absence of magnetic field - it ascends for increasing applied magnetic field, contrary to the experimental observation. This discrepancy between our calculation and the experiment comes from the theoretical definition of the heat capacity C_p which relates only to the superconducting condensate while C_{total} was used in the experiment.

The magnetic field dependence of the critical temperature T_c of the S/N transition is a known signature in mesoscopic superconducting rings [26], which is the Little-Parks effect, are usually studied in transport measurements. In Fig. 5.9 we show that the jump $\Delta C(H)$ in the heat capacity at the S/N transition is yet another "fingerprint" of the same effect. The inset of Fig. 5.9 shows the S/N phase boundary $T_c(H)$ that we obtain by performing scans similar to those shown in Fig. 5.7, for the magnetic field in the range 0 to 10 mT (and corresponding flux of 0 to $5\Phi_0$). The obtained period of oscillations matches roughly an added flux quantum through the ring, and the decaying behavior of the critical temperature $T_c(H)$ (shown in the inset of Fig. 5.9) agrees well with both the experimental data from Ref. [87] and the theoretical work from Ref. [154]. Obtained $\Delta C(H)$ oscillations exhibit decreasing amplitude with H, and their period is in agreement with experiment.

Based on the understanding of the specific heat behavior of the superconducting disk in the previous section, we now take rings of two different widths, to discuss the two different contributions to the heat capacity. The outer diameters of the rings are $D = 1100$ nm, thickness $d = 30$ nm, while the inner diameters are $D_0 = 600$ nm and 400 nm respectively. In Figs. 5.10 and 5.11, the heat capacity C_p as well as its two components C_Ψ and C_J are plotted as function of the applied magnetic field, (where $H_{c2}(0) = 11.9$ mT). One significant difference of the heat capacity of the ring sample and the disk ones is the

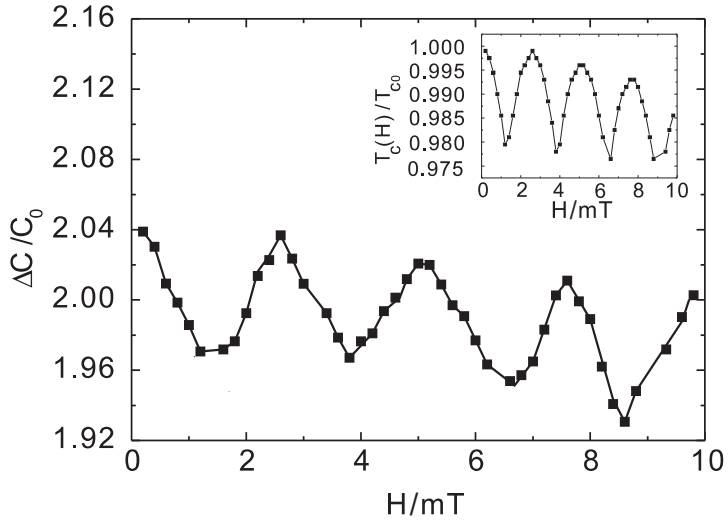

Fig. 5.9 The heat capacity jump at the S/N boundary as a function of the applied magnetic field. The inset shows typical Little-Parks oscillations of the critical temperature $T_c(H)$.

different curvature of the C_Ψ curve. From Figs. 5.3 and 5.4, one can see those curves bending up with field, especially for higher vorticity states, and only the low vorticity states like $L = 0$ and $L = 1$ are an exception where $C_\Psi(H)$ is flat. Here, the C_Ψ curves bend down in the case of rings. The reason for this behavior is the penetration of the magnetic field entirely through the sample. Namely, there is no region inside the ring, where the Cooper-pair density is kept unvaried during the increase of the applied magnetic field and such region exists in the center of the disk when in the Meissner state. However, once vortices enter inside the sample, the distribution of the Cooper-pair density becomes similar in the disk and ring samples, and the tendency of bending down becomes weaker (see Fig. 5.10(a)), and can even flatten (Fig. 5.11).

The second difference between the heat capacity of disks and loops is found for e.g. the $L = 1$ vortex state. Due to the narrow width of the ring, the magnetic field must be screened in order to prevent penetration into the sample from the inner surface, which results in Meissner currents that are maximal at the inner edge - opposite to the case of a disk, where the maximum of screening currents is always found at the outer edge. With increasing magnetic field, upon penetration of field inside the superconducting material, the current changes sign and the maximum of the current shifts to the outer edge of the ring, as is the case in disks. Thus the amplitude of the superconducting current exhibits two (displaced) maxima as a function of magnetic field, instead of just one in the case of the superconducting disk. Since heat capacity directly depends on the current profile and its temperature dependence, the specific heat as a function of magnetic field first decreases and then increases, instead of the monotonous increase found for the disk geometry. Comparing Figs. 5.10 and 5.11, one can also find different portion of C_J contributing to the total heat capacity, $0.04C_0$ of $L = 0$ and $L = 1$ for $w = 250$ nm sample and $0.1C_0$ of $L = 1$ for $w = 350$ nm sample. Smaller w also results in a smaller period of $C_p(H)$ oscillations due to easier fluxion quantization in a larger hole. The

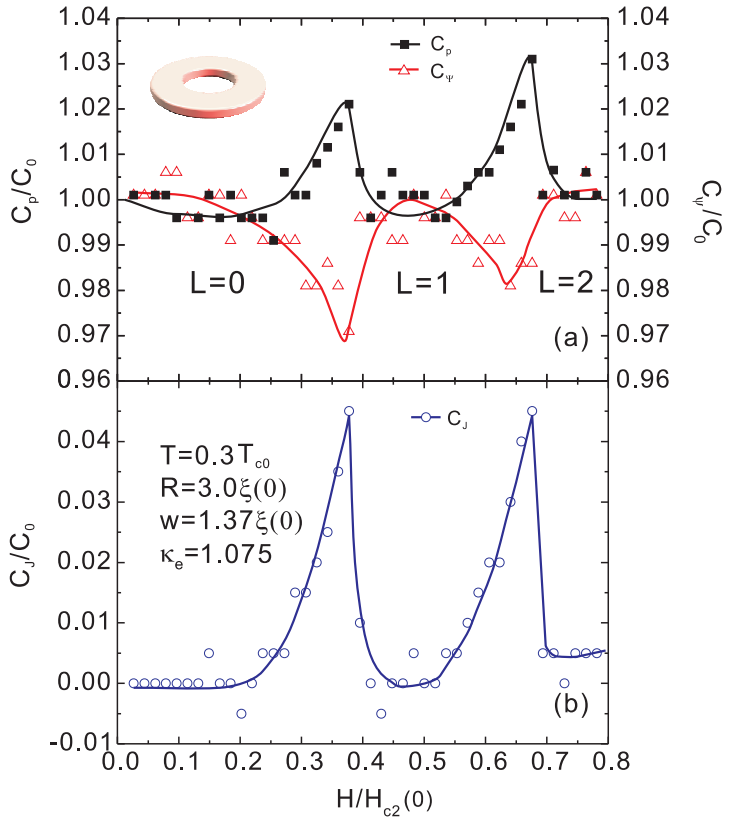

Fig. 5.10 The superconducting part of the heat capacity $C_p(H)$, the contribution from the order parameter $C_\Psi(H)$ (a) and from the superconducting current $C_J(H)$ (b), of the ring with width $w = 250$ nm, at temperature $T = 0.30T_{c0}$, as a function of the magnetic field H. We plot the heat capacity for the $L = 0,\ 1,\ 2$ states.

behavior found for $w = 350$nm is already "disk" like, where the C_J from the $L = 1$ state is much higher than that of the $L = 0$ state.

5.5 HEAT CAPACITY OF A MESOSCOPIC SUPERCONDUCTING CYLINDER

Based on the understanding of the heat capacity in two-dimensional systems, we can conclude that the heat capacity is strongly dependent on the vortex configuration, supercurrent distribution and even the geometry of the sample. Therefore, we explore the potential application of calorimetry to find out the "intrinsic" properties of the superconducting sample. This becomes even more important in the case of three-dimensional superconducting systems, where calorimetry measurements can give an direct insight into the vortex distribution [125], without destroying the sample or the superconducting

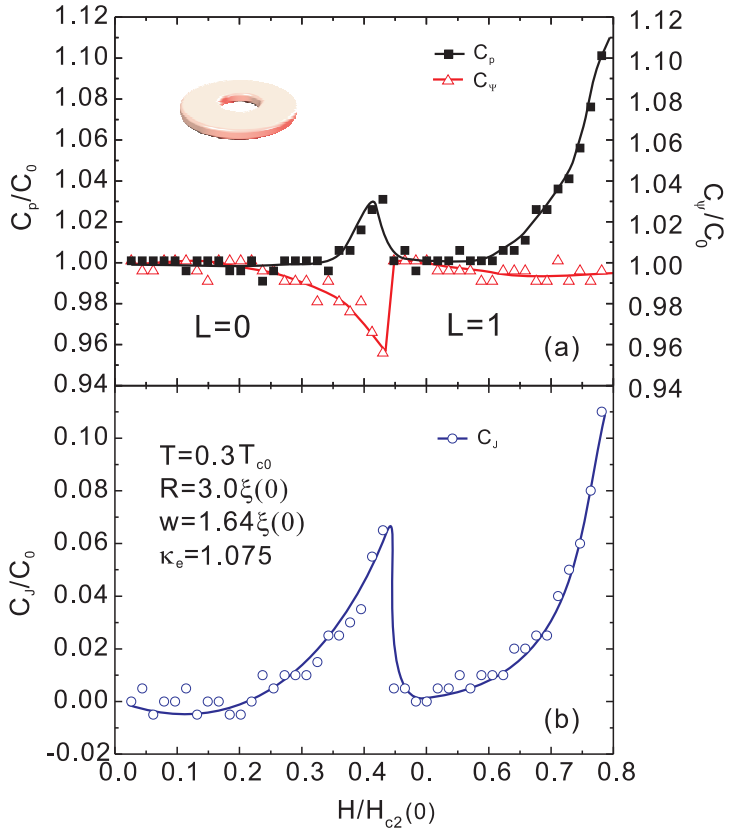

Fig. 5.11 The same as Fig. 5.10, but now for a ring with width $w = 350$ nm, and for the $L = 0,\ 1$ states. (a) The superconducting part of the heat capacity $C_p(H)$ and the contribution from the order parameter variation $C_\Psi(H)$. (b) The kinetic contribution to heat capacity $C_J(H)$.

state itself, and for arbitrary direction of applied magnetic field. To illustrate this, we apply our numerical "experiment" to a 3D mesoscopic cylinder.

The sample is a cylinder with radius $R = 8\xi(0)$, height $h = 16\xi(0)$, and the Ginzburg-Landau parameter $\kappa = 0.7$. We studied the behavior of the heat capacity in the cases where the magnetic field is applied in three different directions: (1) $\theta = 0^o$, along the axial direction; (2) $\theta = 45^o$, along the diagonal direction and (3) $\theta = 90^o$, parallel to the basal surface. Magnetization curves are calculated using an imaginary Hall bar placed above the sample, at a distance $0.5\xi(0)$ and with size $16 \times 16\xi(0)^2$. In Fig. 5.12, the calculated heat capacity and the magnetization curves are plotted for the case (1), as a function of the applied magnetic field. The heat capacity shows several jumps, which indicate different vortex states inside the sample just as in the 2D case. The magnetization curves show corresponding discontinuities, as expected.

In the case of tilted magnetic field ($\theta = 45^o$), the heat capacity shows a profoundly different behavior from what we observed in the previous sections. Because of the coincident direction of applied field with the diagonal of the cylinder, it is energetically

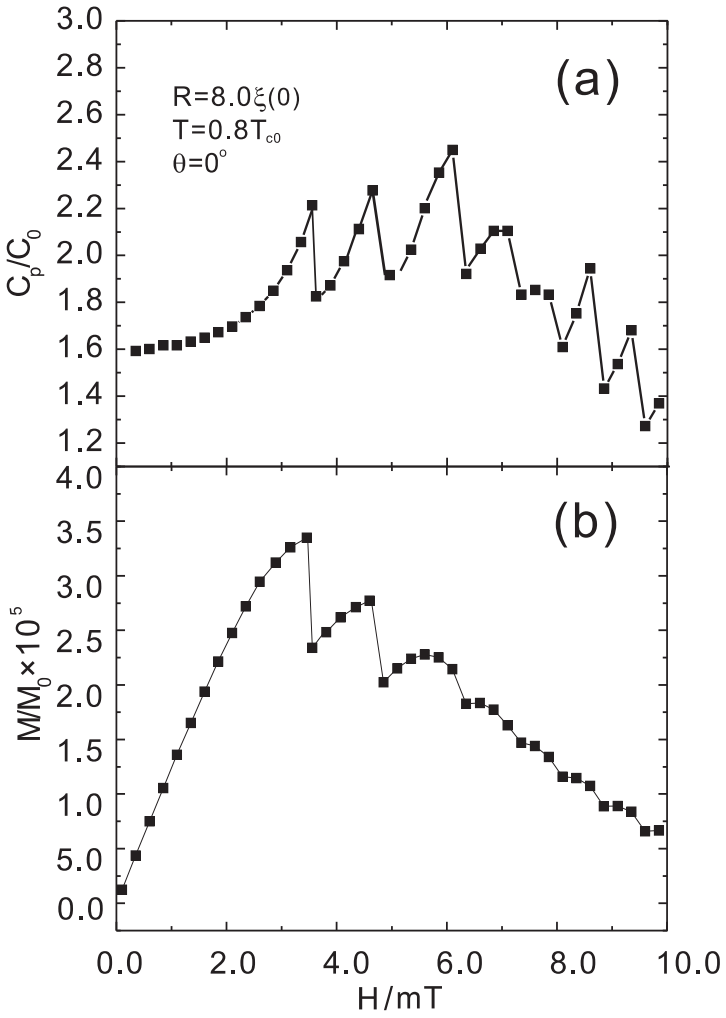

Fig. 5.12 The superconducting contribution to the heat capacity $C_p(H)$ of the sample at temperature $T = 0.80T_{c0}$ as a function of the magnetic field H in the axial direction ($\theta = 0^o$) of the 3-dimensional cylinder (a). The corresponding magnetization of the sample is shown as a function of H (b).

unfavorable for the states of odd vorticity to form inside the sample. Therefore, in the process of sweeping up the applied magnetic field, the states of $L = 1$ (Fig. 5.13, point A), $L = 3$ (Fig. 5.13, point C) and $L = 5$ have very short stability regions. What is reflected on the heat capacity is that the states of those particular vortices are of "low" thermal stability, thus, the heat capacity of these states is much higher than that of the energetically favorable states, with even number of vortices distributed symmetrically parallel to the diagonal of the cylinder (see Fig. 5.13). Note also the behavior of the heat capacity of the $L = 2$ state. Due to the weak stability of the $L = 1$ state, the $L = 2$ state appears at relatively low field, with two vortex branches located at both corners

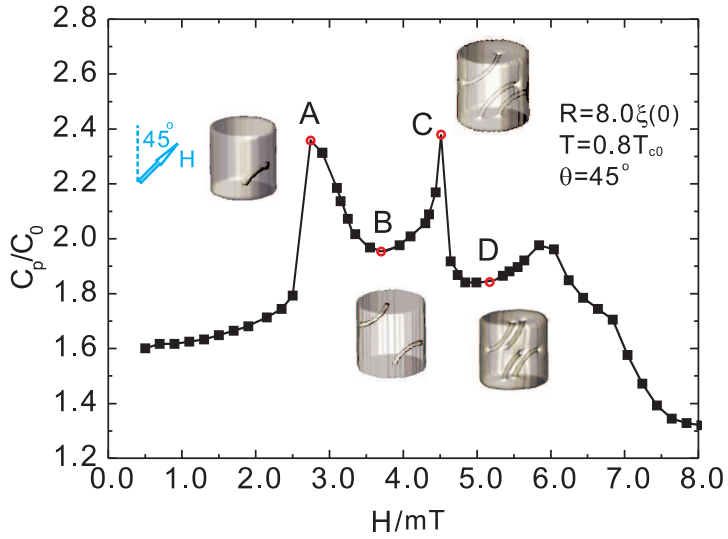

Fig. 5.13 The heat capacity as a function of the applied field H, where the field is applied under an angle $\theta = 45^o$ with respect to the axis of the cylinder. Insets show the 3D-isoplots of the Cooper-pair density ($|\psi|^2 = 0.05$), for different vortex states, corresponding to the H values indicated by open circles.

away from the diagonal line of the sample, which results in a large heat capacity. With increase of the field, both vortices are pushed closer to the diagonal center line, where the system reaches the lowest energy (point B in Fig. 5.13). As the field keeps increasing, vortices keep coming closer to each other, in which case, the repulsion between them becomes stronger and the heat capacity increases again. A similar process is observed also for the $L = 4$ vortex state, which is indicated as point D in Fig. 5.13.

Finally, we discuss the case of $\theta = 90^o$, where the field is applied parallel to the upper surface of the sample. The 3D iso-plots of the Cooper-pair density in Fig. 5.14 show different vortex states for $L = 1, 2, 3$ and 4. First, one can notice the short stability range of the $L = 3$ state, which is caused by the symmetry breaking between the sample and the vortex distribution. Second, during the increase of the magnetic field, the heat capacity curve of the $L = 2$ state shows a short plateau. The vortex configurations are shown before, at, and after this plateau area, as points A, B and C respectively in Fig. 5.14. One can see that before the plateau, two vortices align in plane parallel to the applied magnetic field and the upper surface. With the increase of the magnetic field, these two vortices merge together in the center (which is due to the strong interactions with the boundary at this part), and afterwards the plane of these two vortices becomes tilted at a small angle with respect to the upper surface of the sample. The small plateau in the specific heat curve exactly records these changes of the vortex distribution.

Note therefore that the heat capacity measurement can give a very informative description of the vortex distributions inside the 3D sample, while at the same time, the magnetization curve can be "blind" to all those processes, due to the incompatibility of the direction of the stray magnetic field and the placement of the Hall bar.

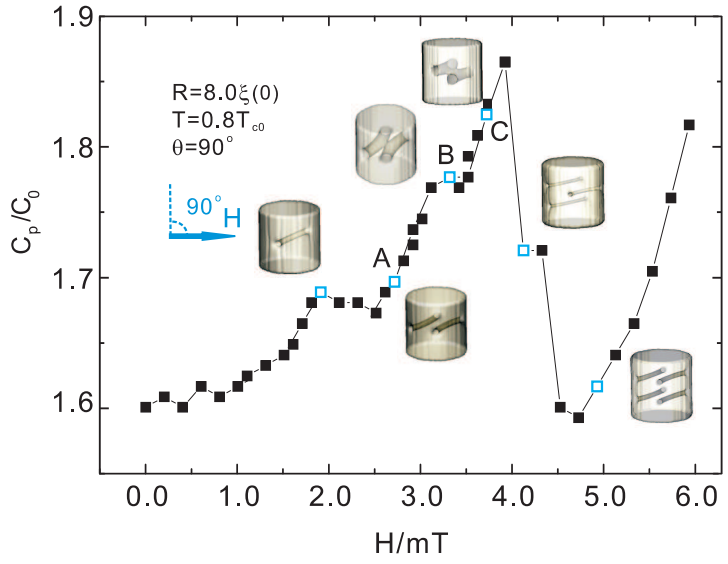

Fig. 5.14 The heat capacity is plotted as a function of the applied field H from $H = 0$ to 6.0 mT, where the field is applied with an angle $\theta = 90^o$ (indicated by the arrow). Insets shows the 3D-isoplots of the Cooper-pair density of the surface with $|\psi|^2 = 0.05$, only for vortex states $L = 1, 2, 3, 4$, which are indicated by blue empty-dots.

5.6 CONCLUSIONS

We developed a numerical approach to calculate the heat capacity within the Ginzburg-Landau formalism for an arbitrary shape of a mesoscopic superconductor. In the present work we focused on disks and rings motivated by recent calorimetric experiments. We studied the heat capacity dependence on magnetic field and temperature, and we proved that different flux (vortex) distribution inside the sample will produce pronounced features in the measured specific heat, different from what is known for bulk superconductors. The heat capacity exhibits large discontinuities at each phase transition, with phases being either different vortex states, or the superconducting and normal phase, in type-I as well as type-II samples. We quantitatively matched the jumps in heat capacity to changes in magnetic susceptibility, following the conjecture of de Gennes. In summary, we show that the thermodynamic properties of a mesoscopic superconductor can be manipulated by the geometry of the system, but also that the S/N phase boundary and other phase transitions can be monitored by calorimetry. Our method is generally applicable to samples of arbitrary 3D geometry, and for magnetic field applied in any direction. We demonstrated this in the case of a mesoscopic cylinder, and showed how subtle 3D changes of the vortex structure leave distinct signatures in the heat capacity. Finally, we also show the use of calorimetry for studies of vortex matter in cases when conventional magnetometry is "blind".

Publications. The results presented in this chapter were published as:

- Ben Xu, M. V. Milošević and F. M. Peeters, *Calorimetric properties of mesoscopic superconducting disks, rings and cylinders*, Phys. Rev. B **81**, 064501 (2010)

6

Quasi-particle excitations in vortex states in mesoscopic superconductors

6.1 INTRODUCTION

In previous chapters we discussed the vortex behavior in a mesoscopic sample in an applied magnetic field and the influence of vortices on the magnetic and thermodynamic properties of the superconducting system. However, these properties are also affected by the intrinsic quasi-particle (QP) distribution in superconductors, which is beyond the theoretical analysis in the phenomenological Ginzburg-Landau theory.

The QP excitations inside a vortex line were first discussed by Caroli and de Gennes [76], by solving the linearized BdG equations. This was done for an extreme type-II superconductor with GL parameter $\kappa \gg 1$ and the field H much smaller than the upper critical field H_{c2}, so that the distance d between vortex lines is much larger than ξ. Then low-lying bound states were found for an individual vortex line, with a fraction of $(\xi/d)^2$ (d is the modulation length of the superfuluid velocity $\mathbf{v}_s(r)$) of the entire volume.

The alternative to a straightforward (but less costly) numerical solution of the BdG-eigenvalue problem is the numerical solution of the Eilenberger equations, provided the fundamental condition of quasi-classical theory, $\mathrm{k}_F\xi \gg 1$, is valid. Using the quasiclassical approach of Eilenberger, it is comparatively easy to determine the low-lying bound states energy of localized vortex core fermions (attached to a single vortex line) by integrating the quasiclassical propagator with respect to the impact parameter ε, which is equivalent to the summation over (exact) eigenenergies of the bound states obtained from solving the BdG-eigenvalue problem (see Ref. [160]). This work not only for the s-wave superconductors, but also for materials where the Cooper pairs display an unconventional symmetry, for example, for cuprates with d_{x2-y2}-symmetry, and for superfluid ^{3}He-B [161], a prominent system with unconventional p-wave pairing symmetry, where the method can be extended to the 4×4-Eilenberger propagator for triplet pairing.

The core structure and low-energy spectrum of isolated vortex lines in the Eilenberger formalism were firstly calculated analytically by Kramer and Pesch [162], for temperature $T \ll T_c$. Afterwards, Klein [163] and Thuneberg [164] solved the equations numerically to describe the vortex lattice in type-II superconductors with or without pinning. The magnetic properties were also studied and fitted the experimental data well. Two kinds of elementary excitations of an isolated vortex were found: bound states which are confined to the vortex core, and unbound states which become BCS QPs far from the core.

For the intermediate flux-line distance, in the vicinity of the lower critical field H_{c1}, vortex excitations are modified by (small) flux-line interactions. Essentially two things happen [165]: first, the sharp lines of the LDOS from an isolated vortex at low energy split into a double-peak structure of finite width. This width is still much smaller than the distance between vortices, so the line-shaped structure of the excitations is preserved. The second modification brought about by the finite flux-line distance is an increased extension of the wave functions in radial direction. If the wave function is nonzero at the boundary of the Wigner Seitz cell, the former bound state of the isolated vortex has changed into a tunneling state. The latter represents a single-particle excitation which extends over the whole flux line lattices. Tunneling states of QPs in a periodic vortex lattice have however been predicted by Canel. He showed that these excitations should behave like Bloch electrons in a magnetic field, without evaluating their wave functions explicitly.

Besides the line splitting and broadening of the single-particle excitations at low energy which was discussed earlier, one notices there is a significant reduction of the scattering states at $E/\Delta_{BCS} \geq 1$. These two effects are related to each other by the sum rule $\int_0^\infty dE[N(E,k,r)-1] = 0$, which requires a reduction of the high-energy states as a consequence of the increased weight at low energies. For an isolated flux-line, scattering states appear for $E/\Delta_{BCS} > 1$ with a divergent behavior of the density of states at the band edge $E = \Delta_{BCS}$. The reduction of states brought about by the vortex interaction takes place in such a way that part of the spectrum near $E = \Delta_{BCS}$ is eliminated and consecutively the band edge is shifted to higher energies and smeared out.

For small flux-line distance, the line-shaped structure of the density of states no longer exists. The region of non-vanishing density of states N extends over most of the space, while the double peak structure discussed is still visible.

Due to demanding numerics, most of the research works on QP of vortex states in superconductors were limited either on the infinite sample with periodic boundary conditions [165, 166, 167], or to the very small region close to the vortex core [168, 169, 170]. In this chapter, the QP excitation is studied for the first time in a mesoscopic superconductor. Further, we discuss the contribution of such excitations to the phase transition between giant and multi-vortex states. The chapter is organized as follows. In Sec. 6.2, several different methods solving Eilenberger equations are introduced and compared; Sec. 6.3 shows the QP's behavior for different vortex states, where the distribution of the LDOS is shown for different materials(s-wave, d-wave and $NbSe_2$). The distribution of LDOS is shown for the case of mesoscopic superconductors in Sec. 6.4. Sec. 6.5 is devoted to the giant-to-multi vortex transition, and the connection between the heat capacity and the LDOS in a mesoscopic sample. Results are summarized in Sec. 6.6.

6.2 THEORY AND FORMALISM

6.2.1 The explosion method

The most straightforward way to solve the Eilenberger equations is the so-called explosion method [171]. Eq. (1.102) has three nontrivial independent solutions. The first is the physical solution $\hat{g}_0$, which is bounded, the other two are unphysical solutions $\hat{g}_+$ and $\hat{g}_-$. The solutions $\hat{g}_\pm$ increase exponentially (on a length scale ξ) in the directions $\pm\mathbf{k}$ respectively and decrease in the opposite directions. Even when we uses the physical solution as an initial value, the unphysical solutions always mix and become dominant during the process of the numerical integration of Eq. (1.102) along a long path in the direction of $\pm\mathbf{k}$. However, the commutation of the two unphysical solutions, leads to

$$[\hat{g}_+, \hat{g}_-] = const \cdot \hat{g}_0. \tag{6.1}$$

In the explosion method, the equation are first integrated from $\mathrm{r}_\parallel \mp r_A$ to $\mathrm{r}_\parallel$, where r_A is large so that an explosion (the integral value goes beyond the upper limit) takes place. Then the physical solution is obtained from the commutator of the two unphysical solutions. In this method, we can obtain the solution for arbitrary $\mathbf{k}$ directions. Using the explosion method, a sixfold star shape of the LDOS, which originates from the triangular

vortex lattice, was found numerically in Ref. [171]. For $E \sim \Delta$, the LDOS distributes mostly around the boundary of the Wigner-Seitz cell of the vortex lattice, with a weak distribution around the vortex core region. As a result the vortex core is detected as a sixfold symmetric object in the STM images.

6.2.2 The Riccati equations

Eilenberger equation is usually written as

$$-i\hbar \mathbf{v}_F \cdot \nabla \hat{g}(\mathbf{r}, i\tilde{\varepsilon}_n) = \left[\begin{bmatrix} i\tilde{\varepsilon}_n & -\Delta(\mathbf{r}) \\ \Delta^\dagger(\mathbf{r}) & -i\tilde{\varepsilon}_n \end{bmatrix}, \hat{g}(\mathbf{r}, i\tilde{\varepsilon}_n) \right], \tag{6.2}$$

where $i\tilde{\varepsilon}_n(\mathbf{r}) = i\varepsilon_n(\mathbf{r}) + \mathbf{v}_F \cdot \frac{e}{c}\mathbf{A}(\mathbf{r})$, and $\hat{g} = \begin{pmatrix} ig & f \\ -f^\dagger & -ig \end{pmatrix}$ satisfies normalization $\hat{g}(\mathbf{r}, i\tilde{\varepsilon}_n)\hat{g}(\mathbf{r}, i\tilde{\varepsilon}_n) = -\pi^2 \hat{1}$. Eq. (6.2) is further parameterized by

$$\begin{aligned} f &= \frac{2a}{1+ab}, \\ f^\dagger &= \frac{2b}{1+ab}, \\ g &= \frac{1-ab}{1+ab}. \end{aligned}$$

Functions a and b now satisfy the independent nonlinear Ricatti equations [166]:

$$i\hbar \mathbf{v}_F \cdot \frac{\partial}{\partial r} a(r) + [i\tilde{\varepsilon}_n(\mathbf{r}) + \Delta^\dagger(r)a(r)]a(r) - \Delta(r) = 0, \tag{6.3}$$

$$i\hbar \mathbf{v}_F \cdot \frac{\partial}{\partial r} b(r) - [i\tilde{\varepsilon}_n(\mathbf{r}) + \Delta^\dagger(r)b(r)]b(r) + \Delta^\dagger(r) = 0. \tag{6.4}$$

As the next step, the LDOS can be evaluated from

$$N(E, \mathbf{r}) = N_0 \int_0^{2\pi} \frac{d\theta}{2\pi} \rho(\theta) Re\ \mathbf{g}(i\varepsilon_n \to E + i\eta, \mathbf{r}, \theta), \tag{6.5}$$

where $\eta(> 0)$ is a small real constant. To obtain $\mathbf{g}(i\varepsilon_n \to E + i\eta, \mathbf{r}, \theta)$, we solve the Eilenberger equations for $\eta - iE$ instead for the Matsubara frequency ω_n. In order to find the LDOS, the above equations should be solved for a bundle of trajectories with different angle θ, running through the given point $\mathbf{r}$ and energy ε. In our calculation we consider only specular reflection for trajectories encountering the outer boundary of the sample. For numerical calculations, this method to solve the Eilenberger equations may be recommended for its intrinsic stability and speed, and general compliance with requirements for parallel computations.

6.2.3 The Doppler-shift method

If one decomposes the order parameter $\Delta(r)$ into amplitude and phase by $\Delta(r) = |\Delta(r)|e^{i\phi}$, and the gauge-invariant expression for function a(r) as well

$$a(r) = |a(r)|e^{-i\phi}, \tag{6.6}$$

the Riccati equation for a(r) can be written as

$$\hbar \mathbf{v}_F \cdot \frac{\partial}{\partial r}|a(r)| + [2\varepsilon_n(\mathbf{r}) + 2i\mathbf{v}_F \cdot m\mathbf{v}_s(r) + \Delta^\dagger(r)a(r)]a(r) - \Delta(r) = 0, \tag{6.7}$$

where

$$\mathbf{v}_s(r) = \frac{1}{2m}\left(\hbar\nabla\phi(r) - \frac{2e}{c}A(r)\right), \tag{6.8}$$

is nothing but the gauge-invariant superfluid velocity of the supercurrent field distribution. Thus, the solution of the equation can be constructed from the bulk result with a contribution from the Doppler-shift energy. In the Doppler-shift method the gradient term in the Eilenberger equations is neglected, which is not a good approximation close to the vortex cores, due to Doppler-shift energy being large compared to the local gap energy $\Delta(r,\theta)$ [172]. Therefore, in this chapter we still opt to use the full numerical methods, such as Runge-Kutta to solve the Eilenberger equations.

6.3 QUASI-PARTICLE EXCITATIONS FOR SINGLE VORTEX STATE

For a single vortex state, we take the isolated vortex in the absence of any interaction with other vortex lines. We assume the position vector $\mathbf{r}$, and the Fermi velocity ν are orientated within the $\mathbf{u}-\mathbf{v}$ plane, so that $r = r_u\mathbf{u} + r_v\mathbf{v}$, and the phase of the order parameter around the vortex core is [173]

$$e^{i\phi} = (r_u + ir_v)/\sqrt{r_a^2 + r_b^2}. \tag{6.9}$$

In that case, the order parameter of the vortex states for superconductors with s and $d_{x^2-y^2}$ symmetry can be approximated by

$$\begin{aligned}
&s\,\text{wave}, && \Delta(r,\theta) = \Delta(T)tanh\left[\frac{r}{\xi}\right]e^{i\phi},\\
&d\,\text{wave}, && \Delta(r,\theta) = \Delta(T)cos(2\theta)tanh\left[\frac{r}{\xi}\right]e^{i\phi},\\
&\text{NbSe}_2, && \Delta(r,\theta) = \Delta(T)\Big(1 + cos(6\theta)\Big)tanh\left[\frac{r}{\xi}\right]e^{i\phi},
\end{aligned}$$

where θ is the azimuthal angle of the Fermi velocity, and $\xi = 1.01\nu/\Delta(T)$ is determined from a fit to the numerical solution for $\Delta(r,\theta)$ as calculated from weak-coupling Ginzburg-Landau theory. In the case of an isolated vortex line, the cohesive functions a and b are related by the symmetry: $b(x) = -a(-x)e^{-2i\theta}$, which comes from the symmetry of the Green's functions f and g. The LDOS found for a single vortex state in different materials, by integrating the quantity $N(E,\theta,\phi,r)$ with respect to θ, where N(E,r) is normalized with respect to the normal-state values, is shown in Fig. 6.1.

For the single vortex state, the order parameter $\Delta(r)$ is zero inside the vortex core and increases exponentially to the zero-field value Δ_0 over a distance of several coherence lengths from the center of the vortex. This space variation of the pair potential is analogous to a potential well for the QPs, of depth $\Delta(0)$ and radius ξ [170]. QPs with

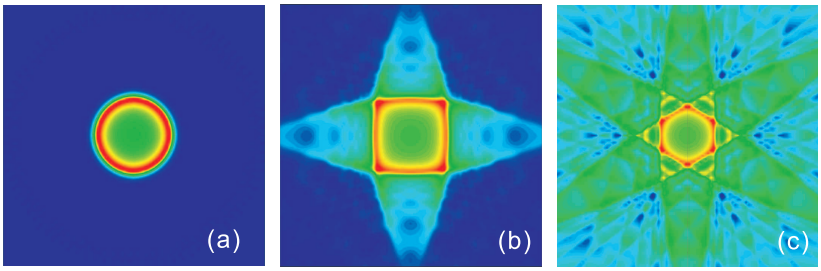

Fig. 6.1 The local density of states (LDOS) distribution for a single vortex state in (a) s-wave superconductor with E/Δ =0.5, (b) d-wave superconductor with E/Δ =0.5 and (c) $NbSe_2$ with E/Δ =0.2.

energies $E < \Delta_0$ will form bound states in the radial direction in this well, with an energy spacing of order $\hbar^2/2m\xi_{\|}^2 \sim \Delta_0^2/E_F \ll \Delta_0$. It is these bound states which yield a nonzero total density of states for energies $E < \Delta_0$, as demonstrated in Refs. [76, 160, 174, 175]. The LDOS, on the other hand, reflects the spatial behavior of the QP wave functions. As shown in figure 6.1, the lowest-energy bound states have a peak in their wave functions closer to the axis of the vortex (just as the low-angular-momentum states of the hydrogen atom are peaked closer to the origin). Therefore, a STM measurement of the local density of states at the vortex core would find an enhancement at small bias since the low-energy bound states have a much greater probability of being close to the center of the vortex. Farther from the center of the vortex the bound-state wave functions have diminished weight, and the local density of states will be dominated by the high-energy scattering states. Thus, sufficiently far from the center of the vortex the local density of states will assume its zero-field BCS form. This is precisely the behavior observed in the experiment.

In summary, the following results were found: LDOS follows the symmetry of the vortex lines and is invariant under simultaneous rotations of **r** and **k**. The bound state of the QPs can be considered as a consequence of Andreev reflection at the order-parameter potential well. Following a QP path passing through the vortex core, the LDOS has a single maximum at $x = 0$ and vanishes for $x = \pm\infty$ [165]. The distance between the vortex axis and the inner barrier of the bound state increase monotonically with energy E. For $E = 0$ the excitation of the bound state shrinks to a line in the vortex center.

6.4 QUASI-PARTICLE EXCITATIONS FOR VORTEX STATE IN MESOSCOPIC SAMPLE

6.4.1 Zero-energy excitation for different winding numbers

In Fig. 6.2 and Fig. 6.3, we plot the calculated LDOS distribution for different Giant and Multi vortex states. One easily observes the presence of the so-called zero mode, i.e., a peak around zero energy at the vortex core for odd vorticity L, and its absence for even L. This low-bias peak and the zero modes discussed above are general characteristics of

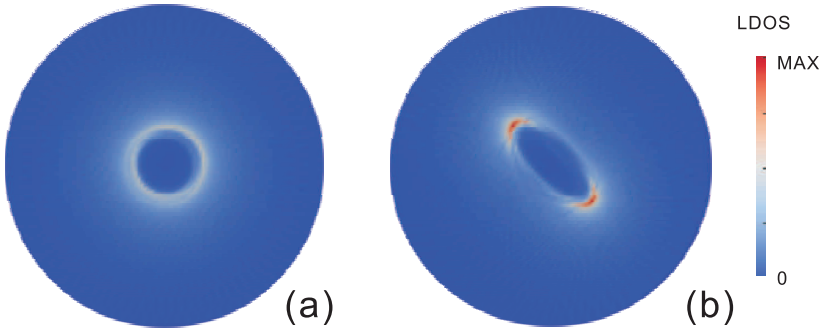

Fig. 6.2 The distribution of the LDOS of the L=2 vortex state in mesoscopic sample of size $R = 4.0\xi(0)$ and $\kappa = 10$, for (a) Giant-vortex state and (b) Multi-vortex state, for $E = 0.01\Delta_0$.

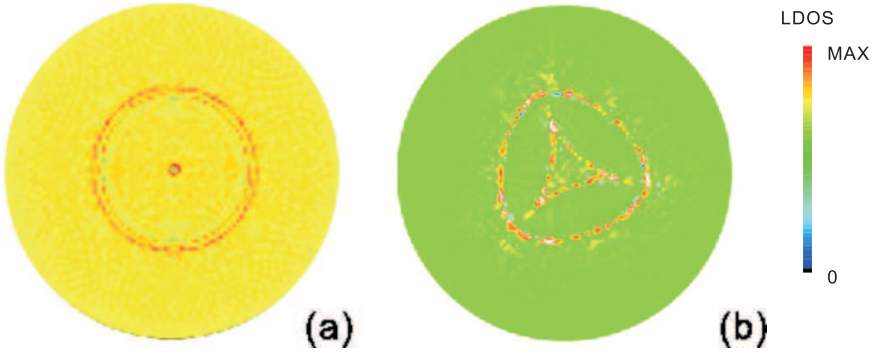

Fig. 6.3 The distribution of the LDOS of the L=3 vortex state in mesoscopic sample of size $R = 4.0\xi(0)$ and $\kappa = 10$, for (a) Giant-vortex state and (b) Multi-vortex state, $E = 0.01\Delta_0$.

the LDOS associated with the winding number of the order parameter. This phenomenon can be explained by the number of anomalous energy branches crossing the Fermi level. According to Ref. [169] the number should be equal to the winding number L, thus, one of the energy branches that crosses the Fermi level at zero impact parameter for odd vorticity is responsible for the peak of the LDOS at the vortex center. The absence of this zero-energy peak for even vorticity is due to the absence of the Fermi-level-crossing energy branch. A more detailed explanation can be found in Ref. [168].

With decreasing applied magnetic field, one can observe that as soon as the constituent single quanta vortices in a giant vortex start to separate, the maxima of LDOS around a giant vortex of vorticity L split into L peaks. In addition to these L peaks at the center of the individual vortices, there still exist strong bounded rings around the whole vortex molecule, which give the wrinkle pattern of the zero energy DOS around the whole molecule, although the size of our mesoscopic sample is quite small (several coherence lengths). This specific peak structure in the DOS distribution around a small-size vortex molecule is a direct consequence of the quantum-mechanical interference of Andreev states.

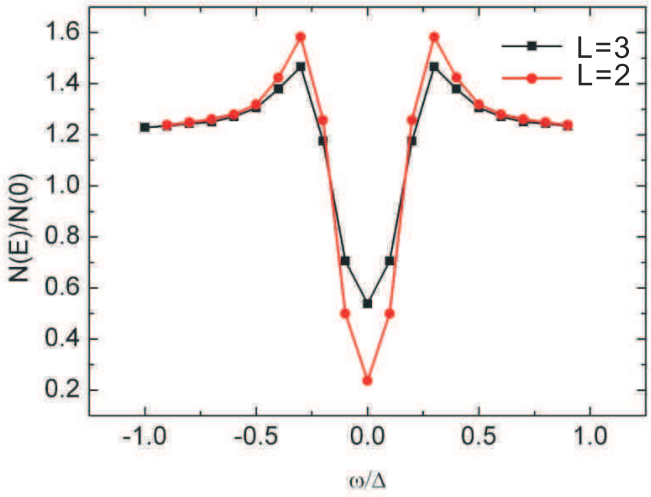

Fig. 6.4 The energy dependence of the total density of states N(E) is calculated at $T/T_c = 0.01$ for two vorticities, showing a characteristic V-shaped structure near the Fermi level $E = 0$.

For the unbounded states of the QP (for $E > \Delta_0$), one finds oscillations of the density of states with respect to the distance away from the center of the vortex. These oscillations were first present numerically in the paper of Tanaka [169], and reflect the "standing waves" arising from the interference of QP states, due to the fact that the system size is comparable to the coherence length ξ. In such a system, the order parameter experiences a recovery from zero in the vortex center to a constant value outside the vortex, and drops back to zero at the boundaries of the sample. An electron-like QP is reflected back as a hole and vice versa, and the Tomasch effect results from the interference between the electron-like and hole-like states in the superconducting region. As a result, Friedel-like oscillations around the bulk value are found near the surfaces.

6.4.2 V-shaped LDOS of the vortex state

The energy dependence of the total density of states N(E) is calculated by summing over all the LDOS in the studied area. The V shape of the density of states was first evaluated by Nakai *et al.* in Refs. [167] and [176]. It implies that the zero-energy peak at the vortex center gives rise to N(E=0), and the finite energy low-lying bound states near the core ultimately gives the $|E|$-dependent term in N(E). The integration of the LDOS is influenced by the circular geometry of the vortex, which is shown in Fig. 6.3. The energy of the shoulders on both sides of zero energy are much lower that in the bulk sample, and far from the value $\omega = \Delta$. This indicates that the superconducting orderparameter is highly surpressed in mesoscopic sample. It is clear that the QP bound states have a characteristic dispersion relation $|E| \sim r$ as a function of the radial coordinate r

from the vortex center, and form ridges extending outwards from the core. Therefore $N(E) = N(E = 0) + 2\pi \int_0^\infty \delta(|E| - \beta r)$rdr per unit length along the field direction. The first term N(E=0) mainly comes from LDOS N(E=0,r) at the vortex core $r = 0$. The second term comes from the QP spectral weight whose spatial trajectory $|E| = \beta r$ is indicated by the ridges for high energy condition. This gives rise to V-shaped total DOS: $N(E) = N(E = 0) + 2\pi|E|/\beta^2$. The V-shape DOS is usually easily smeared by the thermal broadening effect.

Having N(E), the specific heat in the mixed state can be expressed as

$$C(T)/\gamma_n T = \gamma' + \alpha_c \frac{T}{T_c} + O\left[\left(\frac{T}{T_c}\right)^2\right] \tag{6.10}$$

at low T, where $\gamma' = \gamma/\gamma_n = N(E = 0)/N_0$ and $\gamma_n = 2\pi^2 N_0/3$. Nakai *et al.* also confirmed that $\gamma'(B) = \lim_{T\to 0} C/(\gamma_n T)$ shows a B-linear dependence expected for the s-wave pairing state.

6.5 LDOS CONTRIBUTION TO HEAT CAPACITY OF VORTEX STATES

6.5.1 Introduction

One of the most puzzling questions in the area of vortex matter in submicron samples is the distinction between two allotropies of a vortex state - a 'giant' vortex, where all vortices merge into a single singularity, and a multi-vortex, where all vortices can be individually resolved. In type-II superconductors, transitions between the latter two states are of second-order, following the increasing lateral compression by e.g. increasing screening currents in increasing magnetic field [50], or increasing temperature which makes the sample effectively smaller in terms of the superconducting length scales. Even in numerical calculations, it is very difficult to pinpoint the exact value of parameters for the giant-to-multi crossover, as the order parameter is severely suppressed between vortices in close proximity. It is therefore no surprise that imaging experiments could not verify the existence of a giant vortex beyond reasonable doubt [61]. Several years ago, Kanda *et al.* conveyed a clever transport measurement, where the distinction between giant and multi-vortex states was made by symmetry matching between the vortex configuration and the location of several tunnel junctions [98]. Although not always conclusive (e.g. if sample and vortex arrangement match in symmetry), this is the best known method to date for giant-vortex detection.

In this section, we present a universal method for the observation of formation and decay of multi-quanta vortex states. Our theoretical simulations indicate that the experimentally *measured heat capacity* of a mesoscopic superconductor as a function of magnetic field or temperature can unambiguously reveal such transitions. The underlying reason can be traced back to the behavior of the local density of states for QPs, and we demonstrate a direct link between the heat capacity and the sample magnetization. With recent advances in calorimetry [85] and magnetometry [51] of submicron samples, our findings are of immediate relevance to current experimental efforts.

6.5.2 GL description of heat capacity

The Ginzburg-Landau (GL) formalism has been extensively used in the past to gain theoretical insight in the physics of mesoscopic superconductors. The core of the approach is the GL energy functional

$$\mathcal{G} = \int \left[-|\psi|^2 + \frac{1}{2}|\psi|^4 + \frac{1}{2}|(-i\nabla - \mathbf{A})\psi|^2 + \kappa^2(\mathbf{h} - \mathbf{H})^2 \right] dV, \tag{6.11}$$

describing the difference in Gibbs free energy between the superconducting (S) and normal (N) state in units of $\mathcal{G}_0 = H_c^2/8\pi$. Here κ denotes the GL parameter and determines screening of the applied magnetic field $\mathbf{H}$ from the given superconducting material. In Eq. (6.11) all distances are scaled by the coherence length ξ, the vector potential $\mathbf{A}$ by $c\hbar/2e\xi$, the magnetic field $\mathbf{h}$ by $H_{c2} = c\hbar/2e\xi^2 = \kappa\sqrt{2}H_c$, and the order parameter ψ by its equilibrium value in the absence of the magnetic field. The minimization of $\mathcal{G}$ is numerically equivalent to solving two coupled GL equations, and for details of this procedure we refer to previous chapter. Once a stable solution is found, we are able to calculate the specific heat of the superconducting state from the relation $C = -T\partial^2\mathcal{G}/\partial T^2$ [148], as a difference between the total heat capacity and that of the sample in the normal state, in units of $C_0 = H_c^2(0)V/(8\pi T_c)$. We start from the equilibrium states, increase/decrease the temperature of the system by $10^{-4}T_c$, and calculate numerically the second derivative. In what follows, we apply this method to a superconducting disk, a simple geometry already accessible both theoretically [50] and experimentally [61, 98, 85, 51].

Figure 6.5 shows the energy of all the vortex states found in an Aluminum superconducting disk of radius $R = 850$ nm and thickness $d = 100$ nm, at $T = 1.1$ K (we use $\xi(0) = 100$ nm, $\kappa = 1.2$, and $T_c = 1.38$ K [140]). Because of the stronger interaction of the flux quanta with lateral boundaries for increased vorticity, all states in Fig. 6.5 with $L > 5$ are giant vortices. However, for $2 < L \leq 5$ multivortex states can be found at lower magnetic field, which are compressed into a giant-vortex at higher applied field. This is a gradual, second-order transition, and is therefore invisible in the free energy curves [50]. For clarity, we made a distinction between multi- and giant-vortex in Fig. 6.5 by dashed and solid lines respectively. In what follows, we discuss the repercussions of the latter transition on the heat capacity of the sample.

Using attoJoule calorimetry, Ong *et al.* [87] found that the heat capacity of mesoscopic disks is directly linked to the vorticity, exhibiting jumps as a function of the magnetic field - at transitions between vortex states. We argue here that the heat capacity depends not only on the number of vortices in the sample, but also on their configuration. Namely, the susceptibility of the sample to heating is linked to the kinetic energy of the Cooper-pairs in and around the vortex core(s), and the changes in their trajectory upon the multi-to-giant vortex transition. In Fig. 6.6, we show the calculated heat capacity as a function of applied magnetic field for vortex states with vorticity 2 and 3, both exhibiting multi-to-giant vortex transition in Fig. 6.5. For both cases, the general trend of increasing heat capacity with field is interrupted *exactly* at the multi-to-giant vortex transition, where a sharp decrease of heat capacity is found.

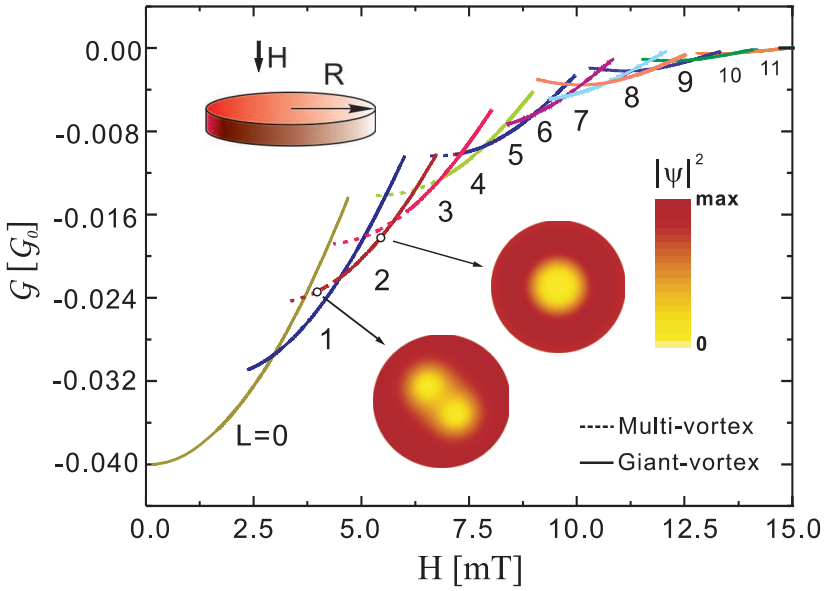

Fig. 6.5 The energy of different vortex states for an *Al* superconducting disk of radius $R = 850$ nm and thickness $d = 100$ nm, at $T = 0.8T_c$, for taken $\xi(0) = 100$ nm and $\kappa = 1.2$. Solid lines indicate giant-vortex states and dashed lines represent multi-vortex states. Insets show the density of the superconducting condensate for a $L = 2$ vortex state in multi and giant form.

6.5.3 The QP's contribution to heat capacity discontinuity of GV-MV transition

In what follows, we show that the cause of the observed change in heat capacity during the merging of vortices is the changing local density of states (LDOS) for QP excitations inside the vortex cores. Actually, already from the early theoretical works (see Ref. [76]), we know that the bound state spectrum inside the vortex is also a function of momentum along the vortex line; as a result, the lowest bound state energy for winding number $L > 1$ is L times larger than that of winding number 1. Therefore, one expects that the low-energy states are pushed toward higher energies during the merging of individual vortices into a giant vortex. To give a quantitative measure of this process, we first obtain the order parameter ψ and vector potential $\mathbf{A}$ of the equilibrium states from the GL calculation, which then serve as inputs for the microscopic Eilenberger equation, as Eq. (6.3), considering only specular reflection for trajectories encountering the outer boundary of the sample.

Here we present the full evolution of the LDOS of QP excitations in a mesoscopic superconducting disk, during the multi-to-giant vortex transition as a function of the magnetic field, where at each step we recalculate the distribution of the superconducting order parameter. In Fig. 6.7, we plot the zero-energy density of states $N(E = 0, T)$ integrated over the sample as a function of the applied magnetic field, for the $L = 3$ vortex configuration. $N(E = 0, T)$ increases with applied magnetic field, as in the case of an isolated vortex [177]. When the giant vortex is assembled from the multi-vortex molecule, the LDOS profile changes from several individual peaks located at each vortex

to a ring-like bound state with/without an enclosed peak for odd/even vorticity (as in Ref. [168]). Bound states are also found near the sample boundary, due to the lowered (non-zero) gap in the presence of strong circular Meissner currents. The representative contour plots of LDOS for $L = 3$ are shown in Fig. 6.7 as insets. As our main observation, we point out a clear drop of $N(E = 0)$ vs. the magnetic field at the multi-to-giant vortex transition (see Fig. 6.5), where the LDOS profile goes through a change of symmetry from three-fold to circular symmetric one. We thus confirm that the evolution of LDOS with magnetic field is directly linked to the specific heat and the thermal conductivity of the sample. To enforce this argument, as explained in Sec. 5.4.2 the LDOS can be expressed as

$$N(E,T)/N_0 = N(E=0,T) + \alpha_E |E|/\Delta_0,$$

with

$$N(E=0,T)/N_0 = \gamma' + \alpha_k T/T_c.$$

Through the relation

$$C(T)/T = (2/T)\int_0^\infty dE[E\ N(E,T)\partial f(E,T)/\partial T],$$

using the Fermi-Dirac distribution function $f(E,T)$, one obtains

$$C(T)/(\gamma_n T) \sim N(E=0,T)/N_0 + \alpha_E |E|/\Delta_0,$$

which unambiguously shows the link between the calculated curves in Figs. 6.7 and 6.8.

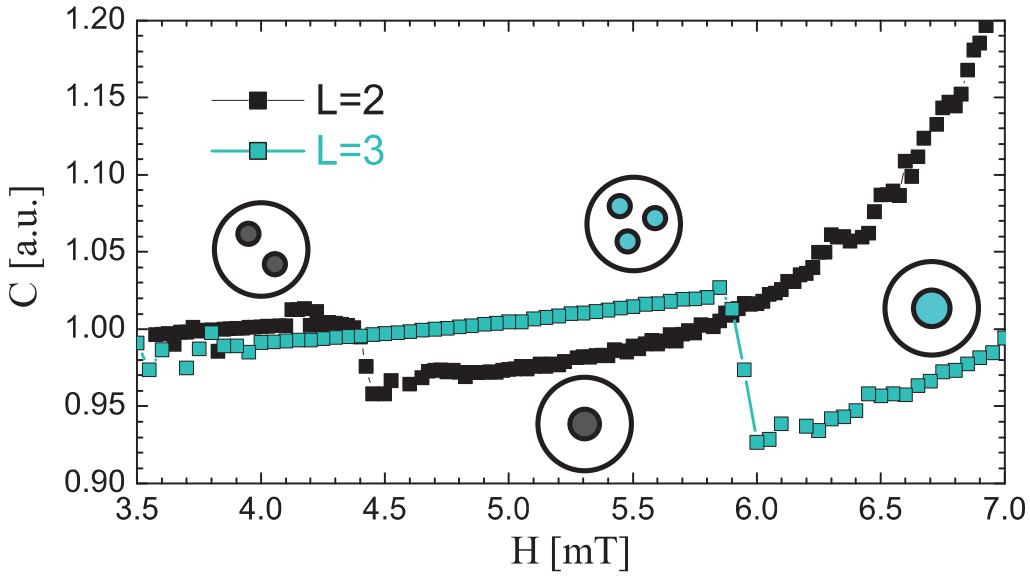

Fig. 6.6 The heat capacity as a function of magnetic field, for states with vorticity 2 and 3 of the sample considered in Fig. 6.5. Insets depict the vortex configuration before and after the multi-to-giant vortex transition.

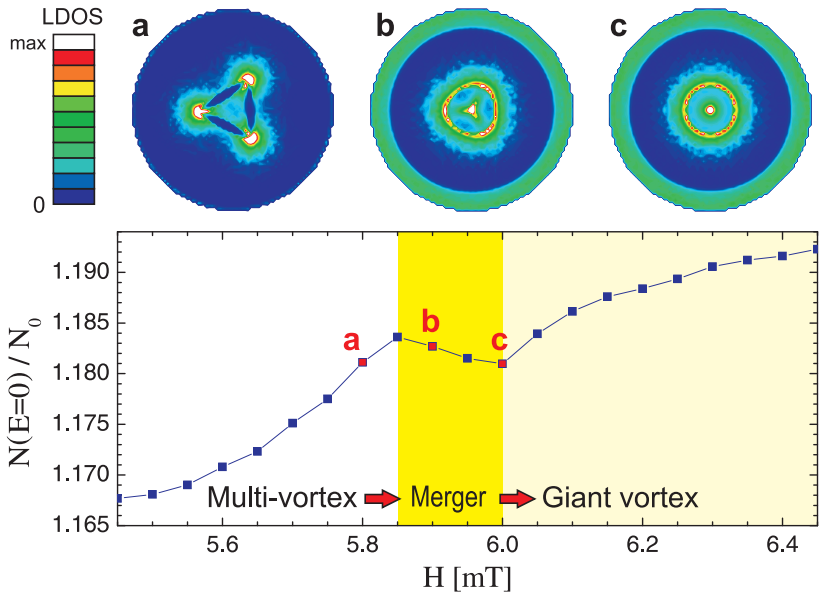

Fig. 6.7 The integrated zero-energy density of states (LDOS) as a function of the magnetic field for L = 3, for a superconducting disk with same parameters as in Fig. 6.5(a-c) are the representative contour plots of LDOS in the disk, at indicated magnetic fields. Interestingly, N (0)[a]≈ N (0)[b]≈N (0)[c].

6.5.4 Correlation between heat capacity and magnetization

The jump of heat capacity between different vortex phases can also be expressed using other thermodynamic arguments. The discontinuity in the specific heat at a phase transition (at field H^*) can be calculated as

$$C_i - C_j = -T\left(\frac{dH^*}{dT}\right)^2\left[\left(\frac{\partial M}{\partial H}\right)_i - \left(\frac{\partial M}{\partial H}\right)_j\right], \tag{6.12}$$

where M denotes sample magnetization. Here we apply above expression to the multi-to-giant vortex transition, where i represents the vortex state of vorticity L just prior, and j represents the L vortex state just after the transition. Knowing the result for heat capacity vs. H at the multi-to-giant vortex transition, we therefore expect to see similar features in the magnetic susceptibility $\chi = \partial M/\partial H$. We calculate the magnetization M as expelled magnetic field from the sample $\mathbf{M} = (\langle \mathbf{h} \rangle - \mathbf{H})/4\pi$, where $\langle \mathbf{h} \rangle$ is the local magnetic field averaged over the sample volume. The results of this calculation are shown in Fig. 6.8. They (i) confirm the link between (independently calculated) sharp changes in heat capacity and χ as a function of the magnetic field, and (ii) show that assembly of a giant vortex in superconductors can be detected even by conventional magnetometry.

The above prediction is of immediate relevance to experiments, since both calorimetry and magnetometry are readily performed on mesoscopic superconductors. Of course, the question of sensitivity and resolution of the measurement is an open one, and we address

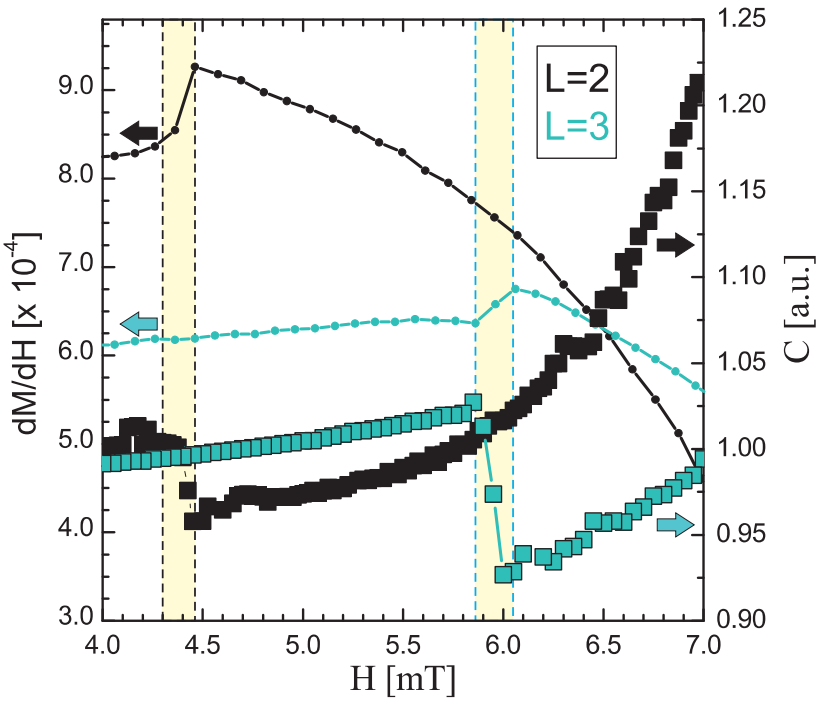

Fig. 6.8 The multi-to-giant vortex transition revealed through the sharp change in magnetic susceptibility as a function of applied magnetic field, showing direct correlations with the heat capacity, for states with vorticity 2 and 3. Shaded areas indicate the observed regions of giant-vortex formation in both quantities.

this issue in Fig. 6.9. First, we determined the multi-to-giant vortex transition field H^* as a function of the size of the *Al* disk. For all considered vorticities ($L = 2 - 4$), H^* was found to increase with the radius of the sample. We then scanned the heat capacity and magnetic susceptibility versus applied field for every size of the sample, and recorded the size of the observed jump between values prior and after H^*. In Fig. 6.9 we show the absolute and relative size of the jump of both magnetic susceptibility (b) and heat capacity (c) at temperature 1.1 K. We found that the susceptibility shows a clearer signal at the multi-to-giant transition for lower vorticity, whereas corresponding discontinuity of heat capacity is more pronounced at higher vorticity. Note however that ΔC and $\Delta\chi$ should be directly proportional, according to Eq. (6.12). They indeed are, when susceptibility is calculated by $\chi = \partial^2\mathcal{G}/\partial H^2$, while we here used the experimental definition of magnetization as the flux expelled from the sample (which is directly measured by Hall magnetometry).

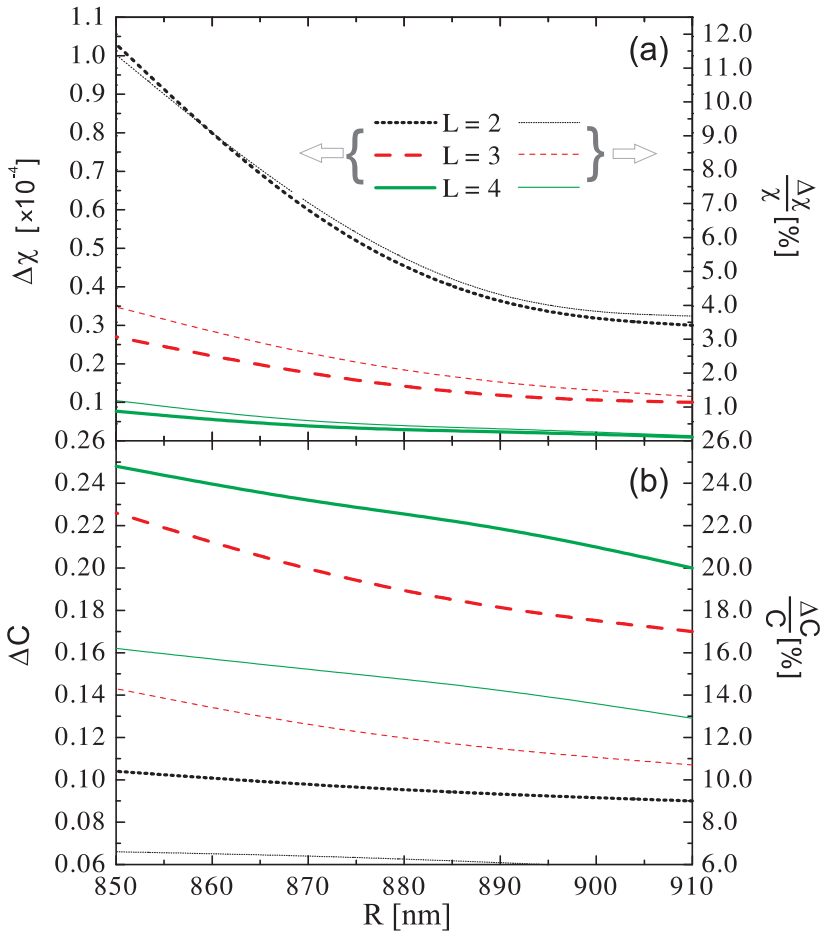

Fig. 6.9 The absolute and relative size of the jump at the multi-to-giant vortex transition, in (a) χ(H) curves, and (b) C(H) curves, for vorticity L=2,3, and 4.

6.6 CONCLUSIONS

In summary, we developed the hybrid method, combining the established GL method and the Eilenberger equations, to investigate the QPs behavior in the mesoscopic superconductors with presence of vortex states. We described the distribution of LDOS around an isolated vortex for different superconducting materials. Furthermore, we depicted the LDOS distribution for giant and multi vortex states in mesoscopic superconductors, and showed the different low-energy excitation behavior of QPs for vortex state with odd/even vorticity. Therefore we built the connection between the heat capacity and the total LDOS distribution in the superconductors. Based on these understandings, we demonstrated that second-order transitions between multi- and giant-vortex states in mesoscopic superconductors can be detected using calorimetry. The local density of states for QPs in and around vortex cores changes when the vortex configuration changes,

which affects the heating properties of the system. The observed sharp change in the heat capacity at the multi-to-giant vortex transition can also be linked to the magnetic susceptibility, enabling the observation of this transition by Hall magnetometry. Our results are therefore of immediate relevance to experimental efforts in the field, and further work is needed to generalize our findings to other systems, such as e.g. Bose-Einstein condensates [178].

Publications. The results presented in this chapter were published as:

- Ben Xu, M. V. Milošević, Shi-Hsin Lin, F. M. Peeters and B. Jankó, *Formation of Multiple-Flux-Quantum Vortices in Mesoscopic Superconductors from simulations of Calorimetric, Magnetic, and Transport Properties*, Phys. Rev. Lett. **107**, 057002 (2011)

Summary

In mesoscopic samples, the vortex structure is strongly dependent on the interaction between vortices and confinements imposed by te sample boundary. The situation is more complicated and vortex phenomenology is greatly enhanced in the case of fully three-dimentional (3D) samples. The aim of this thesis is to investigate theoretically vortex structure as a result of the interplay between the applied magnetic field and 3D sample geometries, hence make predictions on the magnetic, calorimetric and electronic properties of vortex states.

In what follows, we summarize our theoretical findings in the order they are presented in this thesis.

In **chapter 1**, we give a short introduction to some theoretical and experimental aspects of vortex matter in superconductors. The derivations of phenomenological Ginzburg-Landau equations and the microscopic Eilenberger equations are presented. Vortex matter is discussed for bulk samples, two characteristic lengths ξ and λ, and three critical magnetic fields are introduced. In mesoscopic samples, the structure and behavior of the vortex matter is determined by the vortex-vortex, vortex-boundary and vortex-defects interactions. These interactions are briefly discussed and different vortex states are shown for 2D mesoscopic samples. Last, several characterization and imaging methods for vortex matter are discussed, e.g. STS(STM), SQUID, SHPM and calorimetry.

Our study starts from a mesoscopic spherical sample in **chapter 2**. The method used throughout the thesis is to solve the coupled two Ginzburg-Landau equations self-consistently, in the presence of an external magnetic field. From the vortex configurations, we find the vortices bend perpendicular to the surfaces. Inside the sample, the curvature of vortices is influenced by 3D density of shielding currents. The symmetry and three-

dimensionality of the sample strongly influenced vortex penetration field H_p and the stability region of particular vortex states. Ginzburg-Landau parameter κ is another factor determining the vortex configuration. Lower κ disfavors the multi-vortex states, same as in the 2D cases. When $\kappa < 1$, several vortex states are skipped over when system changes from Meissner to normal state with increasing magnetic field. As κ decreases, the skipped vortex states obeyed the following sequence first the $L = 1$ state was missing, then $L = 1$ and 2, then all states from $L = 1$ to $L = n_s - 1$, and finally all the vortex states, which means the system changes directly from the the Meissner to the normal state. The magnetometry measurements are proposed, based on our calculation of the vortex configuration and corresponding magnetic field distribution in 3D cases, where we provide a possibility to distinguish the multi- and giant-vortex states by the specific shape of the measured magnetization curves.

In **chapters 3** and **4**, the spherical superconductors with a cylindrical hole are studied, where confinement is imposed on vortices from both inner and outer boundaries. As a result, profound behavior of the vortices is found. Systematical studies are carried out for samples with different sized perforations in the case of a tilted magnetic field. For axial magnetic field, the entire vortex line can be trapped inside the hole. The trapped vortex effectively increases the Bean-Livingston barrier, which impedes further entry of vortices and elongates the stability region (magnetic field range) of this vortex state. The number of vortices trapped inside the hole increases with the size of the hole, while the vorticity outside the hole but inside the sample decreases. As a result of the competing interactions between the inner and outer surfaces, the vortex configurations with broken-symmetry are found for small hole cases, followed by a narrowed stability region of adjacent vortex states. When the hole becomes larger, the repulsion from the trapped vortices is so strong that a belt of fully suppressed superconductivity(normal belt) is formed instead of vortex state close to the equator of the sample. Moreover, second order multi-vortex entry becomes possible because of the interplay of different forces, which is discussed in detail in **chapter 4**. Contrary to the spherical sample, latter phenomena are not realizable in a cylindrical sample. In the case of the tilted magnetic field, the external magnetic field and the internal cylindrical hole provide two competing guides for the vortex line. The cylindrical hole plays the dominant role when the tilting angle of the field is small, and vice versa. The aforementioned multi-vortex second order transition can be also influenced by the tilting of the field.

The second-order multi-flux-quanta transition between different vortex states is described also in **chapter 4** via saddle-point states between them, where the energy curves are shown for both ground and metastable states. The height of the energy barrier between different vortex states determines whether the transition is of first or second order. This barrier can be influenced by the vortices trapped inside the hole. When the barrier is high enough, the magnetic field can only destroy the superconductivity by multi-vortex entry or by forming an equatorial normal belt. The latter is phenomenologically opposite to the case of surface superconductivity. By changing the ratio between the sizes of the hole and sample, we tune delicately the interactions between inner and outer boundaries and change the phase transitions between successive vortex states from first- to second-order, and from individual to multi-flux-quanta events. We actually tune the competition between the Bean-Livingston barrier and the **geometric barrier**, which is connected to the entrance length of the vortex line in a 3D sample. In the experiment, it is very likely that the phase transition between different vortex states can be stimulated by ther-

mal fluctuations. For this reason, we compared the magnitude of the energy difference between our vortex-vortex and vortex-saddle point states with the thermal energy, and found all energy barriers to be much larger than the thermal one. As a result of the increasing energy barriers, the critical field is also enhanced in a step-like manner as a function of the geometric parameters of the sample.

In **chapter 5** the heat capacity of superconductors is calculated as the second derivative of the Gibbs free energy of the system. Our numerical experiments are first carried out for type-I mesoscopic superconducting disks and rings. When magnetic field was swept from zero up to the critical magnetic field, the calorimetric signal showed the first-order transition for each vortex entry, in a cascade of successive phase transitions. The found vortex states represent the intermediate state of a type-I mesoscopic superconductor. Here we attributed the part of heat capacity change to the depletion of the condensate (C_Ψ) and the superconducting current (C_j). C_j contributes mainly to oscillations of heat capacity in the lower vorticity cases, and C_Ψ contributes most for high vorticity. Field-cooled(FC) and zero-field-cooled(ZFC) simulations are carried out and the critical temperature T_c was found to exhibit cusp-like but decreasing behavior as a function of field. At each of these cusps, the heat capacity difference between superconducting and normal states are shown, for the first time in numerical simulations (and fit the experiments well). The magnitude of these jumps is connected to the magnetic susceptibility. In superconducting rings, the specific heat curve showed periodic oscillation due to vortex entrance. The periodicity agrees well with the one found in the experiment. The specific heat curves for rings are different from the disk ones in two ways. First, the C_Ψ contribution curves down instead of up as a function of field. Second, the heat capacity shows two maxima as a function of the magnetic field instead of one. These differences can be attributed to the different geometric parameters, i.e. the presence of inner and outer boundaries of the sample. In the last part of this chapter, the heat capacity of 3D cylinders is studied, in a tilted magnetic field. The heat capacity measurement gave a very informative description of the vortex distribution inside the 3D sample, while at the same time, the magnetization curve can be "blind" to all those processes, due to the possible incompatibility of the distribution of the stray magnetic field and the placement of the Hall bar.

In previous chapters we discussed the magnetic and thermodynamic properties of the superconducting system connected to the vortex behavior in a mesoscopic sample. In **chapter 6**, those features are connected to the intrinsic quasi-particle (QP) distribution in superconductors, investigated by a hybrid method of mesoscopic GL and microscopic Eilenberger equations. The values of order parameter and vector potential are firstly calculated for the equilibrium state at a given magnetic field. Afterwards, they are used as inputs for the Eilenberger solver. The bound state of the QPs around a single vortex was shown by LDOS plots in the vortex plane. In the lowest-energy case, the bound states shrink to a peak of the wave function close to the vortex core, which is named the zero-energy bias peak. These low-energy lying states exhibit different behavior for vortex states (giant-vortex state) of different vorticity (even or odd). Moreover, the LDOS distribution shows rich wrinkle patterns in the case of multi-vortex state, which is a direct consequence of the quantum-mechanical interference of Andreev states. The value of total DOS is calculated by integration over the sample, and shows a V-shaped structure as a function of the energy near the Fermi level. By integrating it with the Fermi-Dirac distribution, one can get the linear dependence of the specific heat on total

DOS for the mixed state. Using this relationship, the rest of the **chapter 6** is dedicated to found discontinuity of the heat capacity in the phase change between giant- and multi-vortex states. Moreover, the observed sharp change in heat capacity at multi-to-giant vortex transition was also linked to the magnetic susceptibility, which enables the observation of this fascinating transition by Hall magnetometry as well.

Samenvatting

In mesoscopische samples is de vortexstructuur sterk afhankelijk van de interactie tussen de vortices en de opsluitingspotentiaal opgelegd door de samplerand. De situatie is ingewikkelder en de vortexfenomenologie is veel rijker in het geval van volledig driedimensionale (3D) samples. Het doel van deze thesis is om theoretisch de vortexstructuur als gevolg van de wisselwerking tussen het aangelegde magneetveld en 3D samplegeometrieen te onderzoeken, en dus voorspellingen te maken aangaande de magnetische, calorimetrische en elektronische eigenschappen van vortextoestanden.

In wat volgt, vatten we onze theoretische bevindingen samen in de volgorde zoals gepresenteerd in deze thesis.

In **hoofdstuk 1**, geven we een korte inleiding tot enkele theoretische en experimentele aspecten van vortexmaterie in supergeleiders. De afleidingen van de fenomenologische Ginzburg-Landau vergelijkingen en de microsopische Eilenberger vergelijkingen worden gepresenteerd. Vortex materie wordt besproken voor bulksamples, en twee karakteristieke lengtes ξ en λ, en drie kritische magneetvelden worden geintroduceerd. In mesoscopische samples wordt de structuur en het gedrag van vortexmaterie bepaald door de vortex-vortex, vortex-rand en vortex-defect interacties. Deze interacties worden kort besproken en verschillende vortextoestanden worden getoond voor 2D-mesoscopische samples. Tot slot worden verschillende karakterisering en beeldvormingsmethodes besproken, zoals STS(STM), SQUID, SHPM en calorimetrie.

Onze studie begint vanaf een mesoscopisch sferisch sample in **hoofdstuk 2**. De methode die we doorheen deze thesis gebruiken is het zelf-consistent oplossen van de gekoppelde Ginzburg-Landau vergelijkingen in de aanwezigheid van een extern magneetveld. Vanuit de vortexconfiguraties vinden we dat de vortices loodrecht op de oppervlakken afbuigen. Binnenin het sample wordt de kromming van vortices beinvloed door de 3D-

dichtheid van afschermingsstromen. De symmetrie en driedimensionaliteit van het sample oefent een sterke invloed uit op het vortexpenetratieveld H_p en het stabiliteitsgebied van specifieke vortextoestanden. De Ginzburg-Landau κ is een andere factor die de vortex-configuratie bepaalt. Een lagere κ leidt eerder niet tot multivortextoestanden, net zoals in 2D-gevallen. Als $\kappa < 1$ worden verschillende vortextoestanden overgeslagen wanneer het systeem overgaat van de Meissnertoestand naar de normale toestand onder toenemend magnetisch veld. Als κ daalt, volgen de overgeslagen vortextoestanden deze volgorde: eerst ontbreekt de $L = 1$ toestand, dan $L = 1$ en 2, dan alle toestanden van $L = 1$ tot $L = n_s - 1$, en uiteindelijk alle vortextoestanden. Magnetometriemetingen worden voorgesteld gebaseerd op onze berekeningen van de vortexconfiguratie en de overeenkomstige verdeling van het magneetveld in 3D-gevallen, waar we de mogelijkheid voorzien om multi- en giantvortextoestanden te onderscheiden door middel van de specifieke vorm van de gemeten magnetisatiecurves.

In **hoofdstukken 3** en **4**, worden sferische supergeleiders waarin een cilindrisch gat is aangebracht onderzocht. Vortices zijn beperkt door de binnenste en buitenste randen van de supergeleider. Hierdoor wordt een meer complex gedrag van de vortices gerealiseerd. Een systematische onderzoek is uitgevoerd voor zulke supergeleiders in de aanwezigheid van een magnetisch veld, hierbij werden zowel de diameter van de holte als de hoek waaronder het magnetisch veld staat gevariëerd. Voor een axiaal aangebracht magnetisch veld, kan een volledige vortex-lijn in de holte gevangen worden. Deze gevangen vortex vergroot dan de Bean-Livingston barrière, waardoor de introductie van andere vortices bemoeilijkt wordt, en het stabiliteitsbereik van deze vortex-toestand vergroot (d.w.z., de maximale grootte van het magnetisch veld waarvoor geen extra vortex geïntroduceerd wordt, wordt verhoogd). Als de diameter van de holte vergroot wordt dan vermeerdert het aantal vortices dat gevangen wordt in de holte, terwijl de vorticiteit van de supergeleider rondom de holte afneemt. Door het fenomeen van competitie van interacties tussen de sferische (buitenste) rand en de (binnenste) rand van de holte, worden vortex-configuraties met gebroken symmetrie gevonden voor kleinere diameters, vergroten van het magnetisch veld veroorzaakt dan opeenvolgende vortex-toestanden met een klein stabiliteitsbereik. Wanneer de holte verder vergroot, wordt de afstotingskracht van de gevangen vortices uiteindelijk zo groot dat een band van niet-supergeleidende toestand (de normale band) zich vormt langsheen de evenaar. Verder ontstaat de mogelijkheid voor tweede-orde multi-vortex introductie in de supergeleider omwille van een samenspel van verschillende krachten, dit wordt verder toegelicht in **hoofdstuk 4**. In tegenstelling tot in sferische supergeleiders wordt dit fenomeen niet waargenomen in cilindrische supergeleiders. In het geval dat het magnetish veld onder een hoek staat, wordt de vortex-lijn zowel in de richting van het magnetisch veld getrokken, als aangetrokken tot de holte, zodanig dat er een competitie tussen deze twee krachten heerst. De holte zal de belangrijkste rol spelen als de hoek met het magneetveld klein is, en andersom zal het magneetveld het meest doorwegen voor grote hoeken. De voorgenoemde tweede-orde multi-vortex-toestand wordt ook beïnvloed door de hoek waaronder het magnetisch veld staat.

De tweede-orde multi-flux-quanta transitie tussen verschillende vortex toestanden wordt beschreven in **hoofdstuk 4**, alsook de zadelpunt toestanden tussen hen, waarbij energiecurves voor zowel de grond- als meta-stabiele toestanden worden gegeven. De hoogte van een energie-barrière bepaalt of een transitie van eerste- of tweede orde is. Deze hoogte kan mede beïnvloed worden door vortices die gevangen zitten in de holte. Voor voldoende

hoge barrières kan het magnetisch veld de supergeleiding enkel teniet doen doordat er multi-vortices geïntroduceerd worden, of er een normale band rond de evenaar gevormd wordt. Dit laatste is het tegenovergestelde van wat er bij oppervlakte-supergeleiding gebeurt. Door het varïeren van de verhouding tussen de grootte van de diameter van de holte, en van de sferische supergeleider zelf, kunnen we de interacties tussen de binnenste en buitenste randen controleren en kunnen de fase-transities tussen opeenvolgende vortex-toestanden overgaan van eerste- naar tweede orde en van individuele naar multi-flux-quanta gebeurtenissen. In feite passen we hierdoor de competitie tussen de Bean-Livingston barrière en de **geometrische barrière** aan, de laatste heeft betrekking op de lengte van de vortex-lijn die in een 3D supergeleider geïntroduceerd wordt. In een experiment is het zeer waarschijnlijk dat de fase-transities tussen verschillende vortex-toestanden door termische fluctuacties gestimuleerd worden. Omwille van dit feit, hebben we de grootte van de vortex-vortex en vortex-zadelpunt toestanden vergeleken met de thermische energie. In alle gevallen bleken de energie-barrières groter dan de thermische energie fluctuaties. Het verhogen van de energie-barrières, door het veranderen van de geometrische parameters van de supergeleider, resulteert eveneens in een stapsgewijze verhoging van het kritisch magneetveld.

In **hoofdstuk 5** wordt de warmtecapaciteit van supergeleiders berekend als de tweede afgeleide van de Gibbs vrije energie van het systeem. Onze numerische experimenten worden eerst uitgevoerd voor type-I mesoscopische supergeleidende schijven en ringen. Wanneer het magnetische veld werd gevarieerd van nul tot de critische waarde, toonde het calorimetrische signaal de eerste-orde-transitie voor elke vortexingave, in een cascade van opeenvolgende fasetransities. De gevonden vortextoestanden vertegenwoordigen de intermediaire toestand van een type-I mesoscopische supergeleider. Hier hebben we de verandering in warmtecapaciteit toegeschreven aan de uitputting van het condensaat (C_Ψ) en de supergeleidende stroom (C_J). C_J draagt voornamelijk bij tot de oscillaties van de warmtecapaciteit in het lage-vorticiteit-geval en C_Ψ draagt vooral bij tot de hoge vorticiteit. Veldgekoelde (FC) en zero-veldgekoelde (ZFC) simulaties zijn uitgevoerd en de critische temperatuur T_c bleek afnemend "cusp-like" gedrag te vertonen in functie van het veld. Voor het eerst wordt in een numerisch simulatie ter hoogte van deze cusps het verschil in warmtecapaciteit tussen supergeleider en normale toestand getoond. De grootte van deze sprongen is gerelateerd aan de magnetische suscpetibiliteit. In supergeleidende ringen toont de specifieke warmtecurve een periodische oscillatie ten gevolge van de vortexingang. De periodiciteit komt goed overeen met die uit het experiment. De specifieke warmtecurves voor ringen zijn verschillend van die van schijven in twee manieren. Ten eerste buigt de C_Ψ-bijdrage naar omlaag in plaats van omhoog in functie van het veld. Ten tweede toont de warmte capaciteit twee maxima als functie van het magnetische veld in plaats van slechts een. Deze verschillen kunnen toegewezen worden aan verschillende geometrische parameters, zoals de aanwezigheid van binnen- en buitengrenzen van het samples. In het laatste deel van dit hoofdstuk wordt de warmtecapaciteit van 3D-cylinders bestudeerd in een gekanteld magnetisch veld. De warmtecapaciteitmeting gaf een zeer informatieve beschrijving van de vortexverdeling binnen de processen, dankzij de mogelijke onverenigbaarheid van de distributie van het stray magnetische veld en de plaatsing van de Hall bar.

In de vorige hoofdstukken bediscussieerden we de magnetische en thermodynamische eigenschappen van het supergeleidende systeem, verbonden met het vortexgedrag in een mesoscopisch sample. In **hoofdstuk 6**, zijn deze features verbonden aan de intrinsieke

quasi-deeltjeverdeling (QP) in supergeleiders en worden onderzocht via een hybridemethode van mesoscopisch GL en microscopische Eilenberger vergelijkingen. De waarden van ordeparameter en vectorpotentiaal worden eerst berekend voor de evenwichtstoestand bij een gegeven magnetisch veld. Daarna worden ze gebruikt als invoer voor de Eilenberger oplosser. De gebonden toestand van de QP's rond een enkele vortex werd weergegeven door LDOS plots in het vortexvlak. In het laagste-energie-geval, krimpen de gebonden toestanden tot een piek van de golffunctie dicht bij de kern van de vortex, zero-energie bias piek genaamd. Deze lage-energie-toestanden vertonen verschillend gedrag voor de vortex toestanden met verschillende vorticiteit (even of oneven). Bovendien toont de LDOS-verdeling rimpelpatronen in het geval van multi-vortextoestand, wat een direct gevolg is van de kwantummechanische interferentie van Andreev toestanden. De totale waarde van DOS is berekend via integratie over het gehele sample en toont een V-structuur in functie van de energie nabij het Ferminiveau. Door te integreren met de Fermi-Diracverdeling kan men de lineaire afhankelijkheid van de specifieke warmte op de totale DOS voor de gemixte toestand bekomen. Gebruik makend van dit verband is de rest van **hoofdstuk 6** toegewijd aan de discontinuiteit van de warmtecapaciteit in de faseverandering tussen giant- en multi-vortex-toestanden. Bovendien was de scherpe overgang in warmtecapaciteit bij een multi-naar-giant-vortex transitie gelinkt aan de magnetische susceptibiliteit, wat tevens de observatie via Hall magnetometrie van deze fascinerende overgang toelaat.

Outlook

Further work beyond this thesis may include:

- The case of more elaborate 3D shapes, such as ones readily achievable by electrochemical - pyramids, cubes, octahedron - where more complicated interactions of sample boundaries and 3D vortex lines take place.
- Considering the 3D samples of anisotropic or layered materials, such as high-T_c ones, using the Lawrence-Doniach and anisotropic Ginzburg-Landau models. There the spatial anisotropy brings additional comprehensive effect into play.
- Considering the 3D samples of multiband superconductivity, such as MgB_2 and recently discovered pnictrides. There the presence of two(-or more) different bands adds to the complexity of vortex matter.
- Calculate the heat capacity in above cases. Particularly in the case of pnictides, interesting behavior of heat capacity is found as a function of temperature [179], or as a function of magnetic field, which maybe reproduced in the GL calculation.
- Solving the Eilenberger equation self-consistently with magnetic field, especially for the samples smaller than coherence length ξ, where Ginzburg-Landau formalism is no longer a good description of the system.

Bibliography

1. Gelsi. Steve. *Market Watch. Retrieved*, 2008.
2. LHC Design Report. *Vol. I The LHC main ring*, CERN-2004-003.
3. *IEEE Transactions on Applied Superconductivity*, 19:2142, 2009.
4. Yu. Makhlin, G. Schön, and A. Shnirman. *Rev. Mod. Phys.*, 73:357–400, 2001.
5. D. Vion, A. Aassime, A. Cottet, P. Joyez, H. Pothier, C. Urbina, D. Esteve, and M. H. Devoret. *Science*, 296:886, 2002.
6. I. Chiorescu, Y. Nakamura, C. J. P. M. Harmans, and J. E. Mooij. *Science*, 299:1869, 2003.
7. Y. Nakamura, Yu. A. Pashkin, and J. S. Tsai. *Nature*, 398:786, 1999.
8. H. Kamerlingh Onnes. *Leiden Comm.*, 120:122b, 1911.
9. W. Meissner and R. Ochsenfeld. *Naturwiss.*, 21:787, 1933.
10. F. London and H. London. *Proc. Roy. Soc. A1*, 49:71, 1935.
11. V. L. Ginzburg and L. D. Landau. *Zh. Eksp. Teor. Fiz.*, 20:1064, 1950.
12. J. Bardeen, L. N. Cooper, and J. R. Schrieffer. *Phys. Rev.*, 108:1175, 1957.
13. L. P. Gor'kov. *Sov. Phys. JETP*, 9:1364, 1959.
14. A. A. Abrikosov. *Sov. Phys. JETP*, 5:1175, 1957.
15. B. D. Josephson. *Phys. Lett*, 1:251–253, 1962.

16. J. G. Bednorz and K. A. Mueller. *Z. Phys. B*, 64:189, 1986.

17. K. M. Wu et al. *Phys. Rev. Lett*, 58:908, 1987.

18. H. Maeda, Y. Tanaka, M. Fukutumi, and T. Asano. *Jpn. J. Appl. Phys.*, 27:L209, 1988.

19. Z. Z. Sheng and A. M. Hermann. *Nature*, 332:138, 1988.

20. L. Gao. et al. *Phys. Rev. B*, 50:4260, 1994.

21. C. W. Chu et al. *Nature*, 365:323, 1993.

22. US Department of Energy report (2006). *Basic Research Needs for Superconductivity.*

23. Y. Kamihara, T. Watanabe, M. Hirano, and H. Hosono. *JACS*, 3296:130, 2008.

24. H. Takahashi et al. *Nature*, 453:376, 2008.

25. G. Wu et al. *Journal of Physics: Condensed Matter*, 21:142203, 2009.

26. M. Tinkham. *Introduction to superconductivity (McGraw Hill New York).*

27. P. G. de Gennes and New York) *Superconductivity of Metals and Alloys* (Benjamin. 1966.

28. L. D. Landau and E. M. Lifshitz. *Statistical Physics*, page 3rd ed.

29. A. A. Shanenko, M. V. Milošević, F. M. Peeters, and A. V. Vagov. *Phys. Rev. Lett.*, 106:047005, 2011.

30. H. B. Nielsen and P. Olesen. *Nucl. Phys. B.*, 160:380, 1979.

31. G. Stenuit, S. Michotte, J. Govaerts, and L. Piraux. *Supercond. Sci. Technol.*, 18:174, 2005.

32. P. S. Deo, V. A. Schweigert, F. M. Peeters, and A. K. Geim. *Phys. Rev. Lett.*, 79:4653, 1997.

33. J. Romijn, T. M. Klapwijk, M. J. Renne, and J. E. Mooij. *Phys. Rev. B*, 26:3648, 1982.

34. R. Kato, Y. Enomoto, and S. Maekawa. *Phys. Rev. B*, 47:8016, 1993.

35. V. A. Schweigert, F. M. Peeters, and P. S. Deo. *Phys. Rev. Lett.*, 81:2783, 1998.

36. *Lecture notes on Applications of Parallel Computers, University of California, Berkeley.*

37. N. N. Bogoliubov. *Soviet Phys. JETP*, 7:41, 1958.

38. J. G. Valatin. *Nuovo cimento*, 7:843, 1958.

39. W. A. Little and R. D. Parks. *Phys. Rev. Lett.*, 9:9, 1962.

40. F. Loder, A. P. Kampf, T. Kopp, J. Mannhart, C. W. Schneider, and Y. S. Barash. *Nature Physics*, 4:112, 2008.

41. Byers N. and Yang C. N. *Phys. Rev. Lett.*, 7:46, 1961.

42. Onsager. L. *Phys. Rev. Lett.*, 7:50, 1961.

43. Brenig. W. *Phys. Rev. Lett.*, 7:337, 1961.

44. A. A. Abrikosov. *Sov. Phys. JETP*, 5:1175, 1957.

45. U. Essmann and H. Träuble. *Phys. Lett. A*, 24:526, 1967.

46. A. A. Abrikosov. *Sov. Phys. JETP*, 5:1174, 1957.

47. D. Saint-James and P. G. de Gennes. *Phys. Lett.*, 7:306, 1963.

48. G. Stenuit, S. Michotte, J. Govaerts, and L. Piraux. *Supercond. Sci. Technol.*, 18:174, 2005.

49. A. C. Rose-Innes and E. H. Rhoderick. *Introduction to Superconductivity (Pergamon Press)*.

50. V. A. Schweigert, F.M. Peeters, and P.S. Deo. *Phys. Rev. Lett.*, 81:2783, 1998.

51. A. K. Geim, I. V. Grigorieva, S. V. Dubonos, J. G. S. Lok, J. C. Maan, A. E. Filippov, and F. M. Peeters. *Nature (London)*, 390:259, 1997.

52. C. P. Bean and J.D. Livingston. *Phys. Rev. Lett.*, 12:14, 1964.

53. V. V. Schmidt. *The Physics of Superconductors: Introduction to Fundamentals and Applications*. Springer-Verlag Berlin Heidelberg, 1997.

54. G. S. Mkrtchyan and V. V. Schmidt. *Sov. Phys. JETP*, 34:195, 1972.

55. L. F. Chibotaru, A. Ceulemans, V. Bruyndoncx, and V. V. Moshchalkov. *Nature (London)*, 408:833, 2000.

56. R. Geurts, M. V. Milošević, and F. M. Peeters. *Phys. Rev. Lett.*, 97:137002, 2006.

57. F. M. Peeters, V. A. Schweigert, B. J. Baelus, and P. S. Deo. *Physica C*, 332:255, 2000.

58. I. V. Grigorieva, W. Escoffier, J. Richardson, L. Y. Vinnikov, S. Dubonos, and V. Oboznov. *Phys. Rev. Lett.*, 96:077005, 2006.

59. B. J. Baelus and F. M. Peeters. *Phys. Rev. B*, 65:104515, 2002.

60. J. T. Devreese V. R. Misko, V. M. Fomin and V. V. Moshchalkov. *Physica C*, 369:361, 2002.

61. V. R. Misko, V. M. Fomin, J. T. Devreese, and V. V. Moshchalkov. *Phys. Rev. Lett.*, 90:147003, 2002.

62. L. F. Chibotaru, A. Ceulemans, V. Bruyndoncx, and V. V. Moshchalkov. *Phys. Rev. Lett.*, 86:1323, 2001.

63. V. P. Galaiko. *Zh. Eksp. Sov. Phys. JETP*, 23:878, 1966.

64. E. H. Brandt. *Phys. Rev. B*, 58:6506, 1998.

65. E. Akkermans, D. M. Gangardt, and K. Mallick. *Phys. Rev. B*, 63:064523, 2001.

66. L. R. E. Cabral, B. J. Baelus, and F. M. Peeters. *Phys. Rev. B*, 70:144523, 2004.

67. A. L. Fetter. *Phys. Rev. B*, 22:1200, 1980.

68. A. I. Buzdin and J. P. Brison. *Phys. Lett. A*, 196:267, 1994.

69. S. Pedersen, G. R. Kofod, J. C. Hollingbery, C. B. Sorensen, and P. E. Lindelof. *Phys. Rev. B*, 64:104522, 2001.

70. J. R. Kirtley, C. C. Tsuei, V. G. Kogan, J. R. Clem, H. Raffy, and Z. Z. Li. *Phys. Rev. B*, 68:214505, 2003.

71. D. Y. Vodolazov, F. M. Peeters, S. V. Dubonos, and A. K. Geim. *Phys. Rev. B*, 67:054506, 2003.

72. G. R. Berdiyorov, L. R. E. Cabral, and F. M. Peeters. *Journal of Mathematical Physics*, 46:095105, 2005.

73. P. Singha Deo, V. A. Schweigert, and F. M. Peeters. *Phys. Rev. B.*, 59:6039, 1999.

74. H. F. Hess, R. B. Robinson, R. C. Dynes, J. M. Valles, and J. V. Waszczak. *Phys. Rev. Lett.*, 62:214, 1989.

75. Joel D. Shore, Ming Huang, Alan T. Dorsey, and James P. Sethna. *Phys. Rev. Lett.*, 62:3089, 1989.

76. C. Caroli, P. G. de Gennes, and J. Matricon. *Phys. Lett.*, 9:307, 1964.

77. H. F. Hess, R. B. Robinson, and J. V. Waszczak. *Phys. Rev. Lett.*, 64:2711, 1990.

78. François Gygi and Michael Schluter. *Phys. Rev. Lett.*, 65:1820, 1990.

79. Ch. Renner, B. Revaz, J.-Y. Genoud, K. Kadowaki, and Ø. Fischer. *Phys. Rev. Lett.*, 80:149, 1998.

80. A. Oral, S. J. Bending, R. G. Humphreys, and M. Henini. *Supercond. Sci. Technol.*, 10:17, 1997.

81. J. S. Neal, M. V. Milošević, S. J. Bending, A. Potenza, L. San Emeterio, and C. H. Marrows. *Phys. Rev. Lett.*, 99:127001, 2007.

82. S. J. Bending. *Advances in Physics*, 48:449, 1999.

83. M. J. Van Bael, J. Bekaert, K. Temst, L. Van Look, V. V. Moshchalkov, Y. Bruynseraede, G. D. Howells, A. N. Grigorenko, S. J. Bending, and G. Borghs. Local observation of field polarity dependent flux pinning by magnetic dipoles. *Phys. Rev. Lett.*, 86:155–158, 2001.

84. T. McConville and B. Serin. *Phys. Rev.*, 140:A1169, 1965.

85. Bourgeois O., Skipetrov S. E., Ong F., and Chaussy J. *Phys. Rev. Lett.*, 94:057007, 2005.

86. Fon W. C., Schwab K. C., Worlock J. M., and Roukes M. L. *Nano Lett.*, 05:1968, 2005.

87. F. R. Ong and O. Bourgeois. *European Phys. Lett.*, 79:67003, 2007.

88. F. R. Ong, O. Bourgeois, S. E. Skipetrov, and J. Chaussy. *Phys. Rev. B*, 74:140503(R), 2006.

89. H. Kupfer, G. Linker, G. Ravikumar, Th. Wolf, A. Will, A. A. Zhukov, B. Obst, and H. Wuhl. *Phys. Rev. B*, 67:064507, 2003.

90. E. T. Filby, A. A. Zhukov, P. A. J. de Groot, M. A. Ghanem, P. N. Bartlett, and V. V. Metlushko. *Appl. Phys. Lett.*, 89:092503, 2006.

91. Z.-L. Xiao, C.Y. Han, W.-K. Kwok, H.-H. Wang, U. Welp, J. Wang, and G.W. Crabtree. *J. Am. Chem. Soc.*, 126:13817, 1998.

92. V. A. Schweigert and F. M. Peeters. *Phys. Rev. B*, 57:13817, 1998.

93. J. J. Palacios. *Phys. Rev. B*, 58:5948(R), 1998.

94. J. J. Palacios. *Phys. Rev. Lett.*, 84:1796, 2000.

95. V. V. Moshchalkov, L. Gielen, C. Strunk, R. Jonckheere, X. Qiu, C. Van Haesendonck, and Y. Bruynseraede. *Nature (London)*, 373:319, 1995.

96. V. Bruyndoncx, L. Van Look, M. Verschuere, and V. V. Moshchalkov. *Phys. Rev. B*, 60:10468, 1999.

97. A. K. Geim, S. V. Dubonos, I. V. Grigorieva, K. S. Novoselov, F. M. Peeters, and V. A. Schweigert. *Nature (London)*, 407:55, 2000.

98. A. Kanda, B. J. Baelus, F. M. Peeters, K. Kadowaki, and Y. Ootuka. *Phys. Rev. Lett.*, 93:257002, 2004.

99. B. J. Baelus, A. Kanda, F. M. Peeters, Y. Ootuka, and K. Kadowaki. *Phys. Rev. B*, 71:140502, 2005.

100. J. Bonca and V. V. Kabanov. *Phys. Rev. B*, 65:012509, 2001.

101. A. S. Mel'nikov, I. M. Nefedov, D. A. Ryzhov, I. A. Shereshevskii, V. M. Vinokur, and P. P. Vysheslavtsev. *Phys. Rev. B*, 65:140503, 2002.

102. M. Morelle, G. Teniers, L. F. Chibotaru, A. Ceulemans, and V. V. Moshchalkov. *Physica C*, 369:351, 2002.

103. M. Morelle, J. Bekaert, and V. V. Moshchalkov. *Phys. Rev. B*, 70:094503, 2004.

104. B. J. Baelus, A. Kanda, N. Shimizu, K. Tadano, Y. Ootuka, K. Kadowaki, and F. M. Peeters. *Phys. Rev. B*, 73:024515, 2006.

105. A. K. Elmurodov, D. Y. Vodolazov, and F. M. Peeters. *Europhys. Lett.*, 74:151, 2006.

106. F. Mohamed, M. Troyer, G. Blatter, and I. Luk'yanchuk. *Phys. Rev. B*, 65:224504, 2002.

107. B. J. Baelus, D. Sun, and F. M. Peeters. *Phys. Rev. B*, 75:174523, 2007.

108. V. N. Gladilin, J. Tempere, I. F. Silvera, J. T. Devreese, and V. V. Moshchalkov. *Phys. Rev. B*, 77:024512, 2008.

109. J. Tempère, V. N. Gladilin, I. F. Silvera, J. T. Devreese, and V. V. Moshchalkov. *Phys. Rev. B*, 79:134516, 2009.

110. Q. Du and L. Ju. *J. Comp. Phys.*, 201:511, 2004.

111. M. M. Doria, A. R. de C. Romaguera, and F. M. Peeters. *Phys. Rev. B*, 75:064505, 2007.

112. A. R. de C. Romaguera, M. M. Doria, and F. M. Peeters. *Phys. Rev. B*, 76:020505R, 2007.

113. U. Schumann and R. A. Sweet. *J. Comp. Phys.*, 75:123, 1988.

114. B. J. Baelus, F. M. Peeters, and V. A. Schweigert. *Phys. Rev. B*, 63:144517, 2001.

115. N. E. Hussey, J. R. Cooper, R. A. Doyle, C. T. Lin, W. Y. Liang, D. C. Sinclair, G. Balakrishnan, D. McK. Paul, and A. Revcolevschi. *Phys. Rev. B*, 53:6752, 1996.

116. B. J. Baelus, F. M. Peeters, and V. A. Schweigert. *Phys. Rev. B*, 61:9734, 2000.

117. D. Y. Vodolazov, B. J. Baelus, and F. M. Peeters. *Phys. Rev. B*, 66:054531, 2002.

118. A. Kanda, B. J. Baelus, D. Y. Vodolazov, J. Berger. Furugen, Y. Ootuka, and F. M. Peeters. *Phys. Rev. B*, 76:094519, 2007.

119. V. R. Misko, Sergey Savel'ev, and Franco Nori. *Phys. Rev. B*, 74:024522, 2006.

120. A. V. Silhanek, L. Van Look, S. Raedts, R. Jonckheere, and V. V. Moshchalkov. *Phys. Rev. B*, 68:214504, 2003.

121. A. V. Silhanek, L. Van Look, R. Jonckheere, B. Y. Zhu, S. Raedts, and V. V. Moshchalkov. *Phys. Rev. B*, 72:014507, 2005.

122. G. R. Berdiyorov, M. V. Milošević, and F. M. Peeters. *Phys. Rev. Lett.*, 96:207001, 2006.

123. G. R. Berdiyorov, M. V. Milošević, B. J. Baelus, and F. M. Peeters. *Phys. Rev. B*, 70:024508, 2004.

124. Qiang Du. *J. Math. Phys.*, 46:095109, 2005.

125. A. R. de C. Romaguera, M. M. Doria, and F. M. Peeters. *Phys. Rev. B*, 75:184525, 2007.

126. Ben Xu, M. V. Milošević, and F. M. Peeters. *Phys. Rev. B*, 77:144509, 2008.

127. M. M. Doria and G. F. Zebende. *Phys. Rev. B*, 66:064519, 2002.

128. G. R. Berdiyorov, M. V. Milošević, and F. M. Peeters. *Phys. Rev. B*, 74:174512, 2006.

129. H. Nordborg and V. M. Vinokur. Interaction between a vortex and a columnar defect in the london approximation. *Phys. Rev. B*, 62:12408–12412, Nov 2000.

130. I. Baladié and A. Buzdin. Vortex trapping by tilted columnar defects. *Phys. Rev. B*, 61:11704–11710, May 2000.

131. M. V. Milošević, M. T. I. Rakib, and F. M. Peeters. *Europhys. Lett.*, 77:27005, 2007.

132. A. N. Grigorenko, S. J. Bending, I. V. Grigorieva, A. E. Koshelev, T. Tamegai, and S. Ooi. *Phys. Rev. Lett.*, 94:067001, 2005.

133. A. Oral, S. J. Bending, and M. Henini. *Appl. Phys. Lett.*, 69:1324, 1996.

134. G. Piacente, I. V. Schweigert, J. J. Betouras, and F. M. Peeters. *Phys. Rev. B*, 69:045324, 2004.

135. Guo-Qiao Zha, Shi-Ping Zhou, Bao-He Zhu, and Yao-Ming Shi. *Phys. Rev. B*, 73:104508, 2006.

136. D. H. Douglass Jr. *Phys. Rev.*, 132:513, 1963.

137. V. A. Schweigert and F. M. Peeters. *Phys. Rev. Lett.*, 83:2409, 1999.

138. R. L. Hilderbrandt. *J. Comput. Chem.*, 1:179, 1977.

139. C. J. Cerjan and W. H. Miller. *J. Chem. Phys.*, 91:7002, 1981.

140. D. S. Golubović, M. V. Milošević, F. M. Peeters, and V. V. Moshchalkov. *Phys. Rev. B*, 71:180502, 2005.

141. I. V. Grigorieva, W. Escoffier, V. R. Misko, B. J. Baelus, F. M. Peeters, L. Y. Vinnikov, and S. V. Dubonos. *Phys. Rev. Lett.*, 99:147003, 2007.

142. D. E. Prober. *Nature Nanotech.*, 3:459, 2008.

143. D. S. Akeri, M. S. Armel-Funkhouser, and M. J. Attisha. *Phys. Rev. D.*, 72:052009, 2005.

144. G. N. Gol'tsman, O. Okunev, G. Chulkova, A. Lipatov, A. Semenov, K. Smirnov, B. Voronov, A. Dzardanov, C. Williams, and R. Sobolewski. Picosecond superconducting single-photon optical detector. *Appl. Phys. Lett.*, 79:705–707, 2001.

145. T. McConville and B. Serin. *Phys. Rev. Lett.*, 13:365, 1964.

146. Paul Zoller and J. R. Killinger. *Phys. Rev.*, 172:390, 1968.

147. H. Choi, K. Yawata, T. M. Haard, J. P. Davis, G. Gervais, N. Mulders, P. Sharma, J. A. Sauls, and W. P. Halperin. *Phys. Rev. Lett.*, 93:145301, 2004.

148. P. Singha Deo, J. P. Pekola, and M. Manninen. *Europhys. Lett.*, 50:649, 2000.

149. W. C. Fon, K. C. Schwab, J. M. Worlock, and M. L. Roukes. *Nano Lett.*, 5:1968, 2005.

150. Alexander L. Fetter and Pierre C. Hohenberg. *Superconductivity.*

151. Koichi Watanabe, Takafumi Kita, and Masao Arai. *Phys. Rev. B*, 71:144515, 2005.

152. Alan J. Bray. *Phys. Rev. B*, 9:4752, 1974.

153. H. J. Fink and V. Grünfeld. *Phys. Rev. B*, 23:1469, 1981.

154. X. Zhang and J. C. Price. *Phys. Rev. B*, 55:3128, 1997.

155. D. S. Golubović, W. V. Pogosov, M. Morelle, and V. V. Moshchalkov. *Appl. Phys. Lett.*, 83:1593, 2003.

156. D. S. Golubović, W. V. Pogosov, M. Morelle, and V. V. Moshchalkov. *Europhys. Lett.*, 65:546, 2004.

157. J Provost, E Paumier, and A Fortini. *J. Phys. F: Metal Phys.*, 4:439, 1974.

158. R. D. Parks and W. A. Little. *Phys. Rev.*, 133:A97, 1964.

159. S. V. Yampolskii, F. M. Peeters, B. J. Baelus, and H. J. Fink. *Phys. Rev. B*, 64:052504, 2001.

160. C. Caroli and J. Matricon. *Phys. Kondens. Materie*, 3:380, 1965.

161. Weiyi Zhang, J, Kurkijarvi, and E. V. Thuneberg. *Phys. Lett.*, 109A:238, 1985.

162. Lorenz Kramer and Werner Pesch. *Z. Physik*, 269:59, 1974.

163. U. Klein. *Journal of Low Temperature Physics*, 69.

164. Thuneberg E. V. and Kurkijärvi J. *Phys. Rev. B*, 29:3913, 1984.

165. U. Klein. *Phys. Rev. B*, 40:6610, 1989.

166. N. Schopohl and K. Maki. *Phys. Rev. B*, 52:490, 1995.

167. Nakai N., Miranović P., Ichioka M., and Machida K. *Phys. Rev. B*, 73:172501, 2006.

168. A. S. Mel'nikov and V. M. Vinokur. *Nature (London)*, 415:60, 2002.

169. Kaori Tanaka, Istvan Robel, and Boldizsar Janko. *PNAS*, 99:5233, 2002.

170. Joel D. Shore., Huang Ming, Dorsey Alan T., and Sethna James P. *Phys. Rev. Lett.*, 62:3089, 1989.

171. Masanori Ichioka, Nobuhiko Hayashi, and Kazushige Machida. *Phys. Rev. B*, 55:6565, 1997.

172. Dahm T., Graser S., Iniotakis C., and Schopohl N. *Phys. Rev. B*, 66:144515, 2002.

173. Klein. U. *Phys. Rev. B*, 41:4819, 1990.

174. C. Caroli, Ann. Inst. Henri Poincare 4, 159 1966). 5R. Leadon, and H. Suhl. *Phys. Rev.*, 165:596, 1968.

175. J. Bardeen, R. Kummel, A. E. Jacobs, and L. Tewordt. *Phys. Rev.*, 187:556, 1969.

176. Nakai N., Miranović P., Ichioka M., Hess H. F., Uchiyama K., Nishimori H., Kaneko S., Nishida N., and Machida K. *Phys. Rev. Lett.*, 97:147001, 2006.

177. M. Ichioka, N. Hayashi, and N. Enomoto *et al. Phys. Rev. B*, 53:15316, 1996.

178. D. A. Butts and D. S. Rokhsar. *Nature (London)*, 397:327, 1999.

179. P. Popovich, A. V. Boris, O. V. Dolgov, A. A. Golubov, D. L. Sun, C. T. Lin, R. K. Kremer, and B. Keimer. *Phys. Rev. Lett.*, 105:027003, 2010.

Curriculum Vitae

Ben XU ????
Born on July 14^{th}, 1980
in Changde / China

Education

- September 1997 - July 2001: B. Sc in Materials Engineering, Department of Materials Science and Engineering, Central South University, Changsha, China.
- September 2002 - July 2005: M. Sc in Materials Science and Engineering, Department of Materials Science and Engineering, Tsinghua University, Beijing, China.
- September 2005 - September 2006: Advanced Master on Nanophysics, Unversity of Antwerp, Belgium.

- October 2006 - October 2011: Research assistant, Condensed Matter Theory group, Physics Department, University of Antwerp, Belgium. Promotors: Prof. dr. F. M. Peeters, Prof. dr. M. V. Milošević

Scientific award

Chinese Government Award for Outstanding Self-Financed Students Abroad (2009)

Publications

1. Ben Xu, M. V. Milošević, Shi-Hsin Lin, F. M. Peeters and B. Jankó, *Formation of Multiple-Flux-Quantum Vortices in Mesoscopic Superconductors from simulations of Calorimetric, Magnetic, and Transport Properties*, Phys. Rev. Lett. **107**, 057002 (2011)
2. Ben Xu, M. V. Milošević and F. M. Peeters, *Calorimetric properties of mesoscopic superconducting disks, rings and cylinders*, Phys. Rev. B **81**, 064501 (2010)
3. Ben Xu, M. V. Milošević and F. M. Peeters, *Second-order multiple-quanta flux entry into a perforated spherical mesoscopic superconductor*, Phys. Rev. B **82**, 214501 (2010)
4. Ben Xu, M. V. Milošević and F. M. Peeters, *Vortex matter in oblate mesoscopic superconductors with a hole: broken symmetry vortex states and multi-vortex entry*, New Jounal of Physics **11**, 013020 (2009)
5. Ben Xu, M. V. Milošević, F. M. Peeters, *Magnetic properties of vortex states in spherical superconductors*, Phys. Rev. B. **77**, 144509 (2008)
6. V. R. Misko, B. Xu, and F. M. Peeters, *Formation and size dependence of vortex shells in mesoscopic superconducting niobium disks*, Phys Rev B **76**, 024516 (2007)
7. V. R. Misko, B. Xu, and F. M. Peeters, *Size-dependence of vortex shells in mesoscopic superconducting disks*, Physica. C, **468**,726 (2008)

Conferences

- 25th Conference on Low Temperature Physics, Netherlands, 2008
  Poster "Magnetic properties of vortex states in spherical superconductors"
- Vortex VI, vortex matter on nanostructured superconductors, Greece, 2009
  Poster section "Calorimetric properties of mesoscopic superconducting disks, rings, and cylinders"
- International conference of superconductivity and magnetism, Turkey, 2010
  Poster "Second-order multiple-quanta flux entry into a perforated spherical mesoscopic superconductor"

- Vortex VII, vortex matter on nanostructured superconductors, Greece, 2011
  Poster section "Formation of multi-quanta vortices in mesoscopic superconductors: electronic, calorimetric and magnetic evidence"

Summer Schools

- Utrecht summer school on Theoretical Physics, Netherlands, 2007
- Instituto Nicolás Cabrera summer school for Low Temperature Physics, Madrid, Spain, 2008
- Modern theories of correlated electron systems, Les Houches Summers school, France, 2009
- Electronic Oxides: Correlation Phenomena, Exotic Phases, and Novel Functionalities, Helmholtz Institute spring school, Jülich, Germany, 2010
- Multiscale simulation of heterogeneous materials and coupling of thermodynamic models, Leuven, Belgium, 2011